HANDBOOK ON RADIOMETEOROLOGY

RADIOCOMMUNICATION BUREAU
EDITION OF 2013

HANDBOOK ON RADIOMETEOROLOGY

PREFACE

The original Handbook on Radiometeorology was conceived under the chairmanship of Professor Gert Brussaard (Netherlands), developed by Working Party 3J (Propagation fundamentals) of ITU-R Study Group 3 (Radiowave Propagation), and published in 1996.

This revision was updated by experts in Working Party 3J under the chairmanship of Professor Marlene Pontes (Brazil) and incorporates material relevant to recent revisions of ITU-R Recommendations on propagation relating to radiometeorology.

The list of major contributors to this revised version is as follows:

Cesar Amaya

Daniel Arapoglou

Ana Benarroch

Harvey Berger

Pierre Bouchard

Xavier Boulanger

Laurent Castanet

Chris Gibbins

Vaclav Kvicera

Lorenzo Luini

Paul McKenna

Aldo Paraboni

Marlene Pontes

Patricia Raush

Carlo Riva

Theresa Rusyn

Luiz Silva Mello

The Handbook on Radiometeorology was edited by Harvey Berger and Marlene Pontes.

Contents

Page

Page

Page

Page

Page

Page

CHAPTER 1

Introduction

1.1 Purpose of the Handbook on Radiometeorology

The Handbook on Radiometeorology supplies background and supplementary information on radiowave propagation effects, and serves as a companion volume and guide to the Recommendations that have been developed by Study Group 3 (SG3) Working Party 3J (Propagation Fundamentals) of the ITU Radiocommunication Sector (ITU-R). It provides general information on radiometeorology for those who use the ITU-R P series of Recommendations, those who wish to have a more detailed understanding of the Recommendations and those who wish to contribute to their development.

The Recommendations on effects of the atmosphere, named here as radiometeorology, are largely based on scientific studies carried out over a large period of time. They are developed from consensus among the delegates regarding the general knowledge on the subject. Since such knowledge is always developing, it is of prime importance to be able to keep track of the results of scientific studies on which the Recommendations are based. If that information is lost, it is no longer possible to revisit the subjects treated by the Recommendations and improve these for the benefit of the users. Also, reviewing the background information may help the user to appreciate the accuracy and limitations of the models given.

Since the Recommendations intend to objectively present methods for practical applications, it is inevitable that the user will encounter questions about these methods that are not fully answered in the Recommendations themselves. In order to assist the user of the Recommendations and to give him guidance on the basis for the recommended methods, this Handbook provides background information as well as up-to-date summaries of experimental results and preliminary results of further modelling.

It is for this purpose that this Handbook on Radiometeorology has been prepared by ITU-R Study Group 3 (Radiowave Propagation). It should serve both the users inside and outside the Study Group and the members of the Study Group in charge of the development of Recommendations on the effects of the troposphere on radiowave propagation.

1.2 Applicable texts

The Recommendations on radiometeorology and statistical modelling methods for which Working Party 3J on Propagation Fundamentals is responsible and a number of Recommendations that are important to the development of the work carried out in Working Party 3J to which this Handbook provides background information, are listed below (situation as per June 2013).

Recommendation ITU-R P.453-10	The radio refractive index: its formula and refractivity data
Recommendation ITU-R P.525-2	Calculation of free-space attenuation
Recommendation ITU-R P.527-3	Electrical characteristics of the surface of the Earth
Recommendation ITU-R P.581-2	The concept of “worst month”
Recommendation ITU-R P.676-9	Attenuation by atmospheric gases

Recommendation ITU-R P.678-1	Characterization of the natural variability of propagation phenomena
Recommendation ITU-R P.833-7	Attenuation in vegetation
Recommendation ITU-R P.834-6	Effects of tropospheric refraction on radiowave propagation
Recommendation ITU-R P.835-5	Reference standard atmospheres
Recommendation ITU-R P.836-4	Water vapour: surface density and total columnar content
Recommendation ITU-R P.837-6	Characteristics of precipitation for propagation modelling
Recommendation ITU-R P.838-3	Specific attenuation model for rain for use in prediction methods
Recommendation ITU-R P.839-3	Rain height model for prediction methods
Recommendation ITU-R P.840-5	Attenuation due to clouds and fog
Recommendation ITU-R P.841-4	Conversion of annual statistics to worst-month statistics
Recommendation ITU-R P.1057-2	Probability distributions relevant to radiowave propagation modelling
Recommendation ITU-R P.1058-2	Digital topographic databases for propagation studies
Recommendation ITU-R P.1144-6	Guide to application of the propagation methods of Radiocommunication Study Group 3
Recommendation ITU-R P.1322	Radiometric estimation of atmospheric attenuation
Recommendation ITU-R P.1407-4	Multipath propagation and parameterization of its characteristics
Recommendation ITU-R P.1510	Annual mean surface temperature
Recommendation ITU-R P.1511	Topography for Earth-to-space propagation modelling

NOTE – The Handbook (in particular Chapter 8) applies only to the part of Recommendation ITU-R P.372-8 (Radio noise) treating tropospheric noise emission.

1.3 Cross-reference table

The following table providing cross references between the chapters of the Handbook and the Recommendations may be useful in finding the applicable texts.

TABLE 1.1

Relation between Chapters and Recommendations

Chapter / **Recomm.**	**2**	**3**	**4**	**5**	**6**	**7**	**8**	**9**	**10**
P.372							X		
P.453	X	X	X						
P.581									X
P.676					X		X		
P.678									X
P.834			X						
P.835	X				X				
P.836	X								
P.837	X					X			
P.838				X		X		X	
P.839	X					X			
P.840				X		X	X	X	
P.841									X
P.1057									X
P.1322							X		
P.1510	X								
P.1621			X		X	X			
P.1623	X								X

CHAPTER 2

Physical characteristics of the atmosphere

The atmosphere studied here is limited to the troposphere, the lower layer of the Earth's atmosphere. It is characterized by a regular decrease in temperature as altitude increases, at the average lapse rate of –5 to –6°K per km. This is where most meteorological phenomena, including the formation of clouds, develop. The altitude of the upper limit of the troposphere varies between 8 km at the poles and 18 km at the equator depending on the geographical latitude, seasons, and meteorological conditions. In the region immediately above the troposphere, known as the tropopause, the temperature varies between 190°K at the equator and 220°K at the poles. The tropopause constitutes an upper limit for most clouds.

The constituents of the atmosphere vary with altitude, and gases become increasingly light and increasingly rare as the altitude increases. The constituents are generally classified into three categories: constituents with fixed density (major constituents), constituents with variable density (minor constituents) and aerosols.

The major constituents of the atmosphere have a quasi-uniform distribution until an altitude of 15 to 20 km. Among these constituents, the most important are nitrogen (N_2), which is 78.095 percent of the total volume; oxygen (O_2), which is 20.93 percent of the total volume; argon (Ar), which is 0.93 percent of the total volume; and carbon dioxide (CO_2), which is 0.03 percent of the total volume.

The minor constituents of the atmosphere are water vapour (H_20), neon (Ne), helium (He), krypton (Kr), methane (CH_4), and hydrogen (H_2). The concentration of these minor constituents depends on the geographical location, environment (continental or maritime) and weather conditions. Water vapour is the main constituent, and its concentration varies with geography and local climate.

Aerosols are extremely fine suspended particles and have a very low fall rate. Their size generally lies between 10^{-2} and 100 μm. Aerosols may be either liquid or solid, and examples are microscopic dust or salt crystals in maritime environments.

The following sections discuss the variability of water vapour and oxygen density at ground level, the variability of water vapour versus height, the characteristics of precipitation (drop size distribution, hydrometeor shape and orientation, terminal velocity, drop temperature), the statistical characteristics of point rainfall intensity (or rainfall rate), the horizontal structure of rainfall, the characteristics of fog and clouds, and the characteristics of sand and dust storms.

2.1 Variability of water vapour and oxygen density at ground level

Recommendation ITU-R P.835 provides information on the various reference standard atmospheres, comprised of oxygen and water vapour, which can be used for the calculation of attenuation by atmospheric gases. This section discusses the variability of these gases.

Recommendation ITU-R P.836 provides information for obtaining the annual values of surface water vapour density, ρ (g/m^3), exceeded for 0.1, 0.2, 0.3, 0.5, 1, 2, 3, 5, 10, 20, 30, 50, 60, 70, 80, 90, 95, and 99% of an average year. As these maps have a resolution of 1.125 degrees in both latitude and longitude, a detailed interpolation procedure to obtain the corresponding values of columnar water vapour density at any desired location on the surface of the Earth is provided. Example contours of the annual average water vapour density for exceedance probabilities of 0.1, 0.5, 1, 5, 10, 20 and 50%, derived from the digital maps, are presented.

The relationships between water vapour density, ρ, water vapour pressure and relative humidity are given in Recommendation ITU-R P.453.

Water vapour density is highly variable. To a first approximation, the temporal fluctuations of ρ may be assumed to follow a normal law with a standard deviation of approximately one quarter of the mean value.

The statistical variation of water vapour density is affected by atmospheric temperature. The relative humidity rarely reaches 100 percent implying that the maximum water vapour density will not exceed the value corresponding to saturation at the atmospheric temperature.

Water vapour density increases to a value near saturation in clouds and rainfall. At frequencies above about 15 GHz the correlation between the attenuation produced by water vapour absorption and the attenuation produced by rain should be taken into account when estimating attenuation statistics or in interference calculations.

In general, rain occurs during the season with the highest average values of surface water vapour density and the higher values of rain rate are generally correlated with the higher seasonal surface water vapour density values.

Statistical analysis of absolute humidity data for 62 sites in the United Kingdom indicates that the water vapour densities exceeded for 0.1% and 99.9% of the time are approximately 15 g/m^3 and 2.2 g/m^3 respectively, with values approximately 10% larger in the south and 10% smaller in north-east Scotland [UK Meteorology Office, 1976].

2.2 Variability of the height profile of water vapour

The dependence of water vapour density on height (the "height profile") is highly variable. Recommendation ITU-R P.835 provides several reference atmospheric profiles for use in general prediction methods.

The total water vapour content along a path can be used for the calculation of excess path length and for the attenuation due to atmospheric water vapour, where the attenuation due to atmospheric water vapour is assumed to be proportional to the total water vapour content through its specific mass absorption coefficient.

Recommendation ITU-R P.836 provides information for obtaining the annual values of total columnar (at zenith) water vapour content, V (kg/m^2), exceeded for 0.1, 0.2, 0.3, 0.5,1, 2, 3, 5, 10, 20, 30, 50, 60, 70, 80, 90, 95 and 99% of the year, available from digital maps in the Radiocommunication Study Group 3 website. These maps also have a resolution of 1.125 degrees in both latitude and longitude, and a detailed interpolation procedure to obtain the corresponding values of columnar water vapour density at any desired location on the surface of the Earth is provided, as well as example contours for exceedance probabilities of 0.1, 0.5, 1, 5, 10, 20 and 50%.

2.3 Precipitation characteristics

2.3.1 Types of precipitation

The following types of precipitation can be distinguished:

Stratiform precipitation

Stratiform precipitation is characterized by widespread regions with low rain rates and small embedded showers with rain rates up to 25 mm/h. This type of precipitation is horizontally stratified with rain up to the height of the bright band, snow to heights of the order of 7 km and ice crystals to heights near 9 km.

Convective precipitation

Convective precipitation is characterized by localized areas of relatively intense precipitation characterized by strong up- and down-drafts extending through a deep region of the troposphere. The localized regions are columnar in nature sometimes extending to the tropopause. Very intense precipitation may occur with horizontal scales of several kilometres and durations of tens of minutes.

Monsoon precipitation

Monsoon precipitation is characterized by a sequence of bands of intense convection followed by intervals of stratiform precipitation. The bands are typically 50 km across, hundreds of kilometres in length and produce heavy precipitation lasting for several hours.

Tropical storms

Tropical storms are large organized regions of precipitation extending over hundreds of kilometres. The storms are characterized by several spiral bands terminating in regions of intense precipitation surrounding the central region or eye of the storm. The bands also contain regions of intense convection.

2.3.2 Drop size distribution

The size, shape and orientation distributions of raindrops may vary within a storm. Observations show that, on average, the drop size distribution is relatively stable, changing mainly with rain rate. The Laws and Parsons [1943] drop size distribution has been used to develop the specific rain attenuation model in Recommendation ITU-R P.838. The relative densities of small drops having diameters less than 0.5 mm are not well modelled by the Laws and Parsons distribution, and the Marshall-Palmer [1948] distribution can be used in this diameter regime. The relative concentration of small drops can be highly variable and the use of a single model distribution may not be appropriate for all locations. In tropical regions, the raindrop size distribution proposed by Ajayi and Olsen [1985] can be employed. Chapter 7 discusses the impact of drop size distribution models on specific attenuation calculations.

2.3.3 Hydrometeor shape and orientation

Falling rain drops are deformed due to gravity and horizontal wind gradients, and the drops may vibrate and oscillate while falling. The typical drop shape is an oblate spheroid with the symmetry axis nearly vertical. Horizontal forces due to vertical wind gradients may cause the mean orientation to be canted by a few degrees from the vertical symmetry axis. The drop shape distribution has been modelled as a function of drop size by Pruppacher and Pitter [1971], and these shape predictions have been verified by observations made in the laboratory by Pruppacher and Beard [1970]. However, observations in the atmosphere tend to show smaller axial ratios than calculated by the models for the same drop volume.

Snow and ice particles have often been modelled using spheroidal shapes. The bulk density of snow is low (the ice and air mixture has a larger fraction of air within the boundaries of the spheroid), and the snow particles produce little polarization effects. High bulk density ice particles such as ice plates and columns that occur high in the atmosphere produce measurable depolarization when a significant fraction of the particles have the same orientation.

Ice and snow particles are rigid and are apt to tumble while falling. Drag forces tend to force the ice particles to fall with an orientation which maximizes the drag force. Electric fields have also been observed to similarly orient a significant fraction of the ice particles.

2.3.4 Terminal velocity

Gunn and Kinzer [1949] reported the terminal velocities of raindrops as a function of drop size. The measurements were made in laboratory conditions but have been assumed to apply in the atmosphere. The velocities of the drops depend on air density and are therefore a function of height. Radar observations show that, on average, the reflectivity value does not significantly change with height below the rain height. The number and sizes of the drops and the liquid water content of a volume of drops therefore does not significantly change with height. Since the terminal velocity is height dependent, the liquid water flux or rain rate is therefore height dependent; and since the specific attenuation depends primarily on liquid water content, the specific attenuation does not significantly vary with height below the rain height.

2.3.5 Drop temperature

The temperature of falling raindrops approximates the wet bulb temperature for the temperature, pressure, and humidity of the surrounding air. Small liquid droplets can exist at temperatures below 0°C, especially in the updraft regions of convective storms and in super cooled fog. Ice and water mixtures can also exist in downdraft regions below the height of the 0°C isotherm. On average, the most significant liquid water drops that contribute to rain attenuation occur between the height of the 0°C isotherm and the surface.

2.4 Statistical characteristics of point rainfall intensity

2.4.1 Cumulative distribution of rainfall intensity

Measurements carried out with fast-response rain gauges have indicated that high intensity rainfall tends to be concentrated in short periods of time, typically a few minutes. Consequently, experimental cumulative distributions of rainfall intensity depend on the integration time. The monthly, daily and in some instances hourly rainfall accumulations readily available in the publications of the various meteorological services cannot be utilized directly to obtain cumulative distributions of rainfall intensity down to small percentages of time.

Fine time-resolution rainfall data have been obtained by means of fast-response rain gauges in Europe and from tipping-bucket rain gauges in Canada. Corresponding rainfall climatic classifications have been proposed on the basis of these data [Kalinin and Nadenenko, 1975; Fedi, 1979a; Segal, 1979 and 1980a]. Other regions have been categorized by means of rainfall rate distributions generally derived on the basis of somewhat longer integration times, typically five or ten minutes [Lin, 1978; Morita, 1978; CCIR, 1986-90a; Burgueno *et al*., 1987].

In 1999, Study Group 3 adopted a new version of Recommendation ITU-R P.837 (version 2) in which the old rain zone maps (given in version 1) had been replaced by the Salonen-Baptista double exponential model, [Poiares-Baptista and Salonen, 1998]. Recommendation ITU-R P.837 relies on this model and requires as input the following meteorological parameters:

– M_S = mean annual stratiform rainfall amount (mm);

– M_C = mean annual convective rainfall amount (mm);

– P_{r6} = probability of rainy 6-hours periods (%).

Two databases available at ESA [Martellucci, 2004]: NA-4 and ERA 15 have been used to generate maps of input parameters for ITU-R Recommendations. The ECMWF Re-analysis (ERA) 15 database has been used to generate maps of input parameters for Recommendations ITU-R P.837.

The ERA-15 database contains data derived from ECMWF re-analysis activities of the period (January 1979 - December 1993) [ERA 15, 1999]. Each point of a regular grid (1.5×1.5 degrees) that covers the whole globe contains values referred to time 00.00, 06:00, 12:00, 18:00 UTC of the

following precipitation parameters: stratiform accumulated precipitation; convective accumulated precipitation and total accumulated snowfall. These data has been used to generate maps of M_s (mean annual stratiform rain amount), M_c (mean annual convective rain amount) and P_{r6}: (probability of rain in six hours) currently used in Recommendation ITU-R P.837. From these parameters, the mean total rainfall amount (M_t) and the mean annual convectivity ratio that is the convective-rainfall-amount to total-rainfall-amount ratio (β) can be calculated.

More recently, a new product has been available from ECMWF (ERA40 dataset), which is a new reanalysis product generated by ECMWF over a longer period (mid 1957 - 2001) and with a better spatial resolution than ERA 15 (regular grid of 1.125×1.125 degrees) [ERA 40, 2002]. A major difference between the ERA 15 and the ERA 40 datasets is the possibility of deriving for the latter the convective and large-scale rain accumulated over six hours directly from the corresponding precipitation and snowfalls quantities.

The methodology used to improve the prediction method given in Recommendation ITU-R P.837 is described in [Castanet *et al*., 2007a and b].

When appropriate rainfall intensity data exists for a certain location, this data should be used to determine the cumulative distribution of rainfall rate. In the absence of such information, the information presented in Recommendation ITU-R P.837 should be for the prediction of rainfall rate statistics with a 1-min integration time. The data provided in this Recommendation are also suggested for interference and coordination distance calculations.

The digital maps in Recommendation ITU-R P.837 have a spatial resolution of 1.125 degrees in latitude and 1.125 degrees in longitude. The rainfall rate model is divided into two components: 1) large scale (widespread or stratiform) precipitation, and 2) convective scale (shower-type) precipitation.

The ECMWF data parameters globally apply the Rice-Holmberg model [Rice and Holmberg, 1973; Dutton and Dougherty, 1974] and the Salonen-Baptista method [Salonen and Baptista, 1997] for the derivation of short-integration time precipitation statistics from long-integration time data.

The GPCP data set from the Global Energy and Water Cycle Experiments (GEWEX) includes monthly precipitation amounts over land areas with a spatial resolution of 2.5 degrees x 2.5 degrees. The GPCP data is based on rainfall measurements from more than 30 000 rain gauge worldwide stations. The minimum time resolution is one month; however, the GPCP data does not distinguish between rain and snow.

The mean annual precipitation amounts from 1986 to 1995 have been used in the development of Recommendation ITU-R P.837. Since the GPCP precipitation data is based on measured rainfall, it is considered to be more accurate than the ECMWF predictions; however, there are several areas of the world where GPCP measured data is scarce or non-existent. In this case, the GPCP data was spatially interpolated using a technique that accounted for the topography. The GPCP precipitation totals were adjusted using the ECMWF's derived mean annual ratio of snowfall to rainfall to exclude snowfall, and the probabilities of 6-hour rainy periods derived from the ECMWF data were then adjusted to reflect the GPCP precipitation amounts.

Suitably calibrated, continuously-recording rain gauges with adequate sensitivity and time resolution should be used to obtain more accurate information on rainfall rate for a particular location or area. When tipping-bucket gauges are used, measurement of the time interval between successive tips is recommended for the lower rainfall rates. Unless the gauge and recording system are specifically designed for precise operation at the very highest expected rainfall rates, it may be preferable to integrate over several tips when these occur too rapidly to be resolved on an individual basis. Recommendation ITU-R P.311 provides the appropriate formats for the submission of rainfall statistics.

2.4.2 Yearly variability of the cumulative rainfall rate distribution

Rainfall is a natural, time-varying phenomenon. Many of the propagation prediction models employed in the design of RF systems make use of the long-term cumulative distribution of point rainfall intensity. Deviations from these predictions may be expected for any single year or series of years. An understanding of the year-to-year variability is important both in estimating the magnitude of the deviations from average behaviour that may reasonably be expected and in ascertaining the number of years of observations required to establish an accurate estimate of the true long-term mean rainfall rate distribution.

Of the various efforts made to understand the nature of year-to-year variation in the point rainfall rate distribution, only a few have had sufficiently long data samples available to examine the problem in depth. Aresu *et al.*, [1989] showed that for a 10-year observation period, the year-to-year variability is higher than 20%, while Crane [1990] has suggested a year-to-year variability of 35%.

Segal [1979] examined one-minute rainfall records covering a total of 68 years from four widely separated locations in different precipitation climate regimes. On the basis of the limited data available, it was concluded that the yearly values of rainfall rate were well approximated by a cube-root normal distribution. Burgueño *et al.*, [1987] concluded that the variation in yearly rainfall rate over 49 years at Barcelona was similarly distributed.

The problem has also been approached [CCIR, 1986-90b] by means of statistical resampling techniques to improve the sensitivity of the statistical examination of yearly variation of rainfall rate data for several locations in Canada. In that analysis, the distribution of yearly rainfall rate exceedances at fixed probability levels were tested against the full range of power-normal functions.

$$y = \frac{1}{\sigma\sqrt{2\pi}} \int \exp\left(-\frac{x^2}{2\sigma^2}\right) dx \tag{2.1}$$

where the independent variable $x = R^{\lambda}$ and $y = P(R)$. The exponent λ was allowed to vary over the range $0 < \lambda \leq 1$. A value of $\lambda = 1$ corresponds to the normal distribution, while the log-normal process corresponds to the limit $\lambda = 0$.

For probabilities less than about 0.1%, the optimum value of the exponent λ ranged from less than 0.1 at coastal locations to greater than 0.8 in the eastern continental region where both stratiform and convective precipitation are common.

The coefficient of variation σ/μ, where μ and σ are the mean and standard deviation of the appropriate power-normal distribution, was found to vary somewhat as a function of the probability reference level, particularly in the region where precipitation is most frequently orographic. A greater, inverse dependence was noted between the coefficient of variation and the total annual rainfall accumulation.

2.4.3 Conversion of rainfall rate distributions to equivalent one-minute statistics

Because of the rapidly varying nature of rainfall at a given point, the observed cumulative rainfall intensity distribution will depend on the integration time of the rain gauge. Annex 1 of Recommendation ITU-R P.837 includes a methodology to directly predict the Complementary Cumulative Distribution Function of the rain rate, also known as $P(R)$, starting from long-term meteorological information (see § 2.4.1). However, tests have shown that methods able to convert rainfall rate statistics from long (e.g. T = 30 minutes or 1 hour) to short integration time are more accurate than models like the one included in Annex 1 [Emiliani *et al.*, 2010] and, therefore,

whenever local measurements are available, though with coarse integration time, conversion methods should be preferred to estimate the local 1-minute integrated rainfall statistics.

In the literature several models are available for the conversion of rainfall statistics from long to short integration time and can be classified as:

– Empirical, which make use of conversion coefficients to be determined using regression techniques on experimental data.

– Physical, which rely on the processes involved in the formation and development of rain and its evolution in time.

Among all the conversion models available in the literature, the following ones can be applied on a global basis and require as input only the cumulative distribution function with long integration time:

A) Power Law relationship (PL method, see [Emiliani *et al*., 2009])

The method is based on the following expression which converts rain rate values of the P(R)

$$R_1(P) = a(T) R_T(P)^{b(T)} \tag{2.2}$$

where:

T: integration time (min)

P: probability

$R_1(P)$ and $R_T(P)$: rain rate values with integration time of 1 and T minutes respectively, exceeded with the same probability P.

$a(T)$ and $b(T)$: integration time dependent coefficients.

B) Conversion Factor modelled with Power Law (CF-PL method, see [Emiliani *et al*. 2009]).

The conversion depends on P and is expressed as:

$$CF(P) = R_1(P)/R_T(P), \quad CF(P) = a(T)\,P^{b(T)} \tag{2.3}$$

where $R_1(P)$, $R_T(P)$, $a(T)$ and $b(T)$ remain as defined for equation (2.2).

C) Lavergnat and Golé semi-physical method (LG, see [Lavergnat and Golé, 1998]).

The method is given by:

$$CF = 1/T \rightarrow R_1 = R_T / CF^{\alpha} \rightarrow P_1(R_1) = CF^{\alpha} P_T(R_T) \tag{2.4}$$

where α is an empirical conversion parameter.

$R_1(P)$, $R_T(P)$, $a(T)$ and $b(T)$ remain as defined for equation (2.2).

D) ERSC (EXponential CELL Rainfall Statistics Conversion) (see [Capsoni and Luini, 2009]).

The ERSC model, duly described in [Capsoni and Luini, 2009] (which the reader is addressed to for further details), has been recently included in Annex 3 of Recommendation ITU-R P.837-6. The method takes advantage of the EXCELL (EXponential CELL) model [Capsoni *et al*., 1987a] to simulate the accumulation process of a rain gauge with at a given integration time T. The meteorological environment for the site of interest is described by means of an ensemble of synthetic exponential rain cells, whose probability of occurrence depend on $P(R)_1$ and thus, vary from site to site. After being classified as stratiform or convective, such cells are employed to simulate the interaction of the rain field with a virtual rain gauge operating at a given integration

time T and, thus, to convert $P(R)_1$ into $P(R)_T$. To this aim, the synthetic rain cells rigidly translate at an effective velocity, different for stratiform (v_{strat}) and convective (v_{conv}) cells, that takes into account the actual space-time evolution of precipitation:

$$v_{convt} = v_{700}/k_1(T) \quad \text{and} \quad v_{strat} = k_2(T)v_{conv} \tag{2.5}$$

In (1), v_{700} is the wind velocity (relative to the isobar 700 hPa) provided on a global basis by the ECMWF (European Centre for Medium-Range Weather Forecast) on a 1.125°×1.125° geographical grid (ERA40 database), whereas $k_1(T)$ (>1) and $k_2(T)$ (>1) are the reduction factors dependent on the rain gauge integration time T:

$$k_1(T) = 0.185T^{0.498.} + 0.768 \quad \text{and} \quad k_2(T) = -0.017T^{0.746} + 0.69 \tag{2.6}$$

As a final step, in order to estimate $P(R)_1$ from $P(R)_T$, i.e. the actual goal of ERSC, an iterative optimization procedure is used: based on Genetic Algorithms, the goal is to identify the local $P(R)_1$ that, when used as input to the rain gauge simulation described above, provides the best possible estimate of the measured $P(R)_T$.

Whilst the methodology described in point D) is inherently global, the optimum coefficients (valid worldwide) for the empirical models mentioned in points A), B) and C) have been derived from a large set of $P_T(R)$ and $P_1(R)$ curves measured in many sites worldwide. They are summarized in Table 2-1 for different integration times. Note that the LG models propose a single coefficient for all T values.

Based on an extensive testing activity, ERSC was found to show the lowest overall prediction error and to provide the most stable trend of the performance both with the integration time and the climate region. For these reasons it has been adopted in Annex 3 of Recommendation ITU-R P.837 for the conversion of rainfall statistics from long ($5 \leq T \leq 60$ minutes) to short integration times. Further details on ERSC can be found [Capsoni and Luini, 2009], whilst the SG3 makes freely available online a Graphical User Interface for rainfall statistics conversion as recommended by ITU-R.

TABLE 2-1

Empirical parameters obtained by regression to the values in the measurement database

	PL		**CF-PL**		**LG**
	a	***b***	***a***	***b***	***a***
5 min to 1 min	0.906	1.055	0.985	−0.026	
10 min to 1 min	0.820	1.106	0.967	−0.051	
20 min to 1 min	0.683	1.215	0.913	−0.100	0.633
30 min to 1 min	0.561	1.297	0.897	−0.130	
60 min to 1 min	0.497	1.440	0.937	−0.181	

2.4.4 Models for the rainfall rate distribution

High intensity rainfall is highly variable from year to year and is difficult to record and measure experimentally. In system design, however, it is the highest rainfall rates that are frequently of interest, and a suitable mathematical model for the "tail" of the distribution is desirable.

At moderate rainfall rates where accurate measurements are feasible, the cumulative rainfall rate distribution can be well-approximated by a log-normal law. The log-normal law depends on the climatic region and is typically valid for rainfall rates between approximately 2 mm/h and 50 mm/h.

Although the log-normal distribution appeared to provide the best fit for low rainfall rates, studies conducted on measurements taken in Canada suggest that for short integration times, a power-law relationship can satisfactorily approximate the entire cumulative distribution beyond about 5 mm/h [Segal, 1980b].

The gamma function has also been proposed as an approximation to the rainfall rate distribution [Morita and Higuti, 1976] although this function does not appear to be generally applicable in many climatic regions [Fedi, 1979b; Segal, 1979]. Another analysis suggests that the rainfall rate distribution is better described by a model which approximates a log-normal distribution at low rates, and a gamma distribution at high rain rate [Moupfouma, 1987]. Annex 1 discusses the rain climatology and three models that appear to be suitable for global modelling of rainfall rate distributions.

Rather than attempting to find a multi-parameter analytical model to describe the complex variation of climate over the world, digital maps of rainfall statistics were collated using information of the ECMWF which is based on long-term data harmonised within a global circulation model. These maps are introduced in Recommendation ITU-R P.837.

2.4.5 Statistics of rainfall event duration

The statistical distribution of the duration of rainfall events that exceed specific thresholds is also of interest for the forecast of transmission reliability as it provides insight on fade duration statistics. There is a general agreement that this distribution is approximately log-normal. Measurements in Italy and in Greece indicated that the median durations for rainfall events are approximately inversely proportional to the values of the rainfall intensity threshold [Fedi and Merlo, 1977; Fedi, 1979a].

2.5 Horizontal structure of rainfall

The spatial and temporal structure of rainfall rate is inhomogeneous. Rain gauge records show short intervals of higher rain rate embedded in longer periods of lighter rain. Weather radar observations show small areas of higher rain rate embedded in larger regions of lighter rain. Such observations are typical of all occurrences of rain in all climate regions. Rainfall is often typed as widespread or stratiform and as convective. The differences between these types usually lie in the maximum associated rain rate but not with differences in spatial variability.

The rain process is spatially and temporally non-stationary on the time and space scales of importance to rain scatter or attenuation problems [Riva, 2002]. The non-stationarity of the rain process requires caution in the use of concepts such as a spatial correlation function for the estimation of attenuation on a path or the joint occurrence of scattering in a volume and attenuation along paths between antennas and the scattering volume. The variance and spatial covariance of the rain process increase with increased observation times or areas. The spatial correlation function also varies with changes in observation area or time, and the distance for a given correlation value may vary by as much as an order of magnitude.

2.5.1 Application to scattering by rain

Scattering occurs when an intense rain cell lies within the common volume of antenna beams. High resolution measurements are therefore important in determining the width of the cell. For application in statistically-based prediction methods for rain scattering as a factor in interference,

the horizontal extent of the rain cell has been defined as the area containing a peak value of reflectivity and limited by the points where the reflectivity is half (−3 dB) this peak value.

The cell diameter appears to have an exponential probability distribution of the form:

$$P(D) = \exp(-D / D_0) \tag{2.7}$$

where D_0 is the mean diameter of the cell and is a function of the peak rainfall rate R_{peak}.

Radar results indicate that the mean diameter D_0 decreases slightly with increasing R_{peak} (when $R_{peak} > 10$ mm/h). This relationship appears to obey a power law:

$$\mathrm{p}\, D_0 = a\, R_{peak}^{-b} \tag{2.8}$$

for $R_{peak} > 10$ mm/h. Values for the coefficient, a, ranging from 2 to 4, and for the coefficient, b, from 0.08 to 0.25 have been reported. By assuming an exponential shape for the spatial profile of the rain cell, it has been shown [Capsoni *et al.*, 1987a, b] that the peak rain rate distribution can be obtained from the point rainfall rate distribution (EXCELL model). Similar to the EXCELL model, [Feral *et al*., 2003] presented the HYCELL rain cell model, which is a combination of Gaussian and exponential functions, where the cells have an elliptical horizontal cross section.

Values of the mean diameter of the cell may be used in defining the common volume responsible for interference scattering by precipitation. However, in evaluating coupling by rain scatter, the attenuation both outside and inside the common volume must be considered.

The spatial autocorrelation for rain rate used in the Japanese model for rain scatter has the form [Morita and Higuti, 1978]:

$$T(d) = \exp\left(-\alpha\sqrt{d}\right) \tag{2.9}$$

with $\alpha \approx 0.3$.

An exponential model for cell shape, based on radar measurements in Milan, Italy, resulted in a spatial autocorrelation function of the form [Capsoni *et al.*, 1985]:

$$T(d) = \exp(-\alpha d) \tag{2.10}$$

with $\alpha \approx 0.5$.

A different form for the spatial autocorrelation function of rainfall rate has been assumed in [Lin, 1975; Kanellopoulos and Koukoulas, 1987]

$$T(d) = \frac{G}{\sqrt{G^2 + d^2}} \tag{2.11}$$

with $G \approx 1.5$.

2.5.2 Application to attenuation by rain

Since rain cells cluster frequently within small mesoscale areas, terrestrial links exceeding 10 km can traverse more than one cell within a rainy area. In addition, since the attenuation due to the lower intensity rainfall surrounding the cell must also be taken into account, any model used to calculate path attenuation must take these larger rain areas into account. The linear extent of these regions increases with decreasing rain intensity and may be as large as several tens of kilometres.

The concept of an effective path length that accounts for the non-uniform profile of rain intensity along a given path for the prediction of rain attenuation is presently used in attenuation prediction methods such as those in Recommendations ITU-R P.530 and P.618. The effective path length is the length of a hypothetical path obtained from radio data dividing the total attenuation by the specific attenuation exceeded for the same percentage of time. The concept of equiprobability is not consistent with meteorological information and is not entirely satisfactory from a theoretical point of view. However, the accuracy obtained with the above prediction method is consistent with the quality and variability of available rain intensity data.

Site or path diversity improvement results from the inhomogeneous nature of precipitation. The highest values of attenuation occur generally when an intense cell lies along the propagation path.

The probability of the same or a second intense cell simultaneously occurring along an alternative path separated from the first by distances of the order of 10 km or more is small, leading to diversity improvement when switched path or site diversity is used. If the attenuation produced by the larger rain areas outside the cells results in system impairment then much larger separation distances are required for significant diversity improvement. (See § 3.3, "Handbook on Radiowave Propagation Information for Predictions for Earth-space Path Communications", ITU, 1996.)

For application to satellite systems that serve many stations simultaneously within a coverage area, knowledge of the statistical dependence of fading over large distances is required. Studies conducted in Italy [Barbaliscia and Paraboni, 1982] focused on the determination of the joint probability of rain at pairs of sites spaced at distances ranging from 10 to 1 000 km for point rainfall intensities exceeding thresholds from 3 to 10 mm/h. A spatial dependence index has been defined as the ratio between the joint probability of rain at both sites a and b and the joint probability of exceeding the threshold at both sites in the case of statistical independence:

$$X = \frac{P_{ab}}{P_a \times P_b} \tag{2.12}$$

This index, X, which expresses the statistical dependence of rain phenomena at the two sites, decreases with the distance between the sites as follows:

– 0-50 km: where X decreases from the value $1/P_a$ (null distance) to half this value within 30 km;

– 50-600 km: where the rate of decrease of X is less pronounced;

– >600 km: where X tends to unity and statistical independence may be assumed.

For distances in excess of 300 km, the dependence index calculated on the basis of daily rain accumulations is representative of values calculated for hourly and quarter-hourly rainfall accumulations.

Observations by weather radar of the spatial power spectrum of rain rate variations show the same scales as found with rain data. The basic horizontal spatial structure as described by the spatial spectrum does not appear to be a function of climate region or latitude [Crane, 1987].

A methodology to simulate two-dimensional rainfall rate fields at large scale (1000 × 1000 km^2, the scale of a satellite telecommunication beam or a terrestrial fixed broadband wireless access network) is proposed in [Feral *et al*., 2006].

2.6 Vertical structure of precipitation

Information on the vertical structure and extent of precipitation is required for the prediction of attenuation on a slant path and for the calculation of interference due to rain scatter.

A vertically homogeneous and cylindrical model of a rain cell extending from the Earth's surface up to the 0°C isotherm height has been used in provisional rain attenuation models. However, there may be significant vertical structure in rain, in particular, in the leading and trailing edges of moving showers, and during their build-up and decay. The total fall time of drops is of the order of 5 to 15 minutes, which is significant when considering the lifetime of showers and their movement [CCIR, 1986-90c]. As a consequence, the simple rain cell model may overestimate attenuation in climates with heavy rainfall such as tropical regions. This overestimation may be amplified by the different character of tropical rain formation, resulting in a different horizontal and vertical structure and/or different drop size distribution.

Radar observations provide the only direct measurements of the vertical structure of precipitation. On the basis of such observations, two distinct precipitation types have been identified:

– stratiform precipitation, which is characterized by a thin horizontal layer of enhanced reflectivity called a bright band;
– convective precipitation, which is characterized by nearly vertical columnar regions of enhanced reflectivity.

Both types may occur in different areas of the same storm, and have been found to be the basic forms occurring in the major precipitation systems all over the globe [Houze, 1981], with the possible exception of the orographic precipitation systems of which little is currently known.

2.6.1 Vertical variation of reflectivity

Profiles of the radar reflectivity factor Z as a function of height for a given value of Z at the surface display little change below a certain transition height. This is true for both equiprobable profiles and median profiles based on an analysis of individual rain cells. The region below the transition height is predominantly rain and contributes to both attenuation and scattering.

For stratiform rain a distinct narrow layer of enhanced reflectivity exists at around the transition height; the dimension of this layer is on average about 300 m but can sometimes reach values of up to 1 km [Hines *et al.*, 1983]. This layer is composed of mainly snow and melting snow and known as the ”melting layer“ or the ”bright band”.

The region above the transition height is a mixture of ice and snow which does not produce significant attenuation at frequencies below about 60 GHz. Ice crystals in cirrus and cirrostratus clouds can produce reflectivity values as high as 100 mm^6/m^3 and occur for percentages of the year in the 1 and 10% range depending on climate region.

Profiles of Z above the transition height show a decrease with height that appears to depend on climate. The slope just above the transition height varies between about 3 and 9 dB/km. The slope is expected to become steeper at higher altitudes. Significant numbers of ice particles do not occur above the height of the tropopause.

The transition height is expected to be closely related to the height of the 0°C isotherm, which depends on latitude, climate and season. For stratiform precipitation seasonal variation of this height has been seen to be correlated with ground temperature [Fujita *et al.*, 1979].

As a provisional model for use in rain scatter calculations the transition height may be identified with the 0°C isotherm height considered in § 2.6.3. Above the height a constant slope of 6.5 dB/km is suggested.

2.6.2 Vertical variation of specific attenuation

The information on the vertical variation of reflectivity can be used to determine the vertical variation of specific attenuation once the height of the aggregate phase of the precipitation particles has been properly identified.

For stratiform precipitation this leads to the model of three distinct regions each containing precipitation particles in homogeneous aggregate phase. The first region extends from the ground to just below the transition height, contains only liquid particles and has a height-independent specific attenuation value. The second region is the melting layer of about 300 m around the transition height and its contribution to attenuation may not always be negligible due to the large value of the specific attenuation of wet snow. The third region extends above the transition height; it contains only ice and snow and is a small contributor to attenuation for frequencies below 60 GHz.

For stratiform precipitation the transition height is close to the value of the ambient 0°C isotherm height of the atmosphere since the vertical air motion is weak for this type of precipitation.

For strongly convective precipitation the situation is more complex. Strong vertical air motion results in large scale mixing of different particle types; for example, supercooled raindrops can be found far above the 0° C isotherm height in some convective cells.

2.6.3 The 0°C isotherm height and the rain height

As outlined in the previous section the transition height between the lower part of the atmosphere containing only liquid particles and the upper part containing only freezing particles is often assumed to be identical with the ambient 0°C isotherm height.

Generally the height of the 0°C isotherm has negligible yearly variations; the monthly variation is significant in the temperate region, while it is negligible in the tropics [Ajayi and Barbaliscia, 1989]. For a first indication of the value of this height, average values may be used.

Data on the average value of the 0°C isotherm height during the different seasons of the year are readily available [Crutcher, 1971].

Recommendation ITU-R P.839 provides average annual values for the zero-degree isotherm height as a model for the rain height h_R for use in prediction methods.

2.7 Characteristics of fog and clouds

Fog and water clouds consist of suspended droplets of liquid water. The diameters of these suspended droplets typically range from 10 μm (fog) to 100 μm (rain clouds), and their number densities range from 100 to 500 per cm^3. This results in a range of water density from 0.01 gm/m^3 to 1 gm/m^3. Various cloud and fog models have been summarized in [Slobin, 1982]. Water clouds and fog may cause appreciable attenuation values at millimetre wave frequencies, and this attenuation may be the dominant impairment for low-availability systems. In addition to attenuation, ice clouds may result in significant depolarization in the absence of significant attenuation.

The attenuation due to clouds depends on the cloud type, and cloud attenuation is primarily dominated by cumulonimbus and nimbostratus clouds. Cloud type and cloud cover observations are given in [Warren *et al.*, 1986], and a summary of information on cloud type and occurrence is given in [Brussaard and Watson, 1995]. Recommendation ITU-R P.840 and the associated digital maps of cloud liquid water vapour can be used to predict the attenuation due to clouds and fog.

2.8 Sand and dust storms

Sand and dust storms are dense clouds of suspended sand and dust particles in which, under severe conditions, visibility can be reduced to 10 m or less with the dust rising to more than a thousand metres above the ground and stretching over hundreds of kilometres across the land.

The meteorological aspects of sand and dust-storms have been studied by numerous authors and have been reported to occur in the Sudan, Libya, Southern Egypt, Iraq, the Arabian Desert, India, former USSR, Central China (People's Republic of), USA and Australia.

Sand and clay particles represent the main constituents of sand and dust storms with typical sizes of 0.015 cm and 0.008 cm, respectively. Concentration of sand and clay particles may be empirically related to optical visibility.

A review of physical models for sand and dust may be found in [Brussaard and Watson, 1995].

REFERENCES

AJAYI, G.O. and BARBALISCIA, F. [1989] Characteristics of the 0°C isotherm and rain height at locations in Italy and Nigeria. URSI Comm. F. Open Symposium, La Londe les Maures (France).

AJAYI, G.O. and OLSEN, R.L. [1985] Modelling of raindrop size distribution for microwave and millimetre wave applications, Radio Sci., Vol. 20, pp. 193-202, March-April 1985.

ARESU, A., BARBALISCIA, F., DI PANFILO, A., GIORGI, P., and MIGLIORINI, P. [1989] Space-time characteristics of rainfall in the Roma area. URSI Comm. F. Open Symposium, La Londe les Maures, September 1989.

BARBALISCIA, F. and PARABONI, A. [1982] Joint statistics of rain intensity in eight Italian locations for satellite communications network. Electronics Letters, February 1982, Vol. 18, No. 3, pp. 118-119.

BRUSSAARD, G. and WATSON, P.A. [1995] Atmospheric modelling and millimetre wave propagation. Chapman and Hall, London, ISBN 0-412-56230-8.

BURGUEÑO, A., AUSTIN, J., VILAR, E., and PUIGCERVER, M. [1987] Analysis of moderate and intense rainfall rates continuously recorded over half a century and influence on microwave and rainrate data acquisition, IEEE Trans. Comm. COM-35, 382-395.

BURGUEÑO, A., PUIGCERVER M.and VILAR, E. [1988] Influence of raingauge integration time on the rain rate statistics used in microwave communications, Ann. Telecom., Vol. 43, No. 2.

CAPSONI, C., LUINI, L. [2009] A physically based method for the conversion of rainfall statistics from long to short integration time. IEEE Transactions on Antennas and Propagation , Vol 57, No. 11, pp 3692 – 3696.

CAPSONI, C., MATRICCIANI, E. and MAURI, M. [March-April, 1985] Profile statistics of rain in slant path as measured with a radar. Alta Frequenza, Vol. LIV, 2, 50-57.

CAPSONI, C., FEDI, F., MAGISTRONI, C., PAWLINA, A. and PARABONI, A. [1987a] Data and theory for a new model of the horizontal structure of rain cells for propagation applications, Radio Sci., Vol. 22, 3, 395, 404.

CAPSONI, C., FEDI, F. and PARABONI, A. [1987b] A comprehensive meteorological oriented methodology for the prediction of wave propagation parameters in telecommunication applications beyond 10 GHz, Radio Sci., Vol. 22, 3, 387, 393.

CASTANET L., BLARZINO G., JEANNIN N., TESTONI A., CAPSONI C., FERRARO D., LUINI L., ROGERS D., AMAYA C., BOUCHARD P., PONTES M., SILVA MELLO L. [2007a] Assessment of radiowave propagation for satellite communication and navigation systems in tropical and sub-tropical areas, ESA study n°18278/04/NL/US, ONERA Final report RF 4/09521 DEMR,

CASTANET L., CAPSONI C., BLARZINO G., FERRARO D., MARTELLUCCI A. [2007b] Development of a new global rainfall rate model based on ERA40, TRMM and GPCC products, International Symposium on Antennas and Propagation, ISAP 2007, Niigata, Japan.

CRANE, R.K. [October 1987] Space-time structure of precipitation. Preprints of the 10th Conference on Probability and Statistics of the American Meteorological Society, pp. 265-268.

CRANE, R.K. [1990] Rain attenuation measurements: variability and data quality assessment. Radio Science, 25 (4), 455-473.

CRUTCHER, H.L. [1971] Selected meridional cross sections in heights, temperature and dew points for the northern hemisphere. NAVAIR 50-IC-59, National Climatic Centre, Asheville, NC, United States.

DUTTON, E.J., DOUGHERTY, H.T. and MARTIN, R.F. [1974] Prediction of European rainfall and link performance coefficients at 8 to 30 GHz, NTIS, U.S. Department of Commerce, Rep. AD/A-000804, 1974

ECMWF [1997] ECMWF Re-Analysis Project (ERA).

EMILIANI, L.D., LUINI, L., and CAPSONI, C. [2009] Analysis and parameterization of methodologies for the conversion of rain rate cumulative distributions from various integration times to one minute. IEEE Antennas and Propagation Magazine, Vol. 51, No. 3. pp. 70-84.

EMILIANI, L. D., LUINI, L., and CAPSONI, C. [2010] On the optimum estimation of 1-minute integrated rainfall statistics from data with longer integration time. EuCAP 2010, pp. 1-5, 12-16 April, Barcelona, Spain.

ERA 15 [1999] ECMWF Re-analysis project report series, 1. ERA-15 Description, Version 2, European Centre for Medium-Range Weather Forecasts.

ERA 40 [2002] ECMWF Re-analysis project report series, ERA-40 Archive, European Centre for Medium-Range Weather Forecasts.

FEDI, F. [April 1979a] Rainfall characteristics across Europe. Alta Frequenza, Vol. XLVIII, 4, 158-166.

FEDI, F. [April 1979b] Attenuation due to rain on a terrestrial path. Alta Frequenza, Vol. XLVIII, 4, 167-184.

FEDI, F. and MERLO, U. [1977] Statistical data on point rainfall intensity for the design of radio-relay systems at frequencies above 10 GHz. URSI - Open Symposium on Propagation in Non-Ionized Media, La Baule, France.

FERAL, L., SAUVAGEOT, H., CASTANET, L., and LEMORTON, J. [2003] A new hybrid model of the rain horizontal distribution for propagation studies: 1. Modeling of the rain cell. Radio Sci., Vol. 38, No. 3.

FERAL, L., SAUVAGEOT, H., CASTANET, L., LEMORTON, J., CORNET, F., and LECONTE, K., [2006] Large-scale modeling of rain fields from a rain cell deterministic model. Radio Sci., Vol. 41.

FUJITA, M., NAKAMURA, K., IHARA, T. and HAYASHI, R. [1979] Seasonal variations of attenuations statistics in millimetre-wave Earth-satellite link due to bright-band height. Electron. Lett., 15, 654-655.

GUNN, R. and KINZER, G.D. [1949] The terminal velocity of fall for water droplets in stagnant air. J. Meteorol., Vol. 6, 4, 243-248.

HINES, E.L. LEITAO, M.J. and WATSON, P.A. [12-15 April, 1983] The use of dual-linearly polarized radar data to determine rainstorm and hydrometeor types. IEE Conf. Publ. No. 219, Part 2, 51-55. IEE Third International Conference on Antennas and Propagation (ICAP 83), University of East Anglia, Norwich, United Kingdom.

HOUZE, R.A. [1981] Structure of atmospheric precipitation systems: a global survey. Radio Sci., Vol. 16, 671-689.

KALININ, A.I. and NADENENKO, L.V. [1975] Issledovania rasprostranenia UKV do rasstoyanï poriadka priamoï vidimosti. (Study of ultra-short wave propagation up to line-of-sight distances.) In Rasprostranenie radiovoln (Radio wave propagation), Nauka, Moscow, USSR.

KANELLOPOULOS, J.D., and KOUKOULAS, S.G. [1987] Analysis of the rain outage performance of route diversity systems, Radio Sci., Vol. 22, No. 4, pp. 549-565.

LAVERGNAT and J., Golé, P. [1998] A Stochastic Raindrop Time Distribution Model. AMS Journal of Applied Meteorology, Vol. 37, pp 805-818.

LAWS, J.O. and PARSONS, D.A. [1943] The relation of raindrop size to intensity. Trans. Amer. Geophys. Union, Vol. 24, 452-460.

LIN, S.H. [1975] A method for calculating rain attenuation distribution on microwave paths. Bell System Tech. J, Vol. 57, 1545-1568.

LIN, S.H. [1978] More on rain rate distributions and extreme value statistics. Bell System Tech. J., Vol. 57, 1545-1568.

MARSHALL, J.S. and PALMER, W.Mck. [August, 1948] The distribution of raindrops with size. J. Meteorol., Vol. 5, 165-166.

MARTELLUCCI A. [2004] Catalogue of available meteorological and propagation measurements database, Technical Note ESA n°TOS-EEP/2004.178/AM.

MORITA, K. [1978] Study on rain rate distribution. Rev. Elec. Comm. Labs, NTT, Vol. 26, 268-277.

MORITA, K. and HIGUTI, I. [July-August, 1976] Prediction methods for rain attenuation distribution of micro and millimetre waves. Rev. Elec. Comm. Labs. NTT, Vol. 24, 7-8.

MORITA, K. and HIGUTI, I. [1978] Statistical studies on rain attenuation and site diversity effect on earth to satellite links in microwave and millimetre wavebands. Trans. Inst. Electron. Comm. Engrs. Japan, Vol. E-61, 425-434.

MOUPFOUMA, F. [1987] More about rainfall rates and their prediction for radio systems engineering. Proc. IEE. Part H, Vol. 134, No. 6, pp. 527, 537.

POIARES-BAPTISTA P., SALONEN E. [1998] Review of rainfall rate modelling and mapping. Proc. of URSI Commission F Open Symposium on Climatic Parameters in Radiowave Propagation Prediction (CLIMPARA'98), Ottawa, Ontario, Canada.

PRUPPACHER, H.R. and BEARD, K.V. [1970] A wind-tunnel investigation of the internal circulation and shape of water drops falling at terminal velocity in air. Quart. J. Roy. Meteor. Soc., Vol. 96, 247-256.

PRUPPACHER, H.R. and PITTER, R.L. [January, 1971] A semi-empirical determination of the shape of cloud and rain drops. J. Atmos. Sci., Vol. 28, 86-94.

RICE, P.L. and HOLMBERG, N.R. [1973] Cumulative time statistics of surface-point rainfall rates, *IEEE Trans. Comm*., COM-21, 1131-1136

RIVA, C. [2002] Spatial characteristics of propagation parameters: a review, First COST 280 Workshop, doc. PM3-019, Malvern, UK.

RUDOLF B. [1996], "Methods and new results of estimating the global precipitation", *Abstracts of XXVth GA of URSI*, 302.

SALONEN, E.T. and POIARES BAPTISTA, J.P.V. [1997] A new global rainfall rate model, Tenth Int. Conf. on Antennas and Propagation, IEE Conf. Publ. 436, Vol. 2, pp. 2.182-2.185

SEGAL, B. [1979] High intensity rainfall statistics for Canada. CRC Rep. 1329, Dept. of Communications, Ottawa, Canada.

SEGAL, B. [1980a] A new procedure for the determination and classification of rainfall rate climatic zones. Ann. des Télécomm., Vol. 35, 411-417.

SEGAL, B. [1980b] An analytical examination of mathematic models for the rainfall rate distribution function. Ann. des Télécomm., Vol. 35, 434-438.

SEGAL, B. [1986] The influence of raingauge integration time on measured rainfall intensity distribution functions. J. Atmospheric and Oceanic Technology, Vol. 3, 4.

SLOBIN, S.D. [November-December, 1982] Microwave noise temperature and attenuation of clouds: Statistics of these effects at various sites in the United States, Alaska and Hawaii. Radio Sci., Vol. 17, 1443-1454.

UK METEOROLOGY OFFICE [1976] Averages and frequency distributions of humidity for Great Britain and Northern Ireland, 1961-70. Meteorology Memorandum 103.

WARREN, S.G., HAHN, C.J., LONDON, J., CHERVIN, M. and JENNE, R.L. [1986] Global distribution of total cloud cover and cloud type amounts over land. NCAR Technical Notes, NCAR/TN-273+STR, United States.

CCIR Documents

[1986-90]: a. 5/305 (China); b. 5/320 (Canada); c. 5/17 (Sweden).

CHAPTER 3

Atmospheric refraction

3.1 Influence of the atmosphere on radiowave propagation

If we consider the medium through which electromagnetic waves propagate to comprise of atoms whose electrons are driven in an oscillatory manner by the electromagnetic field, then the resulting equation for the index of refraction of the medium is dependent upon the frequency of the electromagnetic radiation, the number of electrons, the natural frequency of the electrons and their damping factors. In this general case, the index of refraction is a complex quantity. The real component of the index of refraction is related to the velocity of the electromagnetic wave through the medium as n = c / v, where c is the velocity of electromagnetic radiation in a vacuum and v is the velocity in the medium.

In the case of electromagnetic wave propagation through air, the refractive index of air depends on the composition of the atmosphere (§ 3.2), which varies both with position (altitude above Earth's surface and geographic location) and with time. In this chapter we consider only clear-air influences; the effect of hydrometeors and other scatterers will be considered in Chapters 5 and 7. In these conditions, the refractive index can be considered as a continuous function. Furthermore, in this chapter, we discuss only the real component of the complex refractive index which is responsible for phenomena such as: ray bending, reflection, refraction, multipath, ducting, beam focusing/de-focusing, and depolarisation. Often the real component is simply referred to as the "refractive index" or the "atmospheric refractive index" when discussing propagation through air. The imaginary component of the complex refractive index is associated with absorption or attenuation effects and is sometimes referred to as an "absorption index" and this topic is discussed in more detail in Chapter 6.

The atmospheric refractive index is larger than unity, since the waves propagate at a speed less than the speed of light in vacuum, denoted by *c*. Moreover the propagation is greatly affected by spatial variations of the index. These effects will be described in some detail in Chapter 4. In brief, large scale variations (large compared to the emission wavelength) change the direction of propagation of the waves, influencing multipath propagation and at times causing radioelectric holes and also enhanced trans-horizon propagation. In fact, the wave propagation depends more on the gradient of the index than on its absolute value.

For the user of a radio link, these phenomena can have various detrimental effects, for example: error in the direction and ranging of a source; attenuation and depolarisation of radiowaves; signal distortions; interference between different systems (especially when atmospheric conditions support trans-horizon propagation). One difficulty in studying and modelling all these interrelated phenomena is that there is no one-to-one relation between the general conditions of propagation and their effects on a particular link.

Computational advances in implementing numerical methods for solving electromagnetic wave propagation equations have led to the physical modelling of several interrelated propagation mechanisms. Examples of these models include implementations of the parabolic equation and also hybrid models which combine the parabolic wave equation and the ray-optics approach. Details of these methods are given in Chapter 4. Nevertheless, a statistical knowledge of the refractive properties of the atmosphere, which can be obtained from measurements by the methods described in § 3.9, is still a necessity for radio link designers. The accuracy and resolution (both spatial and

temporal) with which the atmospheric refractivity has to be known depend on the intended application. For instance, to compare instantaneous radio measurements with the results of propagation computations would generally require very high resolution and is more difficult to model. On the other hand, the average behaviour of the atmosphere, sufficient for gross planning purposes does not require high resolution and accuracy and is, in fact, now rather well known.

3.2 Refractive index and refractivity

The index of refraction of air is always very close to unity. The parameter used to describe its spatial and temporal variations is generally the refractivity N, defined by:

$$N = (n-1)10^6 \tag{3.1}$$

and expressed in dimensionless N units.

The value of the refractive index, or of the refractivity, can be obtained from the pressure, humidity and temperature of the air by a semi-empirical formula based on Debye's theoretical work [Debye, 1929]. Amongst the components of the air, only oxygen (a paramagnetic element) has a permanent magnetic moment; this fact is important when studying the absorption of radio waves (Chapter 6) but the effect is small enough to consider (with an accuracy of 10^{-6}) that the relative permeability of air is in practice equal to unity. The refractive index is thus related to the relative dielectric permittivity ε by the relation:

$$n = \sqrt{\varepsilon} \tag{3.2}$$

Air is in fact a mixture of several components, but the theory is rather straightforward when considering it as a mixture of perfect gases. Under this assumption, and using the fact that the permittivity of each gas is nearly equal to 1, it can be shown that:

– the electric polarisation of each component i of air is independent of the presence of the others and proportional to $(\varepsilon_i - 1)$ with ε_i the permittivity of gas i;

– the polarisation of air is the sum of the polarisations of its components; therefore:

$$\varepsilon - 1 = \sum (\varepsilon_i - 1) \tag{3.3}$$

– for non-polar gases, the polarisation is due to the formation of induced electric dipoles when an electric field is applied, and

$$\varepsilon - 1 = \frac{KP}{T} \tag{3.4}$$

with pressure, P, absolute temperature, T, and K, a gas dependent constant;

– for a polar gas, the polarisation is due both to the formation of induced dipoles and to an orientation of the permanent dipoles in the direction of the applied electric field. This second effect is limited by thermal agitation and decreases with temperature. The result in this case is:

$$\varepsilon - 1 = K\frac{P}{T}\left(A + \frac{B}{T}\right) \tag{3.5}$$

where the constants K, A and B depend on the nature of the gas.

The composition of the air has been described in Chapter 2. All components are electrically non-polar except water vapour. Moreover, the proportions of all components are practically constant, except for water vapour (because of its changes of physical state) and CO_2 (due to exchanges between air and living organisms) both of which are present in very small percentages. As a result the polarisation can be written:

$$\varepsilon - 1 = K_d \frac{P_d}{T} + K_e \frac{e}{T}\left(A + \frac{B}{T}\right) + K_c \frac{P_c}{T} \tag{3.6}$$

where T is the absolute temperature, e is the water vapour partial pressure, P_c is the partial pressure of CO_2 and P_d is the partial pressure of the other atmospheric constituents (mainly oxygen and nitrogen). The pressures are expressed in hPa. The subscripts *d, e* and *c* refer to dry air, water vapour and carbon dioxide, respectively.

The refractive index n is given by:

$$n = \sqrt{\varepsilon} = \sqrt{1 + (\varepsilon - 1)} \approx 1 + \frac{\varepsilon - 1}{2} \tag{3.7}$$

and the refractivity $N = (n-1)10^6 \approx 10^6 (\varepsilon - 1)/2$

Therefore, N is obtained by a multiplicative change of all K constants:

$$N = K_1 \frac{P_d}{T} + K_2 \frac{e}{T}\left(A + \frac{B}{T}\right) + K_3 \frac{P_c}{T} \tag{3.8}$$

namely: $K_1 = 5x10^5 K_d, K_2 = 5x10^5 K_e, K_3 = 5x10^5 K_c$

It must be noted here that we consider only the real part of the atmospheric refractive index. The imaginary part is indeed very small at radio frequencies. It is however, responsible for absorption by gases and will be considered in this context in Chapter 6.

If the theory of gas polarisation leads to equation (3.8), the numerical values of the constants in this relation are not given by the theory and have to be derived from laboratory measurements. The values currently accepted are those given by Smith and Weintraub [1953] from a critical discussion of various measurements. Their equation which assumes a percentage of 0.03% for CO_2 is:

$$N = 77.6 \frac{P_d}{T} + 72 \frac{e}{T} + 3.75x10^5 \frac{e}{T^2} \tag{3.9}$$

where:

P_d : dry air pressure

e : water vapour partial pressure (hPa)

T : temperature (K).

Introducing the total pressure $P = P_d + e$, equation (3.9) can be written as:

$$N = 77.6 \frac{P}{T} - 5.6 \frac{e}{T} + 3.75x10^5 \frac{e}{T^2} \tag{3.10}$$

Equation (3.10), in which the coefficients have been reduced to three figures, gives an overall accuracy of ±0.5%. The main issue of this relation is the derivation of refractivity from meteorological measurements. In fact, available measurements (discussed in § 3.7.2) do not allow for the full accuracy of equation (3.10). It is therefore possible to simplify it to a two-term expression. Indeed, for the range of temperatures of practical interests (between –40 and +40 °C) and typical values of vapour pressure (at 40 °C, the saturation pressure of water is 73.8 hPa), the term in e/T is much smaller and varies much less than the e/T^2 term. It can therefore be evaluated for the mean temperature of 273 K and combined with the e/T^2 term. The resulting equation is:

$$N = 77.6\frac{P}{T} + 3.73x10^5\frac{e}{T^2} = \frac{77.6}{T}\left(P + 4810\frac{e}{T}\right) \tag{3.11}$$

This is the formula which is given in Recommendation ITU-R P.453. The two terms in it are often referred to as the dry and wet air contributions to refractivity.

3.3 Models of the atmospheric refractive index

This discussion deals with the "bulk" refractive index structure as opposed to short period random disturbances resulting from a variety of stochastic atmospheric processes. A more complete discussion of refractive index structure is given in Chapter 4.

The refractive index of the atmosphere changes with time and space as do the temperature and humidity. The atmospheric refractivity may vary both horizontally and vertically. Horizontal refractivity gradients depend on geographic, topographic and on meteorological processes which may vary diurnally or may last several days or simply be transient events such as the passage of fronts. By contrast, vertical refractivity gradients are more dominant with appreciable changes occurring over short distance scales ranging from several metres to 10's or 100's of metres. Horizontal changes in refractive index occur over distance scales ranging from 10's of metres to 10's of kilometres. Simple descriptions of "reference" atmospheres are very useful and we begin by defining several such atmospheres. In so doing we assume the atmosphere to be horizontally stratified; i.e. we consider variations to only occur as a function of height. These model atmospheres represent the real atmosphere averaged over a long period of time and so temporal dependence is neglected in these models.

3.3.1 Linear models

In the simplest model, the refractivity is considered to decrease linearly with altitude. If the ground refractivity is N_s at altitude h_s (above sea level), the refractivity N at height h is given by:

$$N(h) = N_s - \left(\frac{\Delta N}{\Delta h}\right)(h - h_s) \tag{3.12}$$

with $(\Delta N / \Delta h)$ as the absolute value of the refractivity gradient.

In practice, the linear model is an approximation only in the first kilometre of the atmosphere. Above 1 kilometre, the refractivity decreases more slowly (Figure 3.1). This model is applicable to terrestrial links and as is shown in Chapter 4, it is used in simple computations together with the effective Earth radius parameter. As will be described in § 3.6, the refractivity gradient varies with location and with season. For temperate regions, a global average of –40 N-units/km is often used as a first approximation.

3.3.2 Exponential models

For propagation above a height of 1 km, which is the case in applications involving Earth–satellite and Earth–aircraft links as well as some remote sensing operations, the linear model is too crude an approximation. A better approximation is provided by the exponential model [Bean and Thayer, 1959]. In such a model, the refractivity N at height h *(above sea level)* is given by:

$$N(h) = N_s \exp\left[-\left(\frac{h - h_s}{h_0}\right)\right] \tag{3.13}$$

with N_s the refractivity at ground level, at altitude h_s the height of the Earth's surface above sea level. Again parameters N_s and h_s change with location and season. The parameter h_0 is the scale height of the model. In an exponential model, the gradient of refractivity is given by:

$$\frac{\mathrm{d}N}{\mathrm{d}h} = -\frac{N_s}{h_0}\exp\left(-\frac{h - h_s}{h_0}\right) = -\frac{N(h)}{h_0} \tag{3.14}$$

FIGURE 3.1

Typical N versus height distributions (from Bean and Dutton, 1966)

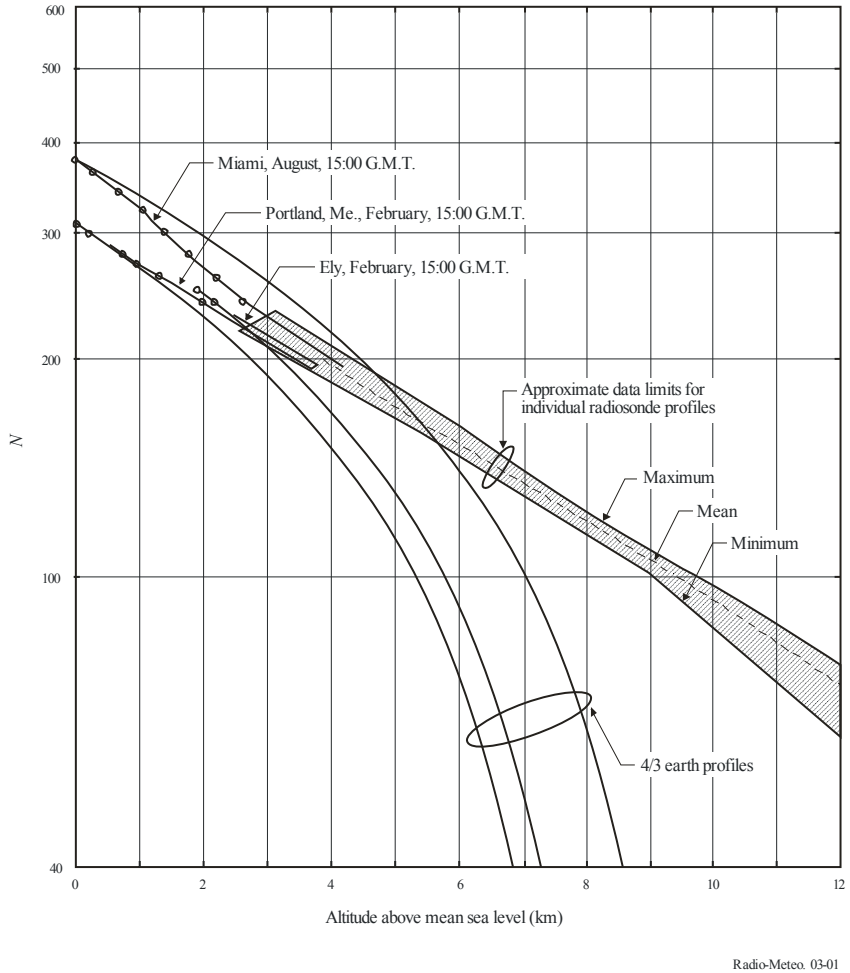

In fact, observations show that there is often a close correlation between the ground refractivity N_s and the gradient of refractivity near the ground (see § 3.3.4). Extending such a correlation to higher altitudes leads to a relation between N_s and h_o and an exponential relation depending on only one parameter.

Figure 3.2, taken from Bean & Dutton [1966], shows the average refractivity profiles for two stations in the United States and their representations by an exponential model (dashed lines). It can be seen that the exponential model fits the data well up to about 5 km. Above this altitude, however, the model refractivity profile decreases with altitude faster than the experimental profile.

FIGURE 3.2

Comparison of reference atmosphere with observed N profiles

(from Bean and Dutton,1966)

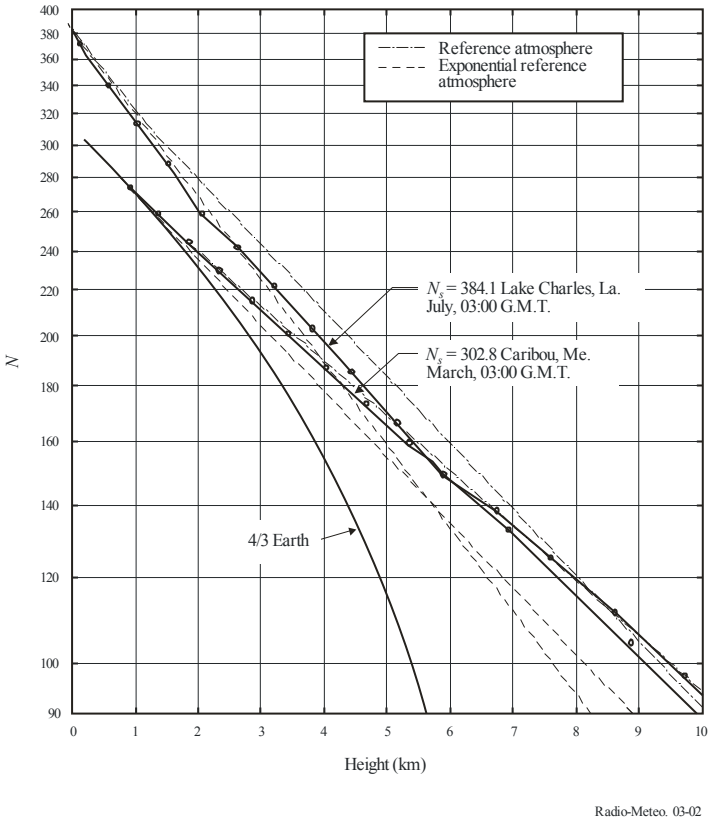

The reference atmosphere recommended for refractivity computations (Recommendation ITU-R P.453) is an exponential model referred to sea level, when h_s = 0, and with parameters N_o = 315 N-units and h_o = 7.35 km.

$$N(h) = 315 \exp\left(-\frac{h}{7.35}\right) \tag{3.15}$$

where $N(h)$ is the refractivity at height h above sea level (km)

3.3.3 Other models

For a better fit to data over a larger range of heights, more elaborate models are sometimes required. One approach is to fit different functions to different parts of the altitude range; an example of such a model is the three-part CRPL 1958 reference atmosphere by Bean and Thayer [1959], which gives

different expressions for the refractivity in the first kilometre, between 1 and 9 km and above 9 km. Although the agreement with data is better than with a simple exponential function, a drawback of such models is the introduction of discontinuities in the refractivity gradient profile, which can induce artifacts in some refraction computations.

Another possibility is to use equation (3.10) or (3.11) to derive a reference profile of refractivity from any atmospheric model, given reference profiles for pressure, temperature and water vapour pressure. In such a procedure, water vapour modelling is by far the most delicate task.

3.4 Departures from the models

As reference atmospheres represent the atmosphere time averaged over long periods, it is useful to consider departures from the reference cases. It may be practical to represent several types of structure superimposed on an average profile. For many applications the atmosphere can be regarded as horizontally stratified, with layers displaying refractivity gradients less than -157 N-units/km, or greater than –40 N-units/km possibly becoming positive. In the first case, ducting radio holes and multipath propagation can occur. In the second case, we have sub-refractive conditions, which can lead to obstruction fading in extreme cases. The statistics of these structures, which are not well known, are discussed in § 3.7. Their effects on propagation will be presented in Chapter 4.

Horizontal gradients of refractivity can occur over both mesoscales as well as macroscales. For instance horizontal gradients may develop when two different air masses interact as may be the case along coastlines or inland when a complicated wind flow exists over rough terrain or as a result of large scale subsidences over land or water. The effects of horizontal gradients on propagation are also presented in more detail in Chapter 4.

Superimposed on a spatial average, the atmosphere also exhibits random irregularities over scales ranging from millimetres to hundreds of meters. These irregularities lead to stochastic propagation effects such as scintillation. The stochastic atmosphere, atmospheric turbulence, its effect on the refractive index and on the propagation of radiowaves is covered in Chapter 4.

3.5 Refractivity at ground level

A large number of data have been published giving the refractivity at ground level. If one displays the average ground refractivity as a function of position, large differences appear which are due mainly to the changes induced by differences in height. It is therefore common practice to refer all data to a common reference height which is usually sea level. The transformation from ground refractivity N_S to sea level refractivity N_O is very easily done by means of an exponential model:

$$N_O = N_S \exp(h_s/h_o) \tag{3.16}$$

with h_s the height of the station above sea level.

The only problem is to choose the scale height h_o to be used in this data reduction. To be coherent it should be the value of the reference exponential model (7.35km). In practice, it does not seem that the reduction of data has always been done with this value. For example, the work done earlier by Bean and Dutton [1966] used a scale height of 9.46 km, a value which is appropriate for dry air. The result of the data reduction, however, is mainly to reduce the range of variation of the refractivity and to allow a more precise interpolation in the world maps discussed in § 3.5.2. The precise value of the scale height used in the reduction is therefore not of paramount importance.

3.5.1 Monthly averages of ground refractivity

As explained in § 3.9, refractivity can be measured either by radio techniques, or indirectly from meteorological data, using equation (3.11). In both cases, data are averaged for analysis, generally over a one-month period. Often, however, when using equation (3.11), the original meteorological data are no longer available. Instead, the refractivity value could be derived from the values of the monthly averaged pressure, temperature and water vapour pressure. The value of the refractivity derived by this method is different from the average refractivity. The difference has been investigated by Bean and Dutton [1966] and Rao and Srivastava [1971]. Bean and Dutton compared the results obtained by the two methods for three stations differing by their climatic conditions; the difference never exceeded 1.5 N-units. Rao and Srivastava determined theoretically the difference as a function of the statistical characteristics of the meteorological parameters (averages, standard deviations and correlation factors) and concluded that in most cases the difference should be very small.

3.5.2 Seasonal and year-to-year variability of ground refractivity

An analysis of ground refractivity (reduced to sea level) on a world basis has been given by Bean and Dutton [1966]. These authors used data from 306 weather stations. For each station, they used five years of data from the period 1949 to 1958 (preferably 1954 to 1958), except for Russian stations for which only one year of data (1958) was available. Values of refractivity over large oceanic areas had to be estimated from sparse available data due to the lack of observing stations in such regions.

The results are presented as charts of average contours of N_O for each month of the year. The results for the months of February and August are given in Figures 1 and 2 of Recommendation ITU-R P.453.

The ground refractivity exhibits both seasonal and year-to-year variability. The seasonal variations are shown in Figure 3.3 which gives world contours of the difference between the maximum and minimum monthly mean of ground refractivity N_S throughout the year. Variation from year-to-year is shown in Figure 3.4, which shows contours of the range of N_S (maximum minus minimum) computed over five years for the months of February. It can be noted that year-to-year variability may be of the same importance as the seasonal variation.

FIGURE 3.3

Annual range of monthly mean N_s (from Bean and Dutton, 1966)

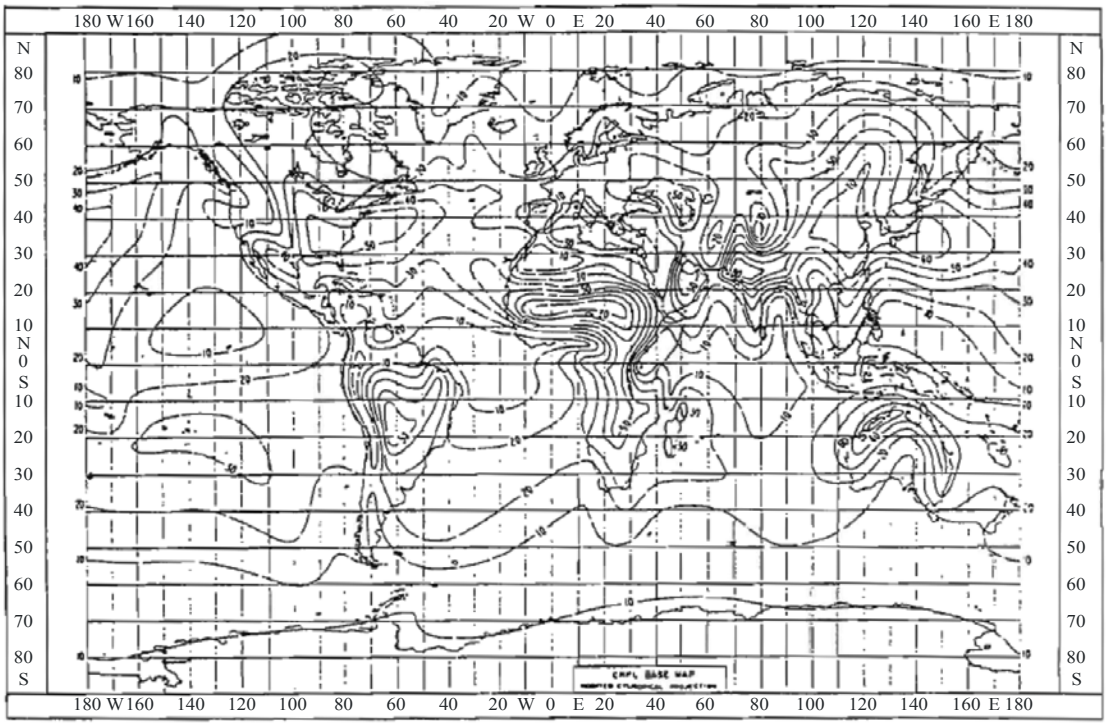

Radio-Meteo. 03-03

FIGURE 3.4

Year-to-year range of monthly mean N_s for February (from Bean and Dutton, 1966)

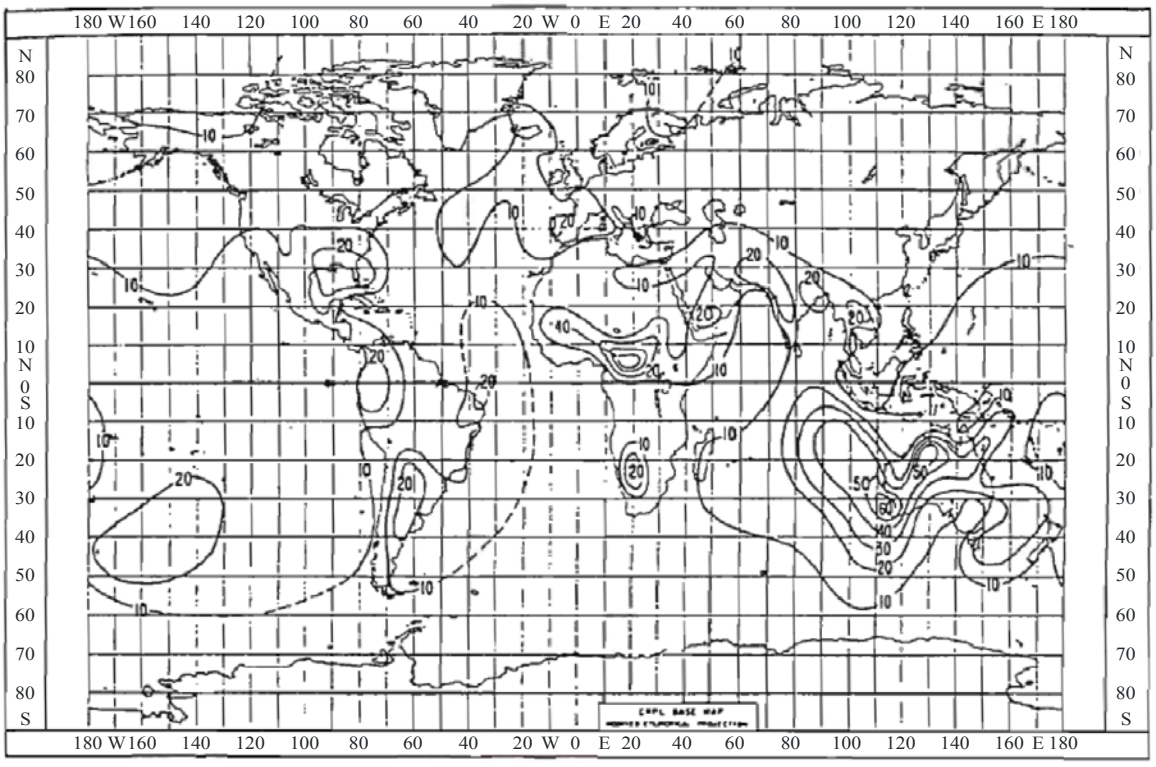

Radio-Meteo. 03-04

3.6 Refractivity gradients

For radiowave propagation, the gradient of radio refractivity in the lower part of the atmosphere is more important than the value of the index itself. For general studies in which horizontally-stratified atmosphere is assumed, only the vertical gradient is relevant.

To be rigorous, the refractivity gradient is a function of altitude. What is derived from experimental data is generally the average gradient α over a thickness Δh, defined as $\alpha_{\Delta h} = \Delta N/\Delta h$. Apart from seasonal and regional variations, the distributions of this quantity depend on the altitude h (slightly) and on the layer width Δh.

Even if a large variability is observed in the presentation of published data, the most common parameters are $\alpha_{0.1}$, the gradient averaged over the first 100 m, or α_1, the gradient averaged over the first kilometre of the atmosphere. The first of these is the most appropriate for studies concerning line-of-sight propagation; it is generally derived from observations using instruments installed on a tower. The second parameter is easily derived from routine radio sounding observations. It is more adapted to studies relative to ground-to-aircraft or ground-to-satellite propagation as well as to trans-horizon propagation. Other parameters such as the values of the gradient exceeded for given percentages of time are also available.

3.6.1 Models for refractivity gradient distribution

As an example to illustrate the discussion below, Figure 3.5 from Boithias [1984], gives the long-term cumulative distribution of the refractivity gradient $\alpha_{0.1}$ over the first 100 m for three stations with different climatic characteristics.

FIGURE 3.5

Examples of refractivity gradient distributions over the first 100 m (from Boithias, 1984)

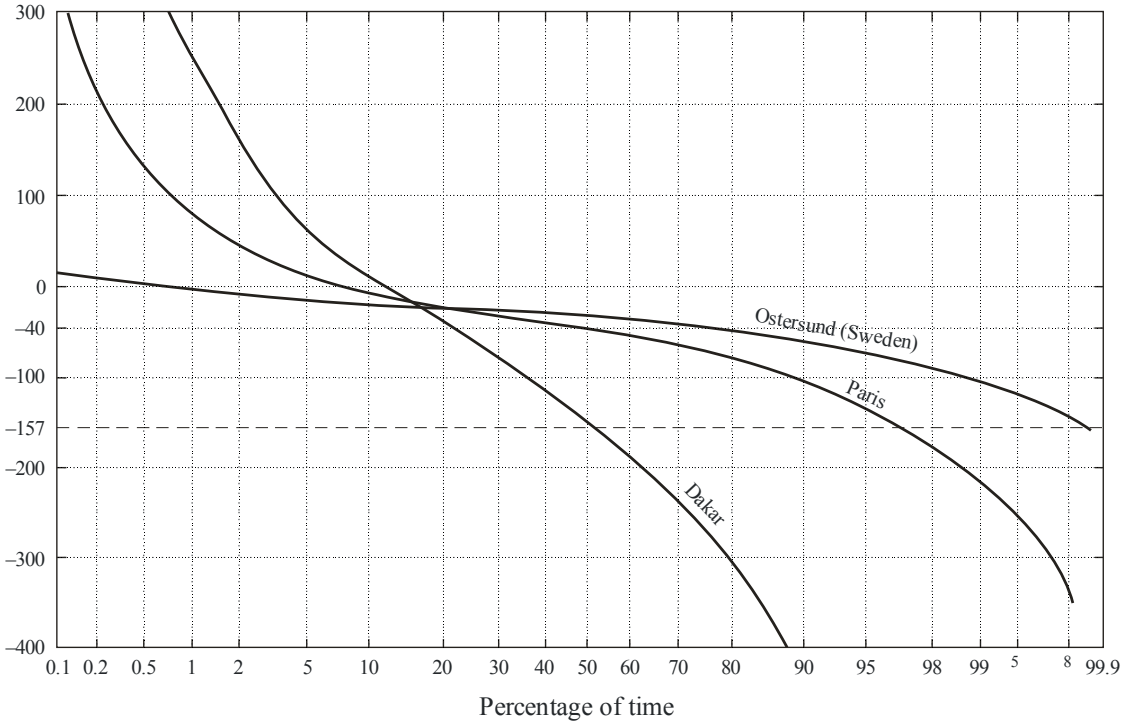

3.6.1.1 The normal model

Whatever the altitude and thickness, the central part of the distribution can be approximated by a normal law. A detailed analysis of Japanese data [Ugai, 1959; Ikegami *et al.*, 1966; Akiyama, 1977; Sasaki and Akiyama, 1982] has shown that the average of the distribution does not depend on the thickness Δh (except in the surface layer) whereas the standard deviation varies as $\Delta h^{-1/2}$. The only altitude effect concerns the first 100 m; the average gradient there is smaller than at higher altitudes, a bias which could be attributed to the frequent occurrence of nocturnal inversion layers. Unfortunately, the normal model fails to describe correctly both tails of the distribution, the one corresponding to the positive gradients leading to obstruction fading, and the other one to very negative gradients leading to ducting and multipath propagation. It can therefore be used only for studies of normal propagation conditions.

3.6.1.2 The exponential normal model

To describe the complete gradient distribution, it is necessary to use a composite distribution. Several such models have been proposed. Using data from Japan and other countries for South-East Asia, Akiyama and colleagues [Ikegami *et al.*, 1968; Akiyama, 1977] developed a composite model of a normal distribution (for most values of the gradient) and an exponential function (for very negative gradients), both functions fitting together for $\alpha = \alpha_p$. The probability density functions are therefore:

$$f(\alpha) = \begin{cases} \dfrac{c}{2}\exp\{c(\alpha - \alpha_m)\} & -\infty < \alpha \le \alpha_p \\ \dfrac{1}{\sigma\sqrt{2\pi}}\exp\left\{\dfrac{(\alpha - \alpha_m)^2}{2\sigma^2}\right\} & \alpha_p < \alpha < \infty \end{cases} \tag{3.17}$$

The cumulative probability $F(X) = \Pr\{\alpha \le X\}$ is obtained by integrating equation (3.17).

$$F(\alpha) = \begin{cases} \dfrac{1}{2}\exp\{c(\alpha - \alpha_m)\} & -\infty < \alpha \le \alpha_p \\ \dfrac{1}{2}\left(1 + \operatorname{erf}\left\{\dfrac{\alpha - \alpha_m}{\sigma\sqrt{2}}\right\}\right) & \alpha_p < \alpha < \infty \end{cases} \tag{3.18}$$

This composite distribution depends on three parameters, α_m (common median value of both distributions), σ (standard deviation of the normal distribution) and c, as well as on the value of α_p. The density distribution is discontinuous for $\alpha = \alpha_p$. The cumulative probability, on the other hand, must be continuous everywhere. This leads to the relation:

$$c\sigma = -\frac{\ln(2P)}{\sqrt{2}\,\text{inverf}(2P - 1)} \tag{3.19}$$

with $P = F(\alpha_p)$ and inverf, the inverse error function. (For the definition of "erf", see Recommendation ITU-R P.1057.)

Experimental data used by the authors show that P is never very different from 0.07. For such a small value of P, the average value and the standard deviation of the composite distribution are nearly equal to those of its normal component, α_m and σ. Moreover, the normal distribution, $\alpha_p = \alpha_m - 1.48\ \sigma$. The refractive gradient is thus given by a two-parameter model. The quality of data fitting is shown on Figure 3.6.

FIGURE 3.6

Examples of refractivity gradient distributions fitted by exponential model (from Akiyama, 1977)

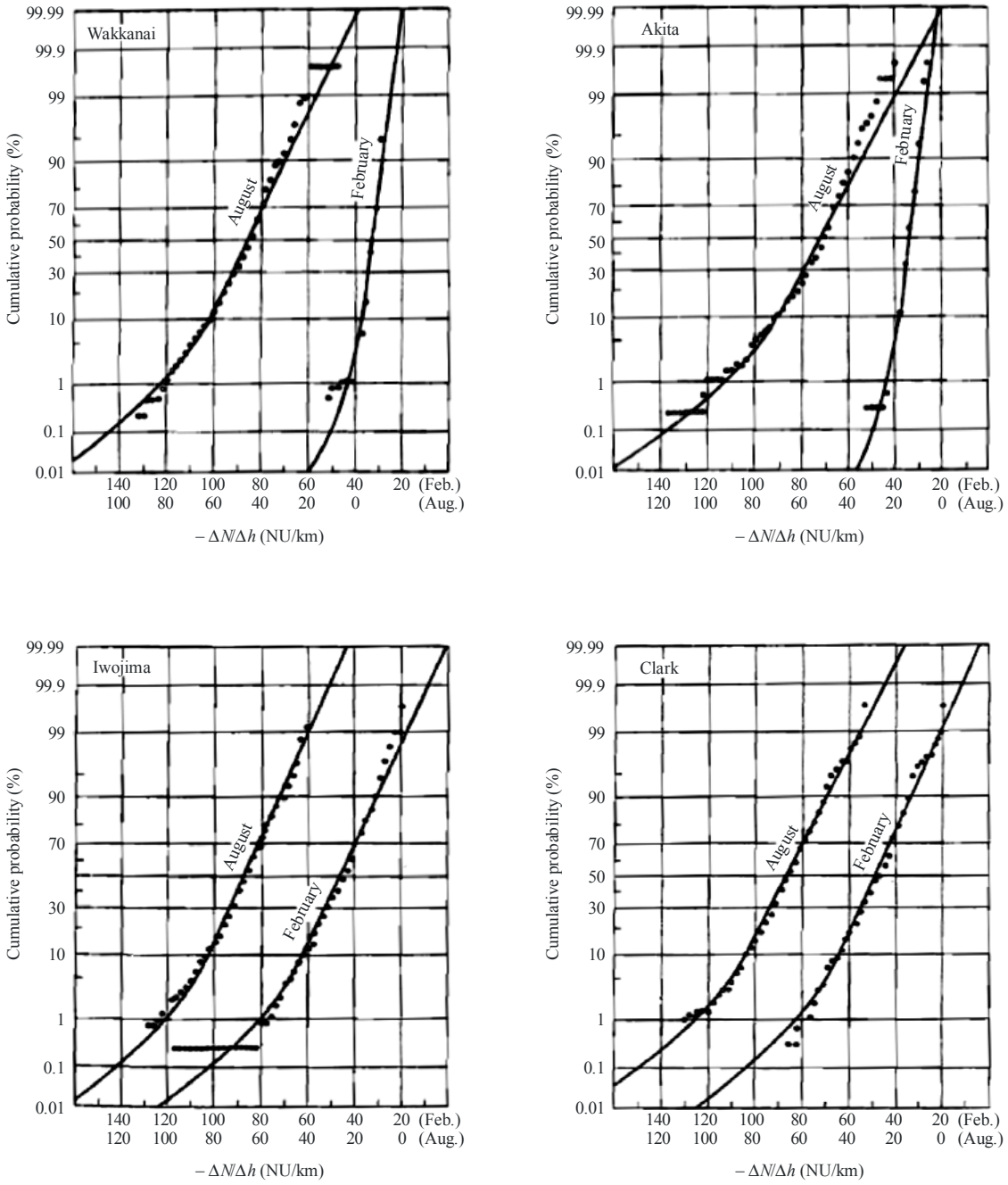

3.6.1.3 Other models

The exponential-normal model improves the representation of the gradient distribution for very negative values. As departures from a normal distribution are evident on both tails of experimental distributions however, it cannot be well adapted to situations of positive gradients.

Zhang [1981] developed a model fitting the whole distribution by introducing two power laws in order to represent tail deviations from the normal. The cumulative probability of this model is given by:

$$F(\alpha)=\begin{cases} P_1\times[(\alpha_1-\alpha_m)/(\alpha-\alpha_m)]^{b_1} & -\infty<\alpha<\alpha_1 \\ \dfrac{1}{2}\operatorname{erfc}\left\{\dfrac{-(\alpha_1-\alpha_m)}{\sigma\sqrt{2}}\right\} & \alpha_1<\alpha<\alpha_2 \\ 1-P_2\times[(\alpha_2-\alpha_m)/(\alpha-\alpha_m)]^{b_2} & \alpha_2<\alpha<\infty \end{cases} \tag{3.20a}$$

where "erfc" is the complimentary error function.

It is expected that the probabilities P_1 and P_2 are small enough so that average and standard deviation α_m and σ of the composite distribution are in practice those of the central normal part of the distribution. The model depends on six parameters b_1, b_2, P_1, P_2, α_1 and α_2. These parameters must satisfy the following conditions:

i) The cumulative probability is continuous for $\alpha = \alpha_1$ and $\alpha = \alpha_2$, that is

$$\begin{aligned} P_1 &= \frac{1}{2}\operatorname{erfc}\left\{\frac{-(\alpha_1-\alpha_m)}{\sigma\sqrt{2}}\right\} \\ 1-P_2 &= \frac{1}{2}\operatorname{erfc}\left\{\frac{-(\alpha_2-\alpha_m)}{\sigma\sqrt{2}}\right\} \end{aligned} \tag{3.20b}$$

and,

ii) The model distribution is made equal to the experimental one at probability levels 0.1% and 99.9%, that is:

$$b_1=\frac{\log(1000P_1)}{\log\dfrac{\alpha_{0.1}-\alpha_m}{\alpha_1-\alpha_m}} \quad b_2=\frac{\log(1000P_2)}{\log\dfrac{\alpha_{99.9}-\alpha_m}{\alpha_2-\alpha_m}} \tag{3.20c}$$

If one chooses P_1 and P_2 from the points of the experimental distribution where deviation from the normal begins to occur, the model is completely specified.

The models presented so far are obtained from an empirical fit to experimental distributions. A more physically-sound approach has been adopted by Schiavone [1981]. He considered that the three parts of the gradient distribution were due to different meteorological situations. The central normal part of the distribution is attributed to a regime of vertical air mixing, and the tails of the distribution to stratified air; as mechanisms leading to strongly-negative or positive gradients are different, the two tails of the distribution are generally not symmetrical. The mixing situations are represented by a normal distribution with average value μ_m and standard deviation σ_m. The problem is to determine the distributions and proportion of the time of the stratified conditions. Schiavone considered only refractive gradients above the average. Arguing that stratified conditions develop from mixed ones he assumed for the distribution of the stratified gradient a normal distribution with the same average μ_m and a standard deviation σ_s. The complete distribution is thus:

$$f(\alpha) = (1 - P^*)N(\mu_m, \sigma_m) + P^* N(\mu_m, \sigma_s) \quad (3.21)$$

N indicating a normal distribution and P^* is the proportion relating to stratified air conditions.

This model (which does not represent situations of super-refraction) depends on four parameters, μ_m, σ_m, σ_s and P^*. Comparing this modelled distribution with available data from North America, the author concluded that P^* and σ_m were relatively invariant with respect to location and season, whereas μ_m and σ_s depend on both.

Other models have been used recently to describe vertical gradient statistics obtained from site specific data. For example, Grabner and Kvicera [2011] provided a model combining three normal distributions in a similar fashion as in equation (3.21).

3.6.2 Statistical information on refractivity gradients

From the previous discussion, it is clear that the parameters needed to define the refractive index gradient distribution depend on the model used. Of prime importance for any model, however are the average and standard deviation of the gradient, both of which depend on the season and location of interest.

Information on a world basis concerning monthly averages of the refractivity gradient between the ground and one kilometre, based on five years of radio-sounding data from 268 stations have been given by Bean *et al.* [1966] from which are extracted Figures 4 to 7 of Recommendation ITU-R P.453. The geographical locations of the stations used in this study are given in Figure 3.7.

FIGURE 3.7

Location of ΔN data stations (from Bean et al, 1966)

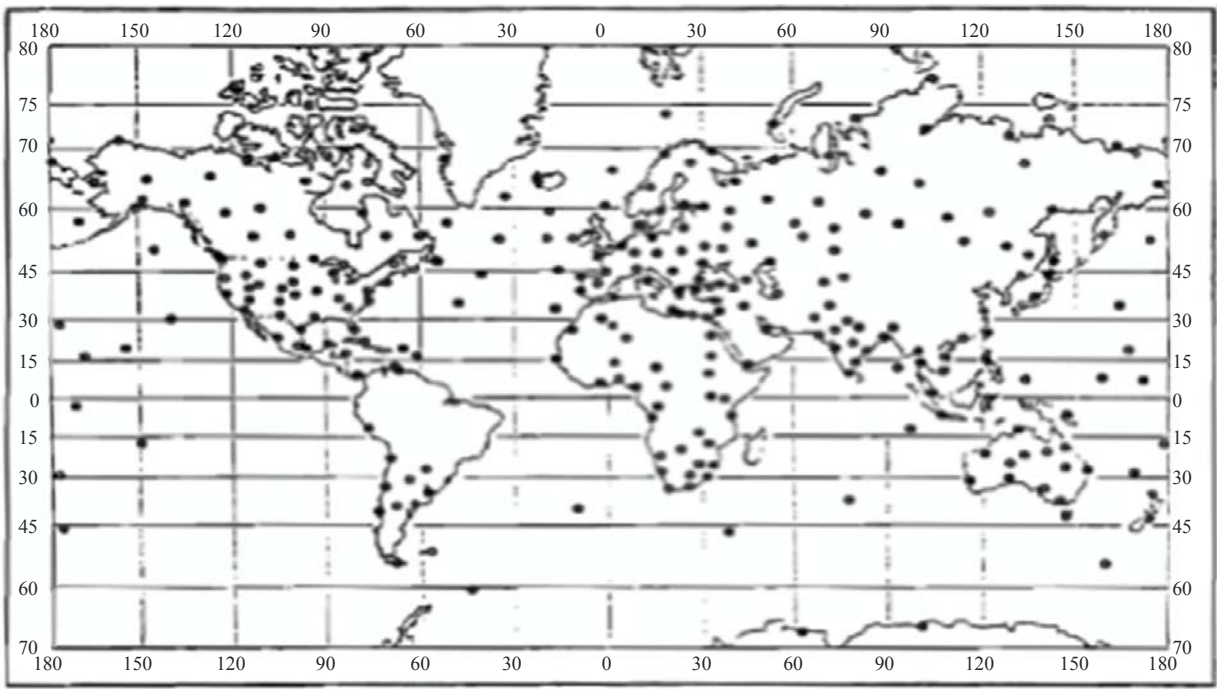

Results concerning the standard deviation are not so easily obtained. Generally, the published data give either the percentage of the time for which a given gradient is exceeded, or the gradient exceeded for a given percentage of time. The selected values generally belong to the tails of the gradient distribution; consequently the measurements are not very precise and the values of the refractive gradients are dependent on atmospheric processes (subrefraction and superrefraction) which show marked daily variations, whereas routine radio soundings are generally made only twice a day at particular times, differing from one station to the other. It is therefore not possible to give a world distribution of this parameter. It is sometimes available, however on a regional basis; we present in Figure 3.8, as an example, the results from Japan from Akiyama [1977]. Existing information can nevertheless be used to estimate the importance of superrefractive conditions or of subrefractive conditions (see § 3.7).

FIGURE 3.8

Contour map showing average value ΔN and standard deviation (from Akiyama, 1977)

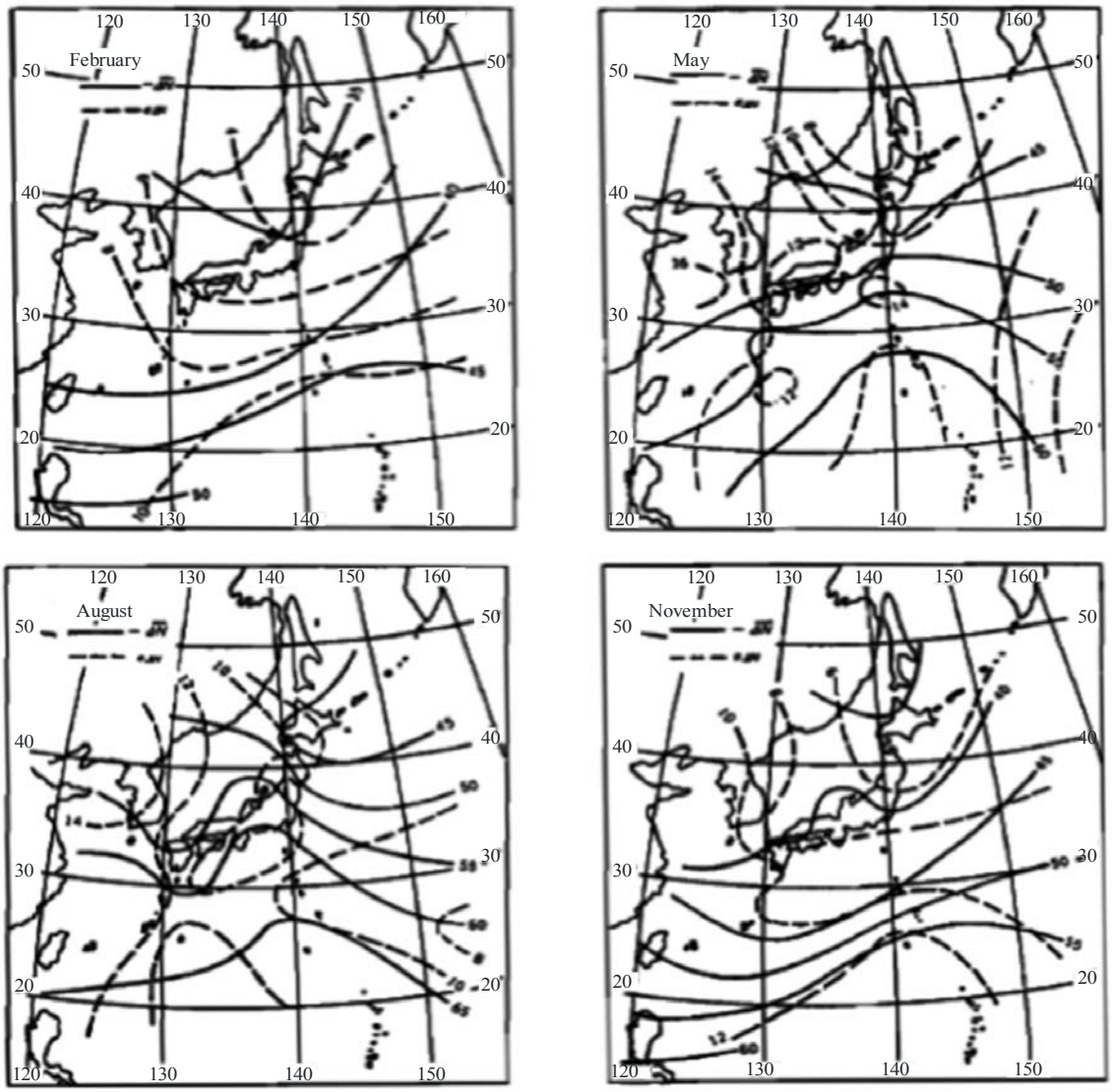

The distribution of the gradient α, over the first kilometre is generally computed from radiosonde data. According to Ikegami *et al.* [1968], it is possible to deduce from such data parameters of the exponential-normal model for any other height range. For a layer of thickness Δh (km), we have:

$$\alpha_m(\Delta h) = \alpha_m(1\text{ km}) \qquad \sigma(\Delta h) = \sigma(1\text{ km})\sqrt{(1/\Delta h)} \qquad \text{(N-units / km)} \tag{3.22a}$$

for an elevated layer.

In the surface layer, the first 100 m of the troposphere, these relations have to be corrected and Japanese data lead to (with subscript g to denote that we are considering the layer just above the ground):

$$\alpha_{mg}(\Delta h) = \alpha_m(1\text{ km}) - 28 \qquad \sigma_g(\Delta h) = [0.755\sigma(1\text{ km})+3.56]\times\sqrt{(1/\Delta h)} \quad \text{(N-units)} \tag{3.22b}$$

Of course, the validity of this last relation is not guaranteed outside Japan.

Finally, cumulative distributions of the refractive index (such as those shown in Figure 3.5) have been published for many stations. In Bean *et al.* [1966] are presented the cumulative distributions of $\alpha_{0.1}$ obtained from radio soundings for 22 stations belonging to various climatic zones. Information based on more stations or more precise measurements may be available for particular areas, such as Canada [Segal and Barrington, 1977], Japan [Akiyama, 1977], the United Kingdom [Hall and Comer, 1969] or the Czech Republic [Grabner and Kvicera, 2005, 2006, 2011].

3.6.3 Correlation between ground refractivity and refractivity gradient

In many countries, a strong correlation has been observed between the monthly averages of ground refractivity and the refractivity gradient in the first kilometre, α_1 [Lane, 1961; Bean and Dutton, 1966; Akiyama, 1977]. A synoptic view of this effect is given on Figure 3.9 [Bean *et. al.,* 1966] which presents contours of the correlation coefficient between both parameters. It appears that this correlation is strong in auroral and temperate regions, and lower in tropical and equatorial regions. Thus, the correlation is not observed where the climate is warm and moist, leading to high values of the partial pressure of water. The correlation is thus probably due to the dry term of the refractivity, whereas a large wet contribution masks the effect.

For regions where a good correlation exists, a regression relation of the form:

$$\alpha_1 = -\,a\,\exp(kN_S) \tag{3.23}$$

gives a good representation of the data. Parameters a and k depend on the climatic region. For the United States, Bean and Dutton [1966] give:

$$a = 7.32 \qquad k = 0.005577$$

For Japan, Akiyama [1977] reports

$$a = 3.42 \qquad k = 0.007576$$

Although these sets of values may seem quite different, they do not lead to significantly different results, as shown in Figure 3.10.

FIGURE 3.9

Correlation coefficient of ΔN and N_s (from Bean *et al.*, 1966)

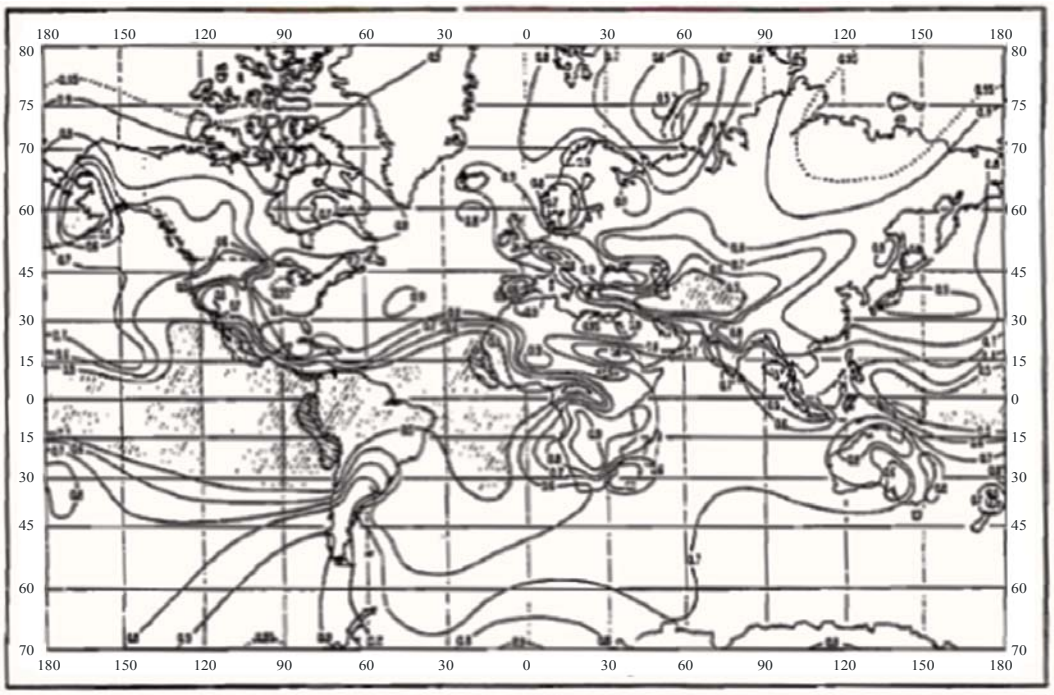

Radio-Meteo. 03-09

FIGURE 3.10

Comparison between bean and Dutton and Akiyama regression curves

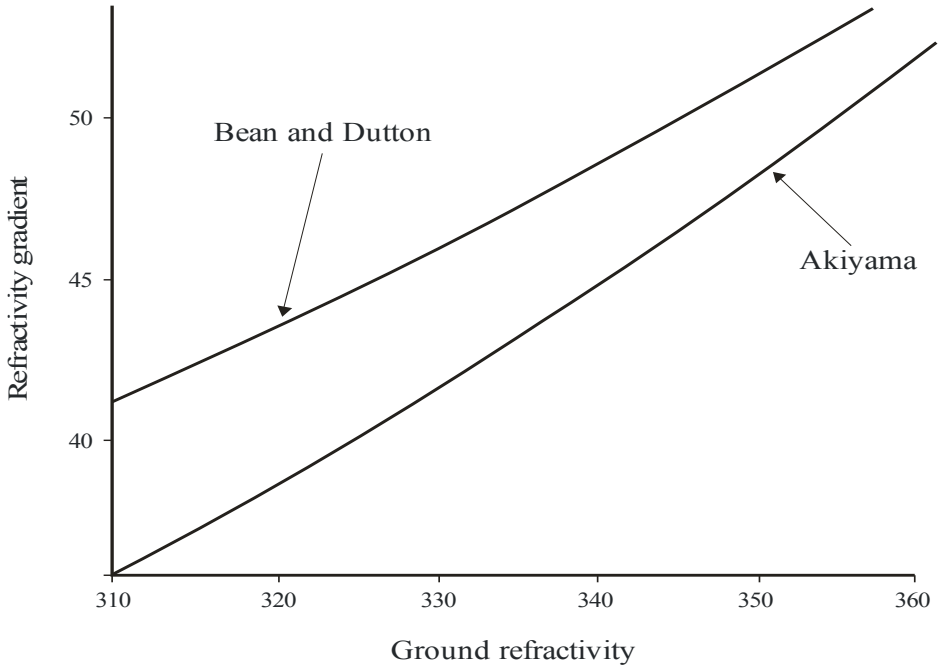

Radio-Meteo. 03-10

3.6.4 Equivalent refractivity gradient along a path

All the information given in the previous sections is relative to the atmospheric refractivity gradient at a given location. When considering a radiowave propagating in the atmosphere, the refractivity gradient along the path is not constant. The effect on the wave is therefore an averaged effect depending of the state of the atmosphere along the path.

This situation leads to the consideration of a new parameter, the equivalent gradient along a path, defined as the gradient of an atmosphere with constant gradient which would give the same refractive effects as the real atmosphere [Misme, 1960]. This parameter, however, is not purely a characteristic of the atmosphere, but it depends also on the radio path. Quantitative methods to estimate this parameter will therefore be considered in Chapter 4. We present here however, a qualitative discussion to consider this phenomenon.

Two kinds of phenomena must be taken into account when looking at the refractive effects of the atmosphere along a path. The first is the change of the refractivity gradient with height. We have seen that the linear model of refractivity is very crude. In the exponential model, the gradient (in modulus) decreases with height (equation (3.14)). As a consequence, the absolute value of the equivalent gradient will be lower than that of the ground gradient and the reduction will depend on the exact trajectory of the waves. This first effect has been analysed by Misme [1960] and Boithias and Misme [1962].

The second phenomenon is the horizontal inhomogeneity of the atmosphere. Frequently, the vertical gradient of the atmosphere is not constant along the path. The distance over which a horizontal homogeneity can be assumed (a kind of correlation length) depends, in fact, on the prevailing meteorological situation, as well as on the terrain profile along the path. For instance, the correlation length of stratified situations is probably shorter than for mixed situations, and decreases still further as the terrain profile becomes hilly.

3.7 Refractivity structures at meso and macroscales

3.7.1 Ducting layers – definition and experimental observations

At times when the atmosphere is thermodynamically unstable and in a state of turbulent mixing, the refractivity gradient is not very different from –40 N-units/km. However, in other cases, the refractivity gradient can be quite different. For instance when the temperature increases with height, there can be a stable stratification of the troposphere resulting in refractivity layering, that is, the presence of layers of very different refractive index gradients.

A layer, with a refractivity gradient below –157 N-units/km immersed in a broader region having a smaller refractive index lapse rate (the lapse rate is the opposite of the gradient), is called a ducting layer. The propagation of waves in the presence of such layers will be described in more detail in Chapter 4. In the presence of such a layer, the radius of curvature of the wave trajectory becomes smaller than the radius of the Earth, and, as a consequence, waves propagating nearly horizontally may be trapped between two levels (the lower one being possibly the ground).

Ducting layers are observed from the surface up to heights of several kilometres. Their thickness can range from a few metres up to several hundred metres. If the layer is bounded by the earth's surface then it is termed a surface duct, otherwise it is known as an elevated duct. Depending on the formation process of the duct and also upon the height above the surface, ducting layers can extend horizontally up to distances of several hundred kilometres. Figure 3.11 shows an example of an elevated duct resulting from large-scale subsidence of dry air. The measurement was carried out by an aircraft fitted out with meteorological sensors. The ducting feature was measured over a distance of 400 km. Figure 3.12 is an example of a ducting layer in the lower part of the atmosphere. It is due to the advection of dry air over the sea surface, as part of a seabreeze

circulation and is an example of a surface duct. The extent of the ducting layer is only a few kilometres out to sea, but considerably longer parallel to the coast. Table 3.1 lists some general characteristics of various duct types.

FIGURE 3.11

Example of a very thin super-refractive layer
(from Lane, 1965)

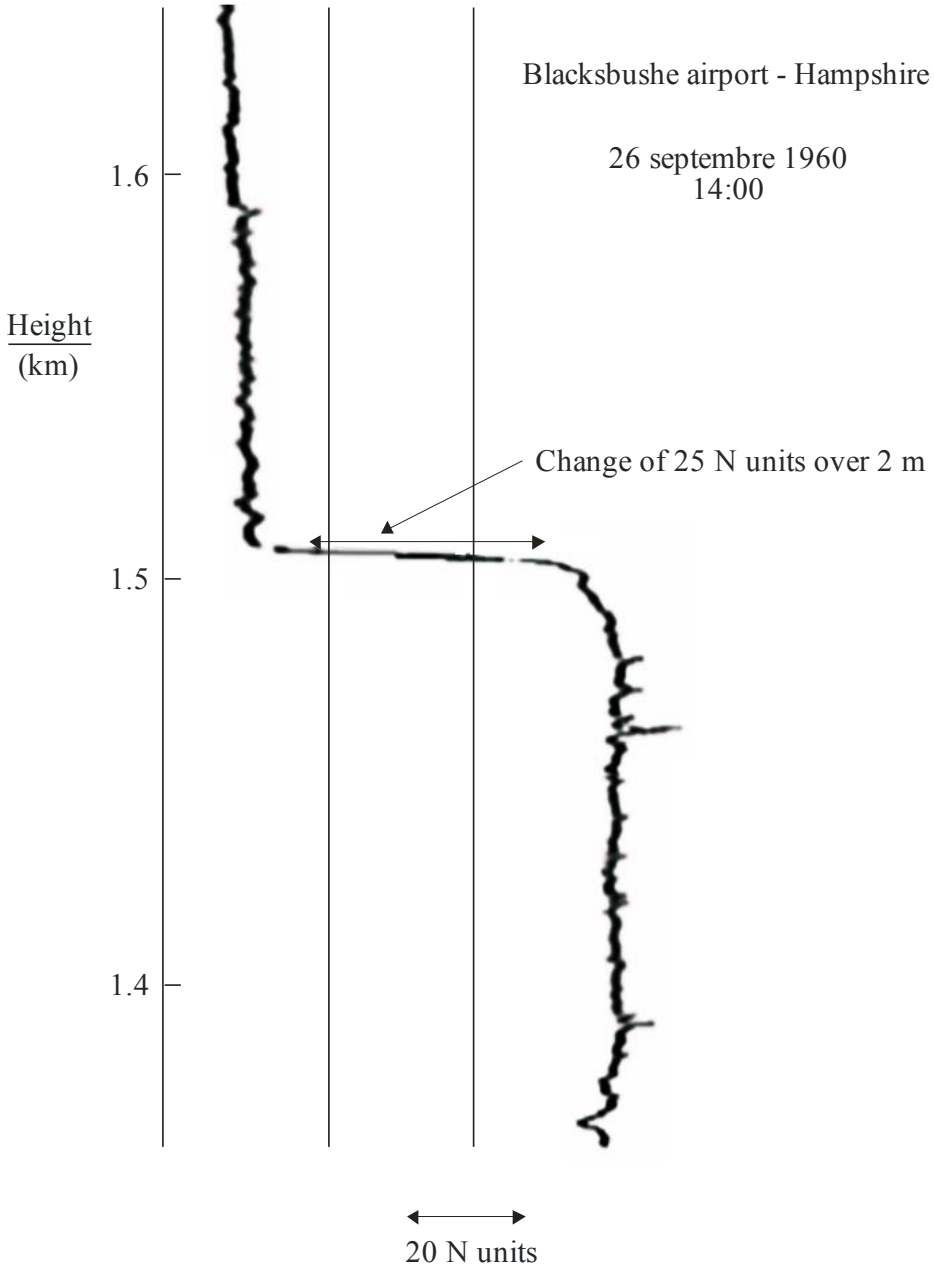

Radio-Meteo. 03-11

FIGURE 3.12

Balloon measured refractivity profile during multipath event (from Sylvain *et al.*, 1983)

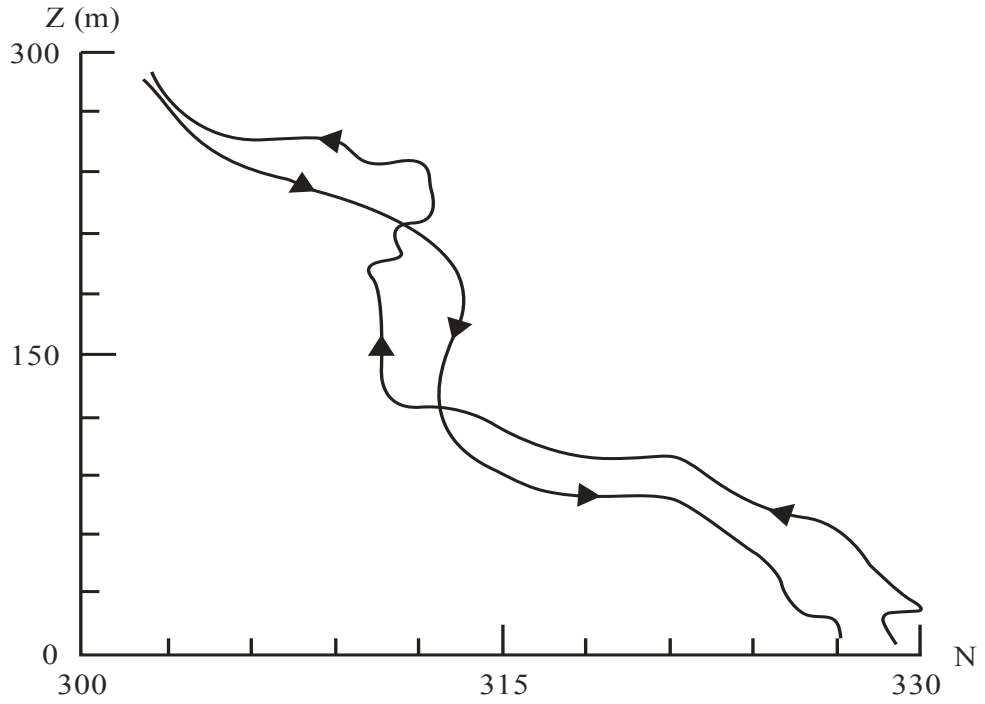

TABLE 3.1

Duct classification

Duct Type	Name	Scale (extent & height)	Duration	Data available:
surface	Evaporation	Macroscale, surface layer phenomenon ~40 m max duct height.	Hours to days (can be diurnal along coastlines)	SG3 databanks
Surface or elevated	Advection – as part of synptic weather patterns or mesoscale diurnal circulations	Mesoscale to macroscale (~100 km), coastal phenomenon Up to ~ 300 m	Diurnal	Coastal radiosonde measurements, aircraft measurements, towers
Surface or elevated	(Mesoscale) subsidence		Diurnal	Radiosonde & Aircraft data
Elevated	Subsidence (macroscale)		Up to several days	Radiosonde & Aircraft data
Surface	Radiative cooling (mesoscale – macroscale)		Diurnal	Radiosonde
Elevated	Frontal systems		1- 4 hours	Radiosonde

Scales: Mesoscale: 10 km – 300 km
Macroscale: 300 km – 3000 km
Global scale: > 3000 km.

3.7.1.1 Duct modelling

Assuming the geometrical optics approximation to radio-wave propagation, ray trajectories are given by the Snell-Descartes law. In a plane earth geometry with a stratified atmosphere (index of refraction depending only on the altitude h) the ray equation is:

$$n(h)\sin\alpha = const. \tag{3.24}$$

with α the angle of the ray with the vertical axis. With spherical geometry, this relation has to be replaced by Bourguer's formula:

$$n(r)\,r\sin\alpha = const. \tag{3.25a}$$

with r being the distance from the Earth's centre.

We have $r = R + h$ (R, the Earth radius) and $n = 1 + 10^{-6} N$. If $h << R$, we can approximate (3.25a) as follows:

$$\left[1+10^{-6}N(h)\right](R+h)\sin\alpha \approx R\left[1+h/R+10^{-6}N(h)\right]\sin\alpha = const. \tag{3.25b}$$

This relation is identical to equation (3.24) if we substitute:

$$m(h) = n(h) + h/R = 1+10^{-6}M(h) \tag{3.26a}$$

Where $m(h)$ is the modified refractive index and $M(h)$ is the modulus of refraction. From equation 3.26a it can be seen that the propagation of a wave near a spherical Earth with refractivity profile $N(h)$ is equivalent to propagation above a plane Earth with refractivity profile $M(h)$. Taking the value of 6370 km for the Earth radius, we have

$$M(h) = N(h) + 157h \quad \text{with } h \text{ in km.} \tag{3.26b}$$

In normal conditions of propagation the modulus of refraction increases with height. It decreases with height only if dN/dh is lower than –157 N-units/km, that is, within ducting layers.

Figure 3.13 shows the relationship between the N and the M profiles, presented for the same situation. The refractivity profile shows clearly the ducting layer, characterised by its height h_0, its thickness, Δh, and its intensity, ΔN. The M profile shows the ducting layer but also the associated duct, limited on the upper side by the top of the ducting layer and on the lower side by the height at which the modulus of refraction has the same value (or by the ground). The duct thickness, D is therefore greater than that of the ducting layer. The other characteristics of the duct are its height h_D, the height of the lower limit of the duct, and the duct intensity, ΔM.

A duct is termed an elevated duct when its lower limit is above the ground. The height h_D of the duct is then the height of its lower limit. In other cases, the duct is called a surface duct, and its lower limit is on the ground; the lower limit of the associated ducting layer can, however be above the ground (Figure 3.14).

FIGURE 3.13

Correspondence between N and M ducting layers representation (from Webster, 1982)

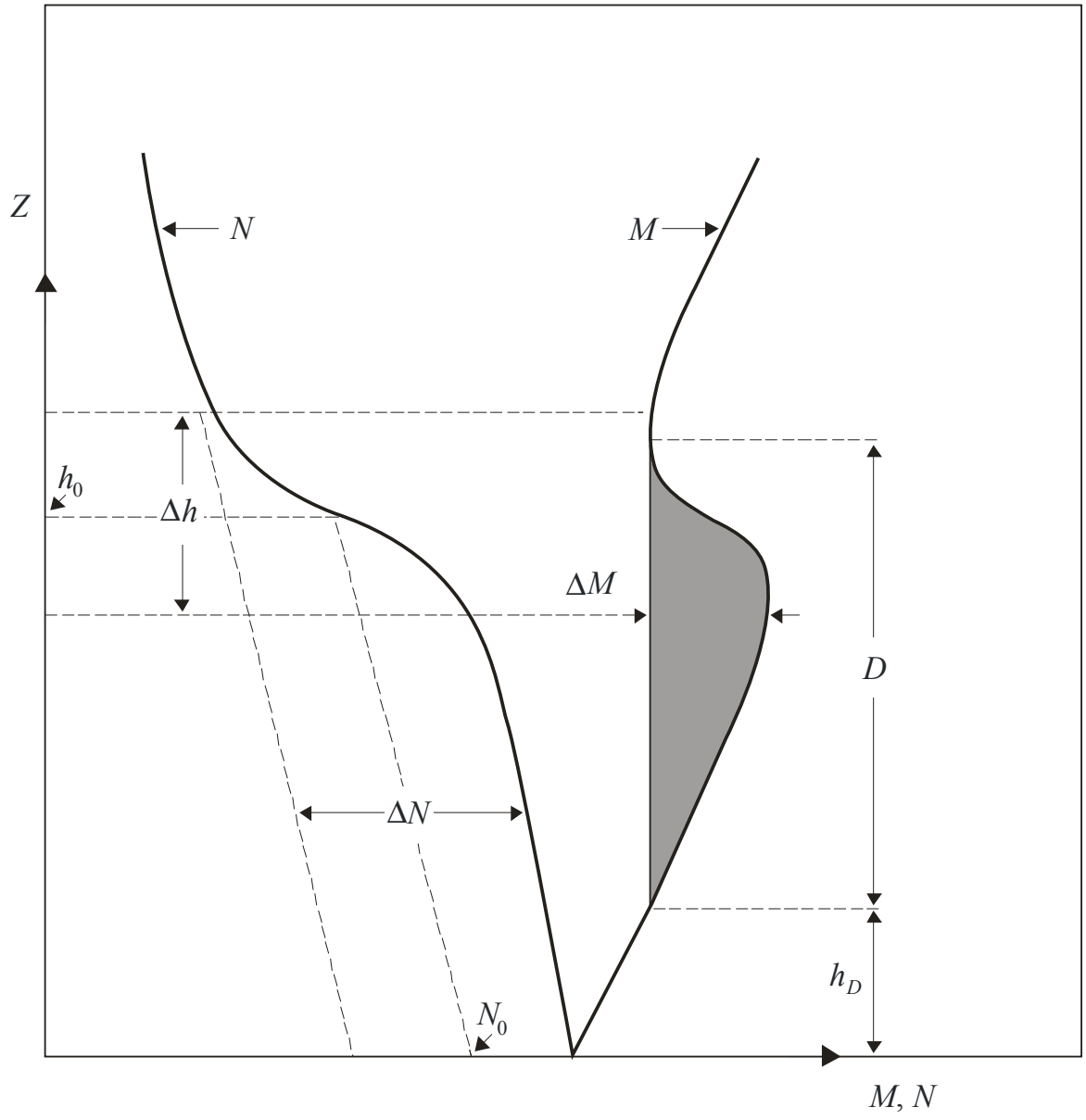

FIGURE 3.14

Elevated and surface duct parameters
(from Dougherty and Dutton, 1981)

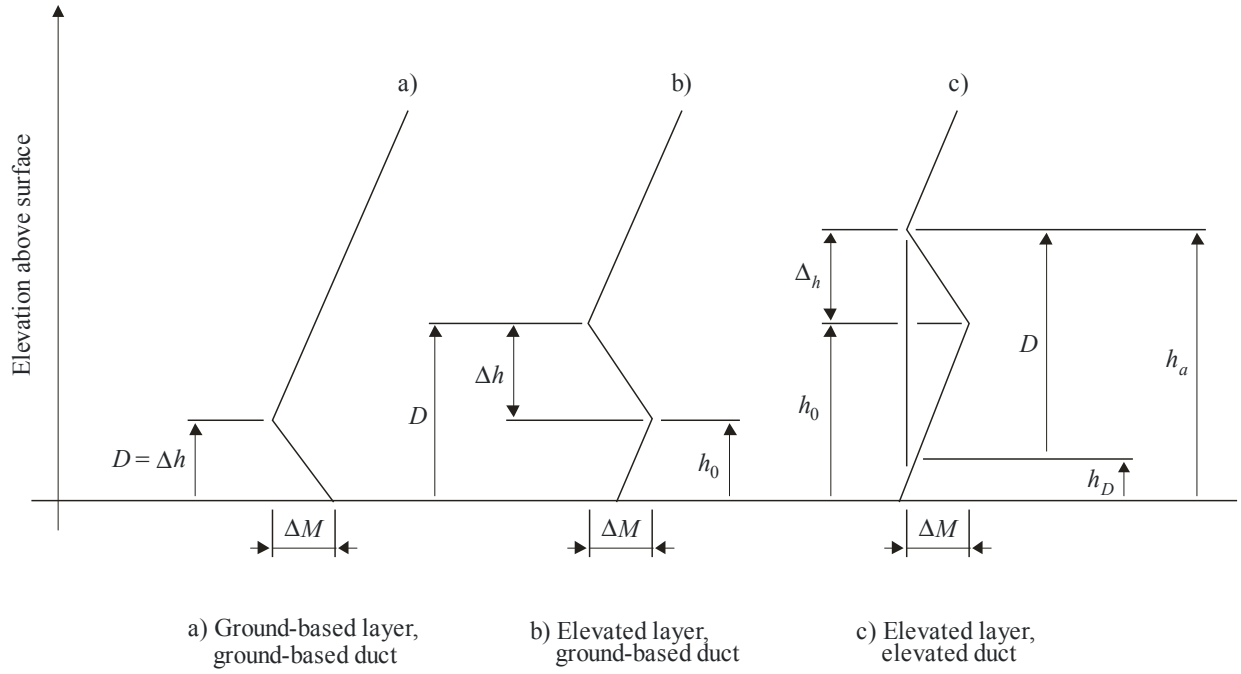

Radio-Meteo. 03-14

To allow analytical or numerical propagation studies in the presence of ducts, the true refractivity profiles are modelled by simple analytical functions. Once a model has been chosen, it is possible to relate by algebraic manipulation the parameters of the N representation to those of the M representation and vice versa. The simplest model which has been very widely used, consists of a three part linear refractivity profile, as shown in Figure 3.14. The drawback of this model is the introduction of unrealistic discontinuities in the refractivity gradient, which can lead to unsatisfactory results with some numerical ray-tracing programmes. To preserve a continuous refractivity gradient, Webster [1982] used an arc tan model in which the refractivity is given by

$$N(h) = N_o - kh + \frac{\Delta N}{\pi}\ arctan\left[\frac{12.63(h-h_0}{\Delta h}\right] \tag{3.27}$$

In this model as Figure 3.13, N_0 is the ground refractivity and k the background lapse rate of refractivity. The ducting layer, which extends theoretically to infinity, is characterised by its height h_0, (the height of the centre of the layer), its intensity ΔN and its thickness, Δh, defined as the height range (centred on h_0) over which occurs 90% of the refractivity variation ΔN. It has been shown that experimental profiles can be fitted by equation (3.27), by superimposing several layers of this type [Claverie and Klapisz, 1985].

3.7.1.2 Duct statistics

What is of interest in propagation studies is a statistical description of ducting layers. Such a description would ideally comprise their probability of occurrence, with its regular (daily and seasonal) variations, a statistical description of their characteristics (height, thickness and intensity, these quantities probably being correlated) and a statistical description of their horizontal extent.

In fact, our knowledge of duct statistics is rather poor. This is due to the limitations of radiosonde data, the only source of information on a worldwide basis. These data have limitations with regard to the accuracy with which refractivity gradients can be estimated (§ 3.9.3); they only give average gradients over a height range and therefore miss very thin and intense ducting layers; they are usually collected only twice a day at given times and can therefore lead to a statistical description which may not adequately reflect daily variations; finally measurement stations are too far apart to give information about the extension of ducts. In some cases, more specific experiments give a better description of ducts but which are applicable only locally.

A global indication of the occurrence of surface ducts can be derived from Figures 3.15 to 3.18 [Bean *et al*., 1966] which give, from radiosonde data obtained from 99 stations, the percentages of time for which the gradient $\alpha_{0.1}$ is less than –157 N-units/km. The percentages of time for which the gradient $\alpha_{0.1}$ is less than –100 N-units/km are presented in Figures 8 to 11 in Recommendation ITU-R P.453. In the second case, there is necessarily a ducting layer in the first hundred metres of the atmosphere; in the first case, it is probable but not certain. Information based on more radiosonde stations is available for selected areas such as Canada [Segal and Barrington, 1977] or India [Majumdar *et al*., 1977].

FIGURE 3.15

Percent of time gradient ≤–157 N/km - February
(from Bean *et al.*, 1966)

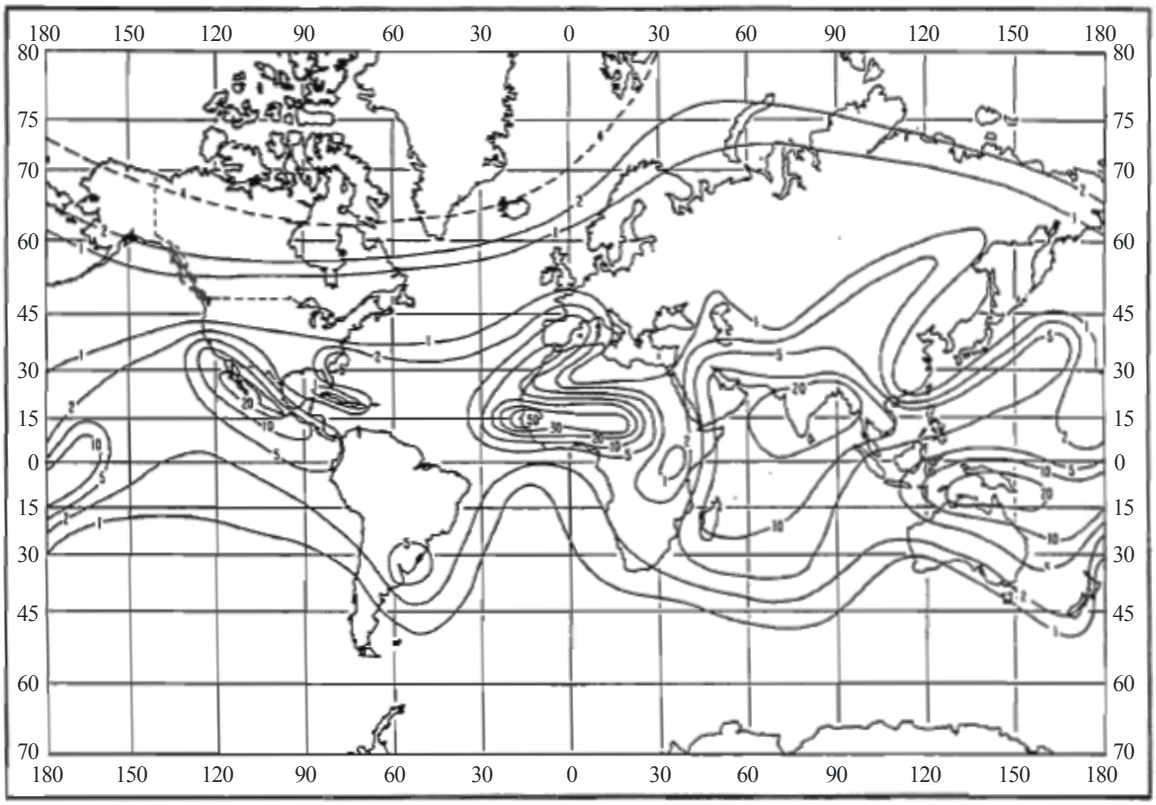

FIGURE 3.16

Percent of time gradient ≤–157 N/km – May
(from Bean *et al.*, 1966)

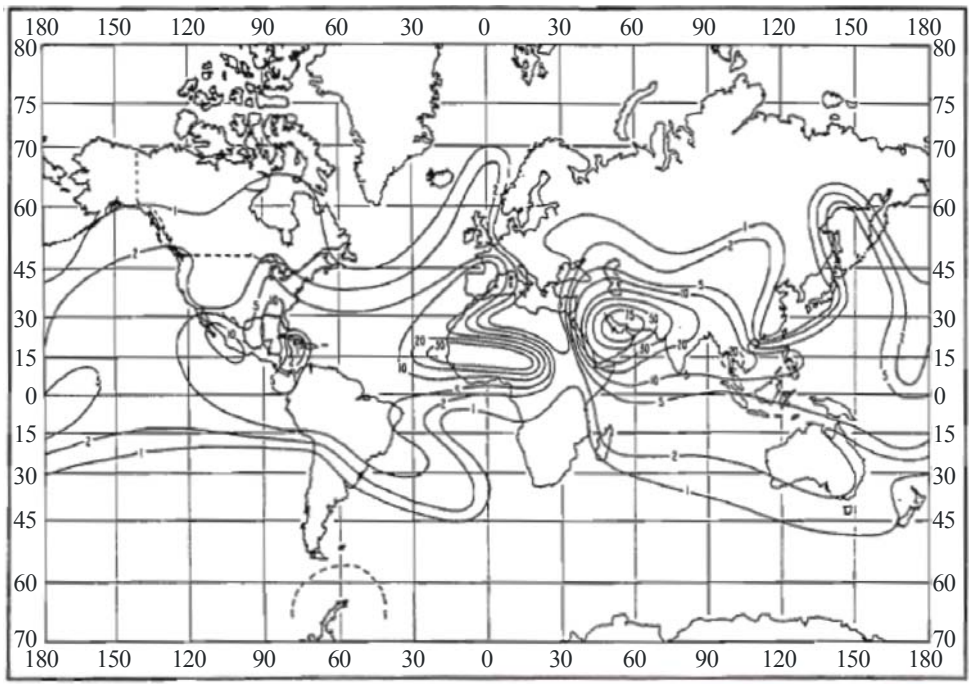

Radio-Meteo. 03-16

FIGURE 3.17

Percent of time gradient ≤–157 N/km – August
(from Bean *et al.*, 1966)

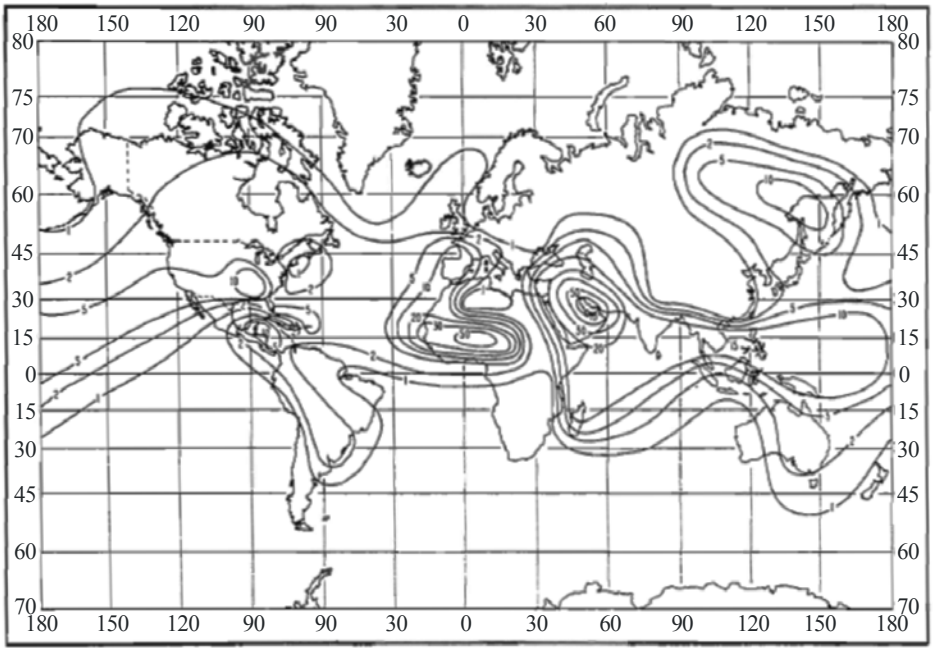

Radio-Meteo. 03-17

FIGURE 3.18

Percent of time gradient ≤–157 N/km – November
(from Bean *et al.*, 1966)

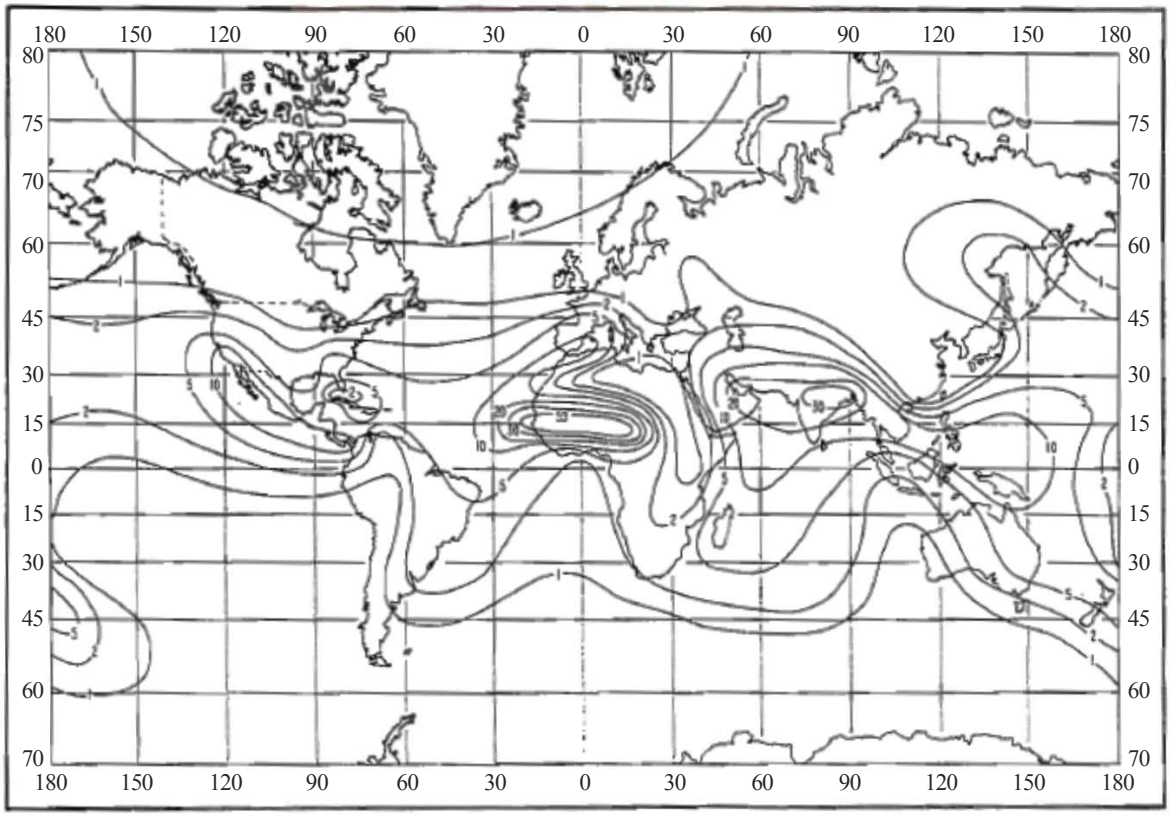

Radio-Meteo. 03-18

Information on the occurrence of ducting layers can also be derived from refractivity gradient models described in § 3.6 for regions for which the parameters of these models are known, see for example [Grabner and Kvicera, 2011].

On the other hand, precise information on the joint distribution of height, thickness and intensity of ducting layers is very scarce. Some data from Japan have been published [Ikegami *et al.*, 1966] derived two weeks of continuous measurements from a 300 m high tower. Some results of this study are presented on Figure 3.19. Figure 3.19a shows the distribution of a duct intensity ΔM; large intensities are less frequent. Figure 3.19b gives the distribution of duct height: the maximum probability occurs in the first 50 m of the atmosphere. Above this, the occurrence decreases slowly up to 120 m and is almost constant from there up to 280 m. As regards relationships between the duct characteristics, it appears that there is no significant correlation between the mean height and the intensity of a duct, but there is a good correlation between the intensity and the thickness of the duct (Figure 3.19c). Such relationships could be used to extrapolate results obtained in one particular region to others exhibiting different climatic behaviour.

FIGURE 3.19

Statistics of ducting layers parameters
(from Ikegami *et al.*, 1966)

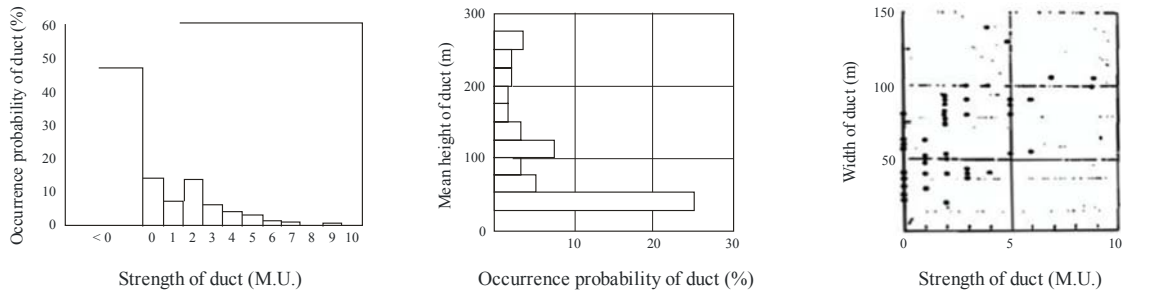

a - Probability distribution of duct occurrence versus strength of duct.

b - Occurrence probability of duct versus height

c - Relation between strength and width of duct.

Radio-Meteo. 03-19

Advances in computer technology have enabled meso-scale numerical weather prediction models to be readily implemented on modest size computers. These models output humidity, temperature and pressure over a given volume and time frame and so they can be used to indicate the variations in radio-refractivity and give an insight into the physical mechanisms that produce and maintain ducts. The vertical resolution of these models may need further refinement, but nevertheless some attempt can be made at investigating the relationships between ducting parameters for different climatic regions. The models give a good indication of the variations in duct occurrence for a particular region which is very useful in designing an experimental campaign aimed to sample the changes in duct structure in the region. Thus more detailed duct statistics have been obtained for a meso-scale region.

3.7.2 Sub-refractive conditions

The standard gradient of refractivity is –40 N-units/km. Situations where the gradient is greater than this (less negative or even positive) are called sub-refractive conditions. On a nearly-horizontal path, a consequence of sub-refraction is that the wave trajectory comes nearer to the ground. In extreme cases, if there is an obstacle (for instance a hill) along the link, the transmitted signal level can be severely reduced by diffraction; such an event is called obstruction fading, and will be considered from a propagation point of view in Chapter 4.

To predict the potential impact of obstruction fading on a given link, information is needed on the occurrence of sub-refractive conditions, that is, on the positive tail of the refractivity gradient distribution.

3.7.2.1 Statistics of sub-refractive conditions

According to the characteristics of a particular link, obstruction fading may occur for different values of the refractivity gradient. A worldwide indication of potential effects due to subrefraction can be inferred from Figures 3.20 to 3.23 which give contours of the occurrence of a positive refractivity gradient in the first 100 m of the atmosphere.

More precise estimations can be made when the complete gradient distribution is known.

FIGURE 3.20

Percent of time gradient ≥ 0 N/km – February
(from Bean *et al.*, 1966)

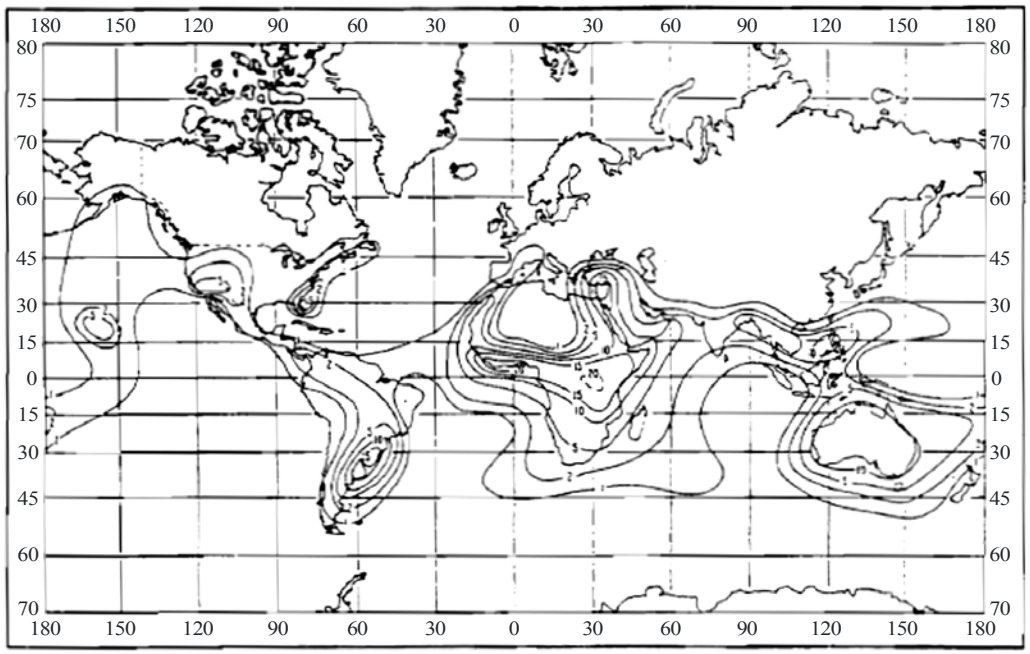

Radio-Meteo. 03-20

FIGURE 3.21

Percent of time gradient ≥ 0 N/km – May
(from Bean *et al.*, 1966)

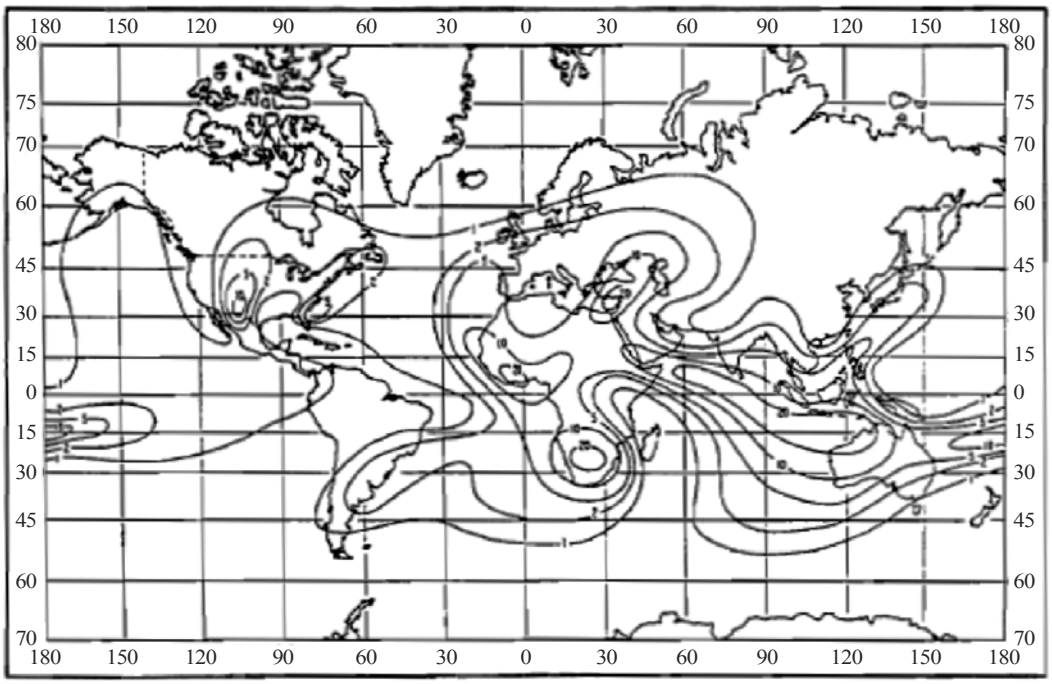

Radio-Meteo. 03-21

FIGURE 3.22

Percent of time gradient ≥ 0 N/km – August
(from Bean *et al.*, 1966)

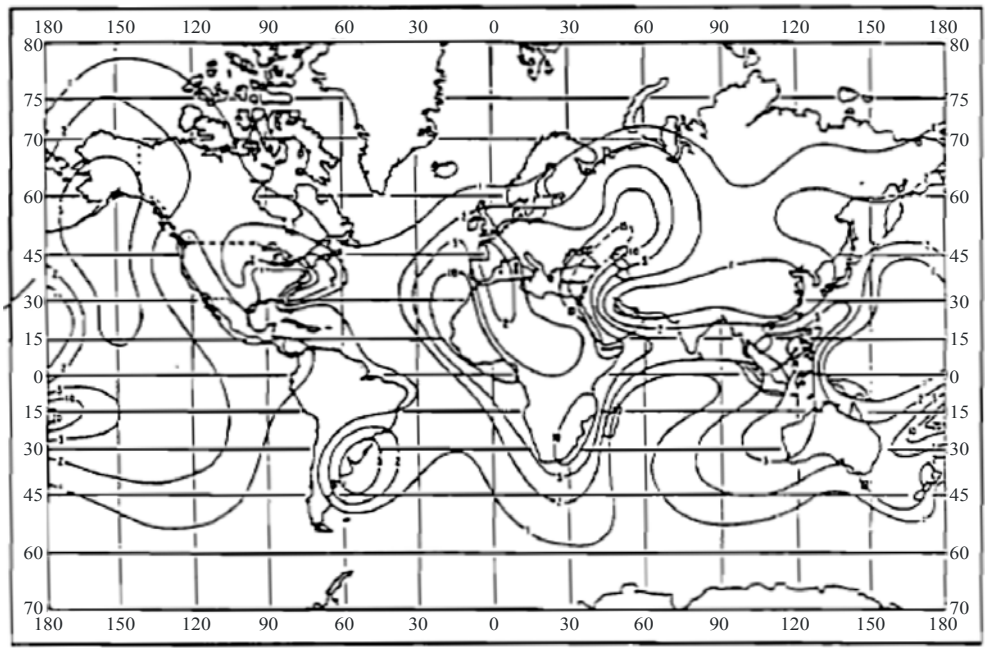

Radio-Meteo. 03-22

FIGURE 3.23

Percent of time gradient ≥ 0 N/km – November
(from Bean *et al.*, 1966)

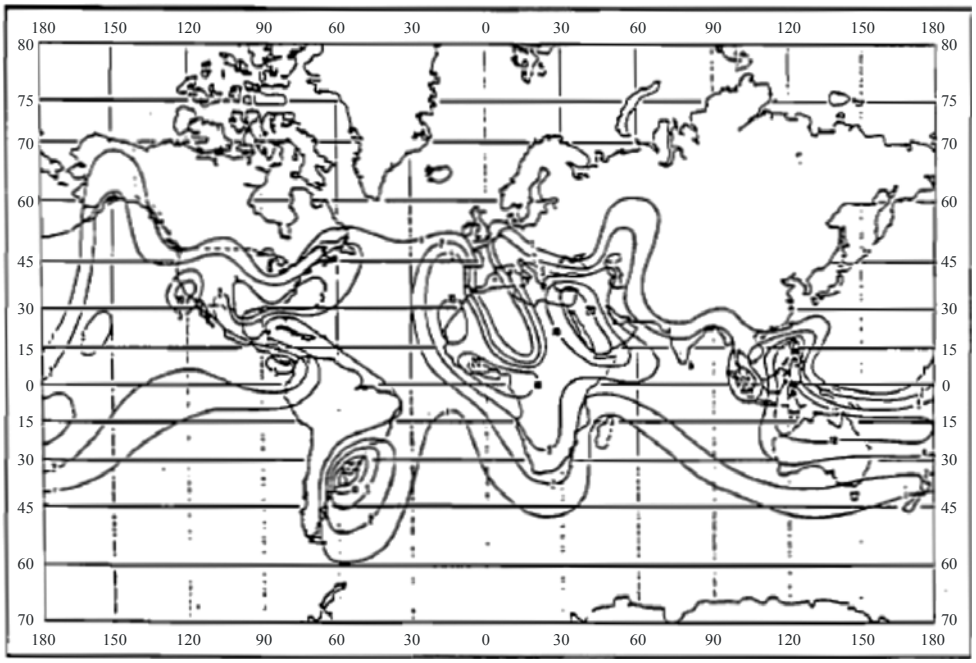

Radio-Meteo. 03-23

3.8 Horizontal refractivity gradients

Horizontal gradients of refractivity may occur in regions where there is more than one air mass. This often occurs where there are large changes in surface conditions such as the land / sea boundary, or the transition from mountainous to flat terrain where the climate changes significantly. The sudden change in terrain conditions can alter atmospheric dynamics which in turn produces circulations and wave structure. Frontal passages produce horizontal gradients in refractivity as do large scale subsidence inversions, although in the latter case, the variations in gradient are observed over large distances. Horizontal gradients can have important effects on wave propagation because they can act over long distances. Disagreement between radio data and ray tracing simulation using a model atmosphere deduced from one refractivity profile measured at one location along the radio path under study, are often attributed to the effect of horizontal gradients [Claverie and Klapisz, 1985].

Various case studies of propagation in laterally inhomogeneous atmospheres have been published, discussing the magnitude of the horizontal variation in refractivity and also the effects on radio-wave propagation. In these cases radio-wave propagation has been modelled by ray tracing techniques and also by the parabolic equation method.

Several examples of atmospheric situations with horizontal refractivity gradients are given in Figure 3.24. Figure 3.24a shows measurements above land and sea made in Australia. While the transition from land to sea is clearly observable, important horizontal gradients above the sea are also present. Horizontal gradients can be observed also above the sea (for instance [Chavance *et al*., 1954]) or above land [Blanchetiere-Ciarletti *et al*., 1989].

FIGURE 3.24

Examples of important horizontal refractivity gradients
a) from Bean and Dutton (1966); b) from Vickers and Lopez (1975)

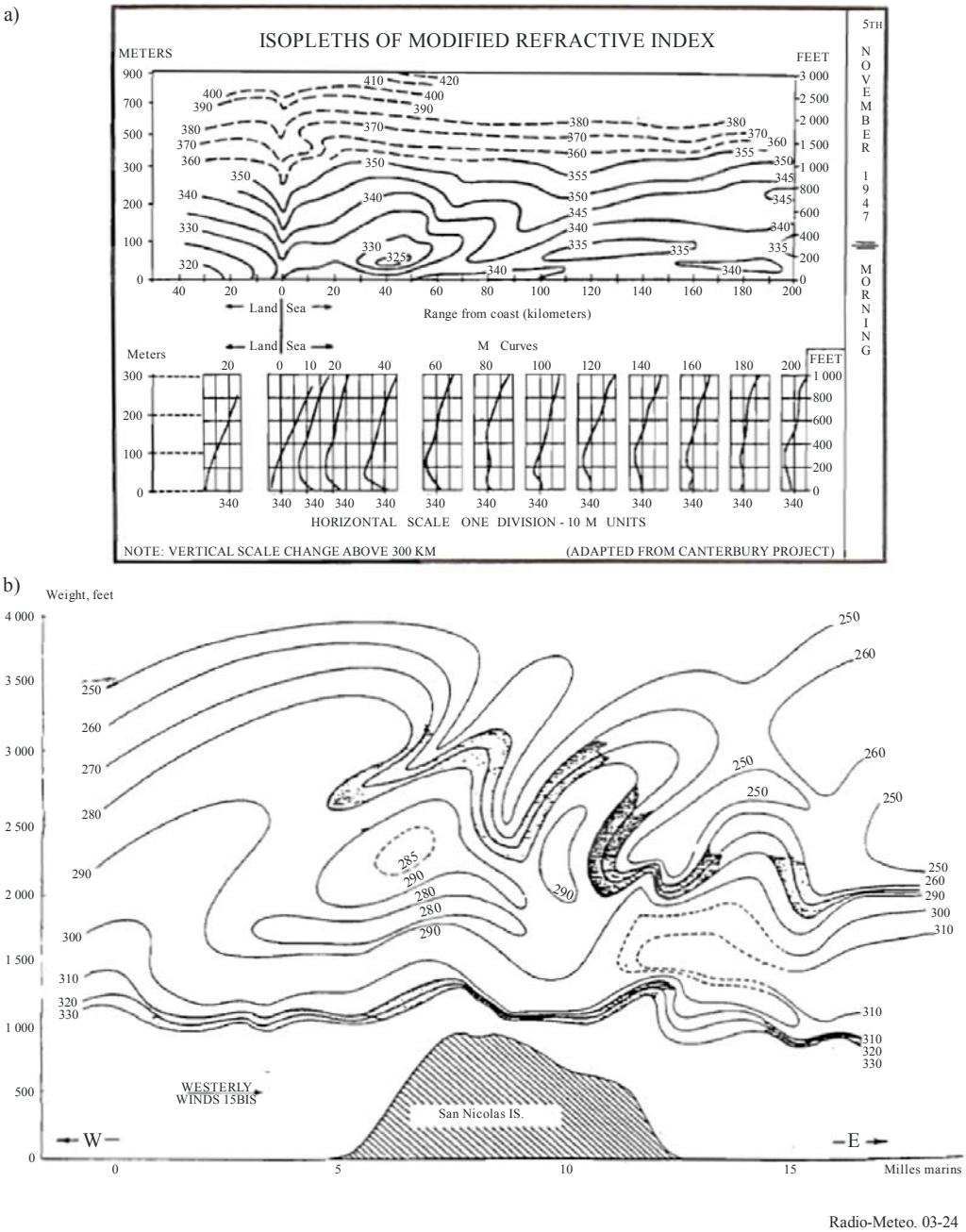

The effects of horizontal refractivity gradients are particularly important when vertical structures such as ducting layers are simultaneously present over the intended propagation path or propagation area. The models used to describe ducting layers can be adapted to such situations by supposing that the parameters of the layer change with horizontal position. For instance, it is possible to make the height of the layer change regularly with distance to obtain an inclined layer, its intensity to be modulated by a Gaussian function to simulate a layer of finite horizontal extension, or some parameters of the layer to vary sinusoidally with position to represent a gravity wave or a similar perturbation. These situations will be considered in the next chapter when discussing their effects on propagation.

Implementations of the parabolic equation method and various hybrid methods can readily accommodate the inclusion of realistic refractive index data. Recent research has focused also on the development of three dimensional parabolic equation codes which handle refractive index variations in both horizontal directions as well as in the vertical.

3.9 Techniques of refractive index measurements

Due to its significance in radiowave propagation, it is very important to be able to measure the refractive index of air. There are, two well proven ways of measuring the refractive index. [Bean and Dutton, 1966; Hall, 1971; Segal, 1985]. This is achieved either directly by means of a microwave refractometer, or by directly measuring the meteorological parameters, pressure, temperature and humidity of air using the relation 3.11. Other methods rely on remote sensing techniques. Close to the sea surface, clutter can be used to infer the refractive index. In addition to this, it has been suggested to infer evaporation duct parameters from signal strength measurements of satellite-to-ship paths, when the satellite is close to the horizon. The use of the GPS satellite network to infer refractive index structure over a given volume is also being investigated. Furthermore, remote sensing of temperature and moisture profiles in the atmosphere has also been carried out successfully, although the vertical resolution attained is somewhat coarse. Various remote sensing techniques for the measurement of refractive index are being developed. Clearly, these techniques are attractive because they do away with the necessity of the difficult task of directly measuring the refractive index or relevant meteorological quantities. A detailed discussion of remote sensing techniques is beyond the scope of this chapter and only the direct measurement methods are discussed.

When considering either refractometer measurements or meteorological measurements, whichever method is used, the measurement of the refractive index with good accuracy of 1 N-unit implies a relative accuracy of 10^{-6}. In principle, a refractometer can give more precise results than the use of meteorological data but other complicating phenomena may interfere, such as dilatation. Nevertheless, recent advances in solid state technology have ensured that refractive index values determined from meteorological measurements are becoming sufficiently accurate for propagation applications.

The measurement of refractive index can be difficult. The difficulty certainly depends on the environment that the measurement is being made in. The measurement of one data point is certainly not sufficient. What is really important for propagation is the gradient of refractivity and its variation with space and time. To deduce the vertical gradient, the vertical refractivity profile needs to be measured and not only must each measurement be accurate (i.e. within 1 N-unit uncertainty) but the measurements must be done at a spatial resolution adequate for identifying fine structure such as thin ducting layers. These problems are discussed in § 3.9.3.

Finally, if two or three dimensional structures are to be characterized, in particular to obtain information on horizontal gradients, the main difficulty lies in the requirement of time to cover all the domains of interest (typically one hour for a two-dimensional mapping by aircraft over a line-of-sight link). This issue leads to the classical problem of separating time and space variations. One way of mitigating this problem is to alter the measurement strategy by employing two or more aircraft instead of one aircraft. (Although this would largely solve the issue of resolving spatial and temporal variations, it is an expensive option.) Suitable housings have been designed for meteorological sensors mounted on aircraft to minimize systematic errors. Furthermore, sensors are located in such a way so that the motion of the aircraft does not interfere with the quantity being measured. In this way, successful airborne measurements of atmospheric parameters such as air temperature, humidity, and pressure have been carried out in Europe, the United States of America, Australia and Japan.

3.9.1 Direct measurements – microwave refractometers

The principle of a direct measurement of the refractive index is very simple. It is based on the fact that the resonance frequency of a microwave cavity is a function both of the geometrical shape and dimensions of the cavity and of the refractive index of its content. In any case, the resonance occurs when a particular relation of proportionality is satisfied between a dimension L, of the cavity and the wavelength λ. The latter is given by:

$$\lambda = v / f = c / (nf) \tag{3.28}$$

with v the propagation velocity of the wave and n the refractive index.

As the dimension L is a constant, the resonance takes place at a constant λ, and therefore a change in the refractive index must be compensated for by a change in the resonance frequency. According to equation (3.28), one has:

$$\Delta f / f = -\Delta n / n \tag{3.29}$$

In the study of the atmospheric refractive index, it is generally possible to use the approximation $n \approx 1$ and therefore:

$$\Delta N = -\Delta f / f \tag{3.30}$$

It is difficult to realize absolute measurements. Indeed, the dimensions of a cavity are never known with sufficient precision to derive theoretically the resonance frequency from the characteristics of the cavity. A calibration is therefore necessary, using a gas of known refractive index.

Two types of refractometer were developed in the fifties [Birnbaum, 1950; Crain, 1950] and much used subsequently [Crain, 1955]. At that time, refractometers used klystrons, the frequencies of which were not stable with changing temperature. To avoid this limitation, refractometers had two similar cavities, one which contained a gas of known properties, used as a reference, and the other filled with a gas under study. Modern electronic components allow the use of only one cavity with precise and stable measurement of the resonance frequency.

If the principle of operation of a refractometer is very simple, its practical implementation is not so straightforward. First, the air to be measured must be introduced into the cavity without decreasing its quality factor too much. Generally, a cylindrical cavity operating in the TE_{011} mode with openings at its ends is used. If the refractive index of the medium changes, the air inside the cavity has to be changed fast enough to follow the variations of the medium. If the refractometer is carried by a plane, the air inside is changed as a result of the motion of the plane. If it is at a fixed point, ventilation has to be supplied. In both cases, it must be verified that the air flow from outside from outside to inside does not induce changes of the air characteristics (pressure and temperature); in particular, there should be no change within the cross-section of the air flow and the flow must be laminar.

The resonance frequency will, of course, depend on the dimensions of the cavity. It will change if the latter changes due to thermal expansion. It is easily verified that a change ΔL of the dimensions of the cavity will appear as a change Δn of refractive index such that:

$$\Delta n / n = \Delta L / L \tag{3.31}$$

and therefore

$$\Delta n / n = \alpha \Delta T \tag{3.32}$$

with α the coefficient of thermal expansion. The metal which has the lowest thermal expansion is Invar (a nickel-steel alloy with $\alpha \approx 6.10^{-6}$); even such a low thermal expansion leads to a change of 6 N-units for a 10 ºC temperature change. Moreover, thermal expansion is often subject to hysteresis.

In summary, refractometers alone have the possibility to measure very fast changes of the refractive index, and a potential precision less than one N-unit. However, they are rather expensive, and their use is delicate, especially if long – term stability or absolute measurements are required.

3.9.2 Indirect measurements - measurement of meteorological quantities

The determination of the atmospheric refractive index can also be based on measurements of the meteorological parameters (pressure, temperature and humidity of air) and the use of equation (3.10). Compared to the refractometer method, this approach has two advantages; its implementation is easier, and the physical interpretation of the observed changes in the refractive index is immediate.

Caution must be taken to reduce errors when making measurements of pressure, temperature and humidity as the inferred refractive index may not be that accurate. From measurements of the humidity and temperature, one obtains the atmospheric water vapour pressure. From the error analysis given below, it is clear that the water vapour pressure is the most important and sensitive measurement that must be made.

A differentiation of equation (3.11) gives the error on refractivity resulting from errors on the values of the meteorological quantities. This can be written as:

$$\Delta N = a\,\Delta P + b\,\Delta T + c\,\Delta e \tag{3.33a}$$

with the coefficients *a, b* and *c* depending on atmospheric conditions

$$a = 77.6/P \qquad b = 77.6P/T^2 + 7.46\ 10^5\ e/T^3 \qquad c = 3.75\ 10^5/T^2$$

Taking as an example typical temperature conditions, $T = 288$ K, $P = 1\,000$ hPa, $e = 10.2$ hPa, we obtain:

$$\Delta N = 0.27\Delta P + 1.25\Delta T + 4.52\Delta e \tag{3.33b}$$

It is evident that the measurement of the water vapour pressure needs to be very accurate, while it is the most difficult to do. Many methods to measure humidity have been proposed and § 3.9.2.2 is devoted to this issue.

Another weakness of the indirect method is related to the time constants of the sensors, which are often large (of the order of several seconds) and not all the same. This leads to difficulties in the determination either of fast changes of the refractivity, or its gradient.

It must be pointed out however, that while ΔP, ΔT and Δe are the maximum errors of the measured quantities, the error in the refractivity given by equation (3.33) is also a maximum, which can be very pessimistic. If assumptions are made about the distributions of the individual errors, for instance that they are independent and uniformly distributed on intervals of respectively $2\Delta P$, $2\Delta T$ and $2\Delta e$, it is possible to compute the probability distribution of ΔN and to characterize the precision of the determination of N by a statistical quantity such as the standard deviation, or an interquantile range.

3.9.2.1 Temperature and pressure measurements

Temperature is the easiest quantity to measure with accuracy and precision. Bulb thermometers are used in ground stations; their time constant is of the order of a second. Faster instruments are the thermistor and the platinum wire. Platinum resistors have been commonly used in a number of platforms ranging from instrumented buoys, towers, to aircraft. Once carefully calibrated, they have provided accurate results, (up to ± 0.02 ºC) at a fast rate. The response rate can depend on how the sensor is housed, but it has successfully been used on board an aircraft to measure atmospheric temperature at rates up to 50Hz.

Pressure measurement is more difficult. The most common device is the aneroid capsule, but it is not very precise due to persistent deformations and it is temperature dependent. The mercury barometer can be used only on ground stations. Some devices use piezoresistors, in which a pressure change is transduced into an electric signal.

As seen above, however, a high accuracy is not needed for pressure and existing devices are generally adequate.

3.9.2.2 Humidity measurements

In the conditions encountered in radiometerological studies, moist air can be considered as a mixture of perfect gases. Its humidity, is related to its water vapour content, can be quantified using several parameters which are related to one another by relations depending also on the pressure and temperature. The physical quantity on which refractivity directly depends is the partial pressure e. This partial pressure is necessarily lower than (or equal to) the saturation vapour pressure e_s, which under the perfect gas assumption depends only on the temperature T. A commonly used derived quantity is the relative humidity H (in per cent) defined as:

$$H = 100e / e_s(T) \tag{3.34}$$

Two other quantities which can be encountered are the mixing ratio r (in kg/kg) which is the ratio of the mass of the water vapour to the mass of the dry air, and the water vapour concentration ρ_v which is the mass of water vapour per unit of volume (in g/m).

It is important to know how the saturation vapour pressure varies with temperature. Several empirical or semi-empirical relations can be used which are nearly equivalent for practical use. In fact, two formulae have to be used, one above 0 ºC, giving the saturation vapour above liquid water, the other below 0 ºC, corresponding to saturation vapour above ice. A simple relation (given in Recommendation ITU-R P.453) is sufficiently accurate between –40 ºC and +50 ºC.

$$e_s = EF \cdot a \cdot exp\left[\frac{\left(b-\frac{t}{d}\right)\cdot t}{t+c}\right] \tag{3.35}$$

and

$$EF_{water} = 1+10^{-4}\left[7.2 + P\cdot\left(0.00320+5.9\cdot10^{-7}\cdot t^2\right)\right]$$

$$EF_{ice} = 1+10^{-4}\left[2.2 + P\cdot\left(0.00382+6.4\cdot10^{-7}\cdot t^2\right)\right]$$

where:

t: temperature (^{o}C)

P: pressure (hPa)

H : relative humidity (%)

e_s : saturation vapour pressure (hPa) at the temperature t (°C) and the coefficients *a*, *b*, *c* and *d* are:

for water	for ice
a = 6.1121	*a* = 6.1115
b = 18.678	*b* = 23.036
c = 257.14	*c* = 279.82
d = 234.5	*d* = 333.7
(valid between –40 °C to 50 °C)	(valid between –80 °C to 0 °C)

Vapour pressure *e* is obtained from the water vapour density ρ using the equation:

$$e = \frac{\rho T}{216.7} \quad \text{hPa} \tag{3.36}$$

Where ρ is given in g/m^3. Recommendation ITU-R P.836 gives representative values.

Several methods have been developed to measure humidity, most of them being based on physical equilibria [Spencer-Gregory and Rourke, 1957], some more recent ones using the propagation of light waves. A brief review of these methods, giving their principle of operation and discussing their advantages and drawbacks, is given below. Note that equation (3.33) can be used to derive the accuracy of the refractivity determination only when the vapour partial pressure is measured. If the equipment measures another humidity parameter, the relation deriving refractivity from the effectively - measured quantities has to be established.

In most cases, it is necessary to carry out regular calibrations of the measuring equipment (called an hygrometer). This can be done by means of salt solutions. It is known, for example, that the vapour pressure above a solution of non-volatile solute is lower than the vapour pressure above the pure solvent at the same temperature (Le Chatelier principle). It is thus possible to have several solutions leading to known relative humidities between, say 10% and 90%. The relative humidities are dependent on the temperature above the super saturated solution and so it is necessary to carefully monitor the temperature as well. For an accurate calibration it is necessary to use at least three or four solutions over the humidity interval of interest. For example, when calibrating humidity sensors for use in a warm marine atmosphere, where the relative humidity is expected to be above 60%, the use of three solutions should suffice. If a larger humidity range is going to be measured, more solutions are required, (e.g. five solutions normally suffice when calibrating over a humidity range of 10% to 90%). More recent calibration devices have been developed which furnish air with given relative humidity by mixing dry air and water saturated air. The operating temperature must also be known for this method.

3.9.2.2.1 Dew point hygrometer

The principle of the dew point hygrometer (introduced by Regnault in 1845) consists in lowering the air temperature down to the point where saturation is obtained. If this happens at a temperature T_D, the vapour pressure e is given by

$$e = e_s(T_D) \tag{3.37}$$

This then gives the vapour pressure directly.

The principle of such an instrument is as follows. A polished metal plate, in contact with the air, is slowly cooled down. A light beam is reflected by the plate and focused on to a photo-detector. When condensation of water droplets occurs, the light is scattered and the detected signal decreases. The thermometer then gives the dew point. In modern equipment, temperature is measured with thermistors or thermocouples and the cooling is obtained by Peltier junctions.

In practice, the temperature of the plate is repeatedly lowered and increased, in order to remain around the dew point. As a result, the time constant is rather large, of the order of a few seconds.

Moreover, the process of condensation is somewhat more complicated than in the simplified theory given above. In fact, a very thin film of water is deposited on the plate above the dew point temperature. The dew point is the point where the thickness of this film is transformed into droplets, the thermodynamically stable phase due to the resulting decrease in elastic energy. However, the saturation pressure in contact with droplets is different (higher) from that in contact with a plane, since there is a gradient of pressure in the gas, and an associated gradient of temperature and the measurements have to be corrected for this effect.

3.9.2.2.2 Chemical and thin film hygrometers

A class of chemical hygrometers comprises a deposit of salt (generally lithium chloride) or another hygroscopic substance such as a carbon film on a glass or a plastic substrate. When such a component is in contact with wet air, there is an exchange of water molecules between the air and the salt such that that there is equilibrium between the air an a (electrolytic) salt solution. This absorption of water by the salt, which increases with the relative humidity, causes changes to the physical properties of the salt, for instance, its electrical resistivity, which can easily be measured, and gives the relative humidity after calibration. Note also that the resistivity depends on temperature.

This type of hygrometer is sensitive to pollution. In direct current operation, a polarization of the electrodes occurs, which is why it is generally operated with alternating current. Another chemical hygrometer is capacitive. In this type, the sensor is a capacitance with a dielectric whose electrical properties change by absorption of water vapour, which in turn depends on the relative humidity of the ambient atmosphere. The classical dielectric for this application is alumina. Some devices use multilayer dielectrics.

The time constant depends on the thickness of the dielectric and also on the thickness and type of protective covering that may be placed over the sensor. Thus, it may range from about 3 seconds to 15 seconds. Provided the sensor and protective covering is kept clean, thin film hygrometers are ideal for measuring humidity in a variety of environments and can easily be mounted on towers or buoys or balloons. Accurate calibration of the device can be achieved through use of different salt solutions as already described. When used in conjunction with well calibrated platinum resistors for temperature measurement and solid state pressure transducers, a refractivity measurement of better than ± 1 N-unit can be obtained.

3.9.2.2.3 Psychrometer

The psychrometer, or dry and wet bulb thermometer, is a very common hygrometer, where one thermometer gives the air pressure, and a second thermometer (the wet thermometer) is clothed with a wet tissue. If the ambient air is not saturated in water vapour, some water evaporates from the tissue, and as a result the wet thermometer indicates a temperature T_W, which is lower than the air temperature T_A. From the difference between the two temperatures (which is called the temperature depression), it is possible to derive the partial pressure of vapour by a semi-empirical relation

$$e = e_s(T) - AP(T_A - T_W) \tag{3.38}$$

with P the pressure.

The problem is to determine parameter A, the psychrometric constant, which depends, in fact, on the air velocity, and each equipment has thus to be calibrated.

The classical psychrometer has bulb thermometers; more recent devices use thermisters.

The psychrometer is very easy to use. There are however some practical limitations. In order to have a long enough automatic operation, a water reservoir must be implemented. The device is very sensitive to contamination of the material surrounding the wet thermometer by dust. Operation becomes impossible when the wet thermometer is below 0º C, because the material then becomes frozen. Finally, the time constants of the two thermometers are different, that of the wet thermometer being the longer (at least several seconds).

3.9.2.2.4 Lyman-α hygrometer

The Lyman-α hygrometer is faster than the devices above (its time constant may be of the order of a few hundredths of a second). Its principle consists in emitting the Lyman-α line of the hydrogen spectrum (situated in the ultra violet domain of 121.6 nm) and measuring its attenuation over a distance L due mainly to water vapour absorption. If I_0 is the emitted intensity, and I the intensity of measured over a distance L, then

$$I = I_0 \exp(-k \rho_v L) \tag{3.39}$$

which gives access to the vapour concentration.

The main drawback of this instrument is a lack of stability, due to the fact that the spectrum emitted by the light contains in fact several lines and changes with time. In practice, a Lyman-α hygrometer is therefore used together with another, slower device, such as a dew point hygrometer for example, which is used to correct for temporal drift. The combination of using a Lyman–α hygrometer together with a dew point mirror has successfully been used by aircraft to measure vertical and horizontal refractivity structure at low altitudes right up to the stratosphere.

3.9.3 Measurement of vertical profiles

The vertical refractivity gradient is more important than the absolute value of the refractivity. If information is desired on atmospheric structures such as ducting layers, it is the vertical profile which needs to be measured. This can be done basically in several ways. A radiosonde can be used to probe the troposphere and lower regions of the stratosphere. For refractivity measurements in the first one or two hundred metres, instruments mounted on towers, can provide accurate refractivity estimates at high spatial resolution. Measurements over water can be carried out by instrumented spar buoys. Spar buoys are an excellent platform for measuring the refractivity structure in the first 10 metres, which is important as evaporation ducts prevail over water during clear-air conditions.

Other means of measuring the vertical refractivity structure include the use of dropsondes, rocketsondes and tethered balloons.

A typical meteorological radiosonde consists of a set of sensors (among those described above) carried by a small balloon going up to 20 to 40 km, the data being transmitted to the ground by means of a radio transmitter. Instruments have to be cheap and robust; their accuracy, particularly that for humidity, is generally less than required for radiometeorological purposes unless only a statistical description is desired (typically 1 or 2 hPa in pressure, 0.2 ºC in temperature and 2 to 5% in humidity). Nevertheless, radiosonde measurements have successfully been used in measuring ducting layers near the surface (i.e. within the first kilometre) and also at heights of several kilometres.

To determine a profile, two conflicting difficulties have to be recognized. If the radiosonde ascension speed is too fast, the sensors, due to their time constants, are not in local equilibrium, and measured gradients can be seriously in error. If, on the other hand, the ascension speed is low, individual measurements are more precise but the atmosphere may change during the time it takes to obtain them. In practice the accuracy of the radiosonde measurements near the ground is limited due to the high initial speed of ascent and often, data from the first 100 metres may not be very reliable.

In order to obtain more reliable data in the first few 10's of metres and also through the troposphere, a dropsonde rather than a radiosonde can be used. The dropsonde instrument package is similar to that of a radiosonde, giving refractivity accuracies of ± 5 N-units. A dropsonde, as the name implies is dropped from an aircraft. A small parachute is attached to the instrument package giving a descent rate of somewhere between 5 and 10 m/s. Sensor response times are approximately 2 seconds, so the best vertical spatial resolution is around 10 metres. The location of the unit is monitored by a small GPS receiver which gives a height estimate of around ± 20 metres. Alternatively, the height can be inferred from the pressure reading in the same way as a radiosonde. The telemetry range of a dropsonde is about 300 km. Dropsondes are also very useful when profiling the atmosphere over the ocean. For simultaneous operation a maximum number of four sondes can be used.

Instrumented towers and buoys are clearly useful only for a limited range of heights. However, in this limited range it has two advantages over the radiosonde or dropsonde; it discriminates spatial and temporal variations (the latter if they are comparable with the sensor time constants) and it allows for continuous monitoring, while radiosonde profiles are generally obtained only between one and four times per day at regular times as part of standard meteorological services. For any long term experiment where continuous monitoring is intended, the meteorological sensors may drift and systematic errors may be induced. For this reason all sensors must be periodically cleaned and re-calibrated. This is particularly the problem with instrumented spar buoys. Sensors mounted close to the sea surface (i.e. below about 5 metres above sea level) accumulate salt deposits which can badly affect the accuracy of temperature and humidity measurements and also lengthen the time constant of each device. Thus instruments closer to the sea surface become less accurate and out of time with the other instruments. Significant discrepancies in measurements can be detected after only two or three days of deployed time.

3.9.4 Measurement of vertical and horizontal structures

To obtain the two-dimensional structure of atmospheric refractivity is the most difficult task. The sensors have to be carried either on an aircraft or a helicopter. Small, slow aircraft such as motor gliders are suitable for the measurement of a variety of atmospheric parameters including the three important quantities necessary for the determination of the atmospheric refractive index as well as mean and turbulent wind flows. When making airborne measurements of temperature, pressure, and

humidity, the exact location and attitude of the aircraft must be taken into account as well as systematic errors that creep into the measurements of meteorological quantities. Fast response instruments such as platinum resistors and Lyman–α hygrometers combined with a digital data logging system, when installed on a slow aircraft, (20-25 m/s) ensure that the spatial resolution of measurements is of the order of two measurements per metre. Measurements of refractive index have successfully been made between the heights of 10 and 13000 metres using different aircraft. Aircraft measurements of the horizontal and vertical structure of the refractive index can be made by flying a sawtooth pattern over the region of interest. Such measurements have successfully been carried out, for example, in Australia in an attempt to investigate large scale subsidence ducts.

When making airborne measurements of temperature and humidity systematic errors must be carefully taken into account. The sources of error for temperature and pressure measurements include:

(i) The motion of the aircraft through the air, perturbing still air quantities.

(ii) The adiabatic heating of the sensors due to airflow over the sensors.

(iii) The difference in temperature of the sensor and sensor housing. This effect is most noticeable when the aircraft is flying a sawtooth pattern. It is minimized when flying straight and level.

When flying a sawtooth pattern, there are various corrections that must be applied to the data to negate these systematic errors. Details of necessary corrections are found in [Lenschow, 1986] and [Hartmann & Hacker, 1990]. Briefly, these corrections include the application of:

(i) A recovery factor – based upon the airspeed of the aircraft and Bernoulli's equation governing adiabatic changes of a perfect gas.

(ii) An airspeed correction – temperatures can be corrected for airspeed using a formulation based on the true airspeed of the aircraft, static and dynamic pressure, the dew point, and the recovery factor.

(iii) A static pressure correction – this is fundamental to the calculation of speed corrected temperature and is derived from pressure altitude information for consecutive ascents and descents together with radar altimeter data.

(iv) A sensor housing correction – need to know the response time of the housing due to temperature changes. Details of sensor housing corrections are found in [McCarthy, 1973].

The position and attitude of the aircraft must also be known. This is achieved through using a combination of pressure and radar altimeters, differential GPS, and accelerometers. Some aircraft employ an inertial positioning system which uses a combination of gyros and accelerometers. The information that is logged includes the aircraft altitude, heading, track, yaw, pitch and roll fluctuations and time. Logging frequencies are around 10 – 15 Hz.

REFERENCES

AKIYAMA, T. [1977] Studies on the radio refractive index in the tropospheric atmosphere, Review of the E.C.L., 25, No. 1-2, pp. 79-95.

BEAN, B.R. and DUTTON, E.J. [1966] Radio Meteorology, National Bureau of Standards Monograph 92, U.S. Government Printing Office, Washington.

BEAN, B.R., CAHOON, B.A., SAMSON, C.A. and THAYER, G.D. [1966] A world atlas of atmospheric radio refractivity, ESSA Monograph 1, U.S. Government Printing Office, Washington.

BEAN, B.R. and THAYER, G.D. [1959] Models of the atmospheric radio refractive index, Proc. I.R.E., pp. 705-755.

BIRNBAUM, G. [1950] A recording microwave refractometer, Rev. of Scien. Instr., 21, No. 2, pp. 169-176.

BLANCHETIERE-CIARLETTI, V., LAVERGNAT, J., SYLVAIN, M. and WEILL, A. [1989] Experimental observation of horizontal refractivity gradients during periods of multipath propagation, Radio Science, 24, No. 6, pp. 705-724.

BOITHIAS, L. and MISME, P. [1962] Le gradient equivalent, nouvelle détermination et calcul graphique, Annales Telecom., 17, No. 5-6, pp. 134-139.

BOITHIAS, L. [1984] Propagation des ondes radioélectroniques dans l'environnement terrestre, Collection Technique et Scientifique des Télécommunications, 2nd Edition, Editions DUNOD, Paris, France.

CHAVANCE, P., BOITHIAS, L. and BLASSEL, P. [1954] Etude de propagation d'ondes centimétriques dans la région méditerranéenne, Ann. Telecomm., 9, No. 6, pp. 158-185.

CLAVERIE, J. and KLAPISZ, C. [1985] Meteorological features leading to multipath propagation observed in the Pacem 1 experiment, Ann. Telecom., 40, No. 11-12, pp. 660-671.

CRAIN, C.M. [1950] Apparatus for recording fluctuations in the refractive index of the atmosphere at 3.2 cm wave-length, Rev. of Scien. Instr., 21, No. 5, pp. 456-457.

CRAIN, C.M. [1955] Survey of airborne microwave refractometer measurements, Proceedings of the I.R.E., 43, pp. 1405-1411.

DEBYE, P. [1929] Polar Molecules, Chemical Catalog Co., New York. Reprinted by Dover Publ. Co. in 1957.

DOUGHERTY, H.T. and DUTTON, E.J. [1981] The role of elevated ducting for radio service and interference fields, NTIA-Report-81-69, U.S. Department of Commerce.

GRABNER, M. and KVICERA, V. [2005] Statistics of lower atmosphere refractivity in Czechia, APMC 2005, Suzhou, China, Dec 4-7.

GRABNER, M. and KVICERA, V. [2006] Refractive index measurements in the lowest troposphere in the Czech Republic. In Journal of Atmospheric and Solar Terrestrial Physics, June, no. 68, pp. 1334-1339.

GRABNER, M. and KVICERA, V. [2011] Atmospheric Refraction and Propagation in Lower Atmosphere. Electromagnetic Waves, IN-TECH, Vienna, Austria, Rijeka, Croatia, June 2011, pp. 139-156.

HALL, M.P.M. [1971] Radiosondes for radiometeorological research, Proceedings of NATO Advanced Study Institute on Statistical Methods and Instrumentation in Radiometeorology, Tretten, Norway.

HALL, M.P.M. and COMER, C.M. [1969] Statistics of tropospheric radio-refractive-index soundings taken over a 3-year period in the United Kingdom, Proc. I.E.E., 116, No. 5, pp. 685-690.

IKEGAMI, F., AKIYAMA, T., AOYAGI S. and YOSHIDA, H., [1968] Variation of radio refraction in the lower atmosphere, I.E.E.E. Trans. on Ant. and Prop., AP-16, No. 2, pp. 194-200.

IKEGAMI, F., HAGA, M., FUKUDA, T. and YOSHIDA, H., [1966] Experimental studies on atmospheric ducts and microwave fading, Review of the E.C.L., 14, No. 7-8, pp. 505-533.

LANE, J.A. [1961] The radio refractive index gradient over the British Isles, J.A.T.P., 21, pp. 157-166.

LANE, J.A. [1965] Some investigations of the structure of elevated layers in the troposphere, J.A.T.P., 27, pp. 969-978.

LENSCHOW, D. H., [1986] Aircraft Measurements in the Boundary Layer, Chapter in. Probing the Atmospheric Boundary Layer

MAJUMDAR, S.C., SARKAR, S.K. and MITRA, A.P. [1977] Atlas of tropospheric radio refractivity over the Indian subcontinent, National Physical Laboratory, New Delhi, India.

MISME, P. [1960] Le gradient équivalent, mesure directe et calcul théorique, Annales Telecom, 15, No. 3-4, pp. 92-99.

RAO, K.N. and SRIVASTAVA, H.N. [1971] Errors in the computation of mean monthly values of radio refractive index, Radio Science, 6, No. 8-9, pp. 753-755.

SASAKI, O. and AKIYAMA, T. [1982] Studies on radio duct occurrence and properties, I.E.E.E. Trans. on Ant. and Prop., AP-30, No. 5, pp. 853-858.

SCHIAVONE, J.A. [1981] Prediction of positive refractivity gradients for line-of-sight microwave radio paths, B.S.T.J., 60, No. 6, pp. 803-822.

SEGAL, B. [1985] Measurement of tropospheric refractive index relevant to the study of anomalous microwave propagation - review and recommendations, CRC Report No. 1387.

SEGAL, B. and BARRINGTON, R.E. [1977] The radio climatology of Canada, Tropospheric refractivity atlas for Canada, CRC Report No. 1315-E.

SMITH, E.K. and WEINTRAUB, S. [1953] The constants in the equation for atmospheric refractive index at radio frequencies, Proc. I.R.E., 41, pp. 1035-1037.

SPENCER-GREGORY, H. and ROURKE, E. [1957] Hygrometry, Crosby Lockwood & Son Ltd., London.

SYLVAIN, M., BAUDIN, F., KLAPISZ, C., LAVERGNAT, J., MAYRARGUE, S., MON, J.P., NUTTEN, B., ROORYCK, M. and MARTIN, L. [1983] The Pacem experiment on line-of-sight multipath propagation, ESA SP-194, pp. 13-23.

UGAI, S. [1959] Statistical consideration of the structure of atmospheric refractive index, Review of the E.C.L., 7, No. 8, pp. 253-289.

VICKERS, W.W. and LOPEZ, M.E. [1975] Low angle radar tracking errors induced by nonstratified atmospheric anomalies, Radio Science, 10, No. 5, pp. 491-505.

WEBSTER, A.R. [1982] Raypath parameters in tropospheric multipath propagation, I.E.E.E. Trans. on Ant. and Prop., AP-30, No. 4, pp. 796-800.

ZHANG, M.C. [1981] A study of statistical law of depth for line-of-sight microwave fading. IEE Conf. Publ. No. 195, Proc. Second Int. Conf. on Antennas and Propagation, York, UK, 297-301.

CHAPTER 4

Influence of refraction on propagation

4.1 Introduction

The influence of atmospheric refractive conditions on the propagation of radio waves is very important, particularly on horizontal or quasi-horizontal paths. Due to large-scale atmospheric conditions with negative vertical refractive gradient occurring, for example, in radio duct conditions, as described in Chapter 3, the propagation direction and the nature of radio waves can change considerably along a path. Therefore, depending on the relative positions of the receiving antennas and the radio duct on a given path the characteristics of the received signals will vary from one antenna to another.

Received signals can suffer either strong mean depression or enhancement over a large frequency band. The dependence of signal level on frequency can be important when selective fading over a small band occurs. Therefore, it appears that the effects of refractive conditions on the radio path must be described. There are different approaches found in the literature that are briefly presented hereafter.

4.1.1 Ray approximation

The atmosphere is a heterogeneous propagation medium in which the magnetic permeability can be considered constant while the dielectric permittivity depends on location and time. For that reason in general there is no complete solution to Maxwell's equations, except when using some approximations. One of these is the geometrical optics approximation, which can be used in the high-frequency domain of radio links and in optics and is valid if both the permittivity of the medium and the field amplitude vary only slightly over distances of the order of a wavelength.

It will be assumed hereafter that there is no loss in the propagation medium, therefore the refractive index n is approximately equal to 1.0003 and decreases with height at a rate of –40 N units per km, in standard conditions. The Poynting vector is perpendicular to the wave front and thus at each point tangential to the trajectories of signal energy which are the rays. Taking $\vec{r}$ as the position vector associated with each point along a ray and s the curvilinear abscissa along this ray, it has been shown that the ray equation can be written as

$$\frac{d}{ds}\left(n.\frac{\vec{dr}}{ds} \right) = \nabla n \tag{4.1}$$

which is the vectorial form of the ray equation. The gradient ∇n has its main component in the vertical direction.

If only the variations of the refractive index with altitude are taken into account, the ray bending at a point can be expressed by:

$$\frac{1}{\rho} = -\frac{\cos\varphi}{n} \times \frac{dn}{dh} \tag{4.2}$$

where:

ρ: radius of curvature of the ray

$\frac{dn}{dh}$: vertical gradient of the refractive index

h: height over the Earth's surface

φ: angle of the ray with the horizontal plane at the point considered

The ray bending is taken positive for a curvature oriented towards the Earth's surface.

Considering that n is close to 1, then for approximately horizontal paths equation (4.2) can be written as:

$$\frac{1}{\rho} \approx -\frac{dn}{dh} \tag{4.3}$$

Therefore, it is clear that if the gradient is constant the ray trajectories are arcs of a circle. This approximation implies, of course, that the path is short enough for the ray to remain nearly horizontal. The ray equation given above is equivalent to the refraction law of Snell-Descartes.

In a spherically stratified medium the refraction law takes the form:

$$n.r.\cos\varphi = \text{constant} \tag{4.4}$$

known as Bouguer's formula, where r is the distance from a point on the ray considered to the centre of the Earth. The constant in equation (4.4) depends on the initial conditions of the ray.

4.1.2 Modified refractive index and effective Earth radius

The refractive index is very close to unity. It can be written as (see Recommendation ITU-R P.453):

$$n = 1 + N.10^{-6} \tag{4.5}$$

where N is the refractivity, expressed in "N-units" (see Chapter 3).

When a ray path in the atmosphere has a radius of curvature equal to the Earth radius a, it follows from equation (4.3) that:

$$\frac{dn}{dh} = -\frac{1}{a} \tag{4.6}$$

and hence

$$n + \frac{h}{a} = \text{constant} \tag{4.7}$$

or:

$$N + 10^6 . \frac{h}{a} = \text{constant} \tag{4.8}$$

The quantity

$$M = N + 10^6 . \frac{h}{a} \tag{4.9}$$

is called the refractive modulus, expressed in M-units. When the refractive modulus M is used, the propagation can be considered to occur over a flat Earth in an atmosphere with refractivity M. The curvature of the rays relative to the (flat) Earth ρ' is given by:

$$\frac{10^6}{\rho'} = -\frac{dM}{dh} \tag{4.10}$$

Conversely, this may be considered to be a representation of a situation where propagation is rectilinear over an earth with an effective radius r_e given by:

$$\frac{10^6}{r_e} = \frac{10^6}{ka} = \frac{dM}{dh} = \frac{dN}{dh} + \frac{10^6}{a} \tag{4.11}$$

where k is the effective Earth radius factor.

4.2 Refractive effects in normal conditions

4.2.1 Sub-refraction and super-refraction

In standard conditions dN/dh = –39 N-units/km, giving for the bending radius of ray paths ρ = 25 641 km. In these conditions the ray curvature is lower than the curvature of the surface of the Earth (Figure 4.1). For values of dN/dh larger than –39 N-units/km the atmosphere is said to be sub-refractive. Super-refractive conditions exist for $dN/dh < -39$ N-units/km. The bending radius is equal to the Earth radius for $dN/dh = -157$ N units/km. For $dN/dh < -157$ N-units/km, ducting conditions exist. The ray paths intersect the Earth's surface and ground reflections occur (Figure 4.1).

It follows that the effective Earth radius factor k_e is given by:

$$k_e = \frac{10^6/a}{dN/dh + 10^6/a} = \frac{157}{157 + dN/dh} \tag{4.12}$$

For standard conditions (dN/dh = –39 N units) it follows that k_e is approximately equal to 4/3.

FIGURE 4.1

Atmospheric refraction effects on radio signal propagation

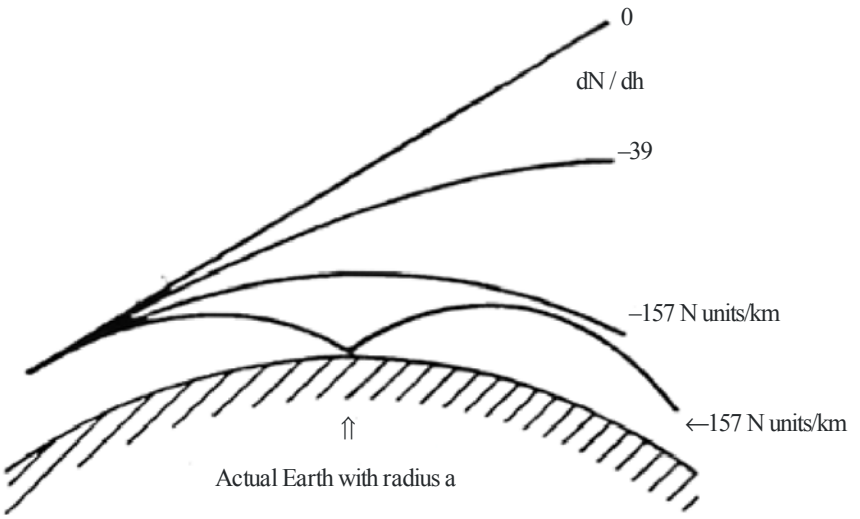

4.2.2 Apparent elevation angle

The decrease in refractive index with height produces an increase in the apparent elevation angle of a distant source. There will be fluctuations about this apparent angle due to local variations in the refractive-index structure. The ray-bending due to refraction is substantially independent of frequency. It is observed that a large part of the curvature of a radio ray takes place in the most dense and variable part of the atmosphere closest to the surface of the Earth. In the case of Earth-space propagation, errors in the apparent elevation angle of a satellite due to refraction rapidly decrease as the satellite moves from the horizon to the zenith.

Published information concerning measurements of angular deviation is not extensive. Some measurement results are given in Table 4.1.

TABLE 4.1

Angular deviation values

Elevation angle θ (degrees)	**Average total angular deviation, Δθ (degrees)**			
	Polar continental air	**Temperate continental air**	**Temperate maritime air**	**Tropical maritime air**
1	0.45	–	–	0.65
2	0.32	0.36	0.38	0.47
4	0.21	0.25	0.26	0.27
10	0.10	0.11	0.12	0.14
20		0.05	0.06	
30		0.03	0.04	
	Day-to-day variation in Δθ (for columns 1 and 4 only)			
1	0.1 r.m.s			
10	0.007 r.m.s			

The smaller the antenna beamwidth, the greater is the required accuracy for antenna pointing. The atmospheric models are at times insufficient to determine the antenna pointing angle and, under these conditions, the measured values of the refractive index as a function of altitude must be used.

4.2.3 Radioelectric path length

Since the tropospheric refractive index is higher than unity and varies as a function of altitude, a wave propagating along a line-of-sight has a radio path length exceeding the geometrical path length. The difference in length can be obtained with an error of less than 2 cm for an elevation angle φ_0 greater than 3 degrees, by the following integral:

$$\Delta L = \int_0^\infty (n-1)ds \tag{4.13}$$

If the deviation between the actual wave path and the straight line connecting the two ends of the path is neglected and if an exponential atmosphere is assumed (exponential decrease of n-1 with height), equation (4.13) can be integrated to give [Boithias, 1984]:

$$\Delta L = \frac{(n_s - 1)^2}{\left[\frac{dn}{dh}\right]_s \sin\varphi_0} \tag{4.14}$$

where n_s and $(dn/dh)_s$ are the index of refraction and its vertical gradient near the Earth's surface respectively. However, due to some inaccuracies of the exponential atmospheric model, equation (4.14) can introduce an error of a few tens of centimetres on a vertical Earth-satellite path. It is useful when the vertical gradient of refractive index is known, either from in situ measurements, or from maps of the ground refractivity gradient.

However, in some applications, the excess path length must be known with an average accuracy better than 10 cm on a vertical path. Moreover, the instantaneous ground values of refractivity gradient are seldom available, whereas the measurement of surface meteorological variables is feasible. A semi-empirical model has been proposed by [Berrada-Baby *et al.*, 1988], to predict the vertical excess path ΔL_v based on surface measurements of atmospheric pressure P, temperature T and relative humidity U, using the atmospheric radio-sounding profiles provided by the one-year worldwide 1979 GARP campaign (500 meteorological stations, 365 days, 2 soundings per 24 hours). According to this model, the general expression of the excess path length ΔL, for any given elevation angle ϕ_0 is:

$$\Delta L = \frac{\Delta L_v}{\sin\varphi_0 \left\{1 \div k\cot^2\varphi_0\right\}^{1/2}} + \delta\left(\varphi_0 \cdot \Delta L_v\right) \tag{4.15}$$

where ΔL_v is the vertical excess path length and k and δ (φ_0, ΔL_v) are corrective terms in the calculation of which the exponential atmosphere assumption is used.

ΔL_v is obtained by computing separately the contributions of the "dry" and "wet" components of the troposphere and is thus given in metres by:

$$\Delta L_v = 0.02228 \frac{P}{g} + f(T)U \quad \text{(m)} \tag{4.16}$$

where P is atmospheric pressure in hPa, U is the relative humidity (%) and g is the acceleration due to gravity at the measurement location in m/s^2. The function $f(T)$ depends on the geographical location of interest and was found, from the above-mentioned data bank to be of the form:

$$f(T) = v10^{\gamma T} \tag{4.17}$$

T (in °C), v (in metres/% of relative humidity) and γ (in °C^{-1}) are given according to the geographical location in Table 4.2.

TABLE 4.2

Values for *f(T)* for geographical location

Location	v (m/%)	γ (°C^{-1})
Coastal areas (islands, or locations less than 10 km away from sea shore)	5.5×10^{-4}	2.91×10^{-2}
Non-coastal equatorial areas	6.5×10^{-4}	2.73×10^{-2}
All other areas	7.3×10^{-4}	2.35×10^{-2}

The vertical excess path length caused by the dry troposphere is given by the first right-hand side term of equation (4.16). It should be noted that this component of the model implies only theoretical considerations (hydrostatic equilibrium and ideal gas law). Its magnitude is approximately 2.3 m. The standard deviation σ_d between this dry component and that obtained from the one-year worldwide data bank of radio-sounding atmospheric profiles mentioned above, is smaller than 5 mm.

The vertical excess path length caused by water vapour, given by the second term of equation 4.16, may be as large as 50 cm. However, an analysis of the effects of water vapour [Berrada-Baby *et al.*, 1988], shows that its variations introduce errors in the determination of the excess path, which are greater than those due to the dry troposphere. With the above formulae, this error ranges from 2 to 6 cm according to the geographical location of interest. The standard deviation σ_w between the estimation and that derived from the above-mentioned data bank increases exponentially with ground temperature as:

$$\sigma_w = 1.89 \cdot 10^{0.0164\ T} \tag{4.18}$$

For the calculation of the excess path length at any elevation angle φ_0, equation (4.15) must be used. The corrective term k takes into account the variations of elevation angle φ along the path due to refraction.

Assuming that the atmospheric refractivity varies exponentially with height h, as mentioned in Chapter 3:

$$N(h) = N_s \cdot \exp(-h / H) \tag{4.19}$$

where N_S is the average value of refractivity at the Earth's surface and H is the scale height. Using an exponential model for the refractivity profile, one has:

$$H = 10^6 \cdot \Delta L_v / N_s \tag{4.20}$$

To compute the corrective term k, H is derived from equation (4.20) in which ΔL_v is as defined in equation (4.16). Then, k is computed from the following expression:

$$k = 1 - \left[\frac{n_s \, r_s}{n(H) \, r(H)} \right]^2 \tag{4.21}$$

where n_S and $n(H)$ are the values of refractive index at the Earth's surface and at height H, respectively, and r_S and $r(H)$ are the corresponding distances to the centre of the Earth. The surface value of refractivity N_S is given in Chapter 3. The value of k has been found to be approximately 10^{-2}.

For small elevation angles, the corrective term $\delta(\varphi_0, \Delta L_v)$ in equation (4.15) can be used to improve the value of ΔL. However, its order of magnitude is only a few centimetres at 10 degrees, which is generally negligible in relation to other uncertainties.

Several methods are available for estimating the average delay in propagation over a slant path within or beyond the troposphere. A method is also available for estimating the variance of the delay on an Earth-space path, based on the monthly variance of the surface refractivity and semi-empirical estimates of the frequency spectrum of the delay fluctuations [Nuspl *et al*., 1975].

4.2.4 Beam spreading on slant paths

Signal loss may also result from additional spreading of the antenna beam caused by the variation of atmospheric refraction with the elevation angle. This effect is negligible for all elevation angles above about 3 degrees. Figure 4.2 below [Crane, 1971] shows the losses through the complete atmosphere due to atmospheric refraction effects. At 1 degrees elevation, the losses are about 0.8 dB ± 0.3 dB. At the horizon, the loss becomes greater than 2 dB with uncertainties of the same order as the average loss. These results were obtained by ray tracing through numerous day and night refractive index profiles from Albany, New York over a several year period. They may be considered typical of effects observed over inland (continental) locations. For sites located near coastal areas, islands, at sea, or in tropical regions, the losses may increase somewhat due to increased surface refractivity and different near-surface refractive index gradients [Yokoi *et al*., 1970]. Losses are independent of frequency over the range of 1 to 100 GHz where water vapour is contributing to the refractive profile. The effects due to dry air alone and at higher frequencies have not been estimated but should be smaller.

4.2.5 Range rate error

When a radio wave intersects the atmosphere or propagates within it along an Earth-space path, the atmosphere gives rise to ray-bending, excess phase and group delay, thus causing not only errors in the range and elevation angle measured, but also errors of Doppler velocity (or radial velocity) as observed from ground stations, i.e. deviation of the apparent range rate (dLe/dt) from the actual range rate (dL/dt):

$$\Delta \frac{dL}{dt} = \frac{dLe}{dt} - \frac{dL}{dt} \tag{4.22}$$

FIGURE 4.2

Loss due to the additional spreading of a beam and standard deviation about the average

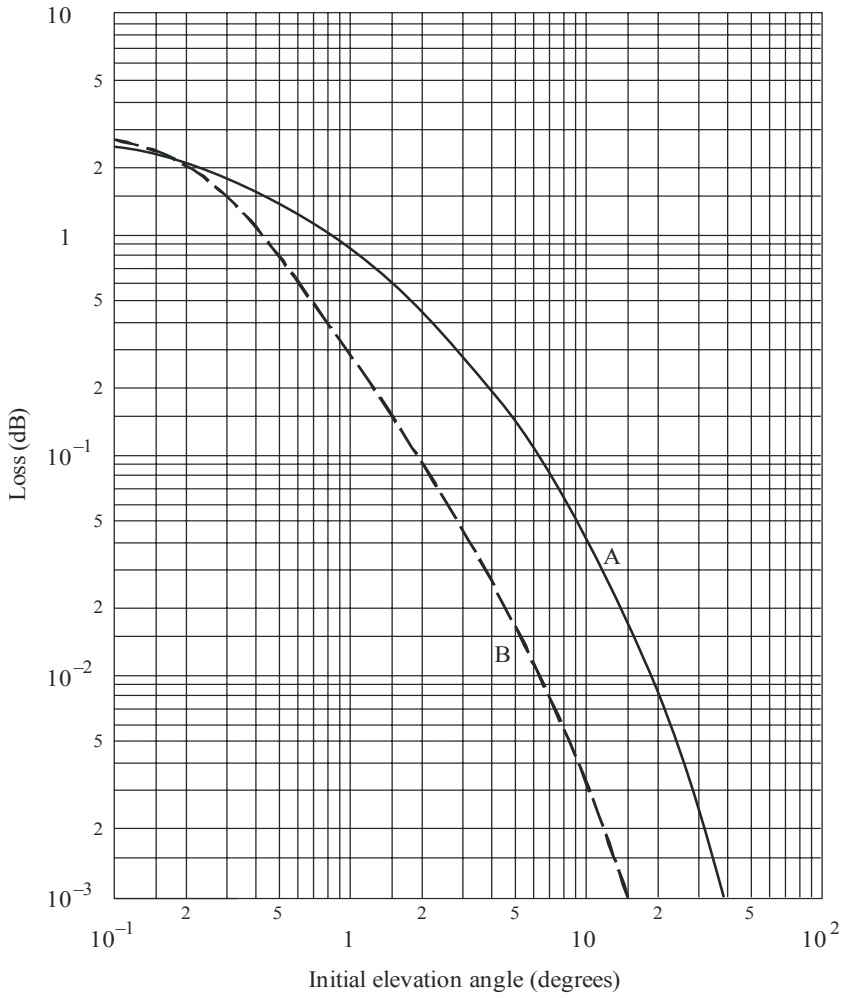

Curves A: average loss
B: standard deviation

Radio-Meteo. 04-02

If we assume a spherically layered atmosphere, the expression of the apparent range rate can be derived from Snell's law.

$$\frac{dLe}{dt} = n_t \left[\frac{\cos\varphi_t}{\cos\alpha_t} \vec{L}_0 - \frac{\sin(\alpha_t - \varphi_t)}{\cos\alpha_t} \vec{a}_{t_0} \right] \cdot \vec{V} \tag{4.23}$$

where:

φ_t: local elevation of the ray at the target

α_t: local elevation (at the target) of the line L between transmitter and the receiver

n_t: refractive index of the atmosphere at the target

a_t: radial range of the target from the Earth centre

$\vec{L}_0$ and $\vec{a}_{t_0}$: unit vectors in the directions of L and a_t

$\vec{V}$: velocity vector of the target.

Moreover,

$$\frac{dL}{dt} = \vec{L}_0 \cdot \vec{V} \tag{4.24}$$

$\Delta \frac{dL}{dt}$ decreases rapidly as the target moves from the horizon to the zenith.

4.3 Propagation during sub-refractive conditions

4.3.1 Effective Earth radius factor for the path, k_e

Small values of the *k*-factor can cause obstruction fading on some paths. In order to predict such fading, the statistics of the low values of the *k*-factor have to be known. However, since the instantaneous behaviour of the *k*-factor differs at various points along a given path, an effective *k*-factor for the path k_e (see equation (4.12)), can be considered. In general, k_e is determined from propagation measurements and represents a spatial average, which could only otherwise be obtained from many simultaneous meteorological soundings along the propagation path. The distribution of k_e values so determined displays less variability than that derived from single-point meteorological measurements. The variability decreases with increasing distance.

Measurements conducted in Russia, near Moscow, in the frequency band 600 MHz to 2 GHz, over five line-of-sight paths of length 40-60 km, show a value of k_e exceeding 0.86 for 99.9% of the time. However, the value of k_e obtained from meteorological measurements in a 100 m layer was found to exceed 0.7 for the same time percentage [Troitsky, 1957]. This paper also gives the theoretical background to the use of the effective *k*-factor, k_e, taking into consideration the non-linearity of the height dependence of *N* and its variation along the path.

Measurements of angle-of-arrival over a 70 km line-of-sight path in the Federal Republic of Germany carried out at 515 MHz, indicate that, averaged over such a path, k_e does not exhibit such a wide range of values as would be expected from meteorological observations made at a single point in the path. Measurements of refraction over a 55 km line-of-sight path in the United Kingdom show that k_e exceeds 0.9 for 99.9% of the time. Measurements conducted at 6.7 GHz in Japan on a 112.7 km overseas propagation path with the sea-surface-reflected-wave, show that the effective *k* value exceeds 0.99 for 99.9% of the time. Measurements made in Italy on a very long (240 km) link over the sea, at 900 MHz and 2 164 MHz, show that no value of k_e less than 1 was measured during a 10-month period of measurement.

For application to radio-relay links, Recommendation ITU-R P.530 contains an experimental curve showing the minimum value of k_e as a function of path length for a temperate climate.

4.3.2 Prediction of the minimum value of k_e

A procedure for the calculation of the minimum value of k_e has been proposed [Mojoli, 1980]. The steps of this procedure are the following:

– obtain the distribution of the point refractive index vertical gradient G_0 for the location of interest and evaluate its mean and standard deviation μ_0, σ_0.

The value of σ_0 is estimated from the distribution of G_0 above the median value. Although the distribution of G_0 is not in general a normal distribution, σ_0 will be estimated assuming a normal distribution.

Bearing in mind that the positive refractivity gradients giving rise to obstruction fading occur in the low atmosphere, the distribution for the ground-based 100 m layer should be used;

– the point distribution of G_0 is assumed to be the same along the whole path. To take into account the fact that the instantaneous behaviour of G_0 at two points can be different an "effective gradient" G_e is considered.

– the effective gradient G_e can be shown to be the average of G_0 gradients along the hop. It can also be shown that:

  – the distribution of G_e tends to a normal distribution as the length d (km) of the path increases;

  – the mean μ_e and standard deviation σ_e of G_e can be given by the following empirical expressions:

$$\mu_e \approx \mu_0$$
$$\sigma_e \approx \frac{\sigma_0}{\sqrt{1 + d / d_0}} \tag{4.25}$$

Simultaneous measurements of the radio refractive index gradient at two points along a path in a northern European climate confirmed the results of the statistical model and the value of $d_0 \approx 13.5$ km;

– once μ_e and σ_e are found then the values of G_e, and therefore of k_e with equation (4.12), exceeded for any percentage of time can be found. For example, we obtain:

$$G_e \approx \mu_e + 3.1\,\sigma_e \tag{4.26}$$

for probability 99.9%, and:

$$G_e \approx \mu_e + 3.7\,\sigma_e \tag{4.27}$$

for probability 99.99%;

– the above procedure is suggested for path lengths d greater than about 20 km. Short hops with length less than 20 km are conservatively designed by directly using the point vertical gradient statistics G_0. That is $\mu_e \approx \mu_0$ and $\sigma_e \approx \sigma_0$.

This procedure has been applied to three locations. For one location, i.e. Trappes in France, the computed curve representing the minimum value of k_e versus the path length for 99.99% of the time is in good agreement with the curve, based on purely radio measurements, represented in Figure 2 in Recommendation ITU-R P.530.

Another application of this procedure undertaken for eight other locations gives the following conclusions. In general, if the worst month data were used and a conservative estimate of the standard deviation of refractivity gradient were employed (e.g. using the 99.9% value) the method mentioned above would give a good indication of the k_e for a particular area. The method should not be generally used for percentages greater than 99.9% of the month. Also, the method is not applicable to areas where the median refractivity gradient is lower than approximately -100 N/km.

The value of d_0, in equation (4.25), has been estimated from brief measurements carried out in Finland. Very different values of d_0 could probably be obtained with data from countries at low latitudes.

Other techniques for estimating the statistics of k_e or other parameters relevant during sub-refractive conditions have also been employed for other geographic regions [Schiavone, 1981; Kalinin, 1979].

4.4 Propagation with super-refractive layers

Usually the refractive structures with super-refractive layers are not simple to describe because the vertical profile of refractivity N does not have a regular shape. Figure 3.12 gives an example. Nevertheless it is often better to consider schematic vertical profiles of refractivity N or of refractive modulus M, as shown on Figures 3.14 and 3.15.

4.4.1 Qualitative description by ray tracing

Several researchers have employed the ray tracing techniques to simulate the influence of a ducting layer on radio propagation along a line-of-sight path. These simulations may show graphically the caustics, ground reflected rays and areas with radio holes. An example is given by Figure 4.3 [Boithias, 1984].

FIGURE 4.3

Example of ray tracings

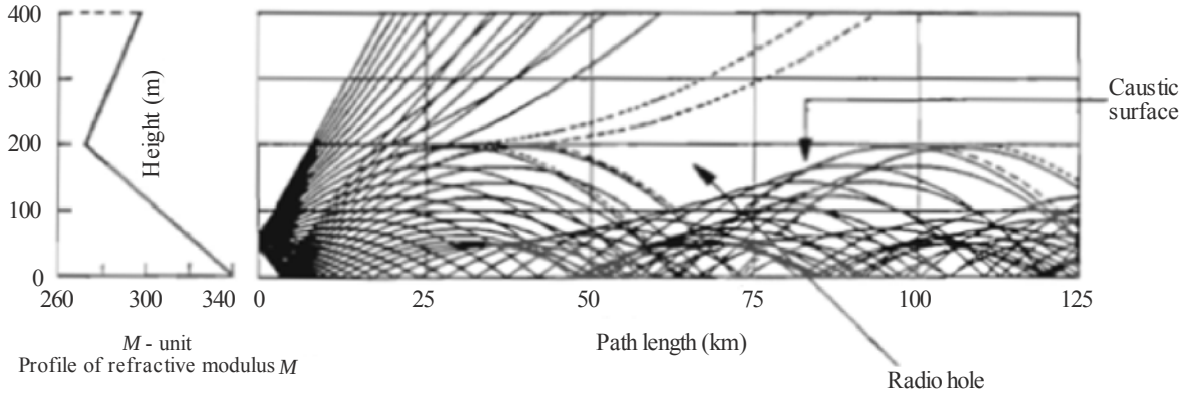

Radio-Meteo. 04-03

Applications of the ray tracing technique give evidence that signal level enhancement, selective fading due to multipath and flat fading within a large bandwidth, observed in experiments, are inseparable aspects of the same phenomenon which depends on the relative height of the transmitter and receiver antennas and on the ducting layer height relative to the transmitter antenna [Parl,

1983]. At the receiver antenna, the number of rays and their amplitude /A/ relative delay time δτ and angle-of-arrival AOA vary with the ducting layer height "h_0" with respect to the terminal heights (see Figure 4.4) [Webster, 1983].

FIGURE 4.4

Variation of received amplitude /A/, delay time δτ between rays and angle-of-arrival AOA with ducting layer height h_0

(The numbers 1, 2, 3 refer to the three different rays due to the ducting layer.)

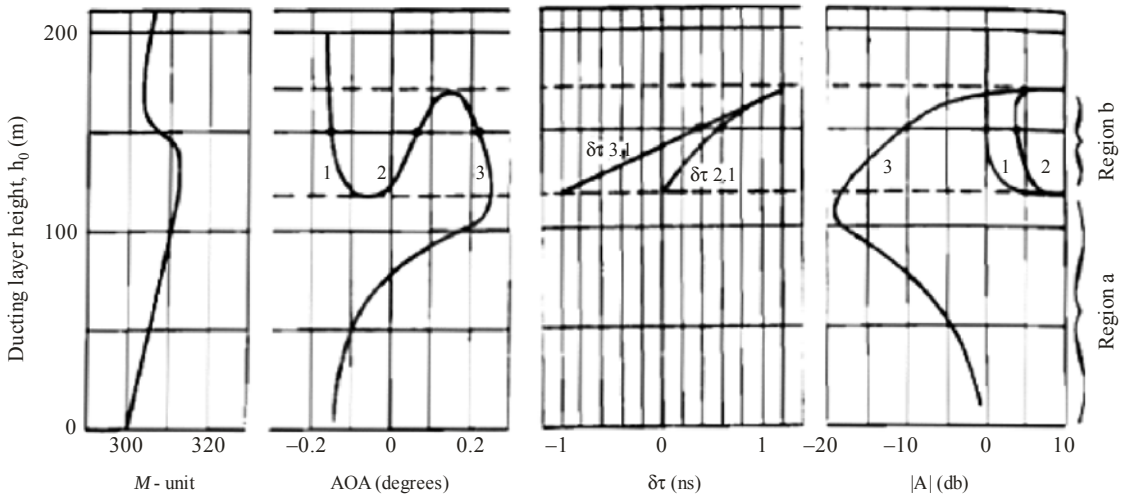

Radio-Meteo. 04-04

TABLE 4.3

The standard values used in Figure 4.4

Original ground refractivity, N_0 (N units)	300
Basic refractivity gradient, (N units/km)	-40
Variation in refractivity, ΔN (N units)	-20
Ducting layer thickness, H (m)	100
Transmitter height, h_{0T} (m)	100
Receiver height, h_{0R} (m)	100
Path length, L (km)	50

Within a particular range of h_0 in Figure 4.4, region a shows defocusing effects and angle-of-arrival deviations occurring simultaneously and in region b three rays are present. In the case of atmospheric multipath, when h_0 and the heights of the two terminals are equal, up to 11 rays have been observed [Parl, 1983]. Some rays have a small amplitude, but not a negligible influence if the sum of the other rays produces a small amplitude. The relative delay spread of the rays is proportional to "d^3" for small distances and to "d" for larger distances.

The angular variations of the path when there is a single path (see Figure 4.4) have the same order of magnitude as the angle-of-arrival deviations during multipath. Therefore, the multipath problem cannot be reduced by simply increasing the antenna gain, owing to antenna decoupling effects.

There have been few theoretical studies of the propagation mechanisms causing severe fading on low-angle slant paths. One study using a ray-tracing simulation suggests that defocusing may be the principal cause [Strickland, 1980]. Simulations of the influence of a large antenna height difference between terminals indicate that atmospheric multipath becomes impossible but antenna decoupling effects can be important. Moreover, during low received signal conditions even a weak ground-reflected ray can have an important influence.

4.4.2 Ducting effects

Ducting layers have significant effects, both on line-of-sight paths and on paths which would not be line-of-sight under normal conditions of refraction.

In the presence of a ducting layer, the concept of horizon no longer has any meaning, and very distant points may be "in line-of-sight". The existence of ducting layers is therefore one of the main causes of interference between two services. A general study of interference mechanisms is found in Recommendation ITU-R P.452.

The effect of ducting layers to produce caustics and areas of low signal level is seen in Figure 4.3.

The combination of two or more rays, which have been subjected to different propagation delays, causes selective frequency fading that may result in amplitude and phase variations inside the bandwidth of the transmission channel. For this effect to be characterized with a view to its use by system designers, the complex transfer function of the atmospheric channel on its impulse response during multipath propagation conditions must be known.

In many experimental results, there is evidence of relatively fast changes in the propagation conditions during multipath activity, i.e. changes within fractions of a second.

Whether a ducting layer causes a radio wave that is incident upon the layer from below to be scattered, reflected, or refracted, depends largely upon the refractive index gradient, the small-scale fluctuations in refractive index, the angle of incidence, and the ratio of the radio wavelength to layer thickness. Ducting occurs for grazing angles of incidence θ less than a critical value θ_c:

$$\theta < \theta_c = \arcsin\left(\sqrt{2\left|\Delta M\right|\times 10^{-6}}\right) \tag{4.28}$$

where ΔM is the lapse of refractive modulus across a ducting layer of thickness δ [Dougherty and Dutton, 1980]. For efficient duct propagation, the wavelength λ must be less than a critical value, λ_c:

$$\lambda < \lambda_c = 1.9\times 10^{-4}\ D^{1.8} \tag{4.29}$$

where D is the tropospheric radio duct thickness in metres.

Reflection will occur when the grazing angle of incidence is below the critical angle. The reflection coefficient for an incident field may be approximated by:

$$|C_R| \approx \frac{1}{4\pi}(\theta_c / \theta)^2 \left(\frac{\sigma}{\delta}\right) \tag{4.30}$$

where $\sigma/\delta = \lambda/2\delta \sin\theta$ is of the order of 1 or less [Hall, 1980]. Efficient specular reflection occurs when the vertical scale $\sigma = \lambda/2 \sin\theta$ is larger than δ.

A thin turbulent layer will also produce specular reflection when the vertical scale is larger than the vertical outer scale of the turbulence:

$$\sigma > L_{ov} \approx \delta \tag{4.31}$$

Where $\sigma < L_{ov}$, the thin layer will produce turbulent volume scattering.

For layer reflection or elevated duct propagation, the requirement is the presence of tropospheric layers of sufficiently strong gradients. These layers are observed to occur bounded by thin turbulent laminae. Depending upon the frequency and incidence angle, the layer will produce ducting, reflection from the entire layer, reflection from the turbulent laminae or volume scattering by turbulence within the laminae.

4.4.2.1 Theoretical approaches to propagation in duct conditions

To solve some theoretical problems encountered in propagation studies during duct conditions, different methods can be used depending on the carrier frequency and the characteristics of the duct. For frequencies lower than about 300 MHz the mode theory method gives satisfactory results while the geometrical optics method is more suitable for frequencies in the UHF band and higher. However, for practical applications of the mode theory simple geometries are needed.

4.4.2.1.1 Cut-off frequency of a duct

As in a metallic waveguide, an electromagnetic wave can travel into a tropospheric duct with different wave modes. The number of modes depends on the ratio of the duct thickness and the wavelength of the travelling signal. The analogy between a metallic waveguide and a tropospheric duct is limited however to the case of a very smooth and perfectly conducting Earth's surface. Assuming also that the duct height is constant along the radio path under study, that the refractive modulus M decreases linearly with height in the ducting layer and that the M gradient is constant along the path, then [Boithias, 1984]:

$$\frac{H}{\lambda} = \frac{A_n}{\sqrt{\Delta M}} \tag{4.32}$$

where:

H: minimum duct thickness for the wave mode n

A_n: a constant depending on the mode order

ΔM (duct intensity): total decrease of M in the ducting layer and

λ: wavelength.

For a ground-based ducting layer with fixed height and given value ΔM, the maximum wavelength of a ducted signal can be computed using $A_1 = 400$, $A_2 = 930$, $A_3 = 1\,460$ for the first three modes. The values of A_1 and A_2 are lower for an elevated duct.

However, the calculated cut-off frequency for a given tropospheric duct does not correspond to a rigorous limit. It is better to consider that when the frequency decreases below this limit more and more electromagnetic energy escapes from the tropospheric duct.

For tropospheric surface ducts with a thickness of about one hundred metres, the number of modes is some tens in decimetric-waves but some hundreds in centimetric-waves. In these cases it is better to use geometrical optics.

4.4.2.1.2 Influence of path inclination

The signal transmitted by a radio source located in a duct cannot be trapped in the duct if its elevation angle is too large. For a horizontal ground-based duct over a flat Earth's surface ($k = \infty$), with only a vertical refractivity gradient, the limit of the elevation angle φ_0 can be found [Boithias, 1984]. If:

$$|\varphi_0| \geq \sqrt{-2b_1 (H - h_0)} \tag{4.33}$$

the signal will escape from the duct and atmospheric multipath and associated phenomena will not occur. In this equation b_1 is the refractive modulus gradient, H is the duct thickness and h_0 is the altitude of the transmitter antenna.

In this schematic example φ_0 is also the angle of the ray with the upper surface limit of the ducting layer. Over sloping terrain with a fairly flat surface it can be assumed that the ducting layer will follow the slope of the terrain. In this case the radio propagation will depend on the difference between the path inclination and the mean terrain slope rather than on the path inclination alone.

According to [Parl, 1983], atmospheric refractive phenomena are still more complicated because the limit angle φ_0 also varies linearly with the path length d. To summarize, one can say that the path inclination plays an important role in multipath occurrence, but it is necessary to take into account the mean terrain slope, the antenna position h_0 in the duct and obviously the local meteorological conditions.

4.4.2.2 Losses in duct propagation

In free-space propagation the energy passing through unit area decreases as the square of distance. In the case of duct propagation the spread of energy in the vertical direction is eliminated and energy decreases as the inverse of distance. That is, over a distance d' within the duct, the basic transmission loss L_b is related to that for free space L_{bf} by:

$$L_b = L_{bf} - 10 \log d' + A \tag{4.34}$$

Such low transmission losses have been observed over water. Of course, this significant improvement over free-space propagation is normally off-set by the term A for various attenuation mechanisms including, for example, leakage losses due to duct irregularities or losses due to ground reflection, etc. However, it has been observed that at frequencies between about 0.8 and 3 GHz, the received field after propagation above water is well in excess of the free space value at 370 km and approximately equal to the free-space value at 1 000 km. These events are unusual but not rare; they may persist for several hours and at some locations even for several days.

These situations are especially common on or near large bodies of water.

Observations on a 920 km path over the Black Sea, at frequencies of 150, 821, 4 800 and 6 000 MHz, have demonstrated a frequency dependence of field strength with a maximum value of L_{bf} at 821 MHz [Troitsky, 1989].

There are also additional losses attributable to duct characteristics and other atmospheric conditions:

– the frequency dependent absorption by the gaseous atmosphere (Recommendation ITU-R P.676);

– the leakage of energy from non-uniform ducts (i.e. ducts whose characteristics vary horizontally). For instance, propagation measurements carried out in the area from Shatt-al-Arab to the Gulf of Oman have shown that non-uniform ducts regularly exist.

In addition, there are losses associated with the coupling of radio wave energy into and out of ducts. These are sensitive to the vertical limits of the ducts relative to the positions of radio system terminal antennas. Elevated layers have a horizontally cyclical (wave like) variation in their characteristics that affect the coupling losses into and out of the elevated duct [Crane, 1981; Dougherty and Hart, 1979].

4.4.2.3 Surface reflection in duct conditions

The power reflected specularly from the Earth's surface varies with duct conditions. It has been found theoretically that on radio paths located over flat terrain the reflectivity and the reflection point vary slightly when the clear air situation changes from standard to strong refractive conditions. Small flat sections (a few kilometres or less) of irregular terrain profiles can also reflect radio power specularly. It appears that the power reflected specularly from irregular terrain varies strongly with refractivity, the stronger the duct conditions, the higher the reflection power. Depending on the refractive conditions, the antenna apertures and the path and terrain inclination, the level of the power reflected from the surface can exceed the free space level.

4.4.3 Multipath propagation

The propagation mechanisms that cause severe fading and phase effects on horizontal and low-angle slant paths are related to the occurrence of multipath and related propagation phenomena, which may cause the formation of a caustic surface, of a radio hole on one side of that surface and of interference between several rays on the other side (Figure 4.3). The mechanisms exist principally during periods of large negative values of refractive index gradient, and tropospheric stratification.

Multipath propagation is usually described in terms of two or more discrete rays, with different amplitudes and propagation delays, combining at the receiver. By using a high resolution antenna system, four ray paths have been observed during severe fading conditions [Crawford and Jakes, 1952]. The analysis of the data collected in a large bandwidth experiment suggests that some severe selective fades could be due to seven components [Kaylor, 1953]. Propagation delay differences between these components have been estimated to be as large as 12 ns.

Measurements carried out in various countries have shown that the number of multipaths can at times be very high. However, it was found in Japan, from measurements of the amplitude distortion in 500, 750 and 4 000 MHz bandwidths on 20 km to 80 km paths, that the number of multiple rays during the fading period was two or three in most cases [Sasaki and Akiyama, 1979]. In Japan, measurements have shown that most of the deep fades are caused by destructive interference between two dominant rays and that the path-length difference between these rays varies to a considerable extent with propagation path conditions. The relative amplitude ratio of multiple rays showed a rapid variation over a wide range resulting in an almost uniformly distributed probability

density. Delays can sometimes correspond to extremely high path length differences, even on short paths.

The results also suggest that the relative amplitude of a ray associated with a particular propagation path decreases with the increase in delay. It was found, for example, for fades in excess of 12 dB measured at 11 GHz on a 50 km link, that in 90% of the cases where a delay of at least 6 ns was observed, the amplitudes of the secondary rays were at least 27 dB below the free-space level. However, no distinct relationship between amplitudes and delays has been established. Large amplitudes normally correspond to delays of less than about 1 ns. Additional results and corresponding references can be found in [Stephansen, 1981].

Depression of the amplitudes of the rays and large flat fading of the received signal in large bandwidth [Kaylor, 1953] have been observed with respect to the free-space level. These level depressions can be due to the existence of a radio hole which occurs as a consequence of the ray-bending effect of a ducting layer. Moreover large angular deviations of the received signal measured on some hops could cause antenna decoupling.

4.4.3.1 Meteorological and orographic conditions associated with multipath propagation

On a 155 km path over the English Channel, between the French and the English coast, signal levels at 11.6 GHz exceeding the free-space value have been measured. In one case the high level signal persisted for more than 36 hours. During this period it appeared that the unusually warm air from France moving north-west over the cold sea generated an advection duct. The duration of the high level signal was consistent with the observed duration of these weather conditions [Vilar *et al*., 1988]. On the same troposcatter path, in normal conditions, it has been observed that strong signal enhancements have occurred during anticyclonic situations: once with the centre of high pressure over the Atlantic, another time with the centre of high pressure over the continent [Spillard *et al*., 1989].

Experimental results at a single frequency obtained on different paths show that the propagation events during nights with strong negative refractivity conditions frequently follow the same process. First, the signal level increases above the free space value and can remain several hours in that situation with only slow variations. After that, during another period of the night, strong and fast level variations occur above and below the free space value. When this second period ends, often the level increases again above that of free space. However, simultaneous recordings at several frequencies show, for example, that the level at 3.8 GHz is less disturbed than at 6.1 GHz. Simultaneous meteorological measurements and radio observations during this type of propagation event have shown, in one case, that a ground based multilayered structure existed with a mean temperature of 0 °C and a high atmospheric pressure (1 035 hPa) at ground level [Mon *et al*., 1980].

In another case, it had been observed that the strong level enhancement (10 dB), which was developed during the early morning, coincided with the decrease of the ground temperature and the occurrence of thick fog at the receiver location. Minimum temperature (0 °C) was attained at 0700 UT when strong and fast signal level variations occurred.

4.4.4 Angle-of-arrival variations

The angle-of-arrival has been measured using a steerable beam antenna [Crawford and Jakes, 1952] and by space domain interferometry [Webster and Scott, 1987]. A good correlation exists between the angle-of-arrival and the gradient of the modified refractive index. In the vertical plane, angular deviations as large as 0.7 degrees above the normal direction and 0.8 degrees below have been observed. Angle-of-arrival deviations were usually absent and never larger than 0.1 degrees in the horizontal plane. Angle-of-arrival variations of the main ray path as large as 0.9 degrees have been observed.

4.5 Representation of the propagation channel during super-refractive conditions

When multiple rays are derived from ray tracing simulations, they are obviously physical rays (in the frame of the considered model). Things are not so clear when ray parameters are derived from experimental data because ray retrieving methods are generally not robust due to both the bandwidth limitation and to noise affecting the data.

4.5.1 Multi-ray model

The multi-ray model is the physical model most used for closely describing the physical reality and is justified by simulation studies using ray tracing techniques (§ 4.4.2); these studies show that the presence of certain atmospheric structures such as super-refracting layers may produce interference regions in which superimposed waves propagated over several paths are received. Some of these rays may be due to reflections from the ground or from atmospheric stratifications, others to atmospheric refraction. The transfer function of this model may be expressed by:

$$H_A(\omega) = \sum_{i=1}^{N} A_i \mathrm{e}^{-\mathrm{j}(\omega T_i + \varphi_i)} \tag{4.35}$$

where $\omega = 2\pi f$ and A_i, T_i and φ_i are the amplitude, delay and phase of the i^{th} ray, respectively.

Amplitudes are usually normalized in relation to a reference level, e.g. the free-space level, delays and phases in relation to one of the rays taken as the reference. The transfer function may then be written:

$$H(\omega) = a_0 + \sum_{i=1}^{N-1} a_i e^{-\mathrm{j}(\omega T_i + \varphi_i)} \tag{4.36}$$

where a_0 and a_i are the ray amplitudes in relation to the reference level and T_i and φ_i the delays and phase shifts of the other rays in relation to the reference ray with amplitude a_0.

One characteristic of the model is the variability of the number N of rays, which depends on the physical situation. N should therefore be regarded as a model parameter.

Wideband measurements (≥400 MHz) often give a high number of rays. Measurements in a bandwidth of 450 MHz have given a_i and τ_i value sets for a four-ray model [Crawford and Jakes, 1952] and a seven-ray model [Kaylor, 1953] assuming zero phase differences ($\varphi_i = 0$) in both cases. From measurements in a bandwidth of 1.3 GHz, four rays were found to be sufficient but allowing a variation of the parameters during a frequency sweep. However, the model does not necessarily imply a high number N of rays. Ray tracing simulations on a model atmosphere with only one ducting layer often give only three rays of atmospheric origin.

In the approximation of geometrical optics on which the multi-ray model is based, the field in the radio hole region cannot be characterized. It may be analysed with the aid of other methods, e.g. the parabolic equation method.

4.5.2 Theoretical considerations on single-frequency statistics

At a single frequency, the received signal is the vectorial sum of the various rays. Its amplitude and phase distributions can then be derived theoretically if reasonable assumptions are made concerning the individual signals. The method to follow is well described in [Beckmann, 1964].

An important consideration is the presence of a direct dominant signal, considered as a deterministic one. If a dominant component is not present, one obtains a Rayleigh distribution (if the phases of the individual signals are uniformly distributed) or otherwise, a more general distribution.

When a constant signal is present and all the others combine into a Rayleigh vector, one obtains a Rice-Nakagami distribution. More general distributions can be found in [Kalinin, 1992].

All previous calculations make use of the central limit theorem. When it is not applicable (too small number of signal components, or random number of components), the situation is more complex and has not been generally considered.

It has been shown however that when restricting oneself to deep fades, the variation of the probability distribution function varies as the square of the signal amplitude (as does a Rayleigh distribution) under very general assumptions. This domain of fading is sometimes called Rayleigh fading.

4.5.3 Models for the multipath transfer function

In bandwidths of less than about 60 MHz, the multipath transfer function (MTF) can be represented by mathematical models which are far simpler than the multi-ray model but whose parameters a priori have no physical meaning. Such models may be classified as polynomial or hypothetical ray models.

4.5.3.1 Polynomial models

It is possible to represent the MTF by real or complex polynomials, thus using a conventional mathematical approximation of a function. Within the 20 to 60 MHz bandwidth of a transmission channel, distortions of the MTF are often sufficiently small to be described adequately by polynomials of order 2 or lower.

Available methods include:

a) The polynomial expression of amplitude and group delay as a function of frequency, the general form of which is:

$$P(\omega) = C_0 + C_1\omega + C_2\omega^2 + ... + C_N\omega^N \tag{4.37}$$

[Smith and Cormack, 1982; Liniger, 1983]. However, such models have a high number of parameters.

b) The complex polynomial for the transfer function with the general form:

$$H(\omega) = R_0 + \sum_{k=1}^{N} (R_k + jX_k)\omega^k \tag{4.38}$$

[Sylvain and Lavergnat, 1985].

The polynomial model b), using the first order terms, has been found to be in good agreement with experimental data obtained on a 42.5 km hop at 6 GHz in a 26 MHz band and with data on a 37 and 50 km hop at 11 GHz in a 55 MHz band. Statistics on the model parameters have been obtained and are described in the "Handbook on Digital Radio-Relay Systems", ITU, 1996.

4.5.3.2 Hypothetical ray models

The MTF can also be described using different models having a mathematical form similar to equation (4.36) with a fixed and limited number *N* of rays. Such models are traditionally called "ray models". However, due to simplifications in the expression of the transfer function, these "rays" generally bear no direct relation to the real propagation paths. To avoid ambiguity, they may be referred to as "hypothetical rays". In the following ray model descriptions, such hypothetical rays are always assumed.

A theoretical analysis based on the multi-ray model shows that a hypothetical two-ray model generally affords a satisfactory approximation in bandwidths of less than about 100 MHz [Rummler, 1980] and even allows a certain freedom for reducing the number of parameters to three. It must be noticed that the estimation of the model parameters from experimental data is not always straight forward and needs some care, because it is a non-linear estimation. However, Sakagami and Hosoya [1982] found that certain experimental transfer functions were poorly represented by a hypothetical two-ray model and accordingly resorted to a hypothetical three-ray model.

The transfer function of the general two-ray model (also called "simplified three-ray model") is expressed by:

$$H(\omega) = a\left(1 - b\ e^{\pm j(\omega-\omega_M)\tau_f}\right) \tag{4.39}$$

where:

a and b: coefficients related to the amplitude and the shape of the selective fading respectively

τ_f: delay of the second hypothetical ray

ω_M: angular frequency of the maximum fade depth.

The value of b is less than 1, a minus sign in the exponent corresponding to minimum phase shift situations and a plus sign to non-minimum phase shift situations. This ambiguity can be removed only if group delay measurements are available.

[Metzger and Valentin, 1989] have shown that this model can be fitted satisfactorily to the transfer functions measured in a 44 MHz bandwidth at 9.5 GHz on a 55 km path. A theoretical study of the statistics of the model parameters can be found in [Grünberger, 1989].

4.6 Simplified representations of the propagation channel

4.6.1 Ray models

4.6.1.1 Two-ray and fixed-delay model

The number of parameters can be reduced to three by having a fixed delay value τ_f. Such a model, with $\tau_f = 1/6B$ (B being the bandwidth), adequately represents the transfer functions measured; it has been applied to the data of a 42 km link at 6 GHz and a 26.6 MHz bandwidth (with $\tau_f = 6.3$ ns [Rummler, 1979]), and to the data of two links of 37 km and 50 km at 11 GHz and a 55 MHz bandwidth ($\tau_f = 3.03$ ns).

Measurements over a line-of-sight path at 4 GHz (40 MHz bandwidth) have been analysed in the Federal Republic of Germany. In contrast with the previous results where a fit to an MTF with a fixed hypothetical delay was possible, it was found here necessary to use a variable hypothetical delay. This might be explained by the long delays of the rays reflected by the ground.

The model has been extended on the basis of measurements over two links in the United States to represent the transfer function of a space diversity channel [Rummler, 1983].

4.6.1.2 Normalized two-ray model

The number of parameters may also be reduced to three, taking $a = 1$. The three parameters are then b, τ_f and ω_M. This gives the normalized two-ray model. It has been shown that this adequately represents the transfer functions measured in a 55 MHz bandwidth and statistics have been obtained for 37 and 50 km hops at 11 GHz.

4.6.1.3 Centred two-ray model

A number of authors have used a centred two-ray model derived from the normalized two-ray model and taking $\omega_M = \omega_c$, being ω_c the centre frequency. The attenuation notch is then fixed at the centre of the band studied. This model is useful for certain applications, particularly when the centre frequency is the carrier frequency. Such a model, however, cannot represent experimental data for which the attenuation notch is generally not centred, and is therefore not suitable for representing the transfer function in the same way as those described above.

4.6.2 Parametric representation of amplitude distortion

The parametric methods described here are "two point" methods, in which the amplitude differences at two discrete frequencies are used to characterize the amplitude distortion. In the first method, the two frequencies are fixed, being selected at the edges of the frequency band under consideration. In the second method, a large bandwidth is used and the two frequencies correspond to the points of maximum and minimum fade depth relative to the free-space level. The spacing between these frequencies is therefore variable, depending on propagation conditions.

4.6.2.1 Two point method with fixed frequency spacing

A statistical description of dispersion using this model is given in [Sakagami and Hosoya, 1982]. A method, giving the statistical distribution of linear amplitude dispersion due to fading caused by radio wave reflection from tropospheric layer inhomogeneities, is described in [Kalinin, 1985]. This method is based on the distribution, assumed to be normal, of the jumps in permittivity $\Delta\varepsilon_m$ in the tropospheric layers.

The two point method has been found useful in describing improvements obtained by space diversity reception for links of various lengths [Babler, 1973; Sakagami and Hosoya, 1982; Vigants, 1983].

4.6.2.2 Two point method with variable frequency spacing

The two frequencies chosen in this model are those corresponding to A_m and A_n, the maximum and minimum fade depths below the free-space level respectively within the received bandwidth [Kaylor, 1953]. The model parameter is the difference $DA = A_n - A_m$, termed the maximum in-band amplitude distortion. A_m and A_n values can also be used to compute the parameters of the ray model (a) with variable delay [Martin, 1982].

4.7 Signal scintillations due to atmospheric turbulence

Turbulent irregularities of the refractive index can give rise to amplitude scintillations and angle-of-arrival fluctuations of the received signal. These effects are present on all line-of-sight paths at microwave frequencies and above but can be masked by multipath fading and related phenomena on horizontal paths and on slant paths at elevation angles lower than 3°.

4.7.1 Amplitude scintillation

The variance in the logarithm of the amplitude of the received signal due to scintillations is given by [Tatarskii, 1967]:

$$\sigma_x^2 = 42.5\left(\frac{2\pi}{\lambda}\right)^{7/6} \int C_n^2(r) r^{5/6} dr \tag{4.40}$$

where:

σ_x: the standard deviation of the logarithm of the received power

λ: wavelength (m)

C_n^2: the refractive index structure function ($m^{-2/3}$)

r: distance along the path (m).

The constant, 42.5, is an average value; values varying from 42.2 to 42.9 may be derived from [Tatarskii, 1967]. For the derivation, see [Brussaard and Watson, 1994]. Measurements of the amplitude scintillation variability along satellite paths have been made by Crane [1976a]. The observed data from the Haystack measurements show a range of variability at 7.3 GHz through the seasons as indicated in Figure 4.5, showing the r.m.s. fluctuations in log received power σ_x (dB) versus the apparent satellite elevation angle. Measurements at 0.4 GHz as well as 7.3 GHz produced tropospheric scintillation observations which were in qualitative agreement with predictions of weak scintillation theory for elevation angles above 2 or 3 degrees; at lower elevation angles, atmospheric multipath fading was dominant.

Precise knowledge, therefore, of the amplitude scintillation depends on a knowledge of the refractive index structure function along any given oblique path. Since this is usually unknown in detail, approximations would need to be made to model C_n^2 for a specific location. At 7 GHz and elevation angles above 3 degrees, the signal may fluctuate at levels between 0.1 and about 1.0 dB depending upon elevation angle and antenna beamwidth (see Figure 4.5).

FIGURE 4.5

Standard deviation of amplitude scintillation
(antenna diameter: 37 m)

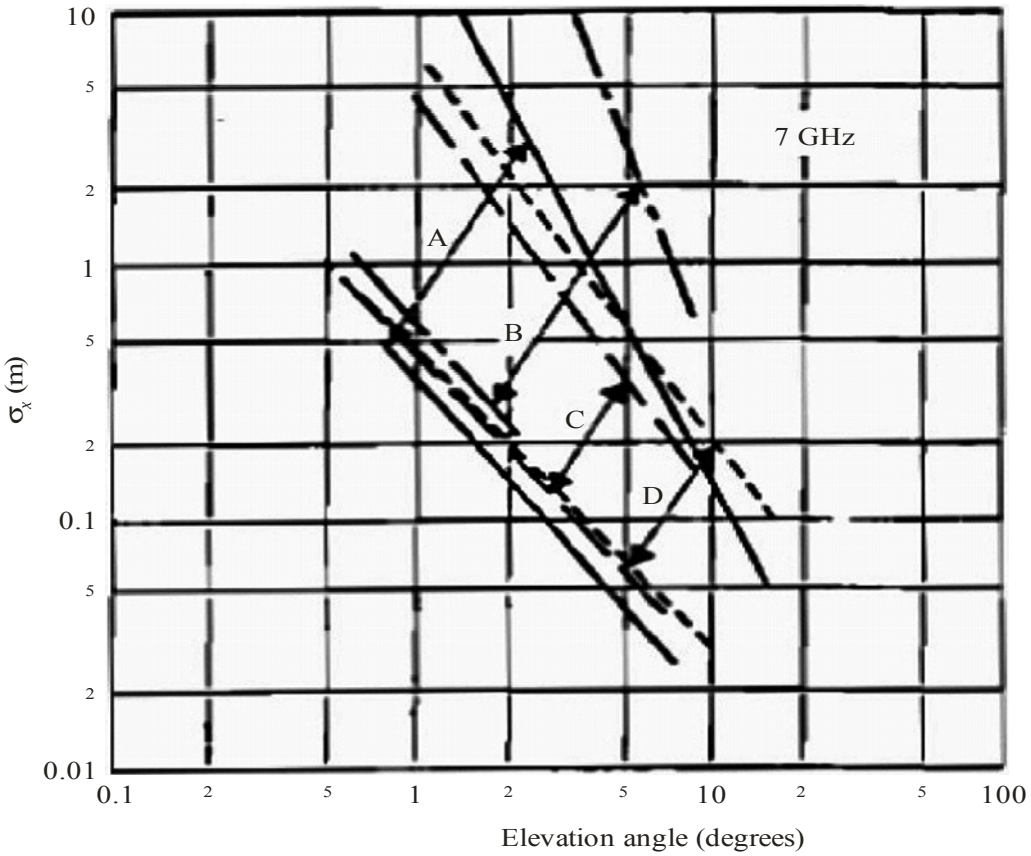

A: Spring
B: Summer
C: Autumn
D: Winter

Radio-Meteo. 04-05

In Europe, measurements have been carried out with the OTS satellite in the 11 GHz band. These are aimed at collecting meaningful statistics of the signal variance and its seasonal dependence [Ortgies, 1985]. Also, statistics of amplitudes exceeding pre-specified thresholds and their respective diurnal and seasonal variations were collected [Vander Vorst *et al.*, 1982]. [Moulsley and Vilar, 1982] studied in detail the relationship between short-term r.m.s. amplitude density distributions and the long-term distributions, both experimentally and theoretically.

There is considerable evidence from experiments that the spectral power density of the scintillation process is band limited. Typical values of the cut-off frequency are of the order of 1 to 3 Hz at 11 GHz [Rücker, 1985]. A correlation of the turbulent layer height h producing scintillations with the average near-ground water vapour content has been found [Rücker and Dintelmann, 1983].

The other effect of significance, antenna aperture degradation, is dependent on the scale sizes of the refractive inhomogeneities relative to the antenna diameter. The effect, sometimes expressed as antenna gain-loss, occurs because the antenna aperture and the propagating medium are coupled.

For a propagation path traversing the troposphere to a distant satellite, the Fresnel zone sizes may be defined as:

$$F = \sqrt{n\lambda z} \tag{4.41}$$

where:

n: order of Fresnel zone

λ: operating wavelength

z: the reduced path length $\frac{r(L-r)}{L}$

L: total length of ray path, and

r: distance along ray path.

Turbulent refractive index fluctuations occur over a wide range of scale sizes. At scales small compared to the Fresnel zone size, the scattering can be described as isotropic; at scales larger than the Fresnel zone the scattering is anisotropic and considerable spatial curvature of the incident wavefront can result. The largest amplitude spatial fluctuations observed in the antenna aperture plane are produced by fluctuations on scale sizes of the order of the Fresnel zone size. For antenna apertures larger than the Fresnel zone size, the fluctuations due to the corrugated wavefront are spatially averaged by the antenna. Further, as the elevation angle increases the Fresnel zone size decreases due to the rapidly decreasing distance r between the turbulent layer and the antenna. The result is therefore a reduction in the fluctuation depth due to aperture averaging and a slight reduction in the effective antennas gain (i.e. gain-loss). Tatarskii [1967] indicated that the r.m.s. fluctuations are reduced by 20% when the antenna diameter of a uniformly weighted circular aperture is one-half the first Fresnel zone size $\left(D_a = \frac{1}{2}\sqrt{\lambda z} \right)$.

The tropospheric scintillation model presented below is based upon measurements covering elevation angles in the range of 4 to 32 degrees, antenna diameters between 3 and 36 m, a frequency range of 7 to 14 GHz, and several different climatic regions [Lo *et al.*, 1984; Rücker and Ortgies, 1985; Karasawa *et al*., 1988; Banjo and Vilar, 1986]. As a result, the standard deviation describing the scintillation amplitude can be predicted as follows:

$$\sigma_{pre} = \frac{\sigma_{ref} \quad f^{n}\, g(x)}{(\sin\theta)^{b}} \tag{4.42}$$

where f is the operating frequency (GHz), n is equal to 7/12, b is equal to 1.2 and θ is the apparent elevation angle in degrees. The meteorological influence is described by:

$$\sigma_{ref} = 3.6\times10^{-3} + N_{wet}\times10^{-4} \tag{4.43}$$

N_{wet}, the wet term of refractivity, is the second term in equation (3.11) and can be obtained from Recommendation ITU-R P.453 (see Figure. 4.6).

The antenna averaging function $g(x)$ is given as follows [Haddon and Vilar, 1986]:

$$g(x) = \sqrt{3.86(x^2+1)^{11/12}\sin\left(\frac{11}{6}\arctan\left(\frac{1}{x}\right)\right) - 7.08x^{5/6}} \tag{4.44}$$

where:

$$x = 0.0584\frac{D_{eff}^2 k}{L} \tag{4.45}$$

$$D_{eff} = D\sqrt{\eta} \tag{4.46}$$

$$k = \frac{2\pi f}{c} \tag{4.47}$$

$$L = \frac{2h}{\sqrt{\sin^2\theta + (2h/R_e)} + \sin\theta} \tag{4.48}$$

c: velocity of light (m/s)

D: antenna diameter (m)

η: antenna efficiency

L: effective turbulent path (m)

R_e: effective Earth radius (R_e = 8.5 x 10^6 m)

h: height of turbulence (m).

The height of turbulence, h, varies both with season [Rücker and Dintelmann, 1983] and climate. However, as little is known on climatic dependence, a value of h = 1 000 m may be assumed.

Signal fading A expressed in dB, in the long term cumulative distribution, does not appear to be normally distributed. The fade level $A(p)$ exceeded for p% of the time is given by:

$$A(p) = a\sigma_{pre} \tag{4.49}$$

where factor a can be approximated by:

$$a = -0.061(\log_{10} p)^3 + 0.072(\log_{10} p)^2 - 1.71\ \log_{10} p + 3.0 \qquad (for\ \ 0.01 \le p \le 50) \tag{4.50}$$

The input parameters surface temperature and relative humidity which are used in the model are supposed to be averaged over a period of the order of one month or longer. Because of the relatively long averaging time of these meteorological parameters, it is not possible to use the model on a shorter time scale.

FIGURE 4.6

Wet term of the surface refractivity (ppm) exceeded for 50 % of the year

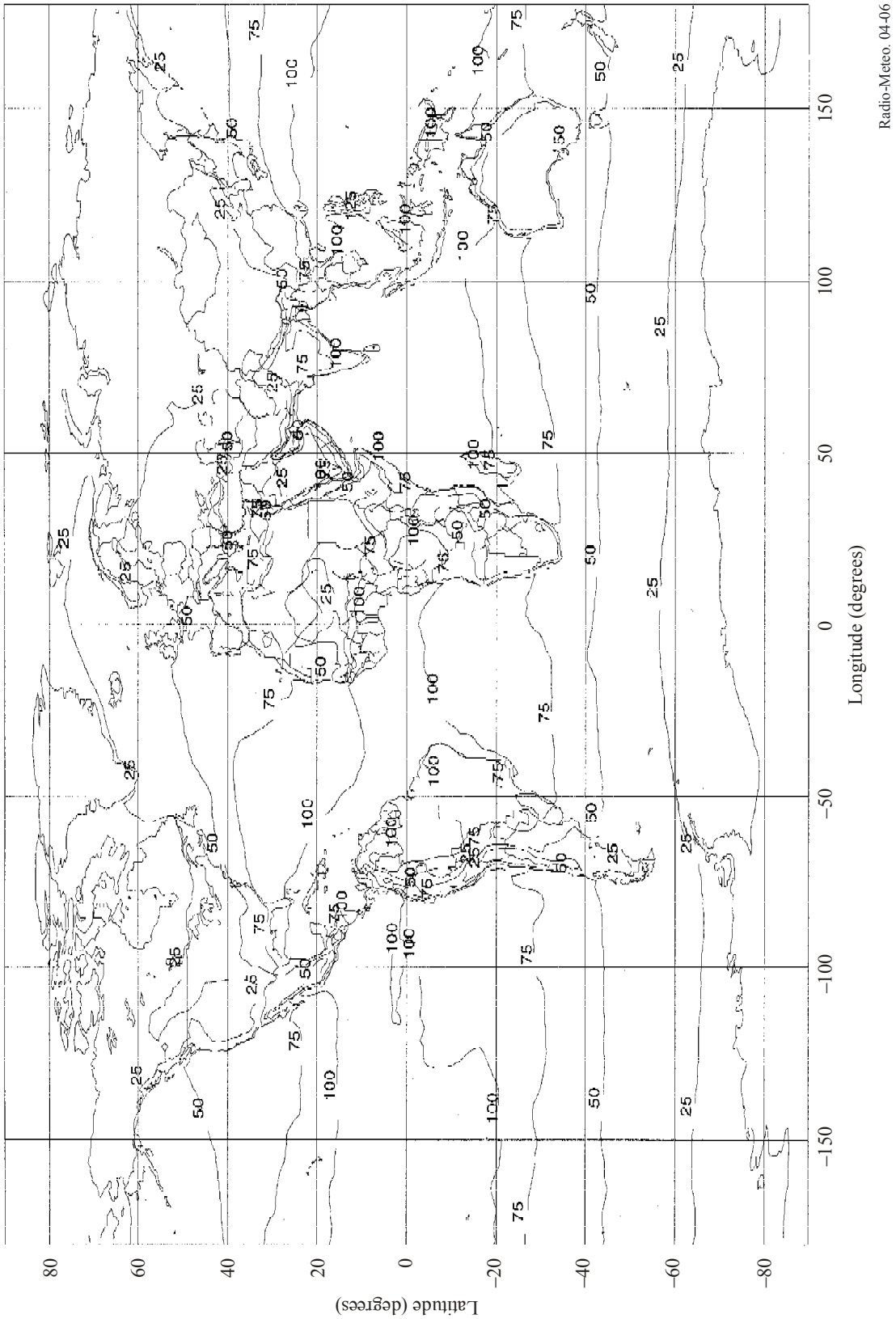

It has been found that the scintillation model described above, which has been developed based on measured data excluding rainy periods, can for practical applications also be used during rainy conditions.

4.7.2 Angle-of-arrival scintillations

Data obtained from satellite observations made using a large aperture tracking antenna at Haystack Observatory, Westford, (Massachusetts) (at 7.3 GHz), suggest that angle scintillations are not likely to be important for antenna beamwidths larger than 0.3 degrees at all elevation angles or for beamwidths larger than 0.01 degrees at elevation angles higher than 10 degrees. The elevation angle fluctuations are of the same order of magnitude as the expected uncertainty in refraction correction using surface refractivity values [Crane, 1976a]. Figure 4.7 indicates the range of extremes in the r.m.s fluctuations in elevation angle versus elevation on the 36.6 m (120 foot) antenna at 7.3 GHz. A seasonal dependence was identified, as shown, throughout a year of observations sampled at different times of day, seasons and meteorological conditions. It is anticipated that these magnitudes of angle-of-arrival effects may be expected over a variety of operating conditions relatively independent of frequency. For reference also, the median r.m.s. fluctuations by season are shown in Figure 4.8 [Crane, 1976b]. These data, ranging in initial elevation angles from the horizon to 43 degrees, represent the median elevation angle measurement uncertainties (within a five-minute observation period) to be expected due to the troposphere. Single antenna radar or communication systems probably will not achieve better measurement accuracies or lower angular position uncertainties, respectively, than these for paths traversing the complete troposphere.

The Haystack observations were made over the period of a year and were representative of values to be expected in a temperate climate. Angle-of-arrival fluctuations due to tropospheric turbulence are not frequency dependent and the values in Figures 4.7 and 4.8 may be used throughout the 1 to 30 GHz range. At lower frequencies, angle-of-arrival scintillation produced by the ionosphere can be important.

FIGURE 4.7

Standard deviation of elevation angle scintillation (antenna diameter = 37 m)

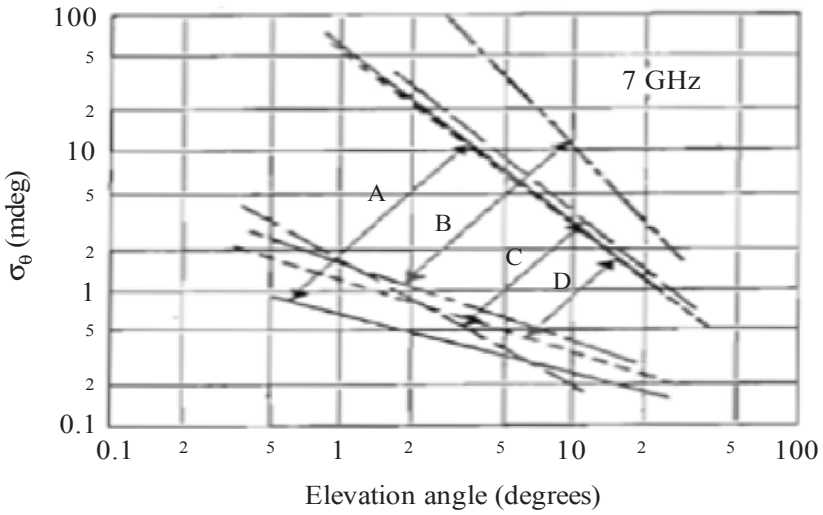

A: Spring
B: Summer
C: Autumn
D: Winter

FIGURE 4.8

Median standard deviation in elevation angle scintillation

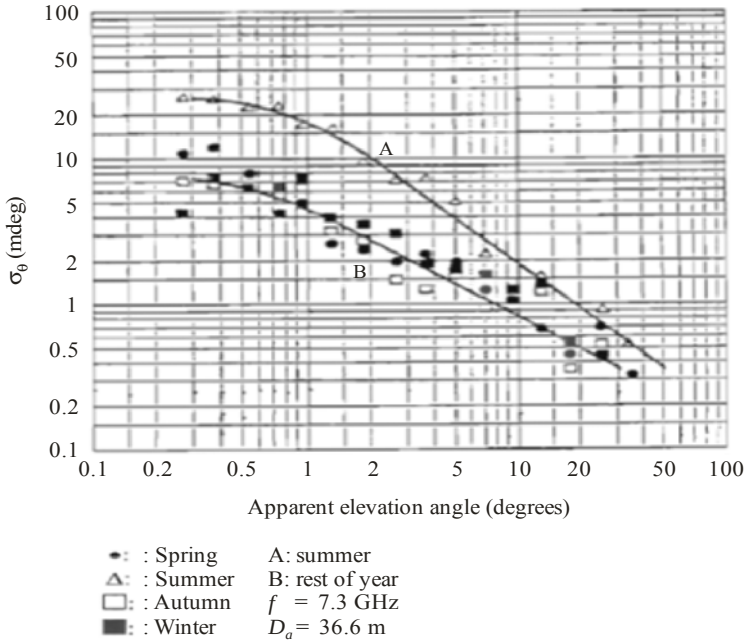

Radio-Meteo. 04-08

4.8 Tropospheric scatter propagation

Troposcatter propagation occurs due to the presence of a sufficiently large number of small-scale inhomogeneities in the radio path, or deviations from the mean refractivity, in a region located several hundred metres (and even perhaps up to a few kilometres) above the Earth's surface (Figure 4.9). In contrast to scintillation phenomena, there is no direct signal on which the fluctuations are superimposed. Scattering is strongest in the near-forward direction. The scatter cross-section depends on the magnitude of the deviation ΔN in the median refractivity. Received signals are generally 50 to 100 dB below free space values and are characterized by short-term fluctuations superimposed on long-term variations. The statistical distributions are Rayleigh for the short-term and log-normal for the long-term variations.

FIGURE 4.9

Troposcatter propagation

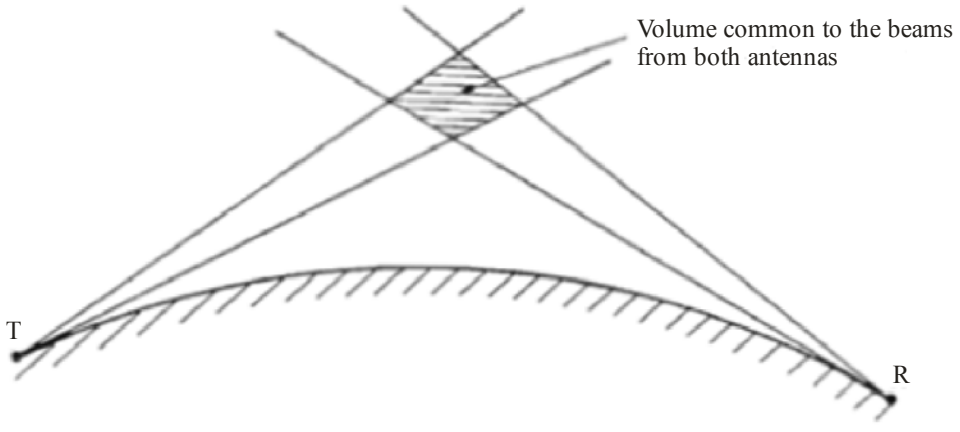

Radio-Meteo. 04-09

Strong spatial irregularities of field strength and antenna gain degradation have been observed in troposcatter propagation.

4.8.1 Modelling of long-term variations of field strength

As the small scale fluctuations are not known it is essential for applications to find a correlation between the characteristics of the troposcatter propagation and a "macroscopic" parameter of the troposphere. Several possible parameters have been investigated [Boithias and Battesti, 1983].

4.8.1.1 Correlation with the refractive index of the air near the ground

The search for such a correlation has received widespread attention, for the following reasons:

– refractivity at the surface of the ground (N_S) is easy to determine;

– in many cases, this correlation has appeared to hold true, particularly in temperate climates or in regions where N_S has low values.

However, this correlation is in no way universal. Firstly, it does not exist at any time during the year in equatorial or tropical regions. Secondly, even in temperate regions, the ratio of the loss variations to the refractive-index variations (expressed in dB per N unit) may range from about 0.2 to 0.6 depending on the region. This ratio may attain 1 dB per N unit in tropical regions during that part of the year when the correlation is most pronounced.

It is worth pointing out that this conclusion is not surprising because the propagation mechanism is produced by inhomogeneities located hundreds of metres (up to a few kilometres in certain cases) above the Earth. It cannot be correlated with a meteorological parameter defined and measured at ground level unless of course, in the climate under consideration, this latter parameter is perfectly correlated with certain characteristics in the upper atmosphere. For this reason, in a prediction method utilizing the refractive index near the ground, the limit of validity of such a method must be clearly indicated.

4.8.1.2 Correlation with the vertical refractive-index gradient

The vertical gradient of the refractive index has two different but additive effects:

– the vertical gradient of the refractive index directly influences the path curvature. If its modulus increases in that part of the atmosphere below the common volume of the antenna beams, the height of the common volume is reduced, thus lowering the scattering angle and thereby increasing the received level;

– since propagation results from inhomogeneities in the refractive index, the greater the vertical variation (or gradient) in the common volume, the higher the received level. This second effect is more important than the first one.

Following these remarks, a semi-empirical formula has been obtained [Boithias and Battesti, 1983] for the average transmission loss on a troposcatter path:

$$A = 102 + 30 \log f + 30 \log d + 1.5\, G_c \tag{4.51}$$

where:

A: average transmission loss (dB) between isotropic antennas (basic transmission loss)

f: frequency (MHz)

d: distance (km)

G_C: index gradient in the common volume (N units per km).

With respect to this relationship, which appears to be valid for all climates, the following remarks may be useful:

– the only random element relates to the index gradient. Because the latter shows nearly a normal statistical distribution, losses (in dB) show a similar distribution and the field is distributed log-normally;

– distance occurs in the term 30 log d, however it may also have an effect in the term containing G_C, since, if distance changes, the height of the common volume changes, causing the value of G_C to change, unless the atmosphere is vertically uniform (as in desert climates during the summer). Thus it can be seen that the effect of distance on transmission loss is closely linked to the decreasing rate of refractive index irregularities as altitude increases. This rate may vary greatly depending on the climate.

4.8.2 Troposcatter transfer function

A prediction method of the digital transmission quality on tropospheric scatter paths cannot be based only on the statistics of the long-term median transmission loss. Additional information about the troposcatter transfer function and the statistics of its parameters is necessary. In other words the frequency selective nature of the fading has to be taken into account.

As a result of the troposcatter propagation mechanism, the transfer function of the transmission medium could be expressed in terms of a sum of many ray paths with random amplitudes and phases. The complex transfer function can then be written as:

$$H(f,\ t) = A(f,\ t)\exp(-j\varphi(f,\ t)) \tag{4.52}$$

where $A(f, t)$ is the amplitude component and $\varphi(f, t)$ is the phase component, with random variables of time t and frequency f.

The amplitude component at a fixed frequency $A(f_0, t)$ is Rayleigh-distributed. Moreover, the hourly median values of $A(f_0, t)$ follow a log-normal distribution. The phase component is uniformly distributed between $-\pi$ and π.

4.8.2.1 Correlation bandwidth and multipath spread

The frequency selective nature of the propagation channel can be described by the frequency correlation function defined by [Bello, 1969]:

$$q(\Delta f) = \frac{1}{2} < H^{*}(f,\ t_0)\, H(f + \Delta f,\ t_0) > \tag{4.53}$$

The magnitude of $q(\Delta f)$ expresses the degree of correlation between the amplitudes of waves received at two frequencies spaced Δf apart. The bandwidth B_C at which the correlation function drops to e^{-1} is defined as the correlation bandwidth.

A particularly interesting application is the intensity of scattering $Q(\Delta\tau)$, also called multipath intensity profile or delay power spectrum of the channel because it gives the averaged output power as a function of time delay $\Delta\tau$, due to scatterers providing path delays in the interval $(\tau, \tau + \Delta\tau)$. The width T_M of $Q(\Delta\tau)$, which can be defined by analogy to the definition for B_C given above is called multipath spread of the channel. From the width of $Q(\Delta\tau)$ one can directly determine the amount of inter-symbol interference in digital transmission and the degree of frequency selectivity.

The frequency correlation function and the delay power spectrum are Fourier transform pairs:

$$Q(\Delta\tau) = \int_{-\infty}^{+\infty} q(\Delta f)\exp(j2\pi\Delta\tau\Delta f)\, d(\Delta f) \tag{4.54}$$

As a result of the Fourier transform relationship between $Q(\Delta\tau)$ and $q(\Delta f)$ the reciprocal of the multipath spread is a measure of the coherence bandwidth of the channel.

Assuming a rectangular delay power spectrum [Sunde, 1964] the difference T_M of the maximum and minimum propagation delay between the highest and lowest paths in the common volume of the antenna beams gives the multipath spread and can be expressed as:

$$T_M = \frac{d\alpha}{2c}(\theta + \alpha) \tag{4.55}$$

where:

d: path length (km)

α: antenna beamwidth at half-power points (-3 dB)

c: speed of light (km/s)

θ: scatter angle.

This is only a good approximation if the common volume is small enough so that there exists only a small delay spread; in other words the antenna gains must be large enough to lie in the asymptotic part of the curve of the antenna gain loss.

The frequency correlation function as the Fourier transform of $Q(\Delta\tau)$ has then the form:

$$q(\Delta f) = \sin c(\Delta f \bullet T_M) \tag{4.56}$$

with:

$$\sin c(x) = \sin(\pi x)/\pi x \tag{4.57}$$

For $q(\Delta f = B_c) = e^{-1}$ the coherence bandwidth is then given by:

$$B_c = 0.7/T_M = \frac{1.4c}{d\alpha(\theta + \alpha)} \tag{4.58}$$

In another model it is assumed that the contribution of scattering elements inside the common volume decreases from the centre of this volume according to a three dimensional Gaussian law. Then frequency correlation function and delay power spectrum are given by:

$$Q(\Delta\tau) = \exp\left\{-(\Delta\tau)^2/4\sigma^2\right\} \quad \text{and} \quad q(\Delta f) = \exp\left\{-(2\pi\sigma\Delta f)^2\right\} \tag{4.59}$$

from which the delay spread and correlation bandwidth are obtained as:

$$T_M = 4\sigma = \frac{d\alpha\theta}{\sqrt{3}\,c} \quad \text{and} \quad B_c = \frac{2\,c\sqrt{3}}{\pi d\alpha\theta} \tag{4.60}$$

The two models described above are based on simplifying assumptions on the distribution of propagation delays.

A more realistic model yields an integral representation of the delay power spectrum depending on the path characteristics [Bello, 1969].

4.8.2.2 Experimental approach and statistical results

Measurements of the frequency selective nature of the troposcatter propagation channel were made both in the time and frequency domain, i.e. in terms of the delay power spectrum or the frequency correlation function. Measurements in the frequency domain were described in [Collin and Marguinaud, 1979], where results on the amplitude and group delay distortions in a 20 MHz bandwidth were obtained. A proposal has been made to compute the correlation bandwidth B_C on an experimental link by using the standard deviation of the nearly Gaussian distribution of the group delay. The measured cumulative distribution of B_C approximates a log-normal law. It is characterized by a median value B_C (50%) and a standard deviation b which depend on the characteristics of the link. Empirical expressions of B_C and b, have been proposed [Collin, 1979] and were verified on 15 different links.

Results from experimental and theoretical investigations of tropospheric propagation in Russia are presented in [Vvedensky, 1965].

REFERENCES

BABLER, G.M. [1972] A study of frequency selective fading for a microwave line-of-sight narrow-band radio channel, BSTJ, Vol. 51, 3, 731-757.

BABLER, G.M. [1973] Selectively faded non diversity and space diversity narrow-band microwave radio channels, BSTJ, Vol. 52, 2, 239-261.

BANJO, O.P. and VILAR, E. [1986] Measurement and modelling of amplitude scintillations on low-elevation Earth-space paths and impact on communication systems, IEEE Trans. on Communications, Vol. COM-34, 8, 774-780.

BECKMANN, P. [1964] Rayleigh distribution and its generalizations, Radio Sci., 68 D, No. 9, 927-932.

BELLO, P.A. [1969] A troposcatter channel model, IEEE Trans. Comm. Tech., Vol. 1, 130-137.

BERRADA-BABY, H., GOLE, P. and LAVERGNAT, J. [1988] A model for the tropospheric excess path length of radio waves from surface meteorological measurements, Radio Science, 23, Nr. 6, pp. 1023-1038.

BOITHIAS, L. [1984] Propagation des ondes radioélectriques dans l'environnement terrestre, Collection Technique et Scientifique des Télécommunications, 2nd Edition, Editions DUNOD, Paris, France.

BOITHIAS, L. and BATTESTI, J. [1983] Propagation due to tropospheric inhomogeneities, IEE Proc., Vol. 130, Part F, 7, 657-664.

BRUSSAARD, G. and WATSON P.A. [1995] Atmospheric modelling and millimetre wave propagation, Chapmen and Hall, London, ISBN 0-412-56230-8.

COLLIN, C. [1979] Evaluation empirique de la bande de cohérence en diffusion troposphérique, Rev. Tech. Thomson-CSF, Vol. 11, 3, 549-575.

COLLIN, C. and MARGUINAUD, A. [1979] Evaluation expérimentale de la sélectivité d'une liaison par diffusion troposphérique, Rev. tech. Thomson-CSF, Vol. 11, 1, 103-157.

CRANE, R.K. [1971] Propagation phenomena affecting satellite communication systems operating in the centimetre and millimetre wavelength bands, Proc. IEEE, 59, 173-188.

CRANE, R.K. [1976a] Refraction effects in the neutral atmosphere. Methods of Experimental Physics, Vol. 12, Astrophysics Part B. Radio Telescopes, Ed. L.M. Meeks, Academic Press, New York, NY, USA.

CRANE, R.K. [1976b] Low-elevation angle measurement limitations imposed by the troposphere: An analysis of scintillation observations made at Haystack and Millstone, MIT Lincoln Lab. Tech. Report 518, Lemington, Mass. USA.

CRANE, R.K. [September-October, 1981] A review of transhorizon propagation phenomena, Radio Sci., Vol. 16, 5, 649-669.

CRAWFORD, A.B. and JAKES, W.C. Jr. [1952] Selective fading of microwaves, BSTJ, Vol. 31, 1, 68-90.

DOUGHERTY, H.T. and DUTTON, E.J. [1980] Elevated layer characteristics in the USA - preliminary estimates, NTIA Rep. (NTIS Access) National Technical Information Service, Springfield, Va. 22161, USA.

DOUGHERTY, H.T. and HART, B.A. [July, 1979] Recent progress in duct propagation predictions, IEEE Trans. Ant. Prop., Vol. AP-27, 4, 542-548.

GRÜNBERGER, G.K. [1989] An improved two-ray model providing a new basis for outage prediction, Europ. Conf. on Radio-Relay Systems, Padua, Italy.

HADDEN, J., and VILAR, E. [1986] Scattering-induced scintillations from clear air and rain on Earth-space paths and the influence of antenna aperture, IEEE Trans. Antenna and Propagation, Vol. AP-34, 8, 646-657.

HALL, M.P.M. [1980] Effects of the troposphere on radiocommunication, Ed. Peter Peregrinus, London, United Kingdom.

KALININ, A.L. [1979] Rasprostranenie radiovoln na trassakh nazemnykhi kosmicheskikh radioliny (Propagation on terrestrial and space links), Sviaz, Moscow, USSR.

KALININ, A.I. [1992] Statistical fade depth distributions at radio-relay hops with rough and smooth profiles, TRUDI NIIR.

KALININ, A.A. [1985] Otsenka selektivnosti zamiranii na proletakh RRI, vyzvannykh otrazeniyami ot sloistykh neodnorodnostei v troposfere (Evaluation of fading selectivity on radio-relay path sections due to reflections from tropospheric layer inhomogeneities), Elektrosviaz, 3.

KARASAWA, Y., YAMADA, M. and ALLNUTT, J.E. [1988] A new prediction method for tropospheric scintillation in satellite communication, IEEE Trans. Antennas and Propagation, Vol. AP-36, 11, 1608-1614.

KAYLOR, R.L. [1953] A statistical study of selective fading of super-high frequency radio signals, BSTJ, Vol. 32, 1187.

LINIGER, M. [19-22 June, 1983] One year results of sweep measurements of a radio link, IEEE International Conference on Communications (ICC '83), Boston, MA, USA, Paper C.2.3.

LO, P.S.L., BANJO, O.P. and VILAR, E. [1984] Observations of amplitude scintillations on a low-elevation Earth-space path, Elec. Letters, Vol. 20, No. 7, pp. 307-308.

MARTIN, L. [13-17 June, 1982] Statistical results on selective fadings. IEEE International Conference on Communications (ICC '82), Philadelphia, PA, USA.

METZGER, K. and VALENTIN, R. [1989] On the performance of equalized digital radio systems during frequency-selective fading, AEÜ.

MOJOLI, L.F. [1980] A new approach to the visibility problems in line-of-sight hops (ICC 1979). Telettra Rev., 31, 14-21.

MON, J.P., WEILL, A. and MARTIN, L. [1980] Effect of tropospheric disturbances on a 4.1 on 6.2 GHz line-of-sight path, Ann. des Télécomm. 35, pp. 470-473.

MOULSLEY, T.J. and VILAR, E. [1982] Experimental and theoretical statistics of microwave amplitude scintillations on satellite down-links, IEEE Trans. Ant. Prop., Vol. AP-30, 1099-1106.

` NUSPL, P.P., DAVIES, N.G. and OLSEN, R.L. [1975] Ranging and synchronization accuracies in a regional TDMA experiment, Proc. Third International Digital Satellite Communications Conference, Kyoto, Japan.

ORTGIES, G. [1985] Diurnal and seasonal variations of OTS amplitude scintillations, Electron. Lett,. Vol. 21, 143-145.

PARL, S.A. [1983] Characterization of multipath parameters for line-of-sight microwave propagation, IEEE Trans. Ant. Prop., Vol. AP-31, 6, 938-948.

RÜCKER, F. [1985] Beschreibung von Amplitudenszintillationen von Satellitensignalen im 11 GHz-Band mit Hilfe der Streuung an turbulenten Schichten (Description of amplitude scintillations on an 11 GHz slant path in terms of forward scattering from turbulent layers), Techn. Ber. FTZ, 455 TBr 76.

RÜCKER, F. and DINTELMANN, F. [1983] Effect of antenna size on OTS signal scintillations and their seasonal dependence, Electron. Lett., Vol. 19, 1032-1034.

RÜCKER, F. and ORTGIES, G. [1985] Diurnal and seasonal variations of OTS amplitude scintillations, Elec. Letters, Vol. 21, No. 4, 143-145.

RUMMLER, W.D. [May-June, 1979] A new selective fading model: application to propagation data, BSTJ, Vol. 58, 5, 1037-1071.

RUMMLER, W.D. [1980] Time and frequency-domain representation of multipath fading on line-of-sight microwave paths, BSTJ, Vol. 59, No. 5, 763-796.

RUMMLER, W.D. [1983] A rationalized model for space and frequency diversity line-of-sight radio channels, IEEE International Conference on Communications (ICC '83), Paper E.2.7.

SAKAGAMI, S. and HOSOYA, Y. [1982] Some experimental results on in-band amplitude dispersion and a method for estimating in-band linear amplitude dispersion, IEEE Trans. Comm., Vol. COM-30, 8, 1875-1888.

SASAKI, O. and AKIYAMA, T. [1979] Multipath delay characteristics on line-of-sight radio systems, IEEE Trans. Comm., Vol. COM-27, 12, 1876-1886.

SCHIAVONE, J.A. [July-August, 1981] Prediction of positive refractivity gradient for line-of-sight microwave radio path, BSTJ, Vol. 60, 6, 803-822.

SMITH, D.R. and CORMACK, J.J. [June, 1982] Measurement and characterization of a multipath fading channel, IEEE International Conference on Communications (ICC '82), Philadelphia, PA, USA. Paper 7B.4.

SPILLARD, C., ROORYCK, M., JUY, M. and VILAR, E. [1989] X-band tropospheric transhorizon propagation under differing meteorological conditions, ICAP 89, Warwick, United Kingdom.

STEPHANSEN, E.T. [1981] Clear-air propagation on line-of-sight radio paths: a review, Radio Sci. Vol. 16, 5, 609-629.

STRICKLAND, J.I. [1980] Site-diversity measurements of low-angle fading and comparison with a theoretical model, URSI (Commission F) International Symposium on Effects of the lower atmosphere on radio propagation at frequencies above 1 GHz, Lennoxville, Canada.

SUNDE, E.D. [1964] Digital troposcatter transmission and modulation theory, BSTJ. Vol. 43, 1, 144.

SYLVAIN, M. and LAVERGNAT, J. [1985] Modelling the transfer function in medium bandwidth radio channels during multipath propagation, Ann. Telecomm., Vol. 40, No. 11-12, 97-116.

TATARSKII, V.I. [1967] The effects of the turbulent atmosphere on wave propagation (in Russian), Nauka Publishing House, Moscow, URSS.

TROITSKY, V.N. [1957] Fading of UHF and SHF on radio-relay links, Electrosvjaz, N 10, 32-39.

TROITSKY, V.N. PETRUSHKO, Y.I. *et al.* [1989] Long distance propagation of VHF, UHP and SHF over sea, Electrosvjaz, N 5, 23-28.

VANDER VORST, A., VANHOENACKER, D. and MERCIER, L. [1982] Fluctuations on OTS-Earth co-polar link against diurnal and seasonal variations, Electron. Lett., Vol. 18, 915-917.

VIGANTS, A. [1983] Effect of space on distance variation of two-tone amplitude dispersion, IEEE International Conference on Communication (ICC '83) Vol. 2, Paper C2.1.

VILAR, E., SPILLARD, C., ROORYCK, M., JUY, M., BARBER, P.C. and HALL, M.P.M. [1988] Observations of troposcatter and anomalous propagation signal levels at 11.6 GHz on 155 km path over the sea, Electron. Lett. 24, pp. 1205-1207.

VVEDENSKY, B.A. [1965] Long distance tropospheric propagation under preparation.,"Sov. radio", 415 p.p.

WEBSTER, A.R. [January, 1983] Angles-of-arrival and delay times on terrestrial line-of-sight microwave links, IEEE Trans. Ant. Prop., Vol. AP-31, 12.

WEBSTER, A.R. and SCOTT, A.M. [1987] Angles-of-arrival and tropospheric multipath microwave propagation, IEEE Trans. on Antennas and Propagation, AP 35, No. 1, 94-99.

YOKOI, H., YAMADA, M. and SATOH. T [1970] Atmospheric attenuation and scintillation of microwaves from outer space, Astron. Soc., (Japan), Vol. 22, 4, 511-525.

ANNEX 1

Statistical prediction models of scintillation standard deviation and amplitude

A1.1 Introduction

Most of the statistical methods usually try to link the standard deviation σ or the variance σ^2 of log-amplitude fluctuation χ (in dB) to ground meteorological measurements, like temperature, relative humidity and wet refractivity. Karasawa [Karasawa et al 1988] and ITU-R [ITU-R, 2001] (not defined in reference) methods present similar prediction models for the calculation of the standard deviation of signal fluctuation due to scintillation. Both these models use as input parameter the wet part of ground refractivity N_{wet}, which is a function of relative humidity and temperature, averaged at least over one month. The other models presented in the following can give dependencies with other parameters such as integrated water vapour content or integrated liquid water content. The review of the statistical models presented hereafter has been carried out in the framework of the European actions COST 255 [COST 255, 2002] and COST 280 ("Propagation impairment mitigation for millimetre-wave radio systems", final report in preparation).

A1.2 Prediction models of the scintillation standard deviation

A1.2.1 Karasawa model

The Karasawa method [Karasawa *et al.*, 1988] has been validated by comparison with measurements for elevation angles between 4 and 30 degree, frequencies in the range 7.3 to 14.2 GHz and antenna diameters from 3 to 36.6 m. The average N_{wet} varied from 20 to 130 ppm. The predicted standard deviation is given by:

$$\sigma = \left(3.42\times10^{-3} + 1.186\times10^{-4} N_{wet}\right)\times\sqrt{f^{0.9} G(D_e)/\sin^{2.6}\vartheta} \qquad (1A.1)$$

where f is the link frequency [GHz], ϑ the link elevation angle, and N_{wet} is evaluated from the knowledge of the relative humidity and the temperature at ground level. These meteorological input parameters should be averaged over a period of the order of a month. The factor $G(D_e)$ in equation 1A.1 is the antenna averaging function. [Crane *et al.*,1979]

A1.2.2 Recommendation ITU-R P.618

The ITU-R prediction method is presented in § 4.6. It is very similar to the Karasawa method and models the predicted scintillation variance as:

$$\sigma_p = (3.6\times10^{-3} + 10^{-4} N_{wet})\times\sqrt{f^{7/6} g^2(x)/\sin^{2.4}\vartheta} \qquad (1A.2)$$

However, the expression for N_{wet} is different from the Karasawa one, as it can be obtained directly from the map given in Figure 4.6. An improvement of the ITU-R model, including the sky noise temperature has been proposed by [Belloul *et al.*, 1998].

A1.2.3 Ortgies models

The Ortgies methods [Ortgies, 1993] have been derived from 30 months of Olympus measurements in Germany, at 12, 20 and 30 GHz, and is assumed to be valid for elevation angles ranging from 6.5 to 30 degrees. Two direct relationships between monthly mean value m of $\ln(\sigma^2)$ and surface average values of N_{wet} and temperature have been proposed by Ortgies. The first one (referred to as "Ortgies-N method") relates m to surface N_{wet} and is given by

$$m = \left\langle \ln\left(\sigma^2\right)\right\rangle = \ln\left[g^2\ f^{1.21}\ \left(\sin\vartheta\right)^{-2.4}\right] + \left(-13.45 + 0.0462\left\langle N_{wet}\right\rangle\right) \tag{1A.3}$$

The second relationship (referred to as "Ortgies-T method") relates m to surface temperature T [°C] and is given by

$$m = \left\langle \ln\left(\sigma^2\right)\right\rangle = \ln\left[g^2\ f^{1.21}\ \left(\sin\vartheta\right)^{-2.4}\right] + \left(-12.5 + 0.0865\left\langle T\right\rangle\right) \tag{1A.4}$$

In both equations (1.A.3) and (1A.4) the frequency-scaling factor is very close to the ITU-R one. The standard deviation of $\ln\left(\sigma^2\right)$ appears to be independent of the meteorological data and is found equal to 1.01, from the experimental data.

A1.2.4 Otung model

The model of [Otung, 1996] is very similar to the model given in Recommendation ITU-R P.618. The difference is in the fact that the ITU-R model uses an empirical dependence on the elevation angle whereas the Otung model makes use of a factor obtained from simplified theoretical expressions. The predicted scintillation variance becomes:

$$\sigma_p = \sigma_{ref}\sqrt{f^{7/6}g^2(x)/\sin^{11/6}\varepsilon} \tag{1A.5}$$

This model has been validated with one-year measurements in the United Kingdom, using the Olympus 20 GHz beacon, with an elevation angle of 28.7 degrees and an antenna of 1.2 m diameter.

A1.2.5 Van de Kamp model

A significant correlation between the occurrence of scintillation and the presence of cumulus clouds along the propagation path has been observed several times. This implies that part of the turbulent activity causing scintillation is associated with this meteorological situation. In order to take into account the effects of clouds not adequately described by the parameter N_{wet}, at ground level, Van de Kamp [Van de Kamp *et al.*, 1999] used an improved version of the Salonen-Uppala cloud model, to compute the average water content of heavy clouds W_{hc} to be introduced in a new empirical prediction model for σ_{n} as follows:

$$\sigma_p = \frac{\sqrt{g^2\left(D_e\right)}f^{0.45}}{\sin^{1.3}\vartheta}0.98\times10^{-4}\left(N_{wet}+Q\right) \tag{1A.6}$$

Q is a long-term average parameter that depends on the long-term (at least annual) average of W_{hc}. and therefore constant for each site, so that all seasonal dependence of σ_{p} is still represented by N_{wet}.

A1.2.6 Marzano models

The Direct Physical-Statistical Prediction (DSPS) and Modeled Physical-Statistical Prediction (MPSPS) methods [Peeters *et al.* 1997] and the STH2 (not defined), STN2 (not defined), STHV2 (not defined) and STNV2 (not defined) methods [Marzano et al 1998] allow the prediction of the monthly and hourly mean value of the scintillation variance from the knowledge of ground meteorological measurements. These methods result in the fit of the output of numerical models describing the interaction between microwave radiation and turbulent atmosphere based on

Tatarskii turbulence theory, modified with the introduction of the intermittent turbulence hypothesis [D'Auria *et al.*, 1993]. All methods use the frequency-scaling factor and the antenna aperture averaging factor given by ITU-R.

Specifically, the DPSP method is based on the direct correlation between the monthly average of $\ln(\sigma^2)$ and the surface temperature T and the MPSP method relates the monthly average of $\ln(\sigma^2)$ to the air refractivity due to water vapour, N_{wet}, at ground level.

Marzano has also derived four non-linear prediction methods. In particular, the STH2 method uses as regressive estimators the ground temperature and humidity in quadratic form, and the STN2 one uses the ground temperature and wet-refractivity in quadratic form.

The STHV2 method relates scintillation variance to surface temperature T, relative humidity RH and integrated water vapor V_C. The STNV2 method relates scintillation variance to surface temperature T, wet refractivity N_{wet} and integrated water vapor V_C.

The above prediction methods have been derived not only for the monthly average quantities, but also for the hourly average quantities.

A1.2.7 UCL model

The U.C.L. method [Vasseur *et al.*, 1998] is a statistical-physical model which consists of two main steps. In the first step, the statistical characteristics of the parameters describing the vertical profile of the refractive index structure are extracted from the analysis of long term radiosonde data. For this purpose, a statistical model [Warnock *et al.*, 1985] to estimate turbulence parameters from radiosoundings is used. In the second step, long-term statistics of slant-path scintillation are derived from the inferred tropospheric turbulence feature, using a rigorous statistical approach and the theory of propagation through a turbulent medium. In addition to radiosonde data, the other parameters required for scintillation prediction are the link characteristics: frequency, elevation angle (greater than about 5 to 10 degrees) and antenna diameter.

A1.3 Prediction models of the distribution of the scintillation amplitude

A1.3.1 Karasawa and ITU-R models

Karasawa *et al.* [Karasawa, 1988] proposed some expressions for the long-term cumulative distribution of amplitude deviation (y), as a function of the time percentage and of the predicted long-term standard deviation. The expression was obtained by integrating the distribution function of short-term standard deviation, assumed to be gamma like, with the conditional short-term distribution function of signal level for a given standard deviation, which has been assumed to be Gaussian distributed.

The resulting amplitude deviation y, exceeded for a given time percentage P, is:

$$y = \left(-0.0597 \log^3 P - 0.0835 \log^2 P - 1.258 \log P + 2.672\right) \sigma \qquad (1A.7)$$

where P ranges from 0.01% to 50% and σ is the long-term (usually one year) signal standard deviation. Equation 1A.7 shows good agreement with measurements for signal enhancement, but underestimates signal fade, especially in the low probability region. In order to overcome this limitation, the following relationship has been obtained by fitting signal fade measurements in the 0.01% to 50% probability interval:

$$y = \left(-0.061 \log^3 P + 0.072 \log^2 P - 1.71 \log P + 3.0\right) \sigma \qquad (1A.8)$$

ITU-R adopted only the distribution for signal fade in Recommendation ITU-R P.618.

A1.3.2 Van de Kamp model

Starting from the assumption that the main cause of scintillation on a satellite link is due to turbulence in clouds, i.e. turbulence in thin layers far from the receiver, Van de Kamp [Van de Kamp, 1998, 2000] assumed that the short term received electric field amplitude has a Rice-Nakagami distribution and therefore the distribution of signal level y in dB is asymmetrical as evidenced by observations.

The model proposed is:

$$\begin{aligned} y_f(P) &= \gamma(P) + \delta(P) \\ y_e(P) &= \gamma(P) - \delta(P) \end{aligned} \tag{1A.9}$$

where $y_f(P)$ is the distribution of signal fade [dB] and $y_e(P)$ the distribution of signal enhancement (dB).

$$\begin{aligned} \gamma(P) &= \left(-0.0515 \log^3 P + 0.206 \log^2 P - 1.81 \log P + 2.81\right)\sigma \\ \delta(P) &= \left(0.172 \log^2 P - 0.454 \log P + 0.274\right)\sigma^2 \end{aligned} \tag{1A.10}$$

where σ is the long-term standard deviation [dB]. These relations have been obtained by curve fitting.

REFERENCES OF ANNEX 1

Belloul, B., Saunders, S., Evans, B., 1998, Prediction of scintillation intensity from sky-noise temperature in Earth-satellite links, *Electronics Letters*, Vol. 34, No. 10, pp. 1023-1024.

COST 255 : "Radio wave propagation modelling for new Satcom services at Ku-band and above", COST 255 Final Report, ESA Publications Division, SP-1252, March 2002.

Crane, R.K., Blood, D.W., 1979, “Handbook for the estimation of microwave propagation effects”, NASA Contract NAS5-25341, NASA GSFC Greenbelt, MA, Technical Report n. 1, Doc. 7376-TR1.

D’Auria, G., Marzano, F.S., Merlo, U., 1993, Model for estimating the refractive-index structure constant in clear-air intermittent turbulence, *Applied Optics*, Vol. 32, pp. 2674-2680.

Karasawa, Y., Yamada, M., Allnutt, J.E., 1988, A new prediction method for tropospheric scintillation on Earth-space paths, *IEEE Transactions on Antennas and Propagation*, Vol. 36, No. 11, pp. 1608-1614.

Marzano, F.S., D’Auria, G., 1998, Model-based prediction of amplitude scintillation variance due to clear-air tropospheric turbulence on earth-satellite microwave links, *IEEE Transactions on Antennas and Propagation*, Vol. 46, No. 10, pp. 1506-1518.

Ortgies, G., 1993, Prediction of slant-path amplitude scintillation from meteorological parameters, *Proc. Int. Symp. Radio Propagation*, Beijing, pp. 218-221.

Otung, I.E., 1996, Prediction of tropospheric amplitude scintillation on a satellite link, *IEEE Transactions on Antennas and Propagation*, Vol. 44, No. 12, pp. 1600-1608.

Peeters, G., Marzano, F.S., D’Auria, G., Riva, C., Vanhoenacker, D., 1997, Evaluation of statistical models for clear-air scintillation prediction using Olympus satellite measurements, *International Journal of Satellite Communications*, Vol. 15, pp. 73-88.

Van de Kamp, M.M.J.L., 1998, Asymmetrical signal level distribution due to tropospheric scintillation, *Electronics Letters*, Vol. 34, No. 11, pp. 1145-1146.

Van de Kamp, M.M.J.L., Tervonen, J.K., Salonen, E.T., Poiares Baptista, J.P.V., 1999, Improved models for long-term prediction of tropospheric scintillation on slant paths, *IEEE Transactions on Antennas and Propagation*, Vol. 47, No. 2, pp. 249-260.

Van de Kamp, M.M.J.L., 2000, Experimental verification of asymmetrical short-term scintillation distribution model, *Electronics Letters*, Vol. 36, pp. 663-664.

Vasseur, H., Vanhoenacker, D., 1998, Characterisation of tropospheric turbulent layers from the radiosonde data, *Electronics Letters*, Vol. 34, No. 4, pp. 318-319.

Warnock, J.M., Vanzandt, T.E., Green, J.L., 1985, A statistical model to estimate mean values of parameters of turbulence in the free atmosphere, Preprints 7th Symposium on Turbulence and Diffusion, Boulder (U.S.A.), pp. 156-159.

CHAPTER 5

Single-particle scattering

5.1 General considerations

A number of authors have treated the problem of single particle scattering; however it is difficult to find a systematic approach to get an overview on the subject and above all to understand the limitations and the validity conditions of the different solutions. What follows is not addressed at giving new results but at providing a kind of Ariadne's thread in the labyrinth of the most current methods.

Most of the methods (with the exception of Fredholm integral and finite elements methods) deal with scatterers bounded by a regular surface (there is only one normal at each point of the surface) and made with permanent and isotropic dielectric. One must confess that these assumptions, reasonable for the precipitating hydrometeors, are obviously very inappropriate when applied to ice crystals. The assumptions must therefore be checked carefully when dealing with high altitude clouds. But the technical difficulties are so important that very few people have tried to treat such cases.

FIGURE 5.1

Example of a scattering problem

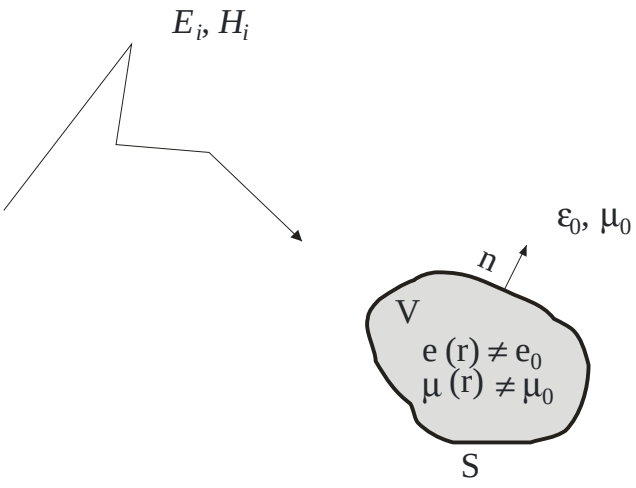

Radio-Meteo. 05-01

V is the volume and *S* the surface of the scatterer. Indices + and - are the symbols for the exterior and the interior of the scatterer respectively. The electrical properties of the scatterer are given by the permittivity $\varepsilon(r)$ and the permeability $\mu(r)$ that are different from those of the surrounding material, which, for sake of simplicity, is assumed to be vacuum.

The scatterer is immersed into an incident electromagnetic field E_i, H_i created by appropriate sources outside the scatterer that we called j_{ext}. The scattering problem is therefore to determine everywhere the resulting field, which can be written as :

$$\begin{cases} E(r)=E_i(r)+E_s(r) \\ H(r)=H_i(r)+H_s(r) \end{cases} \tag{5.1}$$

E_S, H_S is called the scattered field. We are generally interested in its value far away from the particle.

5.1.1 Integral representation of the field

The electromagnetic field satisfies the Maxwell equations which in our case read:

$$\begin{cases} \nabla \times E = -\mu(r)\dfrac{\delta H}{\delta t} \\ \nabla \times H = j_{ext}+\varepsilon(r)\dfrac{\delta E}{\delta t} \end{cases} \tag{5.2}$$

These equations are linear, thus we can write without ambiguity for harmonic fields and sources (we choose the convention $e^{i\omega t}$ to characterise the time dependence meaning that the refractive index is of the form $m = v - i\,k$).

$$\begin{cases} \nabla \times E = -i\,\omega\mu(r)H \\ \nabla \times H = j_{ext}+i\,\omega\varepsilon(r)E \end{cases} \tag{5.3}$$

Assuming $k^2=\omega^2$ the solution of (5.3) is well behaved at infinity (radiation condition for the scattered wave) and obeys the following equation:

$$E(r) = E_i(r)+\overline{G}\otimes\left[\left(k^2(r)-k_0^2\right)E(r)+\nabla\left(\log\mu(r)\right)\times\nabla\times E(r)\right] \tag{5.4}$$

The symbol $\otimes$ is used for the convolution. The dyadic $\overline{G}$ is called the free-space dyadic Green's operator. It can be written as either of two equivalent formulations :

$$\overline{G}(r)=\frac{1}{k_0^2}\left[-\delta(r)+\nabla\times\nabla\times\frac{e^{-ik_0r}}{4\pi r}\right]\overline{I}=\left[\overline{I}+\frac{1}{k_0^2}\nabla\nabla.\right]\frac{e^{-ik_0r}}{4\pi r} \tag{5.5}$$

The second expression is the most used one (e.g. Levine and Schwinger, 1951). There is an alternative for (5.4) which is more commonly used, but does not allow for much development.

$$\begin{aligned} E(r)=E_i(r)+\left(\nabla\nabla.+k_0^2\right)\int_V g\left(r-r'\right)\left(\frac{\varepsilon\left(r'\right)}{\varepsilon_0}-1\right)E\left(r'\right)dr' \\ -i\omega\nabla\times\int_V g\left(r-r'\right)\left(\mu\left(r'\right)-\mu_0\right)H\left(r'\right)dr' \end{aligned} \tag{5.6}$$

where $g(r)=\dfrac{e^{-ik_0r}}{4\pi r}$ i.e. the scalar Green function.

5.1.2 Scattering of a plane wave in the far field. The optical theorem

5.1.2.1 Scattering amplitude

For a defined case it is necessary to specify the coordinate frame of reference. As other conventions (e.g. $\pm\omega t$), this frame varies from one author to another, which has the consequence of making any comparison difficult. In the following, the incident field will be the reference. If it is a linearly polarized plane wave:

$$E_i(r) = E_i e_i e^{-i(k_i . r - \omega t)} \tag{5.7}$$

where:

e_i: unitary vector of the polarisation

k_i: wave vector ($|k_i| = k_0$)

E_i: amplitude.

FIGURE 5.2

Scatterer geometry

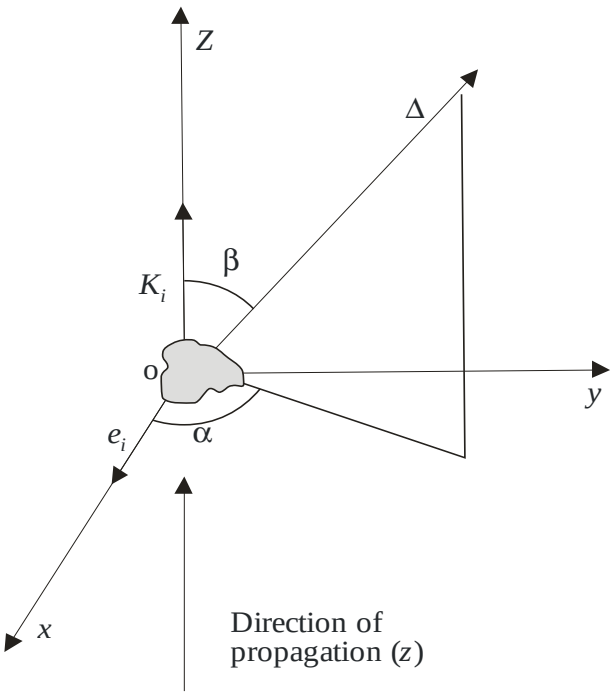

Radio-Meteo. 05-02

With reference to Figure 5.2, Ox is aligned along e_i, Oz is aligned along k_i (direction of propagation of the wave) and Oy completes the frame of reference $\left(\hat{y}=\hat{z}\times\hat{x}\right)$. The position of the scatterer, considered as a solid, is defined by one of its points (preferably its centre of mass) taken as the origin O and one axis Δ. The orientation of the axis Δ is determined by the two angles $0 \leq \beta \leq \pi$ and

$0 \le \alpha \le 2\pi$, and a rotation angle about Δ. If the scatterer is axi-symmetrical, the latter angle is not relevant.

Solutions based on equation (5.6) are valid for every point of space outside the particle, but when the observation point is far from the particle it takes a more simple form. In fact when r tends to ∞ then $\left|r-r'\right| = r - \dfrac{r.r'}{r}$.

As the integration is over a finite volume, this approximation is correct for r large enough (in practice for $r \gg L^2/\lambda$ where L is the characteristic length of the scatterer and $\lambda = 2\pi c/\omega$ is the wavelength of the incident field). The scattered field can then be expressed as,

$$E_s(r) \cong \left(\bar{I} + \frac{\nabla\nabla}{k_0^2}\right) \int_V \frac{e^{-ik_0 r}}{4\pi r} e^{ik_s.r'} \left(k^2(r') - k_0^2\right) E(r')\, dr' \tag{5.8}$$

Remark: $k_S = k_0 r/r$ is the wave vector of the scattered field. It depends upon the origin of the coordinates. Nevertheless, in the far field approximation, it can be easily shown that the choice of origin has a second order effect.

In the first part of the integral, the differential operator bears only on r. Therefore, elementary manipulations of equation (5.8) lead to:

$$E_s(r) \cong \left(\bar{I} - \frac{k_s k_s}{k_0^2}\right) \frac{e^{-ik_0 r}}{4\pi r} \int_V e^{ik_s.r'} \left(k^2(r') - k_0^2\right) E(r')\, dr' \tag{5.9}$$

We deduce that the far field has a spherical structure and that the field itself is perpendicular to its wave vector. Equation (5.9) can be written as:

$$E_s(r) \cong E_i\, S(k_S, k_i) \frac{e^{-ik_0 r}}{ik_0 r} e^{i\omega t} \tag{5.10}$$

$S(k_S, k_i)$ is a vector, generally complex, with no dimensions composed of amplitude functions S and loosely called the "scattering amplitude". It depends upon the direction of observation (k_S), the direction of incidence (k_i) and obviously the properties of the scatterer itself. Let us stress again that $S.k_S = 0$.

Naturally different expressions can be found in the literature concerning the scattering amplitude. This is because of the coefficient set inside the spherical term. Here we have chosen the notation of [Van de Hulst, 1981].

To be more accurate in the description of the field, it is necessary to define the frame of observation (see Figure 5.3). θ is usually called the scattering angle and the plane (k_S, k_i) the scattering plane.

At the observation point $P(r)$, the local frame (e_r, e_θ, e_φ) can be used.

If the scattered field E_s is expressed in this local frame, then: $S(k_s, k_i) = S_1 e_\varphi + S_2 e_\theta$.

The scattering intensity, which should not to be mistaken with the intensity of the scattered field, is: $I_s=S_1^2+S_2^2=|S|^2$

We can now introduce the optical theorem also called the forward scattering theorem.

FIGURE 5.3

Scattering geometry

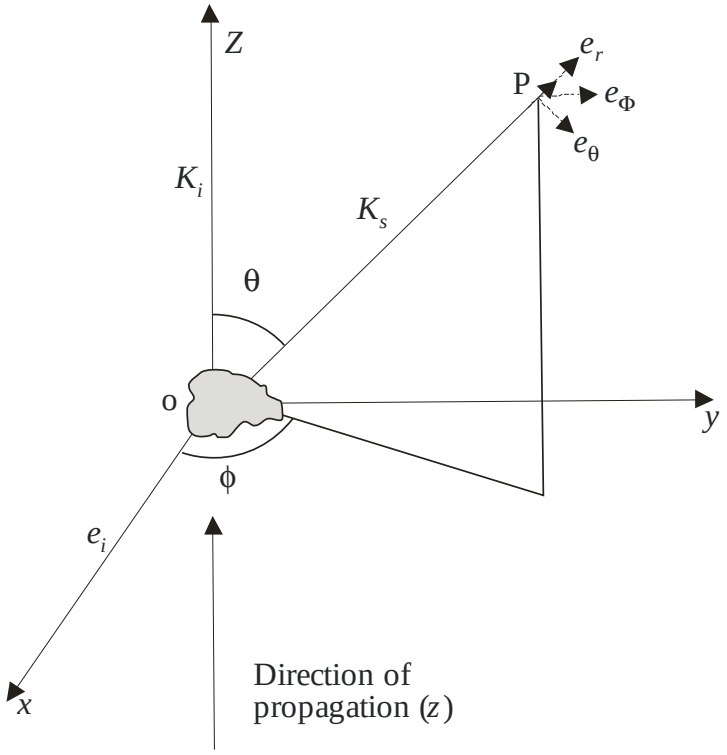

Radio-Meteo. 05-03

5.1.2.2 The optical theorem

The mean value of the energy flux can be obtained from the mean value of Poynting's vector *s* as: $\langle s\rangle = \frac{1}{2}\,\mathrm{Re}\left\{E_i\times H_i^*+E_s\times H_s^*+E_i\times H_s^*+E_s\times H_i^*\right\}$ or as $< s >=< s_i > + < s_s > + < s' >$.

Considering the mean value of the energy flux passing through a sphere centred at O with a radius *R* great compared to the size of the scatterer , the mean value will then be given by the integral over the sphere of the radial component of $< s >$ or $W = W_i + W_S + W'$.

If the scatterer is partially absorbing, a portion of the incident electromagnetic energy will be converted into another form of energy (heat) W_a. The energy conservation leads to: $-W_a = W_i + W_S + W'$.

Supposing that the external dielectric is lossless (free-space), we have $W_i = 0$, and thus:

$$-W' = W_s + W_a \tag{5.11}$$

This last equation shows that W' represents the sum of two effects responsible for the decrease in the incident energy along its initial direction : absorption and scattering. From Physical Optics, this combination of effects has been termed as the extinction; for microwaves, the word attenuation and sometimes apparent attenuation is also used. With clear notations we have:

$$2W' = -\frac{E_i^2}{\omega k_0 \mu_0 R} \int_S \mathrm{Re}\left\{ ie_i \times k_s \times S^* \mathrm{e}^{i(k_0 R - k_i.r)} + iS \times k_i \times e_i \mathrm{e}^{i(k_0 R - k_i.r)} \right\}.k_s \, dS \tag{5.12}$$

where we have used the equations of Maxwell to deduce the different magnetic vectors.

The stationary phase method can be used on the integral of equation (5.12) since its phase terms have very fast variations. The stationary points are intuitively those for which $k_0 R = |k_i.r|$, i.e. $|k_s.k_i\| = {k_0}^2$. By simple transformations (e.g. Born and Wolf, [1980]) and taking into account the important property $S.k_s = 0$ then, $W' = \frac{2\pi E_i^2}{k_0^2 Z_0} \mathrm{Re}\{e.S(k_i, k_i)\}$, where $Z_0 = \sqrt{\mu_0 / \in_0}$ is the vacuum impedance.

The extinction cross section σ_{ext} is defined as the ratio of the energy absorbed and scattered by the particle to the incident energy per unit surface (often the efficiency coefficient Q is also used, Q is the ratio of σ to the surface of the scatterer when projected in a plane perpendicular to the direction of incidence): $\sigma_{ext} = \sigma_a + \sigma_s = \frac{W_a + W_s}{|< s_i >|}$ where σ_a and σ_s are respectively the absorption and scattering cross-sections.

Since $|< s_i >| = E_i^2 / (2Z_0)$, we readily obtain:

$$\sigma_{ext} = \frac{\lambda^2}{\pi} \mathrm{Re}\left\{ e_i.S\left(k_i, k_i\right) \right\} \tag{5.13}$$

This formula is known as the optical theorem. The optical theorem means that in the case of a linearly polarized wave, the extinction cross section is proportional to one component of a certain amplitude of the scattered wave; the amplitude is that of the forward scattered wave, $S(k_i, k_i)$ and the component is the one that is co-linear with the incident electric vector, e_i. This theorem is very general and thus very useful. It applies whatever the scatterer, in particular if the scatterer is composed of many small particles. This is the reason why it will be encountered again in multiple scattering theory.

An important point is that the numerical evaluation of S is almost always performed using some approximations. Therefore, there is no a priori reason for the optical theorem to be verified under such approximations. Care must thus be taken when using it. For instance, in the Rayleigh approximation, a crude application of the optical theorem gives $\sigma_{ext} = 0$ for a lossless dielectric, which is obviously wrong.

The optical theorem gives results that, at first sight may seem contradictory. If the obstacle is opaque and has an apparent surface Σ in the incident direction, it is straightforward to show that according to Huygen principle, $\sigma_{ext} = 2\sum$. This peculiar result must be understood as being the addition of the effects of reflection and/or absorption by the obstacle and the effects of edge diffraction.

5.1.2.3 Cross-sections - radar applications

In the previous section we encountered three cross-sections σ_{ext}, σ_a and σ_s. There are other very useful cross-sections, especially in radar applications.

The scattered power density flux $|< s_s >| = |E_s|^2 / (2Z_0)$ can be used to define the differential scattering cross-section,

$$\sigma_d(k_s, k_i) = \lim_{r\to\infty} \frac{r^2 |< s_s >|}{|< s_i >|} \tag{5.14}$$

σ_d has the dimensions of an area/solid angle. It refers in some manner to the directional pattern of the intensity of the scattered field. The integral of equation (5.14) over 4π is the scattering cross-section $\sigma_s = \int_{4\pi} \sigma_d d\Omega$. Direct calculation from equation (5.10) gives:

$$\sigma_d(k_s, k_i) = \frac{1}{k_0^2} |S(k_s, k_i)|^2 = \frac{\sigma_{ext}}{4\pi} p(k_s, k_i) \tag{5.15}$$

The dimensionless quantity $p(k_s, k_i)$ is called phase function and is frequently used in the context of radiative transfer theory. Additionally, $A = \sigma_s / \sigma_{ext}$ is the albedo of the scatterer.

In the field of radar, one uses the bi-static radar cross-section,

$$\sigma_{bi}(k_s, k_i) = 4\pi\sigma_d(k_s, k_i) \tag{5.16}$$

and the back-scattering cross-section,

$$\sigma_b = 4\pi\sigma_d(-k_i, k_i) \tag{5.17}$$

In equations (5.16) and (5.17), the factor 4π is just a suitable factor which allows one to consider the target as an isotropic source.

Estimation of σ_a is obtained by integrating $< s >$ over the boundary of the scatterer:

$$\sigma_a = \frac{-\int_s n. < s > dS}{|< s_i >|}$$

where *n* is the outward vector normal to the surface of the scatterer. Using the divergence theorem, the last equation reads:

$$\sigma_a = \frac{k_0 \int_V \varepsilon''(r) |E(r)|^2 dV}{\varepsilon_0 E_i^2} \tag{5.18}$$

where ε" is the imaginary part of the permittivity (here we assume $\mu(r) = \mu_0$).

5.2 Solution methods

5.2.1 Analytical methods

In this section we present analytical solutions (closed form) for the scattering of a linearly polarized plane wave. In some rare cases of peculiar scatterers, there is an exact solution. These cases will be discussed first. We shall then focus on approximate methods.

5.2.1.1 Exact solution

The exact solution is obtained when there is a coordinate system within which both the Maxwell equations (5.3) are separable and the surface of the scatterer corresponds to a definite value in one coordinate. It can be shown [Morse and Feshbach, 1953] that these are very restrictive conditions fulfilled in very few cases. Fortunately, hydrometeors (especially raindrops) are reasonably well represented by spheres or spheroids which belong to these cases.

5.2.1.1.1 Spherical scatterer-Mie theory

Mie [1908] obtained the exact solution for an isotropic homogeneous dielectric sphere of arbitrary size using spherical harmonics which are a basis of eigen functions of the Helmholtz operator. Kerker [1969] extended the solution to the case where $\varepsilon(r)$ is spherically stratified.

Details of this approach can be found in many reference books (e.g. Stratton, [1941]; Born and Wolf, [1959]). Briefly, all these techniques consist in determining the coefficients of the expansion by applying the boundary conditions (continuity of the tangential components) at the surface of the scatterer. Here only the solution will be presented.

The sphere has a constant permittivity ε and its permeability is $\mu = \mu_0$. For the sake of simplicity, the surrounding medium is here assumed to have constants ε_0, μ_0. Inside the scatterer the refractive index $\left(m = \sqrt{\varepsilon/\varepsilon_0}\right)$ is denoted $m = v - i\kappa$, where κ represents the dissipative part of the dielectric. Outside the scatterer $m = 1$.

Take the dimensionless parameter $x = k_0 a = 2\pi a/\lambda_0$, where a is the radius of the sphere. In the far field, and in our frame of reference the scattering amplitude $S(\theta, \varphi)$ reads:

$$S(\theta,\varphi) = -S_1(x,m,\theta)\sin\varphi\, e_\varphi + S_2(x,m,\theta)\cos\varphi\, e_\theta \tag{5.19}$$

where

$$S_1 = \sum_{n=1}^{\infty} \frac{2n+1}{n(n+1)}\left(a_n \pi_n + b_n \tau_n\right)$$

$$S_2 = \sum_{n=1}^{\infty} \frac{2n+1}{n(n+1)}\left(b_n \pi_n + a_n \tau_n\right)$$

and

$$\pi_n = \frac{dP_n(\cos\theta)}{d\cos\theta} \qquad \tau_n = \frac{d(\sin\theta\,\pi_n)}{d\theta}$$

P_n is the Legendre polynomial of order n. The computation of π_n and τ_n does not raise any numerical problem. A simple method consists in obtaining the Legendre polynomial coefficients by recursion computation using the relation: $(2j+1)zP_j=(j+1)P_{j+1}+jP_{j-1}$; here z is the argument of the polynomial. To simplify the computation of a_n and b_n, it is better to use the formulae:

$$a_n=\frac{\left(\frac{A_n(y)}{m}+\frac{n}{x}\right)\mathrm{Re}\{W_n(x)\}-\mathrm{Re}\{W_{n-1}(x)\}}{\left(\frac{A_n(y)}{m}+\frac{n}{x}\right)W_n(x)-W_{n-1}(x)}$$

$$b_n=\frac{\left(mA_n(y)+\frac{n}{x}\right)\mathrm{Re}\{W_n(x)\}-\mathrm{Re}\{W_{n-1}(x)\}}{\left(mA_n(y)+\frac{n}{x}\right)W_n(x)-W_{n-1}(x)} \qquad (5.20)$$

where $W_n(x)$ is a function calculated recursively using: $W_n(x)=\frac{2n-1}{x}W_{n-1}(x)-W_{n-2}(x)$ with $W_{-1}(x)=e^{-ix}$ and $W_0(x)=e^{i(\pi/2-x)}$ and where $A_n(y)$ is a function of $y = mx$ recursively computed from: $A_n(y)=-\frac{n}{y}+\left(\frac{n}{y}-A_{n-1}(y)\right)^{-1}$ and $A_0(y)=\frac{\sin\nu x\cos\nu x+i\sinh\kappa x\cosh\kappa x}{\sin^2\nu x+\sinh^2\kappa x}$.

All recursions must be computed in double precision in order to avoid unacceptable results when the arguments are large.

Cross-sections:

By appropriate integration the different cross-sections can be easily found:

- scattering cross-section: $$\sigma_s=\frac{2\pi}{k_0^2}\sum_{n=1}^{\infty}(2n+1)\left(|a_n|^2+|b_n|^2\right) \qquad (5.21)$$

- extinction cross-section: $$\sigma_{ext}=\frac{2\pi}{k_0^2}\sum_{n=1}^{\infty}(2n+1)\mathrm{Re}\{a_n+b_n\} \qquad (5.22)$$

- back-scattering cross-section: $$\sigma_b=\frac{2\pi}{k_0^2}\left|\sum_{n=1}^{\infty}(-1)^n(2n+1)(a_n-b_n)\right|^2 \qquad (5.23)$$

5.2.1.1.2 Spheroidal scatterers

The geometry of the spheroidal scatterers allows a similar way for solving the equation of Maxwell. The mathematical development is nevertheless more complicated than in the case of a spherical scatterer. The main difficulty arises from the fact that the eigen functions are dependent upon the refractive index and this precludes an easy implementation of this technique. In [Asano and Sato, 1980] a detailed exposition can be found.

5.2.1.2 Approximate solutions

5.2.1.2.1 Rayleigh-Gans approximation

The first order approximation of the integral equation (5.9) consists in replacing the field *E(r')* by the incident field $E_i(r')$ in the integral. This is known as the Rayleigh-Gans or Rayleigh-Debye, or yet the Born approximation. Clearly this approximation will be valid only if the scatterer is a "weak" scatterer. In order to establish the limiting conditions one generally proceeds by iteration; at each step the internal field is replaced by the field found at the previous step. It is not straightforward to prove the convergence of such a procedure. Nevertheless, if *L* is a typical dimension of the scatterer, it has been proven that two conditions must be fulfilled for this condition to apply: $|\varepsilon_r - 1| k_0 L \ll 1$ and $|\varepsilon_r - 1| = |m^2 - 1| \ll 1$.

For water drops and microwaves $|\varepsilon_r - 1| = |m^2 - 1|$ has a value of around 25. Therefore, this approximation cannot be used for hydrometeors and current meteorological radar frequencies.

5.2.1.2.2 Rayleigh scattering

If the typical length of a scatterer is smaller than the wavelength $(k_0 L << 1)$, the incident field within and near the scatterer behaves almost as an electrostatic field. The idea of this approximation is thus to take the electrostatic solution inside the scatterer.

The electrostatic solution is however dependent upon the shape of the scatterer; this point is often forgotten. We will give two examples.

Rayleigh scattering for a spherical particle

In this case the electrostatic solution is well known (e.g. Stratton, [1941]); the field inside the sphere becomes :

$$E(r') = \frac{3}{2 + \varepsilon_r} E_i(r') \tag{5.24}$$

Following equations (5.9) and (5.10) the scattering amplitude reads:

$$S(k_s, k_i) = \left(\bar{I} - \frac{k_s k_s}{k_0^2} \right) e_i \frac{i k_0^3}{4\pi} \int_V e^{i(k_s - k_i) r} \frac{3(\varepsilon_r - 1)}{\varepsilon_r + 2} dV \tag{5.25}$$

For an homogeneous sphere of radius *a* one finds easily:

$$S(k_s, k_i) = \left(\bar{I} - \frac{k_s k_s}{k_0^2} \right) e_i \frac{i k_0^3}{k_1^3} \left(\sin(k_1 a) - k_1 a \cos(k_1 a) \right) \frac{3(\varepsilon_r - 1)}{\varepsilon_r + 2} \tag{5.26}$$

where $k_1 = |k_s - k_i|$.

The limit $a \to 0$ allows us to write:

$$S(k_s, k_i) = \left(\bar{I} - \frac{k_s k_s}{k_0^2} \right) e_i \frac{i k_0^3}{4\pi} V \frac{3(\varepsilon_r - 1)}{\varepsilon_r + 2} \tag{5.27}$$

where V is the volume of the scatterer. As previously mentioned $\left(\bar{I} - \frac{k_s k_s}{k_0^2}\right) e_i$ is the component of e_I perpendicular to k_S. If ξ is the angle between e_I and k_S then:

$$S = i \sin\xi \frac{k_0^3}{4\pi} V \frac{3(\varepsilon_r - 1)}{\varepsilon_r + 2} \tag{5.28}$$

The pattern of the scattered field is thus a torus, identical to that of a dipole aligned with e_I. The back-scattering cross-section is:

$$\sigma_b = \frac{k_0^4}{4\pi} V^2 \left| \frac{3(m^2 - 1)}{m^2 + 2} \right|^2 \tag{5.29}$$

where we have used the refractive index inside the scatterer $m = \sqrt{\varepsilon_r}$.

The absorption cross-section is obtained from equation (5.18):

$$\sigma_a = k_0 \varepsilon_r'' V \left| \frac{3}{m^2 + 2} \right|^2 \tag{5.30}$$

The scattering cross-section is obtained by integrating equation (5.28) over the whole space:

$$\sigma_s = \frac{3k_0^4}{2\pi} V^2 \left| \frac{(\varepsilon_r - 1)}{\varepsilon_r + 2} \right|^2 \tag{5.31}$$

and for a sphere

$$\sigma_s = \frac{128\pi^5 a^6}{3\lambda^4} \left| \frac{\varepsilon_r - 1}{\varepsilon_r + 2} \right|^2 \tag{5.32}$$

Equations (5.29), (5.30), (5.31) and (5.32) are the classical formulae of Rayleigh's approximation. Let us recall again that, except for (5.30), they can be applied only for spheres.

More generally, the question of validity of the Rayleigh scattering is not fully resolved. By comparison with Mie results, Kerker [1969] showed that the error is less than 4% for $a = 0.05\lambda$. This is indeed a poor range of validity. Nevertheless, at 5 GHz, it means a = 3mm which includes most of the hydrometeors; however there are significant resonance effects at 6 GHz for a = 2.9 mm < 0.06 λ. At 10 GHz, a = 1.5 mm which is too restrictive for raindrops especially in stormy events. In general, Rayleigh scattering may be applied when $k_0 a |\varepsilon_r|^{1/2} \le 0.1$.

Rayleigh scattering for a spheroidal particle

As hydrometeors generally have an axis of symmetry, we restrict ourselves to the spheroidal case (the generalisation for ellipsoids is straightforward but cumbersome).

The axis Δ of symmetry is defined by angles β, α (see § 5.1.2.1). The frame of reference (O, x, y, z) can be transformed into a frame of reference (O, x', y', z') where the equation of the spheroid $x'^2/a^2 + y'^2/a^2 + z'^2/c^2 = 1$ is by a simple rotation determined by the matrix:

$$\overline{R} = \begin{vmatrix} \cos\beta\cos\alpha & \cos\beta\sin\alpha & -\sin\beta \\ -\sin\alpha & \cos\alpha & 0 \\ \sin\beta\cos\alpha & \sin\beta\sin\alpha & \cos\beta \end{vmatrix} \tag{5.33}$$

In the coordinate system (O, x',y',z'), the incident E_i field becomes $E'_i = \overline{R}E_i$

The electrostatic solution inside the scatterer is then [Stratton, 1941]:

$$E' = \begin{vmatrix} \dfrac{1}{1+(\varepsilon_r - 1)L_1} & 0 & 0 \\ 0 & \dfrac{1}{1+(\varepsilon_r - 1)L_1} & 0 \\ 0 & 0 & \dfrac{1}{1+(\varepsilon_r - 1)L_2} \end{vmatrix} .E'_i = \overline{C}.E'_i \tag{5.34}$$

In the original frame of reference, one therefore has: $E = \overline{R}^{-1}.\overline{C}.\overline{R}.E_i$

As the Rayleigh approximation can be used only for very small scatterers we can take $e^{i(k_s - k_i).r'} \approx 1$ in equation (5.9), and the scattering amplitude becomes:

$$S = \frac{i k_0^3}{4\pi}(\varepsilon_r - 1)V\left(\overline{I} - \frac{k_s k_s}{k_0^2}\right).\overline{R}^{-1}.\overline{C}.\overline{R}.E_i \tag{5.35}$$

with $V = (4/3)\pi a^2 c$.

Clearly, the scattering properties depend on the polarization of the incident wave. In particular one can compute after some manipulations,

Wave polarized along $Ox, e_i = (1,0,0)$:

$$\sigma_{bx} = \frac{k_0^4}{4\pi}V^2|\varepsilon_r - 1|^2\left[\left|\cos^2\alpha\left(p\cos^2\beta + q\sin^2\beta\right) + p\sin^2\alpha\right|^2 + |q-p|^2\sin^2\alpha\cos^2\alpha\sin^4\beta\right] \tag{5.36}$$

Wave polarized along $Oy, e_i = (0,1,0)$:

$$\sigma_{by} = \frac{k_0^4}{4\pi}V^2|\varepsilon_r - 1|^2\left[\left|\sin^2\alpha\left(p\cos^2\beta + q\sin^2\beta\right) + p\cos^2\alpha\right|^2 + |q-p|^2\sin^2\alpha\cos^2\alpha\sin^4\beta\right] \tag{5.37}$$

with $p=1/(1+(\varepsilon_r-1)L_1)$ and $q=1/(1+(\varepsilon_r-1)L_2)$ where L_1 and L_2 are given by [Stratton, 1941]:

prolate spheroid a < c with $e^2=1-(a/c)^2$

$$L_2=\frac{1-e^2}{e^2}\left(-1+\frac{1}{2e}\ln\frac{1+e}{1-e}\right)\text{and } L_1=\frac{1}{2}(1-L_2)$$

oblate spheroid a > c with $u^2=(a/c)^2-1$

$$L_2=\frac{1+u^2}{u^2}\left(1-\frac{1}{u}\text{arctg}u\right)\text{and } L_1=\frac{1}{2}(1-L_2)$$

In the case of a sphere $a=c$ thus $L_1=L_2=1/3$ and $p=q=3/(\varepsilon_r+2)$ and we obtain the previous results.

Note that even if the backscatter depends on the shape of the scatterer, the absorption cross section (equation (5.30)) which is bigger than the scattering section for the frequencies of interest here, has a second order dependence upon shape.

5.2.2 Approximate numerical methods

As the exact methods apply only to few specific cases, several numerical methods have been developed to deal with realistic scatterers such as large hydrometeors. The limited volume of this chapter prevents us to present all of them. We thus concentrate on the four more frequently used ones.

5.2.2.1 Point-matching method

In principle this technique applies to an arbitrary homogeneous scatterer with regular boundary geometry. This method is in fact an extension of Mie's theory based upon the expansion of the fields in terms of eigenfunctions of the Helmoltz equation vector [Oguchi, 1960] $\nabla^2 A+k^2 A=0$ for k = constant.

Contrary to the case of a sphere it is impossible to fit exactly the boundary conditions when the surface of the scatterer is not a coordinate surface. The basic idea is thus to restrict the expansion to a finite number of terms and to fulfil the boundary conditions at a sufficient number of points on the boundary surface in order to determine the unknown coefficients of the expansion.

It is beyond the scope of this document to give a detailed description. We shall just present an overview following Oguchi [1973].

Assuming the origin of coordinates to be inside the scatterer, the basis functions of the Helmoltz equation vector are, in spherical coordinates (r, β, α),

$$\begin{matrix} m_{emn} \\ m_{omn} \end{matrix} = \begin{pmatrix} - \\ + \end{pmatrix} \frac{m}{\sin\theta} z_n(kr) P_n^m(\cos\beta) \begin{matrix} \sin \\ \cos \end{matrix} m\alpha\, e_\beta - z_n(kr)\frac{\partial P_n^m}{\partial B} \begin{matrix} \cos \\ \sin \end{matrix} m\alpha\; e_\alpha$$

$$\begin{matrix} n_{emn} \\ n_{omn} \end{matrix} = \frac{n(n+1)}{kr} z_n(kr) P_n^m(\cos\beta) \begin{matrix} \cos \\ \sin \end{matrix} m\alpha\, e_r + \frac{1}{kr}\frac{\partial}{\partial r}\left[rz_n(kr)\right] P_n^m(\cos\beta) \begin{matrix} \cos \\ \sin \end{matrix} m\alpha\, e_\beta \qquad (5.38)$$

$$\begin{pmatrix} - \\ + \end{pmatrix} \frac{m}{kr\sin\theta}\frac{\partial}{\partial r}[rz_n(kr)] P_n^m(\cos\beta) \begin{matrix} \sin \\ \cos \end{matrix} m\alpha e_\alpha$$

where P_n^m are the associated Legendre functions ($m \le n$), $z_n\,(kr)$ a spherical Bessel function and k the wave number.

The choice of Bessel functions depends on the desired behaviour of the solution near the origin or at infinity. Close to the origin, the spherical Bessel of the first kind has to be preferred and at infinity one chooses a spherical Bessel of the fourth kind (Hankel function). m is called the mode.

Representing the total field inside the scatterer by E_- and the scattered field as usual by E_s, the, following expansion holds,

$$E_- = E_i \sum_{n=1}^{\infty} \sum_{m \le n} i^n \frac{2n+1}{n(n+1)} \left(a_{mn} m_{omn}^{(1)} - i b_{mn} n_{emn}^{(1)} \right) \tag{5.39}$$

$$E_s = E_i \sum_{n=1}^{\infty} \sum_{m \le n} i^n \frac{2n+1}{n(n+1)} \left(c_{mn} m_{omn}^{(3)} - i d_{mn} n_{emn}^{(3)} \right)$$

and similar equations are used for the magnetic fields and include the same unknown coefficients. These coefficients are determined by the boundary conditions on the surface of the smooth scatterer.

$$n \times (E_i + E_s - E_-) = 0 \tag{5.40}$$
$$n \times (H_i + H_s - H_-) = 0$$

where n is the outward normal at the surface of the scatterer.

These boundary conditions lead to four scalar conditions owing to the fact that the tangential components of the fields have two degrees of freedom. Multiplying these equations by $\cos\alpha$ or $\sin\alpha$ and integrating over the range $(0, 2\pi)$ we obtain four expressions like,

$$\sum_{n=m}^{\infty} h_n C_n(\beta) = D(\beta) \tag{5.41}$$

h_n represents the unknown coefficients and C_n and D involve spherical Bessel functions, associated Legendre functions and their derivatives. If the sum is truncated to index N , the number of unknown coefficients are $4(N-m+1)$ and can be determined by using $(N-m+1)$ points $\beta_1, \beta_2, \ldots \beta_{N-m+1}$ regularly spaced over $(0, \pi)$ in order to obtain an algebraic system of the first order.

This procedure should be repeated for every mode from 0 to M. If the scatterers are axisymmetric the computation can be simplified by considering a Fourier series in the plane of the azimuth angle.

The method presented above uses a number of fitting points equal to the number of unknown coefficients and is known as the collocation method. For strongly distorted scatterers a significant improvement is obtained by using least-square fitting on more points than strictly needed [Morrison and Cross, 1974]. For large raindrops, this technique is highly recommended.

The idea of expanding the scattered wave of a non-spherical scatterer as vector spherical waves functions is questionable [Van der Berg and Fokkema, 1979], therefore the point-matching method seems limited to moderately distorted raindrops. These techniques apply, in any case, only to homogeneous scatterers excluding hydrometeors like wet snow.

The scattering amplitudes calculated with this method were used to derive the parameters (i.e. k and α) in Recommendation ITU-R P.838.

5.2.2.2 The T-matrix method

This method also named EBCM (Extended Boundary Condition Method) uses also an expansion in terms of vector spherical functions but the unknown coefficients are determined by using the integral representation of fields (see § 5.1.1). The paper by Barber and Yeh [1975] gives a clear and complete description of this method. Two basic principles underlie this method:

– the "equivalent currents" $n \times E$ and $n \times H$ which produce a null field inside the scatterer are determined. In some manner, the classical surface boundary conditions become volume conditions (the null field), that explains the expression "extended boundary conditions".

– due to the analytical continuity of the field inside the scatterer it is sufficient to impose the null field in any portion of the scatterer, generally chosen as a sphere inscribed within the particle.

The procedure is then

1) to expand E_i and H_i into spherical harmonics. Symbolically,

$$E_i = \sum_n a_n \Phi_n^{(1)}(r, \beta, \alpha) \tag{5.42}$$

2) far from the particle to also expand the scattered fields in spherical harmonics

$$E_s = \sum_n b_n \Phi_n^{(3)}(r, \beta, \alpha) \tag{5.43}$$

Truncating the two previous expansions at a given order *N*, the transition matrix or T-matrix is defined by *[b] = T[a]*, and once it is known the scattering problem is solved.

To determine it we proceed as follows:

3) expand the dyadic $\overline{G}$ in spherical harmonics (once the appropriate determination close to the origin has been chosen). The orthogonal properties of spherical harmonics allow one to relate linearly the coefficients a_n to some surface integrals of the equivalent currents,

4) a similar procedure applied outside the scatterer leads to linear relations between the equivalent currents and coefficients b_n,

5) if we eliminate the equivalent currents between the two previous linear systems, we readily obtain the T-matrix which relates a_n to b_n.

The number *N* (order where the expansion is truncated) that is required to obtain a satisfactory solution depends on the shape, size and refraction index of the scatterer.

This method is easier to implement than the point-matching one. It applies to more deformed shapes and can be extended to multi-layered scatterers. Its convergence is however poor for large particles where the surface integrals involved are difficult to compute.

5.2.2.3 The Fredholm - Integral - Method (FIM)

The starting point of the method is the integral equation (5.4) and for a plane incident field we have shown that (5.4) becomes (5.9). The internal field $E_i(r')$ must be determined by a Fredholm integral equation of the second kind. The difficulty arises from the singularity of the Green function near the origin which prevents the use of the classical solution technique. To overcome this difficulty Holt *et*

al. [1978] have suggested the use of a Fourier transform that leads to a new integral equation, the kernel of which is no longer singular.

Rewriting the integral equation as:

$$E(r) = E_i(r) + \int_V \overline{G}(r - r')\gamma(r')E(r')\,dr' \tag{5.44}$$

Multiplying (5.44) by $\gamma(r)e^{ik_1 \cdot r}$ and integrating over the entire volume of the scatterer one gets (discarding the amplitude E_i),

$$\int_V E(r)e^{ik_1 \cdot r}\gamma(r)\,dr = e_i \int_V e^{i(k_1 - k_i)\cdot r}\gamma(r)\,dr + \int_V \int_V e^{ik_1 \cdot r}\gamma(r)\overline{G}(r - r')\gamma(r')E(r')\,dr\,dr' \tag{5.45}$$

As we only need $E\_(r)$ in order to calculate the scattering (5.44), we may assume that *E(r)* is Fourier-transformable and,

$$E(r) = \int C(k_2)e^{ik_2 \cdot r}\,dk_2 \tag{5.46}$$

Substituting (5.46) in (5.45) gives:

$$\int \overline{K}(k_1, k_2).C(k_2)\,dk_2 = e_i U(k_1, k_2) \tag{5.47}$$

where

$$U(k_1, k_2) = \int \gamma(r)e^{i(k_1 - k_2)\cdot r}\,dr \tag{5.48}$$

and

$$\overline{K}(k_1, k_2) = \overline{I}U(k_1, k_2) - \int\int e^{ik_1 \cdot r}\overline{G}(r - r')\gamma(r')e^{ik_2 \cdot r'}\,dr\,dr' \tag{5.49}$$

$\overline{K}$ is a non-singular kernel since the singularity is removed by analytic integration. Resolution of (5.47) is performed by evaluating the integrals by numerical quadrature. It is equivalent to reducing (5.46) to a finite sum:

$$E(r) = \sum_{j=1}^{n} C_j e^{ik_j \cdot r} \tag{5.50}$$

Therefore, considering equation (5.47) for *n* values of $k_1(k_{1j}, j = 1, n)$ leads to matrix equations which can be easily solved. Holt *et al.* [1978] have shown that if the vectors k_{2j} and k_{1j} are equal, the solution obeys the variational principle of Schwinger and that the process is numerically very stable.

The Fredholm integral method is certainly the most generally applicable numerical method. It applies to any kind of scatterer for which the analytical integration can be performed. General ellipsoids [Holt *et al.*, 1976], particles with edges [Shepherd and Holt, 1983] and non-homogeneous particles [Hardaker and Holt, 1994] have been treated. However, it is difficult to implement and slower than the other methods for homogeneous particles with shapes close to spheres. Its convergence can be checked during calculations without starting all over again. Furthermore a change in refractive index only requires part of the calculation to be repeated.

5.2.2.4 Finite elements methods

The big advantage of these methods is their capability to deal with various irregular shapes of scatterers. In particular we will mention:

5.2.2.4.1 Unimoment method

Sketch of method [Morgan and Mei, 1979, Morgan 1980]: The basis of this method is the coupled azimuthal potential (CAP) formulation of the electromagnetic field, which is valid in generally lossy isotropic non-homogeneous rotationally symmetric media. Electromagnetic fields in such regions can be represented, using the CAP formulation, in terms of two continuous potentials which satisfy a self-adjoint system of partial differential equations, or, equivalently, a variational criterion. Using a variational finite-element algorithm in conjunction with a tri-regional unimoment method, scattering solutions may be obtained for each of the multiple incident fields impinging upon an arbitrarily shaped non-homogeneous penetrable body of revolution.

Application: Besides some other applications, the unimoment method has been used to calculate scattering amplitudes of axi-symmetric raindrops [Fang and Lee, 1978; Morgan 1980]. Drop shapes are either oblate spheroidal or have been taken from Pruppacher and Pitter [1971]; some comparisons with results from different methods are given by Morgan [1980].

5.2.2.4.2 Boundary element method

Sketch of method [Schlemmer *et a1.*, 1993]: The basis of this method is the Green function for lossy media and the surface integral equation formulation of electromagnetic scattering. The domain of integration, i.e. the surface of the dielectric, is subdivided into finite elements in order to perform the integration numerically. This discretisation of the scatterer may be done using eight-node boundary elements. Finally, the integral equation is transformed into a linear system of equations, which can be solved by Gaussian elimination.

Application: Besides various other applications, the Boundary Element Method has been applied to calculate scattering from a sphere, results have been cross-checked against Mie-series solutions [Schlemmer *et al.*, 1993].

5.3 Numerical implementation

The numerical implementation of most of the algorithms described here is available in [Poiares Baptista, 1994]. As a guideline, Table 5.1 shows a short description of the different methods with some useful considerations.

TABLE 5.1

Methods of calculating single particle scattering

Method of calculation	**Particular advantages**	**Constraints**	**Computational requirements**
Rayleigh	Simple analytical	Very small particles $0 < ka < 0.3$	Trivial
Mie	Exact	Homogeneous spheres	Modest
Extended Mie for multi-layered spheres	Exact	Only spheres	Modest
Spheroidal expansion	Exact	homogeneous particles	Significant mass memory Calculations repeated
Collocation Point-matching	Irregular shapes	Convergence tricky. Homogeneous scatterers	Significant mass memory
T- matrix	Irregular, multi-layered particles	Convergence poor and difficult to check	Significant mass memory
Fredholm integral	Highly distorted, non-homogeneous scatterers Stable algorithm	Difficult to implement Slow	Significant mass memory

REFERENCES

ASANO, S. and SATO, M. [1980] Light scattering properties of spheroidal particles. Applied Optics. 19, pp. 962-974.

BARBER, P. and YEH, C. [1975] Scattering of Electromagnetic Waves by Arbitrarily shaped Dielectric Bodies. Applied Optics, 14, 2, pp. 2864-2872.

BORN, and WOLF. [1980] Principles of optics. Ed. Pergamon.

FANG, D.J. and LEE, F.J. [1978] Tabulations of raindrop induced forward and backward scattering amplitudes. COMSAT Tech.Rev.,8(2), pp. 455-486.

HARDAKER, P.J. and HOLT, A.R. [1994] Electromagnetic Scattering from Luneberg lens. J.Electromagnetic Waves and Applications, 8, pp. 391-405.

HOLT, A.R., UZUNOGLU, N.K. and EVANS, B.G. [1978] An Integral Equation Solution to the Scattering of Electromagnetic Radiation by Dielectric Spheroids and Ellipsoids. IEEE-Trans. Ant. and Prop., AP-26.5, pp. 706-712.

HOLT, A.R., UZUNOGLU, N. and EVANS, B.G. [1976] An Integral Equation Solution to the Scattering of Electromagnetic Radiation by Dielectric Spheroids and Ellipsoids. Proc. IEEE/AP-S International Symposium, Amherst, pp. 415-428.

KERKER, M. [1969] The Scattering of Light. Ed. Academic Press.

LEVINE, H. and SCHWINGER, J. [1951] On the theory of electromagnetic wave diffraction by an aperture in an infinite plane conducting screen, in "'The theory of Electromagnetic Waves", Ed. Dover Publications, pp. 355-391.

MIE, G. [1908] *Beiträge zur Optik trüber Medien, speziell kolloidaler Metallösungen*. Ann.Phys.Leipzig, 25, pp.377-445.

MORGAN, M.A. and MEI, K.K. [1979] Finite Element Computation of Scattering by Inhomogeneous Penetrable Bodies of Revolution. IEEE Trans. on Ant. and Prop., 27, 2, pp.202-214.

MORGAN, M.A. [1980] Finite Element Computation of Microwave Scattering by Raindrops. Radio Sci., 15, 6, pp. 1109-1119.

MORRISON, J.A. and CROSS, M.J. [1974] Scattering of a plane electromagnetic wave by axi-symmetric raindrops. B.S.T.J. 15, 6, pp. 955-1019.

MORSE, P.M. and FESHBACH, H. [1953] Methods of Theoretical Physics. Ed. McGraw-Hill.

OGUCHI, T. [1973] Attenuation and Phase Rotation of Radio Waves due to Rain : Calculations at 19.3 and 34.8 GHz. Radio Sci., 8, 1, pp. 31-38.

OGUCHI, T. [1960] Attenuation of Electromagnetic Wave due to Rain with Distorted Raindrops. J. Radio Res. Lab.,7,33, pp. 467-485.

POIARES BAPTISTA, J.P.V. (Editor), [1994] OPEX Reference Book on Radar; Second Workshop of the OLYMPUS Propagation Experimenters. European Space Agency WPP-083, Noordwijk. 8-10 November 1994.

PRUPPACHER, H.R.and PITTER, R.L. [1971] A Semi-Empirical Determination of the Shape of Cloud and Rain Drops. J. Atmos. Sci., 28, 1, pp. 86-94.

SCHLEMMER, E., RUCKER, W.M. and RICHTER, K.R. [1993] Boundary Element Computations of 3D Transient Scattering, from Lossy Dielectric Objects. IEEE Trans. on Magn., 29, 2.

SHEPHERD, J.W. and HOLT, A.R. [1983] The Scattering of Electromagnetic radiation from dielectric cylinders. J.Phys.A. (Math.gen.), 16, pp. 651-662.

STRATTON, J.A. [1941] Electromagnetic Theor. Ed. McGraw-Hill.

VAN de HULST, H.C. [1981] Light scattering by small particles. Dover Publ., NY.

VAN der BERG, P.M. and FOKKEMA, J.T. [1979] The Rayleigh Hypothesis in the Theory of Diffraction by a Cylindrical Obstacle. IEEE Trans. Ant. and Prop., AP-27, 5, pp. 577-583.

CHAPTER 6

Attenuation and dispersion by atmospheric gases

Molecular absorption experienced by radiowaves propagating through the Earth's atmosphere at centimetric and millimetric wavelengths is primarily due to oxygen (O_2) and water vapour. Nitrogen (N_2) - the most abundant gas (78% by volume of air) - has no microwave lines due to lack of permanent dipole moment but exhibits weak non-resonant absorption due to collision-induced dipole moments. This absorption becomes significant above 100 GHz in very dry conditions. Trace gases (e.g. CO, CO_2, N_2O and O_3) exhibit resonant absorption that can be significant in very dry conditions, especially for frequencies higher than about 70 GHz [Waters, 1976]. Some applications like atmospheric remote sensing and navigation require knowledge of the contribution from these minor constituents.

Figure 6.1 shows an example of the specific attenuation (dB/km) due to gases at sea level, as a function of frequency from 1 GHz to 350 GHz. The mean annual global reference atmosphere described in Recommendation ITU-R P. 835-5 is used (P = 1013.25 hPa, T = 288.15 K, ρ = 7.5 g/m^3 at the surface). Figure 6.1 also shows the specific attenuation due to light, medium and intense rain and to a fog dense enough to reduce the visual range to 300 m.

This chapter provides background and supplementary information on the attenuation of radio waves due to atmospheric gases described in Recommendation ITU-R P.676-9. The impact of dispersion due to gases is also examined.

FIGURE 6.1

Specific attenuation due to atmospheric gases (molecular oxygen and water vapour), rain and fog

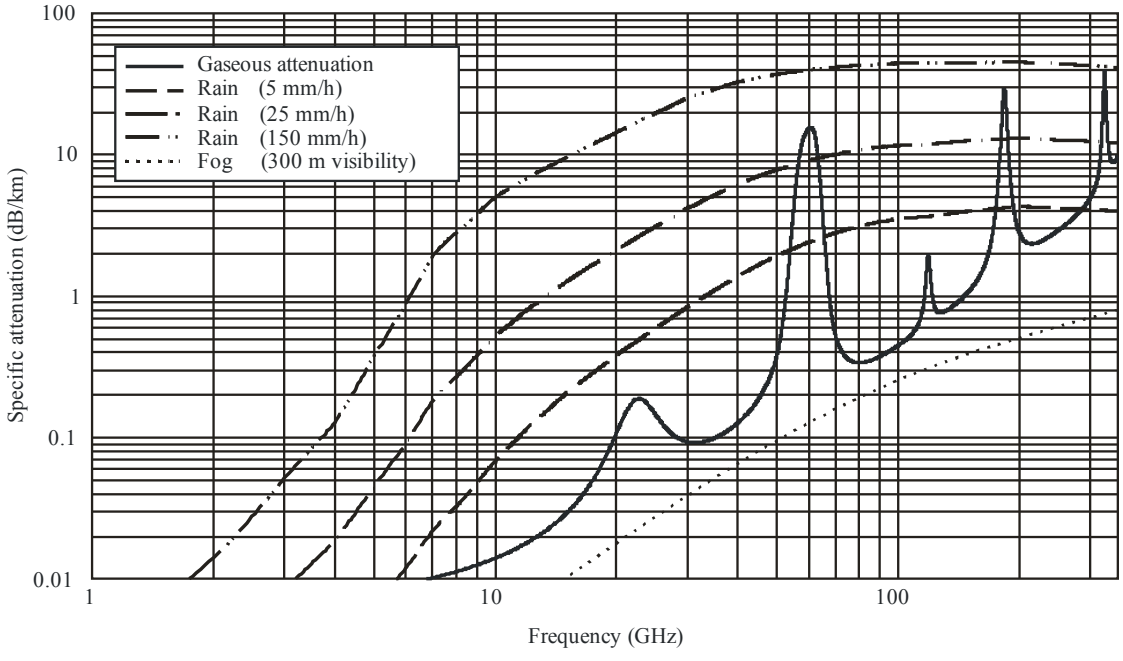

Radio-Meteo. 06-01

6.1 Physical background of gaseous absorption

When electromagnetic radiation interacts with a gaseous polar molecule, i.e. one with a dipole moment, energy from the incident radiation is transferred to the molecule, and the molecule is excited to a higher energy level. The molecule in its excited state may then decay to a state with a lower energy level by emitting energy in the form of an electromagnetic wave. The energy levels of gaseous molecules are well defined and discrete, and thus the related interactions occur at very specific frequencies, giving rise to spectral lines. Environmental factors such as temperature and especially pressure lead to a broadening of these lines to form bands of frequencies over which energy is absorbed, and hence signals are attenuated.

A molecule is a collection of two or more atoms bound together that can vibrate about their equilibrium positions. The molecule as a whole can also rotate. Moreover electrons have both potential and kinetic energies. Thus the total energy of an isolated gaseous molecule may be expressed to a good approximation in terms of components related to the different modes of excitation and motion:

$$E = E_e + E_v + E_r + E_t \tag{6.1}$$

where E_e, E_v, E_r and E_t are the electronic, vibrational and rotational energies, respectively, and E_t is the translational (position and velocity of the centre of mass of the molecule), or kinetic energy. The first three terms in equation (6.1) are quantized and take only discrete values, characterized by one or more quantum numbers which define the energy state or quantum state. Strictly speaking, translational energy E_t is also quantized but the level separation is so small that it cannot be observed [Bohren and Clothiaux, 2006]. Moreover changes in translational energy have a negligible effect on molecular energy levels and can be disregarded in this discussion. Since rotation and vibration are not completely decoupled in a mechanical system (e.g. for two mass points connected by a spring), the decomposition of the total energy of an isolated molecule into its various forms as per equation (6.1) is only approximate [Bohren and Clothiaux, 2006].

Electronic energy levels result from the transfer of electrons between different orbits and correspond to the highest energy levels, therefore transitions between electronic energy levels occur typically in the visible and UV regions of the electromagnetic spectrum.

Vibrational energy levels arise from different vibrational modes of the molecule, while rotational energy levels result from the rotation of the molecule around different axes and correspond to the lowest energy levels; transitions between rotational energy levels typically occur in the microwave, millimetric and sub-millimetric regions of the electromagnetic spectrum [Elachi, 1987].

Rotational energy levels depend on the three principal moments of inertia of the molecule, and there are four different types of rotating molecules [Elachi, 1987]:

1) Two of the moments of inertia are equal and the third one is negligible. This is the case of diatomic and linear polyatomic molecules such as O_2 and CO_2, respectively.
2) Spherical top molecules, in which all three moments are equal; this is the case of methane (CH_4).
3) Symmetric top molecules, in which two of the moments are equal; ammonia (NH_3) is an example.
4) Asymmetric top molecules like H_2O and SO_2, in which all three moments of inertia are different.

The interaction between gaseous molecules and the incident electromagnetic field is manifest in the form of absorption or emission, and takes place through the electric or magnetic dipole or quadrupole moment of the molecule. Thus, for a molecule to interact with an electromagnetic field

and hence absorb or emit a photon of frequency *f,* it must possess, at least transiently, a dipole oscillating at that frequency. For emission or absorption, this dipole is expressed in terms of quantum mechanics by the dipole moment.

Interactions resulting in transitions of the dipole moment can differ widely in strength. Electric dipole interactions are stronger than magnetic dipole interactions by a factor of ~10^5, while electric dipole interactions are ~10^8 times stronger than electric quadrupole interactions. Electric dipole interactions are thus responsible for the strongest spectral lines, generally known as permitted transitions. Other transitions are loosely termed forbidden. The nature of a transition is specified in terms of the quantum numbers of the upper and lower states, and the relationship between the states is determined by selection rules. When a transition occurs between two energy states, the frequency f of the absorbed or emitted quantum of radiation is given by the Bohr's frequency condition $f = \frac{\Delta E}{h}$, where h is Planck's constant and ΔE is the energy gap between the two energy states involved in the transition.

The most general transitions involve simultaneous changes in electronic, vibrational and rotational energy. The smallest energy transitions generally observed vary considerably between the three types and provide a convenient method by which they are distinguished. Typically, the smallest changes in rotational energy are of the order of 1 cm^{-1} (~ 30 GHz), and thus rotational spectral lines, i.e., those arising from changes in the rotational energy state of the molecule, form part of the microwave to the submillimetric or far infrared spectrum. Vibrational transitions generally involve energy changes greater than 600 cm^{-1} (~ 20 THz). Such transitions never occur alone, but in conjunction with many simultaneous rotational changes, giving rise to groups of spectral lines which constitute vibration-rotation bands, usually in the infrared spectrum. Electronic transitions typically involve energy changes of a few electron volts, and the resulting absorption or emission usually occurs in the visible or ultraviolet regions of the electromagnetic spectrum.

At microwave, millimetric and submillimetric wavelengths, the majority of transitions are purely rotational (with a few exceptions) and modelling of the interaction between radio waves and gaseous molecules is generally straightforward. In the Earth's atmosphere, the predominant molecules which interact with electromagnetic radiation at millimetric and submillimetric wavelengths are oxygen and water vapour. Water vapour is an asymmetric top molecule with a permanent electric dipole moment, and possesses a complicated spectrum with transitions between rotational energy levels based on each of its three different moments of inertia. The majority of its spectral lines occur in the submillimetric and infrared regions of the spectrum, although the lowest frequency transition ($6_{-5} \leftarrow 5_{-1}$, involving rotational levels with energies near 500 cm^{-1} or a frequency of ~ 15 THz) is at 22.235 GHz. Figure 6.2 shows the position and relative strengths of water-vapour spectral lines at frequencies up to 1000 GHz.

On the one hand, absorption due to water vapour at microwave frequencies results from the interaction between the electric field and the rotating electric dipole of the molecule. In most molecules with an even number of electrons, the electron spins pair together to cancel out magnetic effects, resulting in only electric dipole moments. On the other hand, oxygen is an unusual molecule, possessing two electrons which are not paired, giving rise to a permanent magnetic dipole moment. It is the interaction of the magnetic field component of the incident electromagnetic radiation with this permanent magnetic dipole moment that forms the absorption mechanism. The oxygen molecule is paramagnetic with an electronic $^3\Sigma_1$ ground state having two unpaired parallel electron spins. Changes in the orientation of these spins produce hyperfine or "spin-flip" transitions, yielding a band of spin-rotation spectral lines near 60 GHz together with a single isolated line at 118.75 GHz. Despite the fact that magnetic dipole moments are considerably smaller than electric dipole moments, some of the transitions are strong due to the large fraction of oxygen molecules in

each state of low rotational angular momentum and because of the high abundance of O_2 in the Earth's atmosphere. Transitions between different rotational levels produce further spectral lines at frequencies of 367 GHz and higher [Gibbins, 1986]. The positions and relative strengths of O_2 spectral lines are shown in Figure 6.2.

FIGURE 6.2

Microwave rotational spectra of water vapour and oxygen molecules

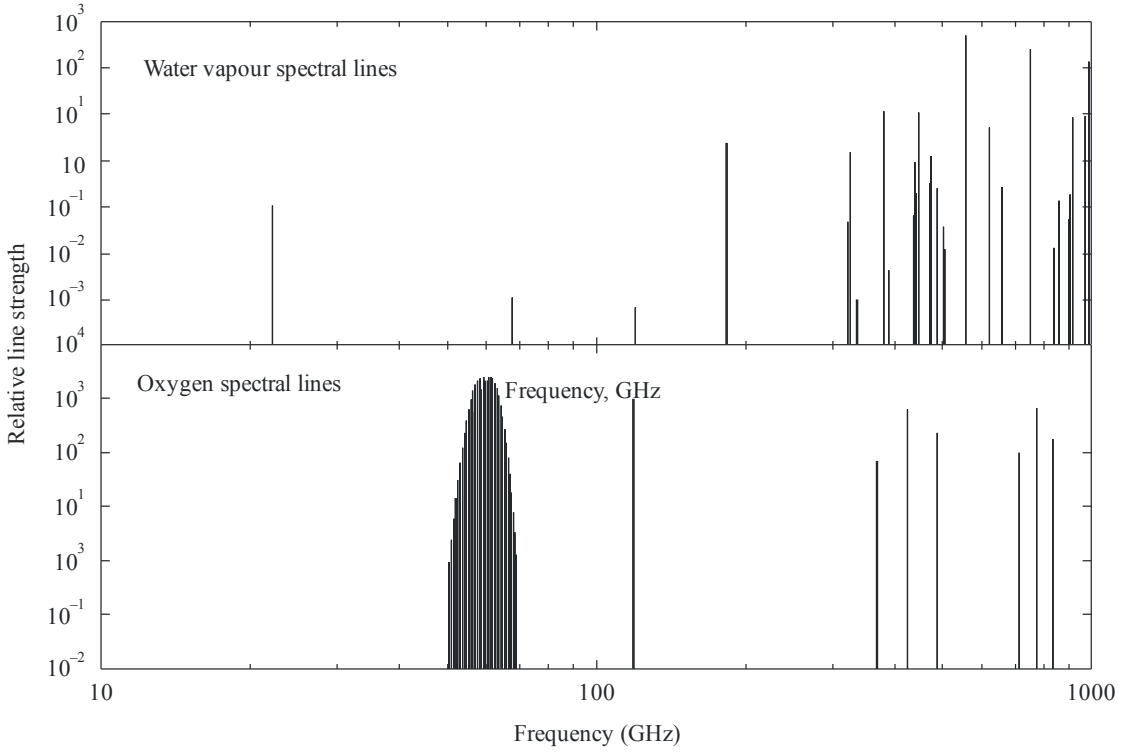

The interaction between absorbing gases and electromagnetic radiation at a frequency f, in the vicinity of a single spectral line, is described by the volume absorption coefficient k_f:

$$k_f = S(x)\, F(f - f_0, x)\, \rho(x) \tag{6.2}$$

where x denotes position, $S(x)$ is the strength of the spectral line, $\rho(x)$ is the density of the absorbing gas and $F(f - f_0, x)$ is a line shape factor describing the perturbations in the energies of the rotational states, which arise from collisions between molecules (the dominant mechanism at sea-level pressures), from the thermal energy of the molecules (important at mesospheric altitudes) and from uncertainties in the molecular positions (generally negligible). The volume absorption coefficient is thus a function of the density of the absorbing gas and the temperature and pressure of the atmosphere, all of which can vary along the transmission path. The volume absorption coefficient $k_f(x_1, x_2)$ between two points x_1 and x_2 along a transmission path resulting from a single absorption line is given by [Papatsoris and Watson, 1993]:

$$K_f(x_1, x_2) = \int_{x_1}^{x_2} S(x)\, F(f - f_0, x)\, \rho(x)\, dx \tag{6.3}$$

and, for a band of spectral lines, by:

$$K_f(x_1, x_2) = \sum_{ij} \int_{x_1}^{x_2} S_{ij}(x)\, F_{ij}(f - f_{ij}, x)\, \rho_j(x)\, dx \tag{6.4}$$

Where:

$S_{ij}(x)$: strength of the i^{th} line of the j^{th} absorbing gas in the path from position x_1 to position x_2

$F_{ij}(f - f_{ij}, x)$: line shape factor

f_{ij}: is the frequency of the line centre

$\rho_j(x)$: density of the absorbing gas.

When spectral lines overlap, their individual contributions to the overall absorption coefficient are customarily assumed to add together linearly, since the spacing of the spectral lines of most atmospheric gases is relatively sparse. However, in the case of the 60-GHz oxygen band, which has many overlapping spectral lines, an interference term is included in order to describe the resulting absorption more accurately [Rosenkranz, 1988].

The strengths and frequencies of spectral lines can be calculated from quantum mechanics and are dependent on temperature, geometrical configuration of the molecule and the population of the lower energy state of the transition. The strength of a spectral line involving a transition from a lower state *l* to an upper state *u* (absorption) is given by [Papatsoris and Watson, 1993]:

$$S_{lu} = \frac{(8\times10^{-36})\pi^3 f_{lu}}{3hc}\left[1 - \exp\left(-\frac{c_2 f_{lu}}{T}\right)\right]\frac{g_l I_a}{Q(T)}\exp\left(-\frac{c_2 E_1}{T}\right)R_{lu} \tag{6.5}$$

where c is the speed of light in a vacuum, f_{lu} is the resonant frequency of the line, E_l is the energy of the lower state of the transition, g_l is the statistical weight describing the nuclear spin degeneracy of the lower level, I_a is the natural isotopic abundance, c_2 is the second radiation constant and R_{lu} is the Einstein transition probability. The rotational partition function $Q(T)$ describing the population of states is given by the following *approximate* expressions valid in the range of temperatures typically found in the atmosphere:

$$Q(T) = \begin{cases} \dfrac{kG}{\sigma hB}T & \text{for linear molecules} \\ \dfrac{G}{\sigma}\sqrt{\dfrac{\pi}{ABC}}\left(\dfrac{kT}{h}\right)^3 & \text{for nonlinear molecules} \end{cases} \tag{6.6}$$

where σ is the order of the symmetry group to which the molecule belongs, h is Planck's constant, k is Boltzmann's constant and A, B and C are the rotational constants of the molecule [Papatsoris and Watson, 1993]. From equation (6.6), it can be seen that for a linear molecule like O_2 the partition function $Q(T)$ is proportional to temperature T, whereas for water vapour (a nonlinear molecule) $Q(T)$ is proportional to $T^{3/2}$. This fact has a direct impact on the temperature dependence of their respective line strengths S_i (see equation (6.10)). The common factor G is given by

$$G = \frac{\prod_i (2I_i + 1)}{\prod_j \left[1 - \exp\left(-\frac{\omega_j hc}{kT}\right)\right]^{d_j}} \tag{6.7}$$

where I_i is the nuclear spin of the i^{th} atom in the molecule and ω_j and d_j are the frequency and degeneracy of the j^{th} normal mode of vibration. The products over i and j in equation (6.7) are taken over all atoms in the molecule and all normal modes of vibration. More information on these partition functions and a more extensive discussion of molecular absorption are given by Herzberg [1945, 1950].

Combining these expressions, the absorption coefficient $k_{lu}(f)$ due to a single absorption line can then be written:

$$k_{lu}(f) = \frac{8\pi^3 Nf\,\mu^2}{3hcQ}\left[\exp\left(-\frac{E_l}{kT}\right) - \exp\left(-\frac{E_u}{kT}\right)\right] g_l |\varphi_{lu}|^2 F(f, f_{lu}) \tag{6.8}$$

where N is the number of absorbing molecules per unit volume, μ is the total dipole moment and φ_{lu} is the transition matrix element. $F(f,f_{lu})$ is the line-shape function, to be described later in this section.

Rewriting equation (6.8) in terms of the specific attenuation coefficient in dB/km, summed over all transitions (spectral lines), with frequency f expressed in GHz, yields the following expression [Liebe, Hufford and Cotton, 1993], given in Annex 1 of Recommendation ITU-R P.676-9:

$$\gamma = 0.1820 f \sum_i S_i F_i(f, f_i) \qquad \text{dB/km} \tag{6.9}$$

with the line strength S_i of the i^{th} transition given by

$$S_i = \begin{cases} a_1 p \left(\frac{300}{T}\right)^3 \exp\left[a_2\left(1 - \frac{300}{T}\right)\right] \times 10^{-7} & \text{for oxygen} \\ b_1 e \left(\frac{300}{T}\right)^{3.5} \exp\left[b_2\left(1 - \frac{300}{T}\right)\right] \times 10^{-1} & \text{for water vapour} \end{cases} \tag{6.10}$$

where p is the pressure of dry air in hPa, e is the water vapour partial pressure in hPa, T is the temperature in Kelvin and the coefficients (a_1, a_2) and (b_1, b_2) are tabulated for each spectral line in Recommendation ITU-R P.676-9. The difference in the exponents of ($300/T$) in equation (6.10) stems from the different temperature dependence of the partition function $Q(T)$ for H_2O (an asymmetric top molecule) and O_2 (a symmetric molecule), as seen in equation (6.6) [Pardo *et al.,* 2001b].

Three mechanisms determine the shape and broadening of spectral lines; collisional interaction between molecules is dominant in the lower atmosphere. Thermal, or Doppler, broadening of microwave lines becomes important only at lower pressures, at altitudes above about 60 km where the molecular collisional frequency is comparable to, or smaller than, the Doppler line width. Natural line broadening, resulting from the finite lifetime of the molecular states due to spontaneous transitions, is ~ 10^{-9} to 10^{-4} Hz for microwave electric dipole transitions (and about 10^4 times smaller for magnetic dipole transitions) and is thus completely negligible.

When molecules collide with each other their energy levels become perturbed, which broadens the spectral distribution of the absorbed or emitted radiation. The effect may be considered classically as a disturbance of the interaction between the molecule and the incident radiation field. The mathematical description of collisional broadening is analogous to the description of the effect of collisions on a classical oscillator, changing its amplitude, phase, orientation or momentum. Under the simplifying assumption that there are no momentum-changing collisions and that all phase changes are equally probable, collisional broadening, more commonly known as pressure broadening, is described by the complex Van Vleck–Weisskopf line shape function, modified by Rosenkranz [1975] to include line overlap effects [Liebe, Hufford and Cotton, 1993]:

$$F(f, f_0) = \frac{f}{f_i}\left[\frac{1 - i\delta}{f_i - f - i\Delta f} - \frac{1 + i\delta}{f_i + f + i\Delta f}\right] \tag{6.11}$$

where the imaginary part gives the absorption spectrum and the real part of this expression yields the spectrum of dispersion (see § 6.5). In this expression, δ is an interference coefficient describing the pressure-induced line interference between overlapping lines, as in the 60-GHz oxygen band; coupling between overlapping lines occurs when collisions between an absorbing molecule and broadening gas molecules induce a change in the population between rotational-vibrational molecular states, and results in a redistribution of spectral intensity within a band. δ is also known as a line-mixing coefficient in the literature [Cadeddu *et al.,* 2007].

The collisional or pressure-broadened line width, Δf, is given by:

$$\Delta f = \Delta f_p = \Delta f_0 \frac{p}{p_0}\left(\frac{T}{T_0}\right)^{-y} \; GHz \tag{6.12}$$

where y varies between 0.5 and 1.0, and Δf_0 is the value of the line width at standard atmospheric conditions, $p = p_0$ and $T = T_0$ [Papatsoris and Watson, 1993]. The magnitudes of y and Δf_0 may also vary for collisions involving different types of molecules, since different intermolecular forces may be involved.

For the molecules of interest in radio wave propagation through the atmosphere, the line width in GHz is given by:

$$\Delta f = \begin{cases} a_3\left[p\left(\frac{300}{T}\right)^{0.8-a_4} + 1.1e\left(\frac{300}{T}\right)\right]\cdot 10^{-4} & \text{for oxygen} \\ b_3\left[p\left(\frac{300}{T}\right)^{b_4} + b_5 e\left(\frac{300}{T}\right)^{b_6}\right] & \text{for water vapour} \end{cases} \tag{6.13}$$

and the interference correction factor, δ, is:

$$\delta = \begin{cases} (p+e)\left(a_5 + a_6\left(\frac{300}{T}\right)\right)\left(\frac{300}{T}\right)^{0.8} .10^{-4} & \text{for oxygen} \\ 0 & \text{for water vapour} \end{cases} \tag{6.14}$$

where coefficients a_i and b_i are given by Liebe, Hufford and Cotton [1993] and in Recommendation ITU-R P.676-9. Note that in equation (6.14), δ for oxygen is now a function of total air pressure whereas it depends only on dry air pressure p in MPM-89 [Liebe, 1989].

At sufficiently low pressures where collisional broadening is small, thermal or Doppler broadening becomes important. The latter is a result of the relative motion between the source of photons and the molecules that absorb them [Bohren and Clothiaux, 2006]. Since molecular velocities have a Gaussian distribution, the Doppler line shape is also Gaussian in form:

$$F(f, f_0) = \frac{1}{\sqrt{\pi}\Delta f_D} \exp\left[-\left(\frac{f - f_0}{\Delta f_D} \right)^2 \right] \tag{6.15}$$

and the Doppler line width is given by:

$$\Delta f_D = 3.58 \cdot 10^{-7} f \sqrt{\frac{T}{M}} \quad (cm^{-1}) \tag{6.16}$$

where M is the molecular weight of the gas [Papatsoris and Watson, 1993].

Figure 6.3 compares typical line widths for collisional and Doppler broadening as a function of altitude, for water-vapour lines at 22 GHz and 998 GHz. Since collisional broadening depends primarily on the number of molecules, i.e. on the pressure, the collisional line width decreases rapidly with altitude, while the Doppler line width, depending on temperature and the frequency of the line, remains fairly constant throughout the atmosphere. At altitudes above about 60 km, where collisional and Doppler broadening become comparable, the resonance frequency in the collisional line shape should be convolved with the Doppler shift probability distribution over all possible Doppler shifts [Liebe, Hufford and Cotton, 1993]. This convolution is known as the Voigt profile. As a simplification, however, it generally suffices to approximate the half width using the following expression:

$$\Delta f = \sqrt{\Delta f_p^2 + \Delta f_D^2} \tag{6.17}$$

using equations (6.12) and (6.16).

FIGURE 6.3

Half-widths due to pressure broadening and Doppler broadening for two water-vapour spectral lines at 22 GHz and 998 GHz

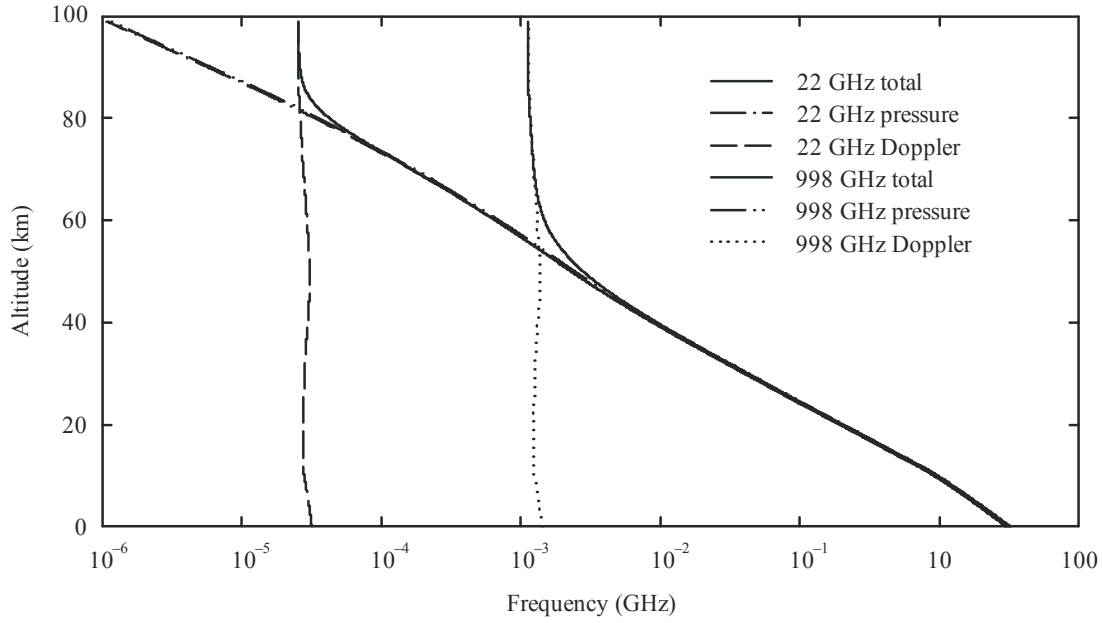

Radio-Meteo. 06-03

6.2 Calculation of gaseous attenuation through the Earth's atmosphere

The calculation of specific attenuation γ (dB/km) using the procedure in Annex 1 of Recommendation ITU-R P.676-9 is based on the line-by-line MPM-93 model of Liebe, Hufford and Cotton [1993]. It requires the summation of contributions from 44 oxygen absorption lines, 34 water-vapour absorption lines, plus continuum contributions from the H_2O spectrum above 1 THz, which are formulated as wing response of a *pseudo-line* centreed at 1780 GHz. Moreover this summation has to account for the non-resonant Debye spectrum due to oxygen below 10 GHz and pressure-induced nitrogen absorption at frequencies above 100 GHz (respectively, the first and second terms of equation (8) in Recommendation ITU-R P.676-9.

As a result of model comparisons and evaluation conducted within the ITU-R Study Group 3, Annex 1 of Recommendation ITU-R P.676-9 uses a slightly modified MPM-93 model based on subsequent work done by Rosenkranz [1998, correction in 1999]: the temperature dependence of the foreign-broadened H_2O continuum term[1] is modified to match MPM-89 [Liebe, 1989]. This modification is equivalent to changing the MPM-93 b_5 spectroscopic coefficient (called b_4 in Table 2 of Recommendation ITU-R P.676-9) for the H_2O pseudo-line at 1780 GHz from 2.0 to 0.5.

In light of the above, the specific attenuation γ is given by:

$$\gamma = \gamma_o + \gamma_w = 0.1820 f N''(f) \quad \text{dB/km} \tag{6.18}$$

where f is the frequency in GHz and $N''(f)$ is the imaginary part of the frequency-dependent complex refractivity:

$$N''(f) = \sum_i S_i F_i + N_D''(f) \tag{6.19}$$

$N_D''(f)$ represents the above-mentioned dry-air continuum due to the Debye spectrum of O_2 together with the nitrogen contribution (respectively, the first and second terms of equation (8) in Recommendation ITU-R P.676-9). The line strength S_i is given by:

$$\begin{aligned} S_i &= a_1 \times 10^{-7} p \theta^3 \exp[a_2(1-\theta)] \quad \text{for oxygen} \\ &= b_1 \times 10^{-1} e \theta^{3.5} \exp[b_2(1-\theta)] \quad \text{for water vapour} \end{aligned} \tag{6.20}$$

where $\theta = 300/T$ with T is the temperature in Kelvin, p is the dry air partial pressure in hPa and e is the water vapour partial pressure in hPa.

---

[1] The "continuum" term is simply an empirical correction added to a line model in order to obtain agreement with a given set of attenuation measurements. In the microwave and millimeter-wave range, the continuum originates in the strong lines centred in the rotational spectrum of water vapour above 1 THz. Furthermore, the water vapour continuum is the main contributor to the gaseous absorption observed at window frequencies of 30 GHz and above for midlatitude or tropical atmospheres [Rosenkranz, 1998].

In parallel with equation (6.11), the line-shape function for the imaginary part of the refractive index is given by:

$$F_i = \mathrm{Im}\{F(f)\} = \frac{f}{f_i}\left[\frac{\Delta f - \delta(f_i - f)}{(f_i - f)^2 + \Delta f^2} + \frac{\Delta f - \delta(f_i + f)}{(f_i + f)^2 + \Delta f^2}\right] \tag{6.21}$$

where f_i is the frequency of the absorption line, Δf is the width of the line and δ is a correction factor which arises from the interference between overlapping oxygen absorption lines. F_i is also called F_i'' in the literature, for example in Liebe [1989].

Expressions for these parameters can be found in Recommendation ITU-R P.676-9 (see also equations (6.13) and (6.14)), together with the centre frequencies of the absorption lines and the corresponding spectroscopic coefficients (Tables 1 and 2 of the Recommendation).

The calculation of path attenuation through the Earth's atmosphere is fully described in § 2 of Annex 1, based on local information on the vertical profiles of pressure, temperature and absolute humidity, if available. In the absence of such local data, the reference standard atmospheres found in Recommendation ITU-R P.835-5 should be used. Attenuation along the path is determined using a numerical integration of Snell's law to account for the vertical gradient of the refractive index of moist air. The atmosphere is divided into layers and the contributions from each layer are summed. In order to ensure an accurate estimate the total path length through the atmosphere at any elevation angle (but critical for angles less than about 5 degrees), the medium is divided into layers sufficiently thin at the lowest altitudes to minimize any errors for each of the entry and exiting angles of the rays (respectively called α_n and β_n in Figure 4 of Recommendation ITU-R P.676-9). As a result, the thickness of the air layers should increase exponentially from 10 cm at ground level up to 1 km at an altitude of 100 km. The atmosphere is thus divided into 918 such layers. Moreover the effect of the spherical Earth is accounted for in these calculations through the use of radii r_n (see Figure 4 of Recommendation ITU-R P.676-9). The Earth curvature causes the slant path at low elevation angles to be smaller than in the atmosphere of a flat Earth, so a simple cosecant law (e.g. denominator of equation (28) in Recommendation ITU-R P.676-9) will overestimate the slant path length (and thus the gaseous absorption) for elevation angles smaller than 5 degrees.

6.3 Algorithms found in Annex 2 of Recommendation ITU-R P.676-9 for specific attenuation in the frequency range 1-350 GHz

The full line-by-line calculation of gaseous attenuation can be time-consuming and intensive in terms of processor time, especially for slant-paths. The simplified algorithms in Annex 2 of Recommendation ITU-R P.676-9 were developed to provide computationally-fast approximations for applications requiring multiple and/or repetitive calculations. They are based on curve-fitting to the line-by-line calculations described in §1 of Annex 1 of the Recommendation ITU-R P.676-9 in the frequency range 1-350 GHz.

The relative error between Annex 2 and the rigorous Annex 1 calculations is generally less than ±10% at frequencies removed from centres of major absorption lines; the absolute error is typically less than 0.1 dB/km and reaches a maximum of 0.7 dB/km near 60 GHz.

The major differences between the two methods occur very close to line centres, since specific attenuation at and very near the centre of absorption lines does not decrease with altitude as rapidly as at other frequencies, and this behaviour is not modelled effectively by the simplified algorithms found in Annex 2.

The line-by-line method expounded in Annex 1 should be used for:

- altitudes above 10 km;
- cases where high accuracy is needed;
- calculations of specific attenuation in the vicinity of absorption lines. As the altitude increases and the pressure decreases, individual absorption lines in the 60-GHz oxygen band start to become resolved, as shown in Figure 2 of Recommendation ITU-R P.676-9.

6.4 Algorithms presented in Annex 2 for slant-path attenuation in the frequency range 1-350 GHz

Zenith attenuation due to gases can be estimated using the specific attenuation multiplied by an equivalent height. Annex 2 of Recommendation ITU-R P.676-9 provides expressions for the equivalent heights, based on the algorithms of Annex 1 for calculations of total zenith attenuation and the simpler algorithms of Annex 2 for specific attenuation.

In the vicinity of resonance lines, especially in the 60-GHz frequency band, the zenith attenuation can exhibit very sharp peaks in attenuation which are not conspicuous in sea-level specific attenuation spectra. These peaks are very difficult to describe using simple algorithms, and in an attempt to reduce their effects and any bias they may introduce, the spectra of zenith attenuation were calculated using the line-by-line method in Annex 1 with the help of a numerical integration over a 500-MHz bandwidth at each frequency.

Attenuation levels were calculated at 1-GHz intervals for both zenith and specific attenuation; the equivalent height was computed by dividing the former by the latter. The zenith and specific attenuations were calculated for sea-level altitudes and for altitudes of 2, 4, 6, 8 and 10 km above sea level, taking the pressure, temperature and water-vapour density from the mean annual global reference atmosphere described in Recommendation ITU-R P.835-5 appropriate to those altitudes. Finally the resulting numerical values for the equivalent heights were used to generate empirical fits that depend on frequency and altitude, the latter through the use of the pressure variable r_p (see equations (25) and (26) of Recommendation ITU-R P.676-9).

The equivalent height of dry air h_o is actually quite a complicated function in the vicinity of the 60 GHz band, and a number of different functions were investigated. For the sake of simplicity a single Gaussian function limited in amplitude for frequencies lower than 70 GHz was found to provide the best overall result (see equation (25) of Recommendation ITU-R P.676-9).

The effective-height algorithms were used in conjunction with the algorithms for specific attenuation to estimate the zenith attenuations due to dry air and water vapour, from sea level and from altitudes of 2, 4, 6, 8 and 10 km.

The error in zenith attenuation for water vapour is less than ±5% compared to the line-by-line method integrated throughout the reference global standard atmosphere.

For dry air, at frequencies away from the 60-GHz oxygen band, the error in zenith attenuation is less than ±10%. At some frequencies within the band 56-68 GHz, the error can exceed 10% since the fitting procedure cannot reproduce the structure shown in Figure 7 of Recommendation ITU-R P.676-9. Therefore it is recommended that the line-by-line calculation in Annex 1 be used within this band, especially for altitudes above about 6 km.

Tables 6.1 to 6.4 below show examples that can be used to verify the correct software implementation for Annex 2 of Recommendation ITU-R P.676-9. Intermediate values are shown to assist users in tracing problems with their implementation.

TABLE 6.1

Validation examples for the dry air attenuation model (first term of equation (28) and equation (29) of Annex 2 of Recommendation ITU-R P.676-9)

Input values						Intermediate values			Result
Latitude (°N)	**Longitude (°E)**	h_s **(km)**	**Elevation angle φ (degrees)**	f **(GHz)**	P **(hPa)**	T **(K)**	γ_O **(dB/km)**	h_O **(km)**	A_O **(dB)**
46.217	6.12	0	33	12	1013.25	279.09	0.0091	5.20	0.09
46.217	6.12	0	33	20	1013.25	279.09	0.0123	5.18	0.12
46.217	6.12	0	33	60	1013.25	279.09	16.2501	10.7	319.27
46.217	6.12	0	33	61	1013.25	279.09	15.7506	10.7	309.46
46.217	6.12	0	33	90	1013.25	279.09	0.0332	4.94	0.3
46.217	6.12	0	33	130	1013.25	279.09	0.044	5.79	0.47

TABLE 6.2

Validation examples for the water vapour attenuation model (second term of equation (28) of Annex 2 of Recommendation ITU-R P.676-9). Column 8 is the surface water vapour density exceeded for 50% of an average year obtained from the maps provided in Recommendation ITU-R P.836-4

Input values						Intermediate values				Result
Latitude (°N)	**Longitude (°E)**	h_s **(km)**	**Elevation angle φ (degrees)**	f **(GHz)**	P **(hPa)**	T **(K)**	ρ **(g/m^3)**	γ_w **(dB/km)**	h_w **(km)**	A_w **(dB)**
46.217	6.12	0	33	12	1013.25	279.09	4.98	0.0071	1.68	0.02
46.217	6.12	0	33	20	1013.25	279.09	4.98	0.0674	1.96	0.24
46.217	6.12	0	33	60	1013.25	279.09	4.98	0.1154	1.66	0.35
46.217	6.12	0	33	90	1013.25	279.09	4.98	0.2557	1.66	0.78
46.217	6.12	0	33	130	1013.25	279.09	4.98	0.5636	1.66	1.72

TABLE 6.3

Validation examples for the water vapour attenuation model using the integrated water vapour content (equation (37) of Annex 2 of Recommendation ITU-R P.676-9)

Latitude (°N)	**Longitude (°E)**	h_s **(km)**	**θ (degrees)**	f **(GHz)**	P **(hPa)**	**% of time**	T **(K)**	V_t	ρ_w	t_{ref} **(°C)**	$\gamma_w(f)$	$\gamma_w(20.6)$	A_w **(dB)**
46.217	6.12	0	33	20	1013.25	10	279.09	17.5311	4.3828	2.4898	0.05996	0.07847	0.4255
46.217	6.12	0	33	20	1013.25	1	279.09	21.9792	5.4948	5.6555	0.07525	0.09839	0.5339

TABLE 6.4

Validation examples for the specific attenuation due to water vapour model (equation (23a) of Annex 2 of Recommendation ITU-R P.676-9)

	12 GHz	**20 GHz**	**60 GHz**	**90 GHz**	**130 GHz**
A_1	3.25891E-02	2.56330E-01	2.59424E-03	8.09416E-04	3.20458E-04
A_2	4.00657E-04	4.40855E-04	7.73012E-04	1.34923E-03	4.12257E-03
A_3	6.91420E-07	7.28631E-07	9.68835E-07	1.23651E-06	1.80781E-06
A_4	3.56459E-05	3.75393E-05	4.97180E-05	6.32106E-05	9.17715E-05
A_5	1.81928E-04	1.90103E-04	2.40600E-04	2.92954E-04	3.94199E-04
A_6	8.78281E-05	9.11421E-05	1.10903E-04	1.30269E-04	1.65102E-04
A_7	2.84515E-03	2.93055E-03	3.42125E-03	3.87493E-03	4.63492E-03
A_8	5.25772E-04	5.37327E-04	6.01241E-04	6.56969E-04	7.44183E-04
A_9	2.44425E-02	2.46652E-02	2.58257E-02	2.67508E-02	2.80635E-02
$g(f,22)$	1.0865052	1.0022676	1.2147531	1.3686224	1.5048476
$g(f,557)$	1.9174206	1.8661576	1.6488472	1.5209850	1.3863156
$g(f,752)$	1.9381596	1.8990577	1.7262734	1.6181470	1.4973288
$g(f,1780)$	1.9733937	1.9560494	1.8738185	1.8167520	1.7462789
P	1013.25	1013.25	1013.25	1013.25	1013.25
r_p	1.0002468	1.0002468	1.0002468	1.0002468	1.0002468
T	5.9435147	5.9435147	5.9435147	5.9435147	5.9435147
r_t	1.0324671	1.0324671	1.0324671	1.0324671	1.0324671
ρ	4.9815429	4.9815429	4.9815429	4.9815429	4.9815429
η_1	1.0061063	1.0061063	1.0061063	1.0061063	1.0061063
η_2	0.9468427	0.9468427	0.9468427	0.9468427	0.9468427
γ_w	0.0070570	0.0674272	0.1153802	0.2556834	0.5635838

Note: Equation (23a) of Annex 2 was rewritten as:

$$\gamma_w = \left\{A_1 g(f,22) + A_2 + A_3 + A_4 + A_5 + A_6 + A_7 g(f,557) + A_g g(f,752) + A_9 g(f,1780)\right\} f^2 r_t^{2.5} \rho \times 10^{-4}$$

6.5 Effects of dispersion due to atmospheric gases

Oxygen and water vapour also introduce dispersive effects in excess of those produced by the normal frequency-independent refractive phenomena (described in Recommendation ITU-R P.453-10). This so-called "anomalous" dispersion is frequency-dependent and arises through the real part of the refractive index of the atmosphere, associated with the major absorption lines as described in § 6.2 and in Recommendation ITU-R P.676-9. Thus on the one hand the method described in Recommendation ITU-R P.453-10 estimates the *bulk* delay through the Earth's atmosphere, which amounts to nanoseconds and is independent of frequency but depends on atmospheric variables (dry air pressure, temperature and water vapour pressure). On the other hand the frequency-dependent real component of the refractive index of air described below introduces additional delays of the order of picoseconds only in the vicinity of absorption lines. Finally, it may be worthwhile to recall that *anomalous* dispersion occurs in the immediate vicinity of the resonance frequency (in a region of high absorption) where the refractive index of the medium decreases with frequency.

The dispersive effect of the atmosphere gives rise to a phase dispersion which can be expressed as:

$$\beta = 1.2008 f N'(f) \quad \text{deg/km} \tag{6.22}$$

where f is the frequency in GHz and $N'(f)$ is the frequency-dependent real part of the refractive index due to atmospheric gases. This can also be expressed in terms of the specific group delay of the radio waves:

$$\tau = 3.3356 N'(f) \quad \text{ps/km} \tag{6.23}$$

The real part of the refractive index due to atmospheric gases is described by an equation similar to equation (6.9):

$$N'(f) = \sum_i S_i F_i^{'} + N_D^{'}(f) \qquad N \text{ units} \tag{6.24}$$

where S_i is the line strength described in equation (6.10). The line shape factor $F_i^{'}$ for dispersion is given by the real part of the complex shape function F described by equation (6.11):

$$F_i^{'} = \mathrm{Re}\{F\} = \frac{f}{f_i}\left[\frac{(f_i - f + \delta\Delta f)}{(f - f_i)^2 + \Delta f^2} - \frac{(f_i - f + \delta\Delta f)}{(f - f_i)^2 + \Delta f^2}\right] \tag{6.25}$$

It may be worthwhile to note that equation (6.25) is rigorously equivalent to the following expression:

$$F_i^{'} = \frac{(f_i - f) + \delta\left(\frac{f}{f_i}\right)\Delta f}{(f - f_i)^2 + \Delta f^2} - \frac{(f_i - f) - \delta\left(\frac{f}{f_i}\right)\Delta f}{(f - f_i)^2 + \Delta f^2} - \frac{2}{f_i} \tag{6.26}$$

found in MPM-89 [Liebe, 1989]. $N_D^{'}(f)$ in equation (6.24) represents the contribution from the non-resonant Debye spectrum of O_2 below 10 GHz:

$$N_D^{'}(f) = 6.14\times10^{-5}\, p\theta^2\left\{\frac{1}{1+\left(\frac{f}{d}\right)^2} - 1\right\} \tag{6.27}$$

where d is the width of the Debye spectrum [Liebe, Hufford and Cotton, 1993]:

$$d = 5.6\times10^{-4}(p+e)\theta^{0.8} \tag{6.28}$$

The dispersive effects of the atmosphere described by this model are illustrated in Figures 6.4 and 6.5, which show the predicted dispersive delay rate in ps/km at sea level from 0-350 GHz and from 300-1000 GHz, respectively computed at 500-MHz intervals. The mean annual global reference atmosphere described in Recommendation ITU-R P.835-5 is used in both of these Figures.

FIGURE 6.4

Dispersive delay rate in ps/km at sea level due to atmospheric gases from 0 to 350 GHz using the ITU-R mean annual global reference atmosphere (P = 1013.25 hPa, T = 288.15 K, ρ = 7.5 g/m^3 at the surface)

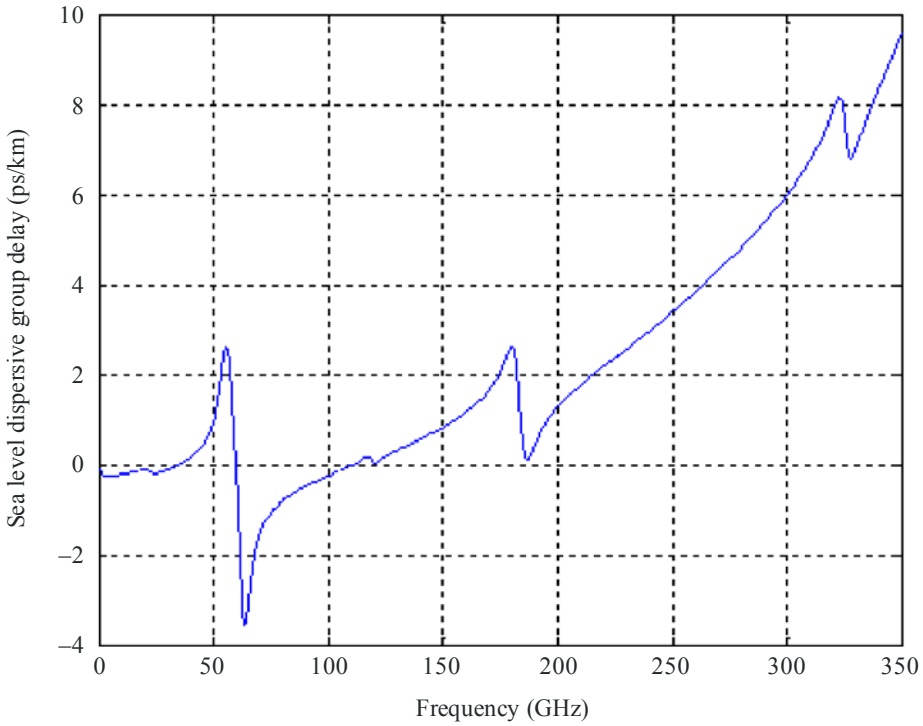

Radio-Meteo. 06-04

FIGURE 6.5

Dispersive delay rate in ps/km at sea level due to atmospheric gases from 300 to 1000 GHz using the ITU-R mean annual global reference atmosphere (P = 1013.25 hPa, T = 288.15 K, ρ = 7.5 g/m^3 at the surface)

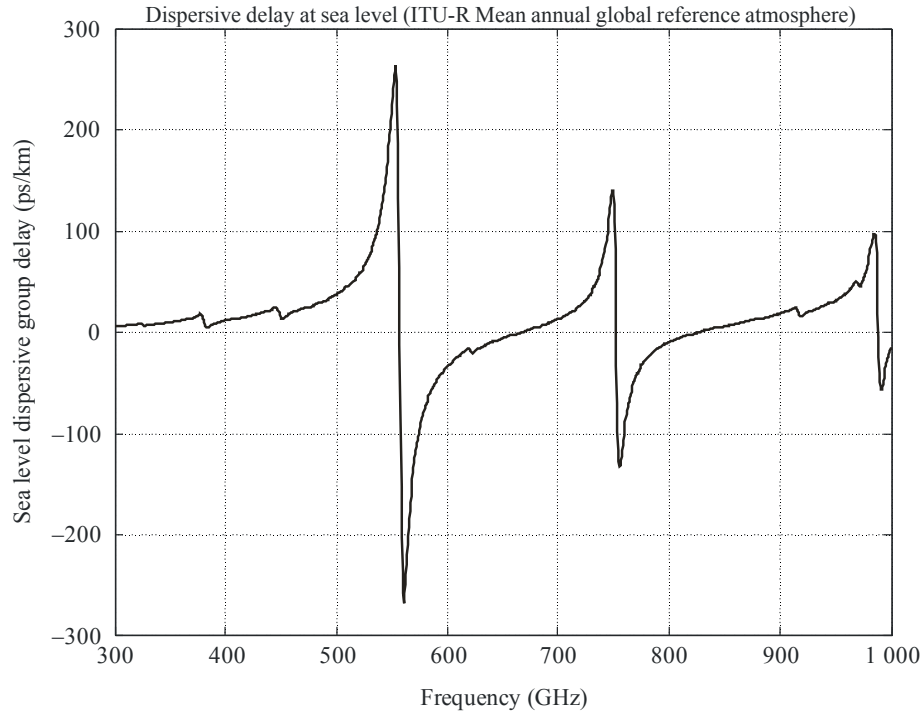

Radio-Meteo. 06-05

The total dispersive delay (ps) for Earth-space paths at zenith is estimated by integrating the dispersive delay rate (ps/km) through the atmosphere up to 100 km. The integration technique is identical to the one described by equations (16) to (20) of Recommendation ITU-R P.676-9 for attenuation; however spherical concentric layers of air of *fixed* thickness (1 km) are used here instead of an array of layers with exponentially-increasing thicknesses (described by Equation 21 of the Recommendation). Figures 6.6 and 6.7 show the results of these computations for the same frequency ranges (0-350 GHz and 300-1000 GHz respectively) at 500-MHz intervals. Once again the pressure, temperature and absolute humidity for each layer is specified by the mean annual global reference atmosphere described in Recommendation ITU-R P.835-5.

For most practical telecommunications applications using relatively narrow-bandwidth transmissions, the effects of this frequency-dependent anomalous dispersion will have little impact. However, with the advent of new digital communications systems with high data rates, and thus wide bandwidths, the combination of absorption and dispersion due to atmospheric gases could have an influence on the characteristics of the received signals, particularly in terms of distortion to the transmitted digital signals. Gibbins [1990] calculated the distortions introduced to the transmission of very short pulses with a Gaussian pulse shape for both terrestrial and Earth-space paths.

FIGURE 6.6

Dispersive delay in ps through the atmosphere at zenith due to atmospheric gases from 0 to 350 GHz using the ITU-R mean annual global reference atmosphere

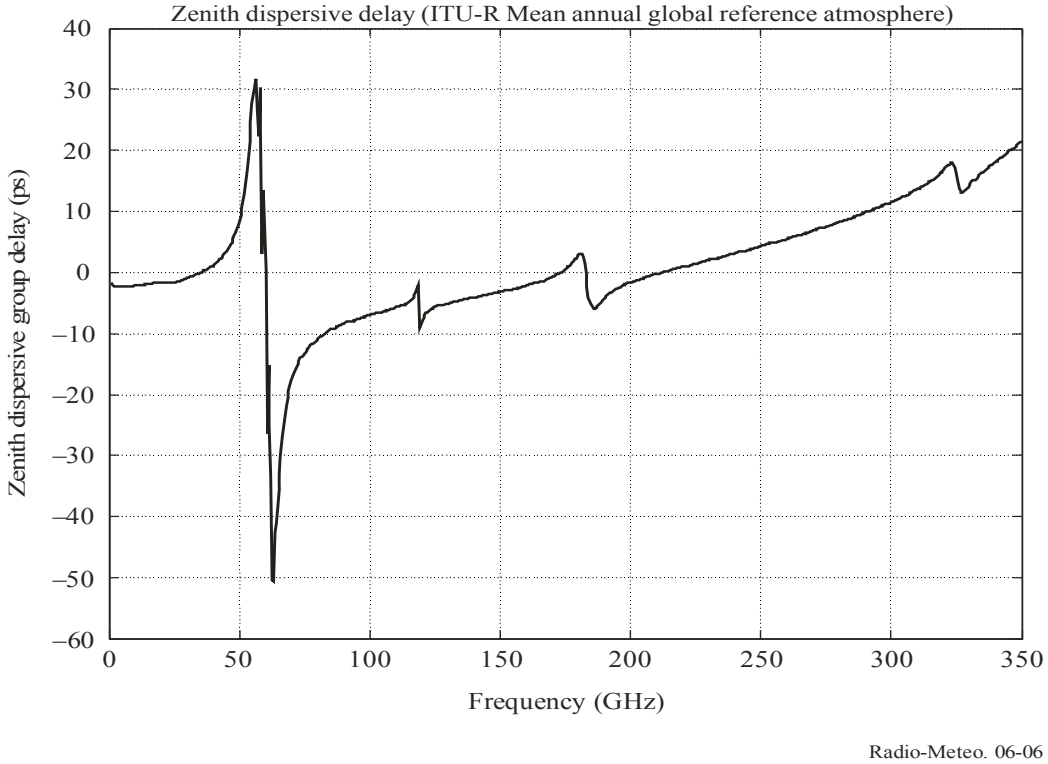

FIGURE 6.7

Dispersive delay in ps through the atmosphere at zenith due to atmospheric gases from 300 to 1000 GHz using the ITU-R mean annual global reference atmosphere

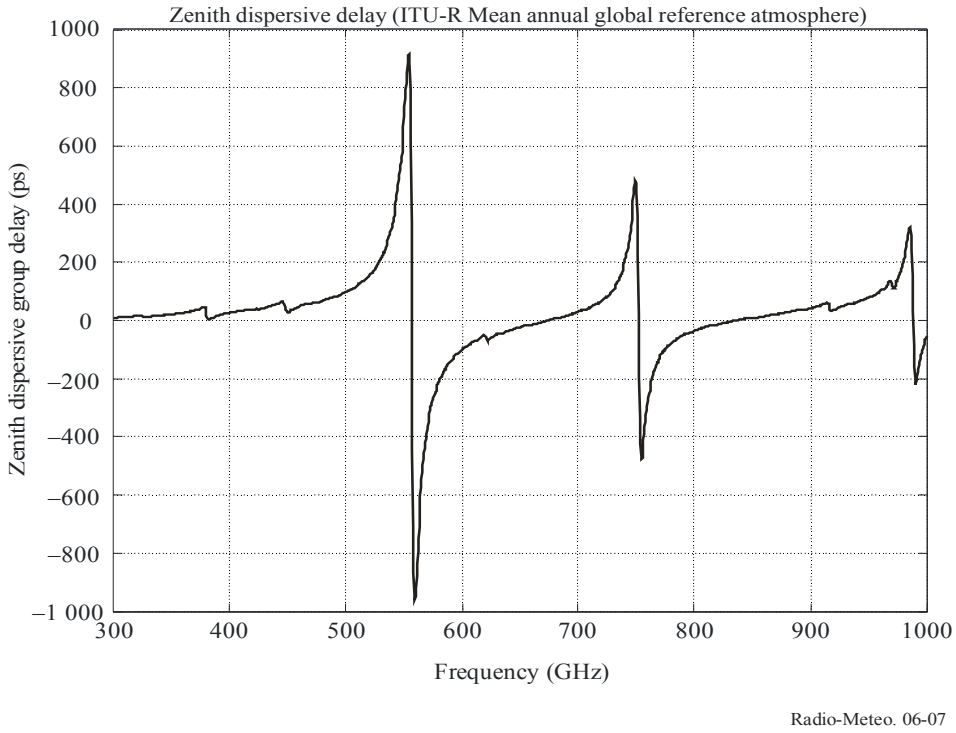

For illustration, Figure 6.8 shows the calculated distortion of a Gaussian pulse in terms of the percentage of broadening or compression (if negative) for two pulse widths (2 and 0.2 ns) over a path length of 10 km at sea level. The ITU-R mean annual global reference atmosphere (with P = 1013.25 hPa, T = 288.15 K, ρ = 7.5 g/m^3 at the surface) is used once again. These computations are based on the previous incarnation of Liebe's model, MPM-89 [Liebe, 1989]. A 2-ns pulse (with a 3-dB bandwidth of 0.8 GHz) becomes broadened by about 7% near 55 GHz. The same 2-ns pulse gets compressed by about 16% near 62 GHz, subsequently broadening again by about 8% at around 64 GHz. For a much shorter pulse of 0.2 ns with a 3-dB bandwidth of 8 GHz, distortion levels are correspondingly higher, with significant broadening and compression occurring around the 22-GHz water-vapour line; near the 60-GHz oxygen band the 0.2-ns pulse suffers broadening in excess of 100% and can actually break up into numerous components similar in effect to ringing. Distorted pulses occur when both the attenuation and propagation delay change significantly over the bandwidth required for the transmission of pulsed signals. As a consequence, increased bit-error rates and intersymbol interference in digital communication systems occur for very-wide-band digital transmissions at frequencies close to gaseous absorption lines.

FIGURE 6.8

Calculated pulse broadening (or compression, if negative) of 0.2-ns and 2-ns Gaussian pulses due to the dispersive effects of the atmosphere, over a 10-km horizontal path at sea level (with P = 1013.25 hPa, T = 288.15 K, ρ = 7.5 g/m^3). Predictions from the MPM-89 model are shown [Liebe, 1989]

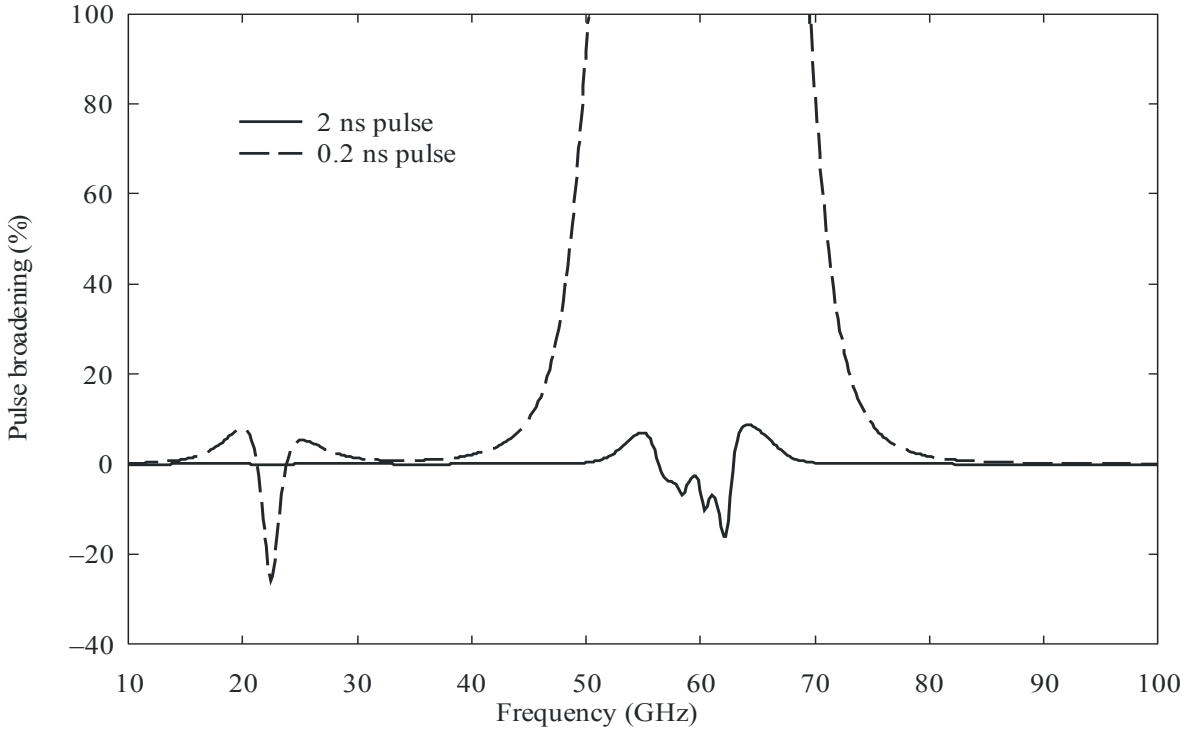

6.6 Comparison of predictions from various gaseous absorption models with measurements

Physical gaseous absorption models like Liebe's MPM are based on various theoretical approximations and laboratory data. The latter are measured in a controlled environment over a limited range of temperature. For example Liebe, Rosenkranz and Hufford [1992] report laboratory measurements of pressure-broadened oxygen absorption in dry air (O_2 + N_2) performed at frequencies between 49.3 and 66.3 GHz at three temperatures (6, 30 and 54°C) for 11 selected pressure values ranging between 13 and 1010 hPa. Clearly oxygen absorption is not completely characterized over the range of tropospheric and/or stratospheric air temperatures (approximately between -89°C and 57°C). Thus uncertainties in the temperature dependence of the line-coupling parameter, δ, (equation (6.14)) in the 50-70-GHz oxygen band impact the modelled brightness temperatures, especially for dry atmospheric conditions.

Validation experiments compare predictions from models to real-world observations. In a typical setting, ground-based radiometers or spectrometers provide measurements of brightness temperature, and the input variables of the model under test are measured by radiosondes. Since radiosondes do not routinely measure cloud liquid, clear sky conditions (i.e. free from visible cloud) must prevail during the validation process in order to avoid unquantifiable emissions from clouds. Comparisons with space borne radiometers are also possible but require extra precautions (e.g. antenna side lobe corrections) and impose strict selection criteria for the *in situ* data (co-located and contemporaneous data from buoys and radiosondes, taking into account the ascent time of the latter). Section 2.11 of Mätzler [2006] provides various comparisons of predictions from gaseous absorption models with measurements from satellite microwave radiometers.

6.6.1 Ground-based radiometric measurements

Westwater *et al.* [1990] measured emissions from clear skies at 20.6, 31.65 and 90 GHz with radiometers deployed in Denver, Colorado and San Nicholas Island, California, and compared these with calculations of brightness temperatures based on data from two different types of radiosondes. It should be noted that the radiometers had equal beamwidths at all three channels; thus emission from a common volume can be observed simultaneously. They compared predictions from the water vapour absorption models of MPM-87 [Liebe and Layton, 1987] and Waters [1976]. Oxygen absorption was calculated using an earlier version of the Rosenkranz model [Rosenkranz, 1988]. These comparisons show that Waters' model outperforms MPM-87 at 20.6 and 31.65 GHz (has the lowest bias and RMS error) and that the converse is true at 90 GHz. At the latter frequency most of the absorption arises from the continuum and/or non-resonant terms which are modelled quite differently by Waters [1976] and Liebe and Layton [1987].

Westwater *et al.* [2003] measured atmospheric emissions at 23.8 GHz and 31.4 GHz with radiometers on the island of Nauru and the surrounding tropical western Pacific Ocean during June and July 1999. As mentioned in Recommendation ITU-R P.836-5, the first channel is most sensitive to water vapour, whereas the second lies in a window region for gaseous absorption (thus dominated by the water vapour continuum absorption) and therefore is more sensitive to cloud liquid. They compared these radiometric data with predicted brightness temperatures from MPM-87 [Liebe and Layton, 1987], MPM-93 and Rosenkranz 98. Radiosonde profiles were used as input to these models. Corrections to radiosonde hygristors were applied to reduce the known dry bias. Results from this comparison, based on the combined Nauru and nearby ship data (with a sample size of 175), are summarized in Table 6.5. The total columnar water vapour content was around 4.7 cm. The average brightness temperature was around 65 K at 23.8 GHz and 32 K at 31.4 GHz.

TABLE 6.5

Comparison of measured and calculated clear-sky brightness temperatures (K) at 23.8 and 31.4 GHz for three gaseous absorption models using corrected radiosonde data at Nauru Island in the tropical western Pacific [Westwater *et al.*, 2003]. Sample size is 175

Frequency (GHz)	Parameter (K)	MPM-87	MPM-93	Rosenkranz 98
23.8	Average error (Bias)	0.80	3.90	0.69
23.8	Standard deviation of the error	3.46	3.59	3.44
23.8	99% confidence interval for the bias	±0.67	±0.70	±0.67
31.4	Average error (Bias)	-0.16	3.37	0.86
31.4	Standard deviation of the error	1.66	1.84	1.69
31.4	99% confidence interval for the bias	±0.32	±0.36	±0.33

Table 6.5 shows that there is a close agreement between MPM-87 and Rosenkranz 98 at 23.8 GHz, with only about 0.1 K of difference separating the two. Assuming that the radiosonde correction algorithm is doing a good job on average, the predictions from the Rosenkranz 98 model are slightly closer to the measured brightness temperature data [Westwater *et al.,* 2003]. However because of the large scatter in the results (standard deviation of around 3.5 to 3.6 K), MPM-87 and

Rosenkranz 98 are statistically indistinguishable within the 99% confidence interval shown in Table 6.5.

There is a 1-K difference in bias between the MPM-87 and the Rosenkranz 98 models at 31.4 GHz and less scatter than at 23.8 GHz. If we assume that the radiosonde correction algorithm is doing a good job on average, then MPM-87 agrees better with radiometer measurements of brightness temperature within the 99% confidence limits [Westwater *et al.,* 2003]. However, uncertainties in the accuracy of either the original or corrected radiosondes do not allow one to make definite statements about the best of the two models: agreement between radiometer measurements and modelled brightness temperatures was noticeably different depending in the radiosonde lots and was not a monotonic function of radiosonde age [Westwater *et al.,* 2003]. Table 6.5 shows that predictions based on MPM-93 differ from the other two models by about 3 K.

It should be noted that in a very cold and dry area (i.e. the Arctic Ocean, north of Alaska), the Rosenkranz 98 model at 31.4 GHz best predict the attenuation due to dry air (also known as dry opacity) since its use result in the smallest radiometrically-retrieved liquid water path values under clear-sky conditions compared to the other two models [Westwater *et al.*, 2001].

Mattioli *et al.* [2005] compared radiometer measurements at 23.8 and 31.4 GHz collected at the U.S. Department of Energy ARM site in north-central Oklahoma with predictions based on the MPM-87, MPM-93 and Rosenkranz 98 models. A model from Liljegren *et al.* [2005] and an update to the Rosenkranz model were also tested. Predictions from the latter were very close to those from Rosenkranz 98. Radiosondes of an improved design (free from dry bias) were used to provide the input atmospheric profiles to these models. Clear-sky brightness temperatures *(T_bs)* ranged from 12 to 42 K at 23.8 GHz (considerably lower than the humid tropical atmosphere observed at Nauru; see Table 6.5) and 11 to 22 K at 31.4 GHz. The largest variability in T_bs between these two climates is clearly due to water vapour and is conspicuous for the 23.8-GHz channel. Three radiometers (called C1, S01 and E14) calibrated using two distinct algorithms (ARM and ETL) were used. Table 6.6 shows the mean (bias) of the error, defined as [measured T_b – predicted T_b] for microwave radiometer C1 calibrated using the ARM method (C1/ARM). This combination yields a bias that generally lies in the middle of the range of bias errors shown in the second and fourth rows of Table 6.6. Based on the modest sample size, it seems that the more recent models (Rosenkranz 1998, Liljegren 2005) are in much better agreement with measurements than the "older" ones (MPM-87 and MPM-93).

Mattioli *et al.* [2005] also present scatter plots of measured versus predicted T_bs for radiometer C1/ARM together with slope and intercept analysis of the regressions. For the 23.8-GHz channel the Rosenkranz 1998 and 2003 models have a slope of nearly unity, whereas the Liljegren 2005 model has a slope that is 2.5% larger. The intercept is very similar for these three newer models (-0.51 to -0.58 K) and is the largest (-1.007 K) for MPM-87. Turning to the liquid-sensitive channel, the Liljegren 2005 model has a slope very close to unity and the smallest intercept (-0.006 K), whereas the Rosenkranz models have a slope of around 1.04 and an intercept of about -0.6 K. MPM-93 has a slope of 1.1519 and an intercept of -1.511 K at 31.4 GHz: it slightly overpredicts water vapour absorption at this frequency. Deviation of the regression slope from unity is mainly a test for the water vapour module of these models since most of the temporal variability in clear-sky brightness temperature arises from the water vapour [Mätzler, 2006].

TABLE 6.6

Comparison of measured and calculated clear-sky brightness temperatures (K) at 23.8 and 31.4 GHz for four gaseous absorption models using radiosonde data at the Oklahoma ARM site in March-April 2003 [Mattioli, 2005]. Sample size is 67 for radiometer C1. The range of bias for the six combinations of radiometers (C1, S01 and E14) and calibration algorithms (ARM and ETL) is also presented [Mätzler, 2006]

Frequency (GHz)	Parameter (K)	Rosenkranz 98	Liljegren 2005	MPM-87	MPM-93
23.8	Average error (bias) C1/ARM	0.44	-0.07	0.60	-0.65
23.8	Range of bias	[-0.03, 0.75]	[-0.55, 0.25]	[0.12, 0.91]	[-1.13, -0.33]
31.4	Average error (bias) C1/ARM	0.09	-0.11	0.64	-0.77
31.4	Range of bias	[-0.005, 0.27]	[-0.11, 0.06]	[0.54, 0.81]	[-0.86, -0.59]

Bouchard [2008] retrieved daytime clear-sky data with a multi-frequency profiling radiometer deployed in Ottawa, Canada. The profiler has five channels in the water vapour band (22.235-30 GHz) and seven channels along the edge of the oxygen complex between 51.25 and 58.8 GHz. In such clear sky conditions, the total path attenuation A_{tot} calculated from the sky brightness temperature using the well-known relationship in Recommendation ITU-R P.1322 should be exactly equal to the absorption due to gases: $A_{tot} = A_{g.}$ A total of 1721 retrievals under clear sky conditions between April 2005 and April 2006 were analysed. Occasional haze and/or non-persistent aircraft contrails were present; both are transparent to microwaves. The surface pressure ranged from 1003 to 1027.1 hPa; the columnar water vapour content from 0.21 to 3.67 cm; the temperature near the surface ranged from -19.9 to 28.8 °C.

Both MPM-93 (without provisions for the spherical Earth and refraction) and the latest version of Rosenkranz's model called Rosenkranz 2007 (obtained directly from the author) are used with retrieved profiles of temperature and humidity from the surface up to 10 km above ground level as input. Both models use a simple cosecant law dependence on the elevation angle. The profiler measures air pressure near the surface only. Therefore, pressure *profiles* from the surface up to 10 km above ground were "reconstructed" from the pressure at the surface and interpolated profiles of temperature and absolute humidity by solving the hydrostatic equation for thin (1-m) layers of moist air. All of these profiles are "topped up" with the most recent radiosonde profiles of pressure, temperature and relative humidity from the Maniwaki (WMO 71722) upper air station (located approximately 105 km away) from 10 km up to the level of balloon puncture (typically at around 30 km). The effective medium temperature T_{mr} in Equation 1 of Recommendation ITU-R P.1322 is computed using the Rosenkranz 2007 model with the same composite (profiler + radiosonde) profiles as input data. This approach is used by Bouchard [2008] to compare gaseous absorption models because facilities for launching co-located radiosondes on a twice-daily basis do not exist. Moreover, the closest radiosonde station (Maniwaki) does not issue surface observations (known as METARs).

Frequencies of interest for this comparison are 30 GHz and 51.25 GHz. At 30 GHz, the Rosenkranz 2007 model has the lowest bias and RMS error compared to observations at the four elevation angles considered (15°-90°); at 51.25 GHz, the MPM-93 model provides the closest match to the observations (i.e., has the lowest bias and RMS error). Figures 6.9 to 6.12 show examples of these conditional CDF plots at 30 GHz and 51.25 GHz for both 90 degrees and 27.45 degrees elevation.

FIGURE 6.9

Conditional cumulative distribution function (CDF) of measured and modelled gaseous attenuation (A_g) at 30 GHz, 90 degrees, for clear sky conditions observed over Ottawa during the daytime. Retrieved profiles "topped up" with radiosonde data from Maniwaki (71722) are used as inputs to models in Figures 6.9 to 6.12

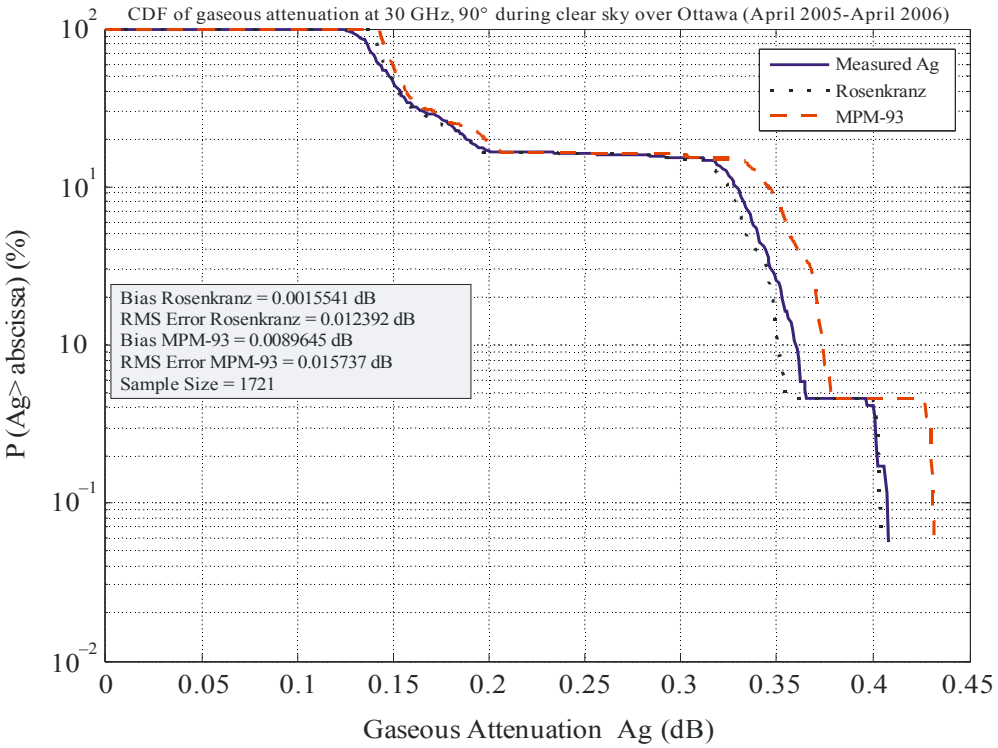

Radio-Meteo. 06-09

FIGURE 6.10

Conditional CDF of measured and modelled gaseous attenuation (Ag) at 30 GHz, 27.45 degrees, for clear sky conditions observed over Ottawa during the daytime (April 2005 - April 2006)

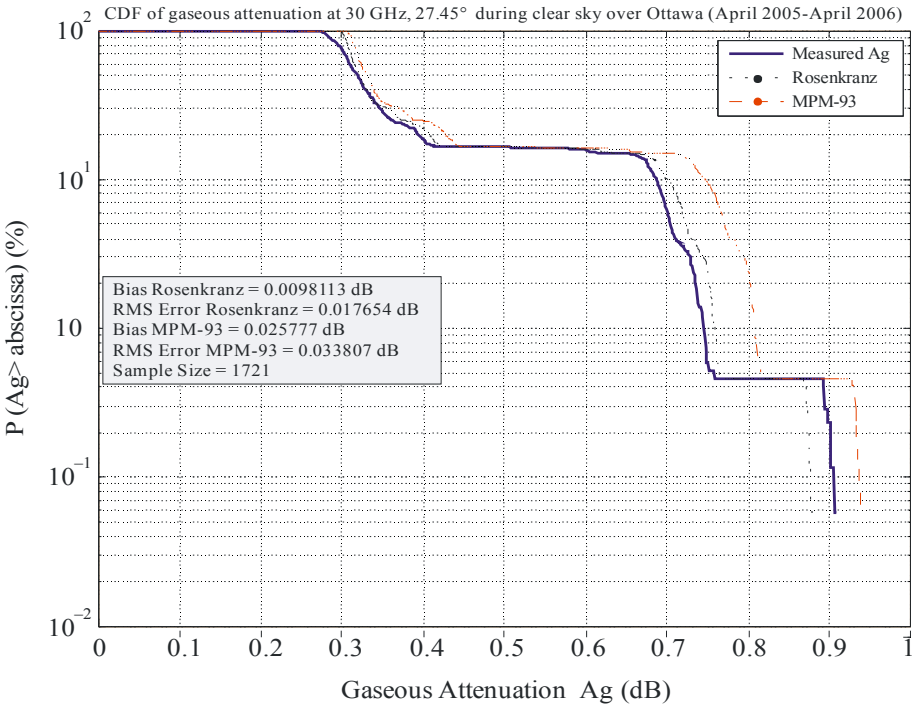

Radio-Meteo. 06-10

FIGURE 6.11

Conditional CDF of measured and modelled gaseous attenuation (Ag) at 51.25 GHz, 90 degrees, for clear sky conditions observed over Ottawa during the daytime (April 2005 - April 2006)

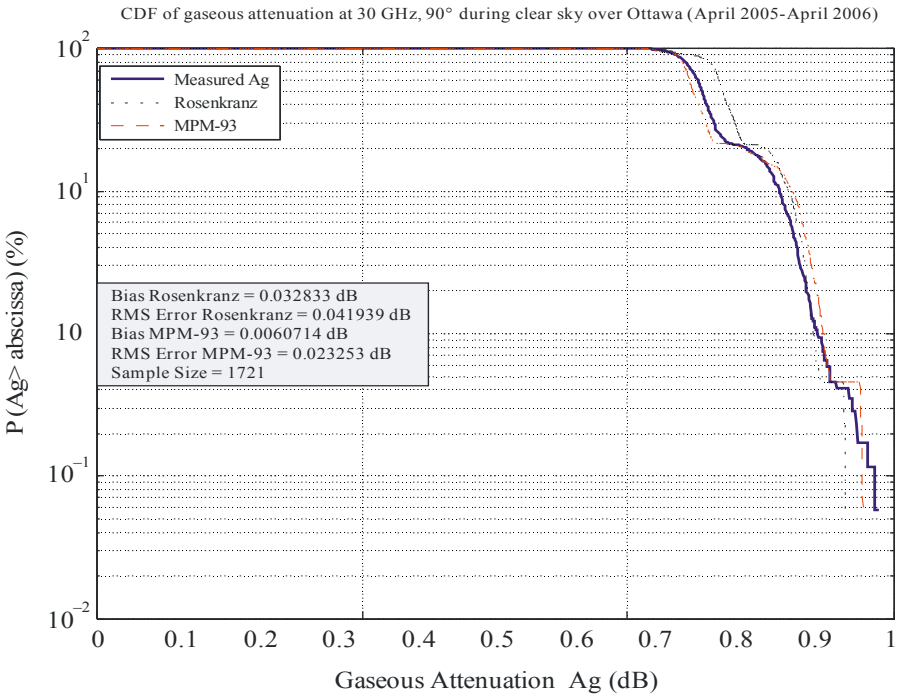

Radio-Meteo. 06-11

FIGURE 6.12

Conditional CDF of measured and modelled gaseous attenuation (Ag) at 51.25 GHz, 27.45 degrees, for clear sky conditions observed over Ottawa during the daytime (April 2005 - April 2006)

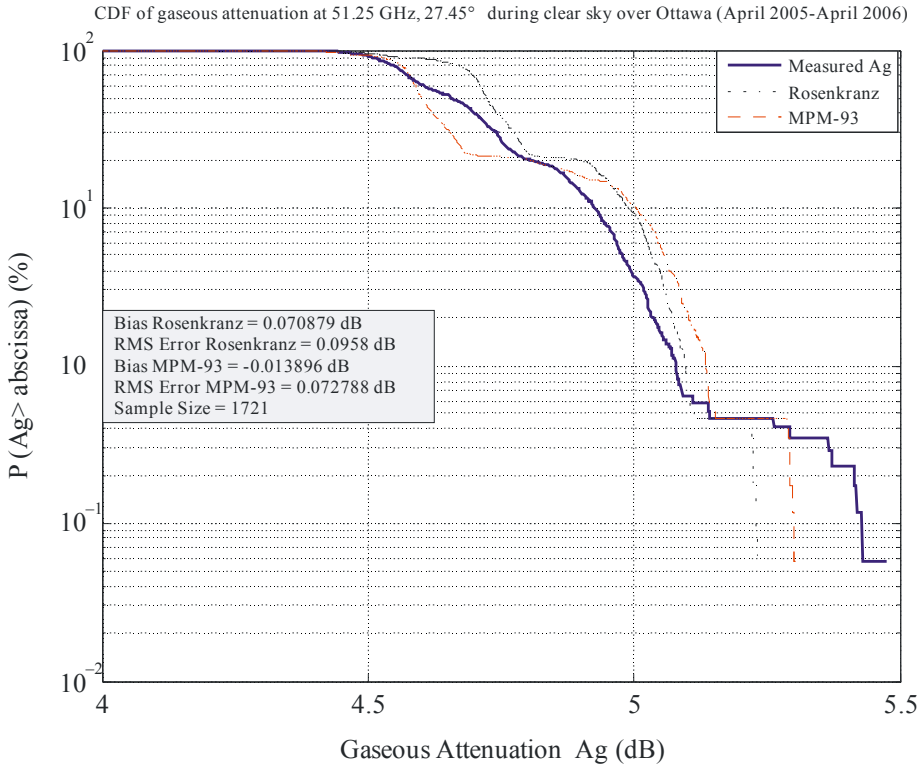

Radio-Meteo. 06-12

It may be interesting to note that Hewison *et al.* [2006] drew similar conclusions on these two gaseous absorption models (more precisely, Rosenkranz 2003) at 30 and 51.25 GHz using a more rigorous approach of comparing *modelled* brightness temperatures from radiosondes launched in clear skies with *measured* brightness temperatures from a co-located profiling radiometer of the same model during the Temperature, Humidity and Cloud (TUC) experiment that took place in Payerne, Switzerland during the winter 2003-2004. During TUC, the radiosondes only produced valid humidity profiles up to 10 to 12 km; above this level, Hewison *et al.* [2006] topped up the *in situ* profiles with a reference mid-latitude winter profile. For the profiler channels dominated by the water vapour continuum (26.235 and 30 GHz), Hewison *et al.* [2006] found that MPM-87, MPM-89, Rosenkranz (both 98 and 2003) and Liljegren [2005] show excellent agreement with measurements; however, MPM-93 overestimates the strength of the absorption. These authors also found that MPM-93 consistently overestimates the gaseous absorption in warmer, more humid conditions for the 22.235-23.835 GHz channels and that MPM-87 has the lowest bias and RMS error at 52.28 GHz compared to the other five models. It should be noted that the 51 and 52-GHz channels combine the influence of the water vapour continuum and the oxygen line coupling parameters, both of which vary from one model to the next; these channels show the largest differences between models and significant differences between the observations and models. Finally, the higher profiler channels (54.94-58.8 GHz) suffered from a T_b bias of about 1 K that was subsequently identified and rectified by the manufacturer. This bias has been empirically corrected in the TUC data set for subsequent analysis presented in papers.

6.6.2 Ground-based Fourier transform spectrometers

Ground-based Fourier transform spectrometers (FTS) deployed on high mountain-top sites provide valuable data sets for validating and further refining gaseous absorption models in dry atmospheres from roughly 0.1 to 2 THz [Mätzler, 2006]. Pardo *et al.* [2001a] present broadband atmospheric transmission spectra using FTS on Mauna Kea, Hilo, Hawaii (4100 m above sea level) between 350 and 1100 GHz. These measurements show that the dry continuum term in MPM-93 has to be multiplied by 1.29 in order to fit measurements of dry opacity in this frequency band, whereas the H_2O pseudo-continuum absorption introduced in both MPM-89 and MPM-93 is not accurate in the submillimeter range (see Figure 5 of Pardo *et al.* [2001a]). Moreover, absorption due to ozone is not modelled in MPM, but its effect is visible in very dry climates in the submillimeter range [Pardo *et al.*, 2001b]. Other trace gases are not modelled in MPM either. On the other hand it should be noted that absorption due to trace gases is modelled in the Atmospheric Transmission at Microwaves (ATM) model [Pardo *et al.*, 2001b]; special effort was devoted during the development of ATM to the validation and measurement of continuum absorption in the submillimeter range.

6.6.3 Conclusion

Unfortunately the comparisons presented in this section do not allow one to identify an overall "best" gaseous absorption model for all microwave and millimetre-wave frequencies and all climatic conditions. These reported works also highlight some of the difficulties faced when meaningful comparisons between theoretical models and measurements are needed: bias in measured brightness temperature need to be identified and corrected and accurate *in situ* humidity data from radiosondes over a wide range of air temperatures is still very much a problem.

6.7 Attenuation of infrared and visible radiation

The use of the electromagnetic spectrum above 1 THz (i.e. frequencies above 1000 GHz or $\sim 33\ \mathrm{cm}^{-1}$ or wavelengths smaller than 300 μm) for free-space communications is becoming of increasing interest. There are important applications in communications, space research and remote sensing for the bands extending from the infrared to the visible regions of the electromagnetic spectrum despite strong frequency-selective absorption and scattering in the troposphere. Therefore

the quantitative assessment of these applications and the appropriate selection of frequencies require detailed propagation information on these bands. Experimental and theoretical data are sometimes sparse and measured attenuation levels frequently depend on the characteristics of the equipment used (e.g. the frequency resolution). As a result only an approximate guide to this region of the electromagnetic spectrum can be given here, and more research is needed to facilitate reliable predictions. However it is possible to indicate those sections of the spectrum which are likely to be most useful and give guidance on how these bands may be affected by atmospheric phenomena.

Infrared and visible radiation is selectively absorbed by atmospheric gases and scattered by aerosols and hydrometeors such as rain, clouds and fog. The term "aerosol" is used for small particles (other than fog or cloud droplets) having sizes which range from clusters of a few molecules to 100 μm and larger [Pruppacher and Klett, 1997] with low terminal velocities. Dust and particles in sea-spray are examples of aerosols, which are discussed in Chapter 2. Aerosol concentration is highly variable in both time and space and depends strongly on the proximity of sources, on the rate of emission, on the strength of convective and turbulent diffusive transfer rates and on the efficiency of the various removal mechanisms. It is estimated that 80% of the total aerosol particle mass is contained below the lowest kilometre of the troposphere [Pruppacher and Klett, 1997]. The concentration of aerosols also decreases with increasing horizontal distance from the seashore towards the open ocean, because the land is a more efficient source of particles than the ocean. Within the Northern Hemisphere (responsible for the introduction of about 60% of the total mass of aerosol in the atmosphere), most of this aerosol mass enters the atmosphere at latitudes between 30°N and 60°N, since this belt contains about 88% of all anthropogenic sources of particulates [Pruppacher and Klett, 1997].

The relative contributions from absorption and scattering to the total attenuation will depend on the wavelength and the particle size. Moreover there will generally be some rapid fluctuations or "scintillation" in the received signal (between 0.01 Hz and 200 Hz), especially for paths close to the Earth's surface. Scintillation also causes distortion of the wave front resulting in beam defocusing. This is due to the random variations in refractive index associated with atmospheric turbulence, which is discussed in more detail in Chapter 4 of this Handbook and in Recommendation ITU-R P.1817 on the design of free-space optical links. The magnitude of scintillation increases with frequency; the variance of the signal, σ^2 (in dB^2), increases approximately as $f^{7/6}$ [Tatarski, 1961].

At wavelengths removed from the centres of molecular absorption lines (i.e. in window regions), the major limitations to system reliability and availability will generally be due to mist, fog, cloud or precipitation; all of these effects are considered elsewhere in this Handbook. However, a strong increase in water-vapour absorption can occur for example during very humid periods, while scintillation may reduce the usable bandwidth of an infrared or visible system.

The dominant factor is frequency-selective molecular absorption, especially in the wavelength region above 1 μm. The absorption is a strong function of wavelength and measurements made with very high spectral resolution show considerable fine structure in the absorption spectrum, arising from many transitions in the vibration-rotation bands of electrically polar atmospheric molecules. Therefore it is difficult to provide quantitative data for absorption without specifying the instrument resolution or bandwidth. Moreover, further spectroscopic measurements are required to provide the necessary detail. It is sufficient to indicate here the locations of the main absorption lines and atmospheric "windows" of relatively low molecular absorption. More information can be obtained from the US Air Force Geophysical Laboratory computer programs for transmittance: HITRAN (high resolution transmittance) listing over 1700000 lines from 37 molecular species over a spectral region from millimeter-wave to ultraviolet at a spectral resolution of 0.001 cm^{-1} (equivalent to 30 MHz) [Rothman *et al.*, 2005] or LOWTRAN 7 (low resolution transmittance), covering a range of frequencies from 0 to 50,000 cm^{-1} with a spectral resolution of 20 cm^{-1} (i.e. 600 GHz) [Kneizys *et al.,* 1989].

Figure 6.13 shows the main features of molecular absorption at sea level calculated using LOWTRAN 7 for the mean annual global reference atmosphere described in Recommendation ITU-R P. 835-5, with a spectral resolution of 20 cm^{-1}, from 100 to 20000 cm^{-1} (1 cm^{-1} corresponds to 30 GHz). The dominant absorption bands are mainly due to water vapour and carbon dioxide. Note that with a spectral resolution of 20 cm^{-1} the longer wavelength absorption lines are smoothed out to form the low-frequency continuum band shown in Figure 6.13.

FIGURE 6.13

Predicted specific attenuation due to gases, fog and rain at sea level from 100 to 20000 cm^{-1} (0.5 to 100 μm) using LOWTRAN 7 with the ITU-R mean annual global reference atmosphere (P = 1013.25 hPa, T = 288.15 K, ρ = 7.5 g/m^3 at the surface). [The frequency scale at the bottom corresponds to inverse wavelengths, also known as vacuum wave numbers: for example 100 cm^{-1} corresponds to 3 THz)]

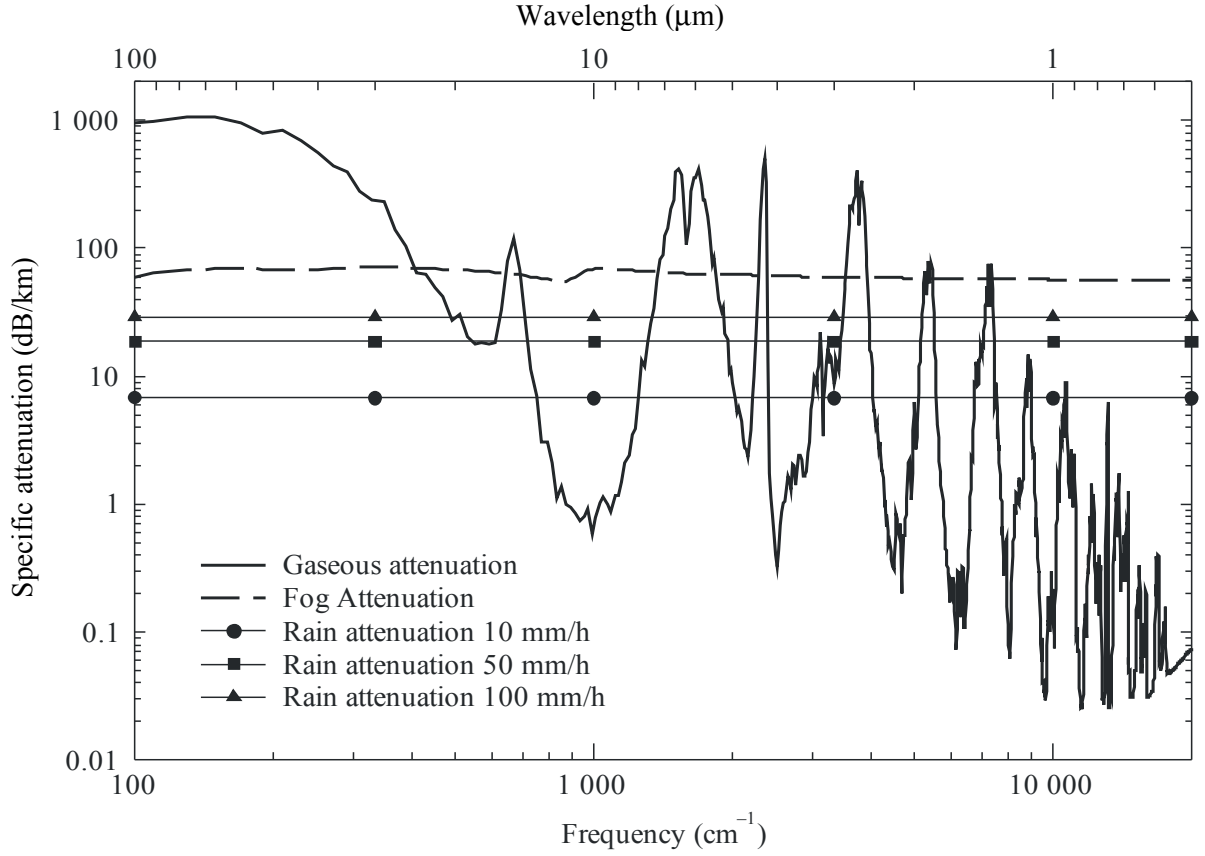

For comparison purposes, Figure 6.13 also shows specific attenuation from a fog dense enough to reduce the visual range to 200 m, and attenuation due to rain for rainfall rates of 10, 50 and 100 mm/h, calculated using a Marshall-Palmer drop-size distribution. It is important to mention that the infrared attenuation due to fog is extremely sensitive to its drop size distribution, which can be highly variable in both time and space; therefore predictions from models like LOWTRAN or HITRAN will vary in magnitude depending on the assumed fog particle distribution.

Relatively transparent atmospheric transmission windows can be seen in Figure 6.13: (a) 0.4 to 0.7 μm in the visible region; (b) near 1.7, 2.2, 3.5 and 5 μm; and (c) from 8 to 13 μm, for example. These bands, notably the 8 to 13-μm band, are of particular interest for communications and radar applications.

Figure 6.14 shows the spectral transmittance (i.e. the exponential of the negative of the total absorption coefficient) measured over a 1.8-km horizontal path at 30 m above sea level reproduced in [Chen, 1975]. The *horizontal* columnar water vapour content was 17 mm. These measurements were made in 1950 along the east coast of Scotland and were originally reported in Gebbie *et al.* [1951]. Transmission windows - where the transmittance exceeds 60% - are clearly visible. Molecular absorption bands for four species (molecular oxygen, water vapour, carbon dioxide and ozone) are identified in the lower part of Figure 6.14. Note the strong absorption bands due to CO_2 at around 4.3 μm and 15 μm and to water vapour at 2.7 μm and 6.3 μm. The latter band extends to 7.5 μm for this particular path given its columnar water vapour content [Gebbie *et al.*, 1951]. Moreover at 4.5 μm there is a band that corresponds to the fundamental vibration mode of nitrous oxide (N_2O). Absorptions measured at 7.7 and 7.9 μm also coincide with another fundamental vibration mode of N_2O, but cannot be unambiguously ascribed to it since several other molecular species absorb infrared energy in this spectral region [Gebbie *et al.*, 1951].

FIGURE 6.14

Measured atmospheric transmittance for a 1.8-km horizontal path located at 30 m above sea level along the east coast of Scotland, with a horizontal columnar water vapour content of 17 mm [Chen, 1975]. Note the presence of tropospheric ozone. Used with permission from the RAND Corporation

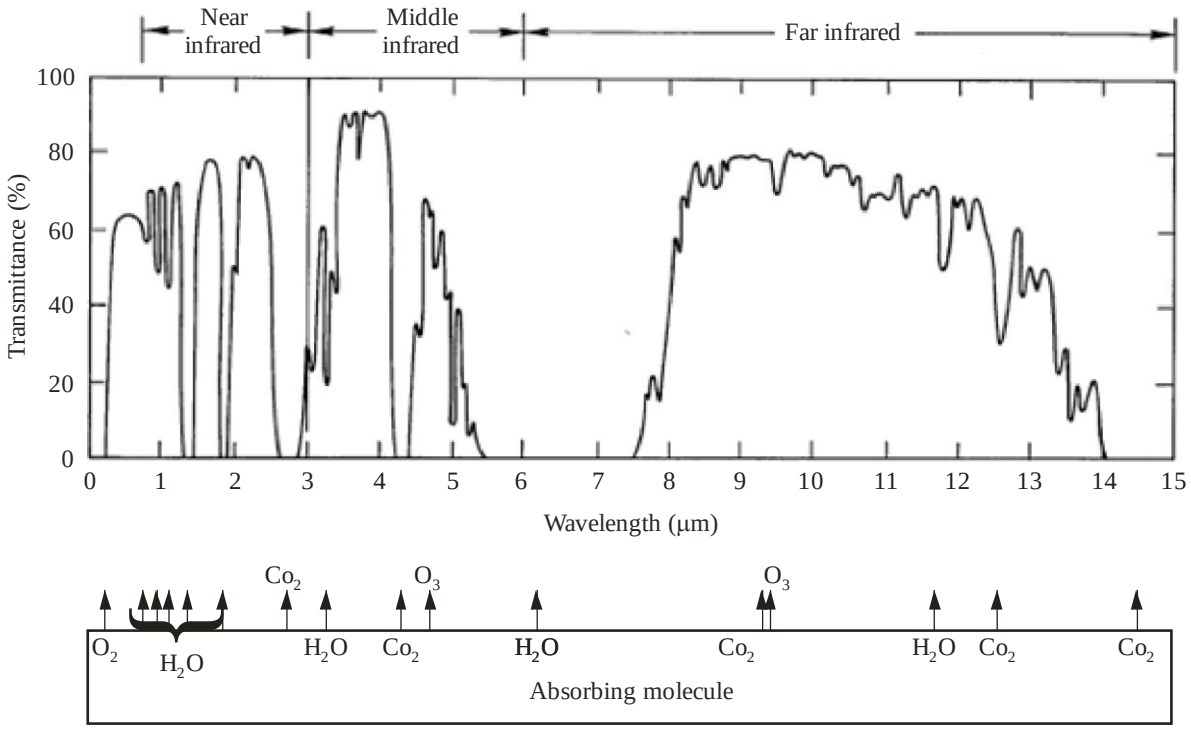

Radio-Meteo. 06-14

REFERENCES

BOHREN, C.F. and CLOTHIAUX, E.E. [2006] Fundamentals of atmospheric radiation, Wiley-VCH, Germany.

BOUCHARD, P. [2008] Observations of attenuation due to liquid-bearing stratocumulus clouds over Ottawa using a multifrequency profiling radiometer, Proc. 10th Specialist Meeting on Microwave Radiometry and Remote Sensing of the Environment (MicroRad'08), Florence, Italy, March 11-14.

CADEDDU, M.P., V.H. PAYNE, S.A. CLOUGH, K. CADY-PEREIRA and J.C. LILJEGREN [2007] Effect of the oxygen line-parameter modeling on temperature and humidity retrievals from ground-based microwave radiometers, IEEE Trans. Geosci. Remote Sens., 45, No. 7, pp. 2216-2223.

CHEN, C.C. [1975] Attenuation of electromagnetic radiation by haze, fog, clouds and rain, RAND Corporation Report R-1694-PR, Santa Monica, CA.

ELACHI, C. [1987] Introduction to the physics and techniques of remote sensing, John Wiley & Sons, New York, USA.

GEBBIE, H.A., HARDING, W.R., HILSUM, C., PRYCE, A.W. and ROBERTS, V. [1951] Atmospheric transmission in the 1 to 14μ region, Proc. Roy. Soc., A206, Issue 1084, pp. 87-107.

GIBBINS, C.J. [1986] Zenithal attenuation due to molecular oxygen and water vapour, in the frequency range 3-350 GHz, Electronics Letters, 22, No. 11, pp. 577-578.

GIBBINS, C.J. [1990] Propagation of very short pulses through the absorptive and dispersive atmosphere, IEE Proc. Pt. H., 137, pp 304-310.

HERZBERG, G. [1945] Molecular spectra and molecular structure II: Infrared and Raman spectra of polyatomic molecules, D. Van Nostrand Company.

HERZBERG, G. [1950] Molecular spectra and molecular structure I: Spectra of diatomic molecules (Second Edition), D. Van Nostrand Company.

KNEIZYS, F.X., ANDERSON, G.P., SHETTLE, E.P., ABREU, L.W., CHETWYND Jr., J.H., SELBY, J.E.A., GALLERY, W.O. and CLOUGH, S.A. [1989] LOWTRAN 7: Status, review and impact for short-to-long-wavelength infrared applications, AGARD Conference Proceedings No. 454, Atmospheric propagation in the UV, visible, IR and mm-wave region and related systems aspects, Copenhagen, Denmark, October 9-13, pp 13.1-13.11.

LIEBE, H.J. and LAYTON, D.H. [1987] Millimeter wave properties of the atmosphere: Laboratory studies and propagation modeling, National Telecommunications and Information Administration (NTIA) Report 87-24, Boulder, CO.

LIEBE, H.J. [1989] MPM-An atmospheric millimetre-wave propagation model, Int. J. Infrared and mm Waves, 10, No. 6, pp. 631-650.

LIEBE, H.J., ROSENKRANZ, P.W. and HUFFORD, G.A. [1992] Atmospheric 60-GHz oxygen spectrum: New laboratory measurements and line parameters, J. Quant. Spectrosc. Radiat. Transf., 48, pp. 629-643.

LIEBE, H.J., HUFFORD, G.A. and COTTON, M.G. [1993] Propagation modeling of moist air and suspended water/ice particles at frequencies below 1000 GHz, AGARD Conference Proceedings No. 542, Atmospheric propagation effects through natural and man-made obscurants for visible to mm-wave radiation, pp. 3-1-3-11.

LILJEGREN, J.C., BOUKABARA, S., CADY-PEREIRA, K. and CLOUGH, S.A. [2005] The effect of the half-width of the 22 GHz water vapour line on retrievals of temperature and water vapor profiles with a 12-channel microwave radiometer, IEEE Trans. Geosci. Remote Sens., 43, No. 5, pp. 1102-1108.

MATTIOLI, V., WESTWATER, E.R., GUTMAN, S.I. and MORRIS, V.R. [2005] Forward model studies of water vapor using scanning microwave radiometers, global positioning system, and radiosondes during the Cloudiness Intercomparison Experiment, IEEE Trans. Geosci. Remote Sens., 43, No. 5, pp. 1012-1021.

MÄTZLER, C. (editor) [2006] Thermal microwave radiation: Applications for remote sensing, The Institution of Engineering and Technology (IET), Herts, United Kingdom.

PAPATSORIS, A.D. and WATSON, P.A. [1993] Calculation of absorption and dispersion spectra of atmospheric gases at millimetre-wavelengths, IEE Proceedings-H, 140, No.6, pp. 461-468.

PARDO, J.R., SERABYN, E. and CERNICHARO, J. [2001a] Submillimeter atmospheric transmission measurements on Mauna Kea during extremely dry El Niño conditions: Implications for broadband opacity contributions, J. Quant. Spectrosc. Radiat. Transf., 68, pp. 419-433.

PARDO, J.R., CERNICHARO, J. and SERABYN, E. [2001b] Atmospheric Transmission at Microwaves (ATM): An improved model for millimeter/submillimeter applications, IEEE Trans. Antennas Propagat., AP-49, No. 12, pp. 1683-1694.

PRUPPACHER, H.R. and KLETT, J.D. [1997] Microphysics of clouds and precipitation, Second edition, Kluwer Academic Publishers, Dordrecht, The Netherlands.

ROSENKRANZ, P.W. [1975] Shape of the 5 mm oxygen band in the atmosphere, IEEE Trans. Antennas Propagat., AP-23, No. 4, pp. 498-506.

ROSENKRANZ, P.W. [1988] Interference coefficients for overlapping oxygen lines in air, J.Quant. Spectr. Rad. Transf., 39, pp. 287-297.

ROSENKRANZ, P.W. [1998] Water vapour microwave continuum absorption: A comparison of measurements and models, Radio Sci., 33, pp. 919-928.

ROSENKRANZ, P.W. [1999] Correction to water vapour microwave continuum absorption: A comparison of measurements and models, Radio Sci., 34, p.1025.

ROTHMAN, L.S., JACQUEMART D. and BARBE, A. [2005] The HITRAN 2004 molecular spectroscopic database, J. Quant. Spectrosc. Radiat. Transf., 96, pp. 139-204.

TATARSKI, V.I. [1961] Wave Propagation in a Turbulent Medium, McGraw-Hill, New York, USA.

WATERS, J.W. [1976] Absorption and emission by atmospheric gases, Methods of Experimental Physics, 12B, Ed. M. L. Meeks, Academic Press, New York, USA.

WESTWATER, E.R., SNIDER, J.B. and FALLS, M.J. [1990] Ground-based radiometric observations of atmospheric emission and attenuation at 20.6, 31.65, and 90 GHz: A comparison of measurements and theory, IEEE Trans. Antennas Propagat., AP-38, No. 10, pp. 1569-1580.

WESTWATER, E.R., HAN, Y., SHUPE, M.D. and MATROSOV, S.Y. [2001] Analysis of integrated cloud liquid and precipitable water vapor retrievals from microwave radiometers during the Surface Heat Budget of the Arctic Ocean project, J. Geophys. Res., 106, No. D23, pp. 32019-32030.

WESTWATER, E.R., STANKOV, B.B, CIMINI, D., HAN, Y., SHAW, J.A., LESHT, B.M. and LONG, C.N. [2003] Radiosonde humidity soundings and microwave radiometers during Nauru99, J. Atmos. Oceanic Technol., 20, pp. 953-971.

CHAPTER 7

Attenuation by atmospheric particles

Hydrometeors in the form of rain, hail or wet snow can produce severe attenuation of radio waves. In most locations, rain is the dominant form of atmospheric precipitation. Although rain absorbs and scatters energy at all frequencies, rain attenuation is only important for frequencies above several gigahertz.

Although rain is the most important type of hydrometeor affecting wave propagation, clouds, fog, snow, hail and the melting layer (mainly on Earth-space paths) are other sources of attenuation. Attenuation due to clouds may be significant for Earth-space links operating at frequencies above 10 GHz and at low elevation angles. Cloud attenuation may represent the most relevant impairment for low-availability systems where there is very light or no rain; and, in this case, cloud attenuation may determine the link margin [Tervonen and Salonen, 2000; Dissanayake *et al.*, 1997, 2001]. The melting layer is the region, just below the 0ºC isotherm level, where ice and snow hydrometeors become water drops. Attenuation due to the melting ice particles increases with increasing frequency [Dissanayake *et al.*, 2002] and can reach significant levels. The impact of this additional attenuation cannot be neglected in slant path radio wave propagation. Many rain attenuation prediction models use an "effective rain height" rather than the melting layer height added to the rain height to obtain the total rain attenuation. Attenuation caused by sand and dust particles appears to be of minor importance in most regions of the world, and significant propagation effects are rare. However, analyses indicate that attenuation could be important at frequencies above about 10 GHz in certain extreme conditions.

Because the rain process is variable in space and time, careful consideration must be given to the vertical and horizontal structure of rain events, to the time-scales over which the intensity and nature of rain changes, and the variation in the various rain characteristics between geographical locations.

7.1 Prediction of specific attenuation from rain intensity data

Attenuation due to rain is important in terrestrial or Earth-space communications systems at frequencies above 10 GHz and increases significantly up to a frequency of 100 or 200 GHz (see Figure 7.1). Above about 200 GHz, depending on the rain rate, the specific attenuation decreases slightly with increasing frequency, until at 1000 GHz, where it has nearly reached its optical limit. The nature of this attenuation has been intensively studied both theoretically and experimentally. Because the free-space wavelengths (30 mm to 1.5 mm) of the radio waves subject to attenuation are comparable with the diameters of the raindrops typically responsible for producing this attenuation (approximately 1 mm to 6 mm), it is usually necessary to use Mie scattering theory to compute the specific attenuation resulting due to rain.

The specific attenuation is defined as the rate of attenuation per unit distance and can be expressed as:

$$\alpha = 0.434 \int_0^{D_{max}} \sigma_{\text{ext}}(D) \bullet N(D)\, dD \qquad \text{dB/km} \tag{7.1}$$

where $N(D)dD$ is the number of raindrops with diameters between D and $D+dD$ per unit volume (m^{-3}), and σ_{ext} is the scattering cross-section, expressed in cm^2 (see Chapter 5).

Another approach to determining the attenuation due to hydrometeors has been to treat the medium as an artificial, complex dielectric [Van de Hulst, 1957]. Kharadly and Choi [1988] extended this approach to include attenuation due to water-coated snow within the melting layer.

Figure 7.1 illustrates the behaviour of the specific attenuation coefficient, derived on the basis of Mie calculations, as a function of frequency for various values of rain rate under the assumptions indicated [Rogers and Olsen, 1976]. Rain intensity, usually expressed in mm/h, is a function of drop-size distribution and the drop-fall velocity and can be expressed as:

$$R = 6 \times 10^{-6} \pi \int N(D) \bullet D^3 \bullet v(D) \quad dD \qquad \text{mm/h} \qquad (7.2)$$

where $v(D)$ is usually assumed to be the terminal velocity (m/sec) for drops of diameter D (mm) in still air.

FIGURE 7.1

Specific attenuation γ_R due to rain

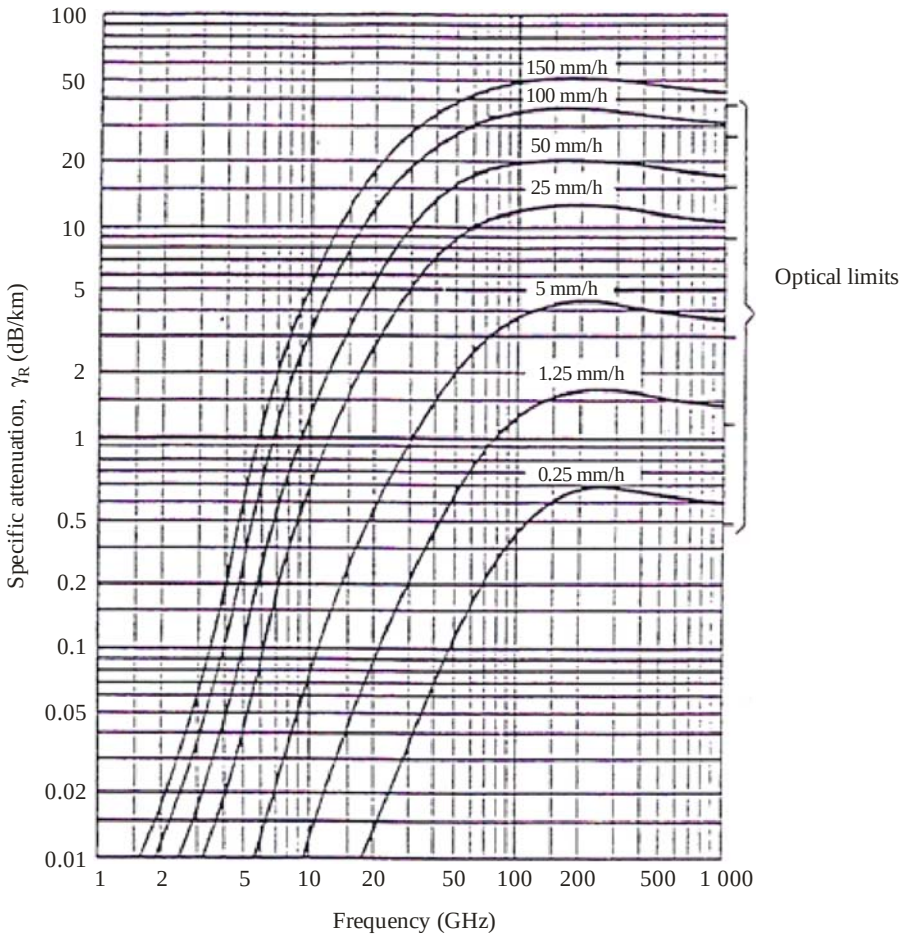

Radio-Meteo. 07-01

Raindrop size distribution [Laws and Parsons, 1943]
Terminal velocity of raindrops [Gunn and Kinzer, 1949]
Index of refraction of water at 20°C [Ray, 1972]
Spherical drops

Variations in temperature from the assumed values are only important at frequencies below 20 GHz and may result in changes of up to 20% from the curves in Figure 7.1.

A limitation of the results shown in Figure 7.1 is the assumption that the raindrops are spherical. Because raindrops falling through a viscous atmosphere are known to be non-spherical [Pruppacher and Pitter, 1971], horizontally polarized waves suffer greater attenuation than vertically polarized waves. In some climates the difference in attenuation may be as much as 35% [Fedi *et al*., 1977; Fimbel and Juy, 1977]. The specific attenuation for vertical and horizontal polarizations, and frequencies up to 100 GHz, may be obtained from calculations that account for the non-spherical shape of the raindrops [Oguchi, 1977].

For practical applications, the relationship between attenuation γ_R (dB/km) and rain rate R (mm/h) can be approximated by the power-law:

$$\gamma_R = k R^{\alpha} \tag{7.3}$$

Values of k and α for a Laws and Parsons drop-size distribution and a drop temperature of 20°C have been calculated by assuming oblate spheroidal drops aligned with a vertical rotation axis and with dimensions related to equal volume spherical drops [Maggiori, 1981].

The results in Figure 7.1 apply generally for an incident plane wave, an isotropic spherical wave, or a spherical wave with a finite beam. Their applicability for rain in the near field of the antennas has been confirmed [Haworth, 1980]. The calculations assume a coherent wave and are only applicable for coherent communications systems. Since only a small amount of power due to incoherent scattering will enter a narrow beam receiving antenna, the calculations can also be used as an approximation for incoherent transmission systems.

Although commonly thought to include only the effects of single scattering, the theory [Van de Hulst, 1957] also includes the effects of the forward multiple scattering processes (i.e. those processes in which the multiple scattering paths between the scatterers all have components in the forward direction). Due to the limited raindrop population in even the heaviest rains, these are the only multiple scattering processes which give a significant contribution to the average (or coherent) field transmitted through the rain [Rogers and Olsen, 1983]. At visible and infrared wavelengths, the specific attenuation due to rain is almost independent of frequency since the drops are much larger than the wavelength.

The Laws and Parsons [1943] raindrop size distribution was based on the first reliable experimental measurement of the distribution of raindrop sizes. While it was based on measurements for rain rates up to 50 mm/h, it can be extrapolated beyond this limit. Subsequent experimental observations have suggested a large number of models for the raindrop size distribution, and these have appeared in the literature. These models are generally expressed in algorithmic form and may be categorized into the following four groups:

1. Negative exponential distributions;
2. Lognormal and shifted lognormal distributions;
3. Gamma function distributions; and
4. Weibull distributions.

Drop-size distributions represented by a negative-exponential function is the most common distribution [Marshall and Palmer, 1948; Joss *et al*., 1968; Manabe *et al*., 1984; Ihara *et al*., 1984; Awaka *et al*.; 1987; Yang *et al*., 2001; Uijlenhoet; 2001].

The distribution of Joss *et al*. differs from the others in that it explicitly recognizes basic differences in the drop-size distributions for three rain types: thunderstorm or convective rain, widespread rain,

and drizzle. At relatively high rain rates, which are important in the design of communications systems at frequencies above 10 GHz, the Laws and Parsons distribution gives higher specific attenuation than the thunderstorm distribution of Joss *et al*. This difference is particularly significant at frequencies above 100 GHz. In comparison, the drizzle distribution of Joss *et al*. gives higher specific attenuations at low rain rates in this frequency regime [Olsen *et al*., 1978].

Multi-frequency attenuation measurements at frequencies between 12 and 240 GHz were found to support the negative-exponential form of the drop-size distribution in Japan [Manabe *et al*., 1984; Ihara *et al*., 1984; Awaka *et al*., 1987]. This negative-exponential drop-size distribution has greater population of small drops than the Laws and Parsons drop-size distribution, and results in greater values of specific attenuation coefficients above about 80 GHz. The slope of the distribution was also found to deviate from the classic Marshall-Palmer values for low and moderate rain rates. A similar deviation in the slope of the distribution has been observed in Europe [COST 205, 1985a].

Other functional descriptions have included the log normal distribution [Ajayi and Olsen, 1985; Massambani and Rodrigues, 1987; Maitra and Gibbins, 1999; Veyrunes, 2000]. In equatorial regions, some measurements of drop-size distributions suggest that the negative exponential form may not be appropriate; however, the specific attenuation coefficients for frequencies below 30 GHz calculated from a log-normal model based on Nigerian data do not differ greatly from those derived from the negative exponential model [Ajayi, 1985; Ajayi and Olsen, 1985].

The Gamma distribution was tested by several authors [Ajayi and Olsen, 1985; Maitra and Gibbins, 1999], and List *et al*. [1987] proposed a tri-modal Gamma distribution on the basis of both theoretical and experimental observation.

The Weibull distribution, described by Assouline and Mualem [1989] and Brussaard and Watson [1995], has been applied to a variety of climates; and Åsen and Gibbins [2002] have investigated the Weibull distribution for temperate and tropical climates.

There is considerable uncertainty regarding the number density of raindrops of very small diameters. These raindrops are relatively difficult to detect, and their number density may have significant variation due to their very low mass and low fall velocities. This variation is particularly significant at higher frequencies where the smaller drops become increasingly important in the calculation of specific attenuation.

Experimental and theoretical studies of rain drop terminal velocities lead to fairly consistent results [Gunn and Kinzer, 1949; Best, 1950; Beard, 1976].

In recent years, a number of works have been published in the literature concerning the calculation of specific attenuation, either analytically or by empirical means [Li *et al.*, 2000; Der-Phone and Hsing-Li, 2002; Zhao *et al.*, 2000; Asen and Gibbins, 2002].

[Gibbins and Walden, 2003] computed the regression parameters k and α for a variety of combinations of raindrop size distributions and raindrops terminal velocity and proposed expressions for these parameters that minimize the error in the prediction of rain attenuation. The raindrop shape as modeled as oblate spheroids, and the specific attenuations was calculated for frequencies from 1 to 1000 GHz for a range of temperatures between 0º and 30ºC using the extended boundary condition or T-matrix method [Mishchenko *et al.*, 2000]. The calculations were performed considering several models for drop size distributions and terminal velocities models. The results were fitted to the power-law equation $\gamma = k R^{\alpha}$ for rain rates between 1 and 150 mm/h, and the power-law coefficients were derived using a nonlinear least-squares fitting procedure based on a finite difference Levenberg-Marquardt algorithm.

These coefficients were applied to the rain attenuation prediction method in Recommendation ITU-R P.530 for terrestrial paths, modified by the use of several different path length reduction factors found in the literature. The performance of each model was assessed using the ITU-R terrestrial links rain attenuation data base and the test variable in Recommendation ITU-R P.311. The best overall performance was obtained using the Ulbrich [1983] rain drop size distribution with path length adjustment factors based on Lin [1977].

Finally, the sets of values of k and α were calculated, for both horizontal and vertical polarizations, with the Ulbrich (Laws and Parsons) rain drop size distribution, and fitted using sums of Gaussian functions of frequency to produce the method currently adopted in Recommendation ITU-R P.838.

7.2 Attenuation over propagation links of finite extent

In addition to the uncertainty in determining the specific attenuation, there is greater uncertainty in determining the attenuation for a terrestrial or Earth-space propagation path.

The total attenuation due to rain over a particular path may be calculated by integrating the specific attenuation over the path. Unfortunately, this detailed information is not generally available. Several methods have been proposed for predicting rain attenuation statistics from rain rate measurements along or near the path. Although many campaigns have measured rain rate distributions at particular locations, usually close to the antenna site, these measurements have limited applicability for describing the rain along the path. Even in cases in which a considerable number of raingauges, spread in some fashion across large area were used, the measured rain profiles showed marked signs of spatial and temporal inhomogeneity. Regarding tropical rain, the meteorological community is in agreement that a convective rain event is a composite of convective and stratiform rain [Houze, 1977]; and radar imagery confirms that in regions subjected to heavy convective rain, there is always a concurrent blanket of stratiform rain [Crane, 1980].

The methods for rain attenuation prediction all make use of the relationship between the specific attenuation and rain rate. It is therefore of primary importance to rely on accurate rain rate prediction models, in order to obtain at the end accurate rain attenuation prediction models. The difficulty comes from the fact that rain rate are highly variable and strongly dependent on the climate (heaviest rain intensities occur in tropical and equatorial regions). The conventional information available from meteorological offices is cumulative amounts of rain, so there were some attempts to develop global models to obtain the cumulative distribution function of rain rate from available meteorological information [Rice-Holmberg, 1973; Dutton *et al.*, 1974; Tattelmann and Scharr, 1983; Moupfouma and Martin, 1995; Boithias, 1990; Flavin, 1996.

Poiares and Salonen [1998] proposed a global method using as input data meteorological data from several organizations such as the European Centre for Medium-range Weather Forecasts (ECMWF) and the Global Precipitation Climate Project (GPCP). The method is based in obtaining the rain, averaged over one year, from the conversion of 6 hour rain measurements and the annual amount of stratiform rain. The Salonen-Baptista model is exponential in nature and is the basis of ITU-R Recommendation ITU-R P.837.

7.2.1 Effects of spatial non-uniformity in rain

Rain intensity is highly variable both in space and in time. The main difference between the various prediction methods is how they account for this variability along the propagation path.

The so-called "synthetic storm method" [Drufuca, 1974; Matricciani, 1996] generates attenuation statistics by converting rain rate/time profiles recorded at a point, to rain rate/distance profiles, using the translation velocity of the rain pattern; and a good estimate of estimating the translation velocity is the wind speed derived at the 700 mb level from a conventional radiosonde [Drufuca,

1974; Bertok *et al*., 1977; Segal, 1982]. Although this method requires a very detailed database, it provides a high degree of physical realism.

Some methods derive the statistical profile of rain along the path assuming a single cell of suitable shape [Misme and Fimbel, 1975; Misme and Waldteufel, 1980; Bryant, 1999] or a statistical distribution of cells sizes of a particular shape [Rue, 1981; Capsoni *et al.,* 1987]. The “effective path length” that multiplied by the point rain rate gives the total attenuation is the average path length intercepted by the rain cell considering that the rain cell can assume any position relatively to the link with equal probability.

Fedi [1981] uses the concept of effective path length, in a simplified model, assuming a single cell with a rectangular cross-section in the plane of the path. This model requires only one value of the cumulative distribution of rain intensity, namely the value exceeded for 0.01% of the time, with an extrapolation to other time percentages.

Numerous modelling and prediction methods have been developed that have provided good agreement with experimental observations. Many of these predictions methods are compared with local measured data and are biased towards local conditions. They generally produce adequate results when applied globally and tested against the ITU-R testing criteria. These prediction methods are semi-empirical, i.e., they combine theoretical analysis and meteorological measured data from several locations. These models adopt the concept of effective path length or effective rain rate to account for the non-uniform rain intensity along the actual path. One approach has been to characterize the horizontal rain structure by a "reduction" coefficient which may be derived from the spatial autocorrelation function of rain [Morita and Higuti, 1976], from measurements using rapid-response rain gauges spaced along a line [Harden *et al*., 1978a; Crane, 1980], or from a semi-empirical law fitted against measured data [Assis and Einloft, 1977; Battesti and Boithias, 1978; García-López *et al.*, 1988; Gibbins and Walden, 2003; Zhao et al., 2007; Silva Mello et al., 2007]. The equivalent path-averaged rain rate is obtained by multiplying the point rain rate by this reduction coefficient.

The reduction coefficient, which initially only depended on the path length, was subsequently modified to depend on the rain intensity [Yamada *et al*., 1987]. A number of path reduction factors, originally intended only to represent the inhomogeneity of rain, have been derived empirically from extensive curve-fitting to experimental data providing expressions including frequency, specific attenuation or related variables in addition to the original path length and rain rate parameters.

Although the ratio of effective to actual rain intensity or path length is referred to as a reduction coefficient, it must be noted that it may be greater than unity for sufficiently small rain rates or large probabilities of occurrence. In view of this, it is more appropriate to denote this term as a “path length adjustment factor”.

Ideally, the slant path rain attenuation prediction method for should be an extension of the terrestrial rain attenuation prediction method, with one of the terminals at an altitude above the rain height. The path length adjustment factor for the horizontal component of the slant path should ideally be the same as that employed in the terrestrial model. With this assumption, it would be necessary to define a “vertical adjustment” factor, to account for the inhomogeneities in the vertical distribution of rain.

The rain attenuation prediction method currently adopted in Recommendation ITU-R P.530 for terrestrial links uses the concept of effective path length to take into account the variability of rain intensity along the path and requires only one value of the cumulative distribution of rain intensity, the value exceeded for 0.01% of the time. The rain attenuation was extrapolated to different exceedance probabilities from the attenuation exceeded for 0.01% of the time. Since the shape of the attenuation probability distribution depends on the climatic region, the extrapolation formula is

latitude dependent. However, this procedure results in non-physical discontinuities in the attenuation distributions at the boundaries between the latitude regions.

The slant path rain attenuation prediction procedure currently adopted in Recommendation ITU-R P.618 uses the concept of vertical and horizontal path adjustment factors to account for the variability of rain intensity along the slant-path. Similar to the prediction method for terrestrial links, the prediction method for slant paths requires only one value of the cumulative distribution of rain intensity, the value exceeded for 0.01%. The rain attenuation is extrapolated to different exceedance probabilities from the attenuation exceeded for 0.01% of the time. Since the shape of the attenuation probability distribution depends on the climatic region, the extrapolation formula is latitude dependent. However, this procedure results in non-physical discontinuities in the attenuation distributions at the boundaries between the latitude regions.

7.2.2 Earth-space links

Similar to terrestrial paths, it is desirable to derive path attenuation statistics from long-term meteorological data. However, because the path attenuation depends on the vertical as well as the horizontal structure of precipitation, the problem is more complicated.

Various models have been proposed to account for the vertical structure [Brussaard, 1981], and a number of these techniques are extensions of those developed for terrestrial paths [Fedi, 1980; Lin *et al*., 1980; Rue, 1981; Moupfouma, 1984; Stutzman and Dishman,1984; Garcia-Lopez *et al*., 1988]. Others models have been derived on the basis of extensive studies of the rain structure [Crane, 1980; Fedi and Paraboni, 1986; Leitao and Watson, 1986; Rue, 1988; Li *et al*., 1987]. More recently, several models were proposed based on measurements of slant path rain attenuation [Matricciani, 1991; Flavin, 1996; Gibbins and Walden, 2003; Zhao *et al*., 2004; 2007; Silva Mello and Pontes, 2008].

The path length adjustment factor is the approach that is most often adopted. The adjust factor for slant-paths is slightly more complicated than for terrestrial paths because the path length through the rain is not determined solely by the link geometry. Instead, the path through the rain is considered to extend from Earth station up to the rain height. Information on the rain height can be derived from Recommendation ITU-R P.839 for the appropriate latitude and longitude, if this is not known for the location of interest. There are then two path length adjustment factors used in the slant-path attenuation prediction method: one for the horizontal component, which accounts for the non-homogeneity of rain near ground level (as in the case for terrestrial paths), and one for the vertical component, to account for the variability of rain rate with height.

The method adopted in Recommendation ITU-R P.618 was developed [Dissanayake *et al*., 1997] by applying two path adjustment factors: one for the horizontal and one for the vertical component. Both of these adjustment factors are empirically derived and depend on the frequency, rain rate at the 0.01% exceedance probability, rain height and path length. Similar to the prediction method for terrestrial links, the prediction method for slant paths requires only one value of the cumulative distribution of rain intensity, the value exceeded for 0.01%. The rain attenuation is extrapolated to different exceedance probabilities from the attenuation exceeded for 0.01% of the time. Since the shape of the attenuation probability distribution depends on the climatic region, the extrapolation formula is latitude dependent. However, this procedure results in non-physical discontinuities in the attenuation distributions at the boundaries between the latitude regions.

Extensive tests performed on the basis of available methods and data have suggested that the accuracy obtainable with the method of Recommendation ITU-R P.618 is about 25% - 30% on a global basis. Long-term statistical data, especially from tropical regions, are needed to improve the prediction accuracy.

7.3 Prediction of attenuation from radio propagation data

Although the prediction of rain attenuation is generally based on some model that utilizes climatic data for a specific location or region, it is sometimes necessary or advisable to adopt a non-meteorological approach. Scaling of rain attenuation statistics in frequency is a useful technique if measured attenuation data is available for a specific location. This technique predicts the attenuation statistics at one or more frequencies from the measured attenuation statistics at a different frequency.

More sophisticated methods of scaling attenuation statistics have been proposed in the literature. For Earth-space paths, the influence of elevation angle may be included; however, this appears to have a small effect [Rue, 1985]. Other proposed methods use measured data at multiple frequencies.

Scaling methods are generally applicable in a statistical sense; that is, they apply to exceedance probabilities averaged over a considerable length of time.

Extensive studies have been performed on frequency scaling of long-term statistical methods [COST 205, 1985b; Upton *et al*., 1987; Boithias, 1989] showing that these techniques are accurate within 10% in the probability range of 0.001% to 0.1%.

This indicates that the application of frequency scaling methods from measured attenuation data may be preferable to predicting attenuation from measured rain rate data, if statistically reliable data is available for a desired location.

It has been observed that the scaling factor is influenced more by year-to-year variability than by site-to-site variability and thus the same formula may be used for different regions as well.

Note that current frequency-scaling formulae fail to take polarization into account.

7.3.1 Single-frequency scaling: constant attenuation ratio

The following empirical formula based on a constant attenuation ratio may be applied for frequency scaling for a given polarization [Boithias and Battesti, 1981]:

$$\frac{A_1}{A_2} = \frac{g(f_1)}{g(f_2)} \tag{7.4}$$

where:

$$g(f) = \frac{f^{1.72}}{1 + 3 \times 10^{-7} \; f^{3.44}} \tag{7.5}$$

A_1 and A_2 are the values of attenuation (in dB) at frequencies f_1 and f_2 (in GHz), respectively, and are exceeded with equal probability.

This formula implies a constant ratio of the attenuations at the two frequencies, whereas the actual ratio will vary with rain rate. However, this formula gives reasonable results over a frequency range of about 7 to 50 GHz and for attenuation values of practical interest.

7.3.2 Single-frequency scaling: variable attenuation ratio

If reliable measured attenuation data at one frequency is available, the following empirical formula, based on an attenuation ratio which is a function of frequency and attenuation, may be used for frequency scaling on the same path in the frequency range 7 to 55 GHz [Boithias, 1989]:

$$A_2 = A_1 \left(\frac{\varphi_2}{\varphi_1} \right)^{1-H(\varphi_1, \varphi_2, A_1)} \tag{7.6}$$

$$\varphi(f) = \frac{f^2}{1 + 10^{-4}\ f^2} \tag{7.7}$$

$$H(\varphi_1, \varphi_2, A_1) = 1.12 \times 10^{-3} \left(\frac{\varphi_2}{\varphi_1} \right)^{0.5} (\varphi_1\ A_1)^{0.55} \tag{7.8}$$

where f is in GHz.

7.3.3 Multi-frequency scaling

Attenuation statistics at two frequencies may be used to predict statistics at another frequency [Hogg, 1973; Matricciani, 1980; Capsoni *et al*., 1980; Kheirallah and Olsen, 1981]. Other methods use experimental data at three different frequencies to derive the parameters of a statistical model for the rain intensity profile [Harris and Hyde, 1977; Muller, 1977] or for the path-averaged raindrop-size distribution [Ihara and Furuhama, 1981; Furuhama and Ihara, 1981] to predict attenuation at another frequency. It is difficult to determine the spatial structure of rain intensity from purely radio frequency measurements due to the variability of the rain microstructure [Fedi *et al*., 1977; Harden *et al*., 1978b; Debrunner, 1980].

7.3.4 Instantaneous scaling: single frequency

For some applications, such as systems that use uplink power control for broadcast satellite feeder links, knowledge of the attenuation on one frequency is used for mitigate fading at a different frequency. For these techniques to successfully mitigate attenuation, knowledge of the variation of the ratio of the instantaneous attenuation at the two frequencies is required. Measurements carried out in Europe [COST 205, 1985b] indicated that the instantaneous attenuation ratio of two frequencies the 11 - 14 GHz band is log-normally distributed.

7.3.5 Path length scaling of rain attenuation statistics for line-of-sight links

Scaling measured attenuation statistics for different path lengths is also a useful technique within a limited region, and asymptotic path length scaling techniques have been suggested [Rogers, 1976]. For example, if the attenuation statistics are dominated either by the occurrence of relatively small cells of heavy rain or by widespread precipitations, their dependence on path length can be described by simple formulae. In the first case, the probability $P_2\{A\}$ that the attenuation A is exceeded on a path of length D_2 is proportional to the probability $P_1\{A\}$ on the path D_1 as:

$$P_2\{A\} = \frac{D_2 \bullet P_1\{A\}}{D_1} \tag{7.9}$$

Assuming widespread precipitations, the attenuation A exceeded with a given probability P is proportional to the path length:

$$P_2\{A_2\} = P_1 \left\{ \frac{D_1\ A_2}{D_2} \right\} \tag{7.10}$$

where $P\{A\}$ denotes the functional relationship between the probability P and the attenuation A.

7.4 Variability of rain attenuation statistics

The highest values of attenuation are produced by rare events. An adequate statistical description of these rare events requires measurements over a number of years to allow for confidence in the statistics of these rare events. Long-term measurements (5-9 years) of rain attenuation in Europe [COST 205, 1985c] show that the year-to-year variability (defined as the percentage variation in the long-term value of attenuation) can be substantial: at 0.01% of the time, the year-to-year variability was greater than 25%. In this experiment, using consecutive years and a sliding average, four years of measurements were needed to reduce the variability to a value higher than about 8%.

7.5 Radiometer and radar measurements

Attenuation can be easily measured on terrestrial paths. Attenuation can be measured at many on Earth-space paths using satellite downlinks; however, these measurements are available for a limited number of locations, frequencies, and elevation angles. Other approaches, such as radiometric and radar measurements, use the physical characteristics of hydrometeors to infer attenuation.

With radiometric techniques, the attenuation can be inferred from measurements of sky-noise temperature or can be using the Sun as a source. Due to the nonlinear relationship between attenuation and sky noise temperature, the maximum value of attenuation that can be inferred with reasonable accuracy is limited. However, in the absence of an available downlink signal source, this radiometric technique provides a simple method of estimating attenuation statistics at any location and elevation angle [Brussaard, 1985]. Inference errors can result from applying data obtained at frequencies at which the scattering contribution to the total attenuation is significant [Zavody, 1974]. Measurements made in the United Kingdom at frequencies in the range of 30 to 37 GHz have shown that the error in underestimating the attenuation is unlikely to exceed 15% of the dB value in vertical polarization, but may reach 35% in horizontal polarization if scattering is ignored. At 20 GHz, however, the error for these same climatic conditions can probably be ignored for practical purposes [Chada and Lane, 1977].

Solar radiometry provides direct and sufficiently accurate measurements of attenuation over a dynamic range of about 15 dB. However, data obtained from solar radiometry has limited applicability due to the motion of the Sun and biasing of the statistics by diurnal effects. Since heavy precipitation events are generally not uniformly distributed over a day, attenuation distributions obtained by Solar radiometry have limited validity and are generally not recommended for providing path attenuation statistics.

Well-calibrated weather radar observations can be used to estimate the attenuation on a slant path since the radar can potentially observe rain extending over large areas and heights [Crane, 1977]. In addition to estimating rain attenuation statistics on a single Earth-space path, weather radar observations can also estimate the joint attenuation statistics on two or more separate paths (site diversity) [Rogers and Olsen, 1976; Goddard and Cherry, 1984a].

Several types of radars have been used for this purpose, including single-frequency radars, dual-frequency radars, and dual-polarization radars. An inherent limitation of single frequency radar is its inability to distinguish rain from ice, since rain and ice have different relations between radar reflectivity and specific attenuation. The melting layer may produce a significant contribution which cannot be estimated by the same means as used for rain. Radar reflectivity is related to rain rate assuming a particular drop-size distribution. In the localized regions of intense rain, drop-size distribution changes will influence the relationship between radar reflectivity and rain rate. One method of partially overcoming this limitation is to use a single-frequency radar simultaneously with other observing instruments such as radiometers, distrometers, rain gauges and satellite beacons. The calibration of a radar with one or more of these devices allows the attenuation

statistics to be estimated with improved accuracy [Strickland, 1974; Hodge and Austin, 1977; Furuhama *et al*., 1980; Goldhirsh, 1980; McEwan *et al*., 1980; Rogers *et al*., 1981]. Another way to avoid errors due to the assumed relation between radar reflectivity and specific attenuation is to use two frequencies, one with high attenuation, and the other with negligible attenuation [Joss *et al*., 1974; Yamada *et al*., 1978]. This method has been shown to give directly a good measurement of the rain attenuation along the radar beam at the frequency of high attenuation up to the melting layer [CCIR, 1978-82].

Dual-polarization radar can be used to distinguish between rain and other hydrometeors [McCormick and Hendry, 1975] and ignore regions of high reflectivity but negligible attenuation due to ice particles [Radio Science, 1984]. In addition, the characteristics of the drop-size distribution can be determined using dual-polarization techniques [Hall *et al*., 1980]. This has been shown to be a good predictor of the attenuation on an Earth-space path, even if the path does not originate at the radar site [Goddard and Cherry, 1984b].

7.6 Propagation delay due to precipitation

In addition to causing attenuation, precipitation can also result in an increase in propagation delay. Calculations of the specific phase delay and group delay through rain have been obtained from Mie scattering theory [Nuspl *et al*., 1975]. These predictions can be combined with rain rate statistics and estimates of effective path length to predict path delay statistics. A more flexible technique, and one less dependent on the drop-size distribution, is to combine delay/attenuation ratios with attenuation and rain rate statistics. However, because of possible errors due to the "resonance" behaviour of the curves of phase and group delay at high frequencies, it is recommended that these techniques only be used for frequencies below 15 GHz.

7.7 Attenuation by hydrometeors other than rain

7.7.1 Aerosols, fog, clouds, hail and snow

Transforming spatial cloud cover values (see Chapter 2) into time percentages of attenuation is not straightforward however, only certain cloud types (stratus, cumulus, nimbostratus and cumulonimbus) are considered important contributors to cloud attenuation statistics [Dissanayake *et al.*, 1997, 2001].

7.7.1.1 Microwave

Studies of the additional attenuation caused by clouds on Earth-space paths have been carried out in the United States and United Kingdom at frequencies up to 150 GHz [Lai-iun Lo *et al*., 1975] and [CCIR, 1974-78]. Table 7.1 shows the range of values likely to be experienced at frequencies of 95 and 150 GHz. For widespread clouds, the attenuation may be expected to vary approximately as cosec θ, where θ is the elevation angle. Recommendation ITU-R P.840 shows values of the specific attenuation coefficient, as a function of frequency, for temperatures between -8°C and 20°C.

TABLE 7.1

Atmospheric attenuation in the vertical direction for 95 GHz and 150 GHz, Slough, United Kingdom: October 1975 - May 1976

Frequency	95 GHz	150 GHz
Attenuation (dB) in clear air: water vapour content at ground-level 4-11 g/m^3	0.7 - 1	1 - 3
Additional attenuation (dB) due to clouds:		
Stratocumulus	0.5 - 1	0.5 - 1
Small, fine weather cumulus	0.5	0.5
Large cumulus	1.5	2
Cumulonimbus (rain cloud)	2 - 7	3 - 8
Nimbostratus (rain cloud)	2 - 4	5 - 7

A semi-empirical model for the estimation of annual cumulative statistics of cloud attenuation from ground based humidity and temperature data has been derived from radiometric measurements at 20 and 30 GHz [Dintelmann and Ortgies, 1989].

Due to the difference in dielectric properties, the attenuation due to ice clouds is about two orders of magnitude less than water clouds of the same water content up to 35 GHz [Crane, 1977]. At higher frequencies the contribution of ice clouds may result in significant attenuation.

Dry snow has a minimal effect on attenuation for frequencies less than about 30 GHz. At 30 GHz and an equivalent rain rate of 10 mm/h, the expected specific attenuation is ~3 dB/km [Battan, 1973]. For higher frequencies, several measurements have shown the importance of attenuation of dry snow [Misme, 1966]. Attenuation by hail may be significant at frequencies as low as 2 GHz. Hail seems to be of important only for exceedance probabilities less than 0.001% of the time in most climate regions.

Although wet snow can result in greater attenuation than the equivalent rain rate, propagation measurements in Japan [Takada and Nakamura, 1966], the former USSR [Nadenenko and Sviatogor, 1974] and Switzerland [Debrunner, 1980] indicate that wet snow does not have a significant effect on attenuation statistics. The degradation of antenna characteristics due to accumulations of snow and ice may be of greater importance than snow along the path.

7.7.1.2 Visible and infrared

Aerosols are always present in the atmosphere to some degree. Unfortunately, their composition, size distribution and concentration are extremely variable, and predicting the attenuation due aerosols is very difficult. Although their concentration is closely related to optical visibility, there is no unique particle-size distribution for a given visibility. As a result, the attenuation can only be estimated from visibility data by very approximate, empirical procedures which must be used with caution. A further complicating factor is the dependence of aerosol size on relative humidity. Consequently, at the present time it is possible to provide only a general estimate of the variation in attenuation with wavelength based on a few representative particle size distributions. The computer program LOWTRAN 6 [Kneizys *et al.*, 1983] contains models for optical signal attenuation due to aerosols.

Figure 7.2 gives an indication of the specific attenuation due to aerosols versus wavelength. Three different models are assumed for the aerosol size distribution: rural, urban (which includes soot

particles) and maritime (largely sea-spray). The concentration of aerosols corresponded to an optical visibility (at about 0.6 μm) of 25 km for the upper set of curves and 5 km for the lower set of curves. For a given model, the attenuation decreases with increasing wavelength, with the maritime model giving the greatest attenuation. The data for this model assume moderate wind speeds, a path located within the first 100 m above sea level, and a relative humidity of approximately 80%. For a relative humidity of 95% the specific attenuation could be three times the values shown in the figure.

An approximate, but useful, formula for attenuation due to aerosols in the visible range (approximately 0.6 μm) as a function of visibility is:

$$\alpha \text{ (dB/km)} = 17/V \tag{7.11}$$

where V is the visibility in km.

FIGURE 7.2

Specific attenuation due to aerosols as function of visibility, *V*

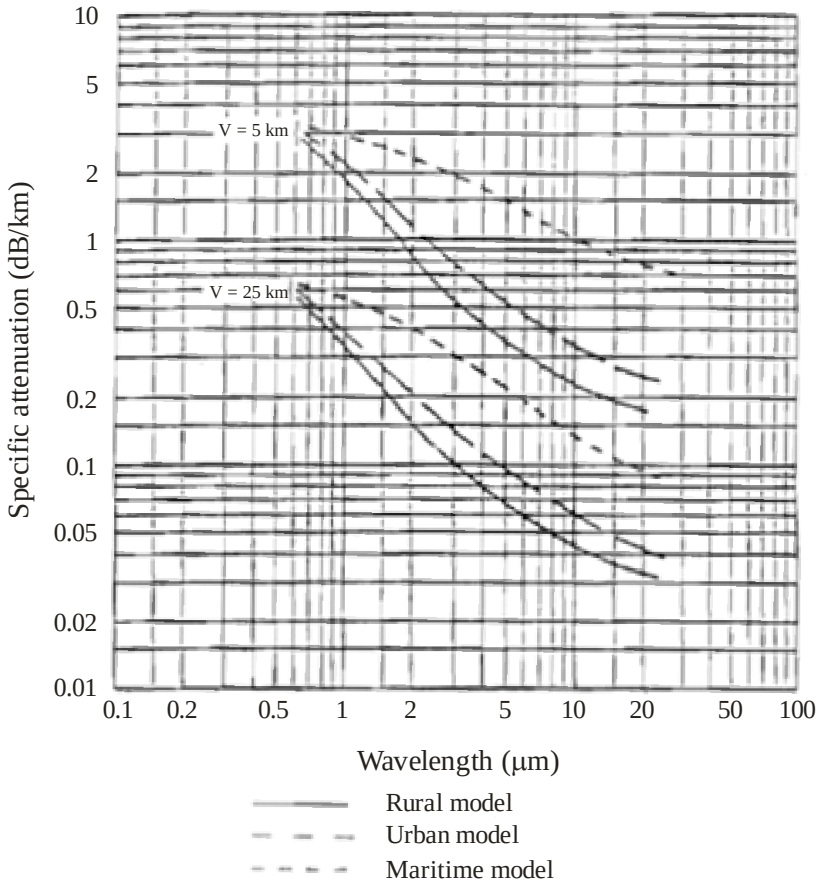

Radio-Meteo. 07-02

The attenuation due to fog depends on the drop-size distribution, and the prediction of attenuation is a complex problem due to the variability of the drop-size distribution (and the difficulty of measuring it). If the maximum drop radius is less than 10 μm, wavelengths of about 10 μm are attenuated less than wavelengths in the visible spectrum. If most of the drops have radii greater than 10 μm, the reverse is true. Hence, the use of optical visibility to characterize fog can provide only

an approximate basis for predicting attenuation. For example, for a given visibility, coastal fog will generally have a greater liquid-water content than inland fog. Nevertheless, visibility is a practical parameter which is often used. Figure 7.3 shows the general trend of attenuation in fog as a function of wavelength and visibility. These results are based largely on calculations, but they are reasonably consistent with the few available measurements. The results of Chu and Hogg [1968], for example, show a general tendency for the attenuation in fog to decrease as the wavelength increases from 0.6 μm. However, a few observations do not conform to this trend, as a consequence of unusual drop-size distributions.

Figure 7.3 shows that even moderate fog, where the visibility is 500 m, can cause significant attenuation of optical and infrared radiation.

FIGURE 7.3

Specific attenuation due to fog as a function of visibility, V

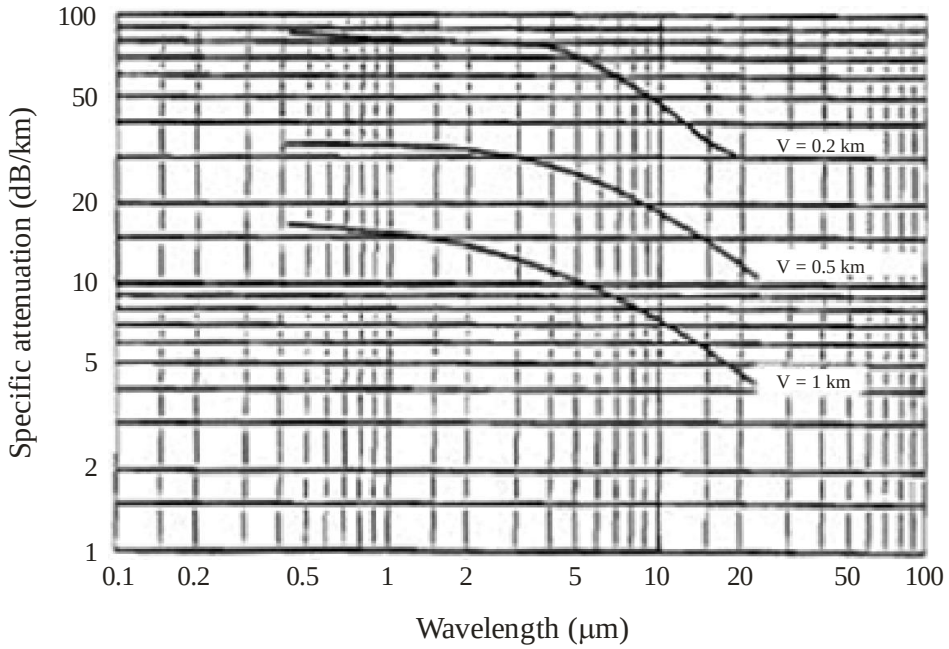

Radio-Meteo. 07-03

The specific attenuation due to clouds is even more significant than fog. Table 7.2 gives calculated values of specific attenuation for various cloud types as a function of wavelength, λ. Fair-weather cumulus clouds results in a specific attenuation greater than 0.05 dB/m, and nimbostratus (rain) clouds result in a specific attenuation of approximately 0.5 dB/m.

TABLE 7.2

Attenuation (dB/m) of visible and infrared radiation in cloud

Cloud type	λ (μm)				
	0.5	**1**	**3**	**5**	**10**
Fair weather cumulus	0.09	0.095	0.1	0.1	0.05
Stratocumulus	0.18	0.18	0.2	0.21	0.12
Nimbostratus (rain)	0.5	0.6	0.6	0.65	0.5

Multiple scattering effects are important in the propagation of light through fog and clouds. Since light that is affected by multiple scattering is detected after recombining with the direct path, multiple scattering by small component particles causes degraded coherence, time and frequency dispersion, and depolarization in addition to the attenuation previously discussed.

In the case of horizontal propagation near the ground, the effects of fog are more important than clouds. There are presently no generally available models; however, a model for blue-green optical communications through fog [Mooradian *et al*., 1979] may be useful. In Earth-to-space optical propagation, the effects of clouds are more significant. A theoretical analysis using computer simulations has been developed [Aruga and Igarashi, 1981] to provide the effects of clouds on polarization and intensity.

There are very few results for attenuation in snow. Chu and Hogg [1968] indicate that, in general, attenuation tends to increase slightly with wavelength over the range 0.6 to 10 μm. In light snow the attenuation may reach approximately 8 dB/km at 0.6 μm and 10 dB/km at 10 μm. For heavy snow, these values may be twice these values.

7.8 Attenuation by sand and dust storms

Sand and dust attenuate electromagnetic waves by the same mechanisms as do hydrometeors. The attenuation characteristics of sand and dust particles can be evaluated at centimetre wavelengths by Rayleigh scattering theory and by Mie theory at shorter wavelengths. Data on the meteorological characteristics of sand and dust-storms are currently insufficient to permit accurate calculations of attenuation statistics, but the effects are expected to be quite small for most locations.

Theoretical calculations for the band 3 - 37 GHz [Ansari and Evans, 1982] indicate that the rate of attenuation, dB/km, in sand and dust-storms is inversely proportional to visibility. The values depend strongly on moisture content, particularly in the range up to 20%. For likely values of the particle size distribution, the attenuation is about 0.03 and 0.15 dB/km at 14 and 37 GHz, respectively for dry particles and 100 m visibility. For moist particles (moisture content 20%) the corresponding values are about 0.65 and 1.5 dB/km.

Laboratory measurements at 10 GHz for simulated sand and dust conditions indicate that, for concentrations of less than 10^{-5} g/cm^3, the corresponding attenuation will be less than 0.1 dB/km for sand and 0.4 dB/km for clay particles [Ahmed and Auchterlonie, 1976].

For distributions of identical particles, the attenuation coefficient is linearly proportional to particle radius. Significant propagation effects at centimetre wavelengths will probably require either high particle concentrations (corresponding to visibilities of no more than 10 to 20 m) or high moisture contents or both [Bashir *et al*., 1980].

McEwan *et al*., [1985] have provided a complete model for attenuation prediction. A review of the subject is also provided in [Brussaard and Watson, 1995].

REFERENCES

AHMED, I.Y. and AUCHTERLONIE, L.J. [1976] Microwave measurement 3 on dust, using an open resonator, Electron. Lett., Vol. 12, 17, 445.

AJAYI, G.O. [1985] Rain induced attenuation and phase shift at cm and mm waves using a tropical raindrop-size distribution model, Proc. Int. Symp. Antennas and Propagation, ISAP'85, Kyoto, Japan, 1095.

AJAYI, G.O. and OLSEN, R.L. [1985] Modelling of a tropical raindrop-size distribution for microwave and millimetre wave applications, Radio Sci., Vol.20, 193.

ANSARI, A.J. and EVANS, B.G. [1982] Microwave propagation in sand and dust-storms. Proc. IEE, Vol. 129, Part F, 5, 315-322.

ARUGA, T. and IGARASHI, T. [1981] Narrow beam light transfer in small particles: image blurring and depolarization, Appl. Opt., Bol. 20, 2698-2705.

ÅSEN, W., GIBBINS, C.J. [2002] A comparison of rain attenuation and drop size distributions measured in Chilbolton and Singapore, Radio Science, vol. 37, no. 3, 6-1 to 6-14.

ASSIS, M.S. and EINLOFT, C.M. [1977] A Simple Method for Estimating Rain Attenuation Distributions, Proc. URSI, La Baule, 301-304.

ASSOULINE, S. and MUALEN, Y. [1989] The similarity of regional rainfall: a dimensionless model of drop size distribution, Trans. ASAE, 32, 1216 – 1222.

AWAKA, J., IHARA, T., MANABE, T., KITAMURA, K. and FURUHAMA, Y. [1987] Statistical results of millimeter wave propagation experiment on the basis of 5-year data. IEE Conf. Publ. No.274, Proc. Fifth Int. Conf. on Antennas and Propagation (ICAP 87), York, UK, 43-46.

BASHIR, S.O., DISSANAYAKE, A.W. and McEWAN, N.J. [1980] Predictions of forward scattering and cross-polarization due to dry and moist habob and sandstorms in Sudan in the 9.4 GHz band, Telecom. J., Vol. 47, VII, 462-467.

BATTAN, L.J. [1973] Radar observations of the atmosphere, The University of Chicago Press, Chicago and London.

BATTESTI, J. and BOITHIAS, L. [1978] 6th Colloquium on Microwave Communications, Budapest, Hungary.

BEARD, K.V. [1976] Terminal velocity and shape of cloud and precipitation drops aloft ,J. Atmos. Sci., 33, 851-864.

BERTOK, E., De RENZIS, G. and DRUFUCA, G. [1977] Estimate of attenuation due to rain at 11 GHz from rain-gauge data. Proc. URSI, Open Symposium on Propagation in Non-Ionized Media, La Baule, France, 295-300.

BEST, A.C. [1950] Empirical formulae for the terminal velocity of water drops falling through the atmosphere, Quart. J. Roy. Met. Soc., 76, 302-311.

BOITHIAS, L. and BATTESTI, L. [1981] Au sujet de la dépendence en fréquence de l'affaiblissement dû à la pluie, Ann. des Télécomm., Vol. 36, 7-8, 483.

BOITHIAS, L. [1989] Frequency scaling for rain attenuation, Ann. des Télécomm., Vol.44, 5-6, 186-198.

BOITHIAS, L. [1990] ITU-R Doc 5A/40.

BRUSSAARD, G. [1981] Prediction of attenuation due to rainfall on Earth-space links, Radio Sci., Vol. 16, 5, 745-760.

BRUSSAARD, G. [1985] Radiometry: a useful prediction tool? ESA publication SP-1071.

BRUSSAARD. G. and WATSON, P.A. [1995] Atmospheric modelling and millimetre wave propagation, Chapman and Hall, London, ISBN 0-412-56230-8.

BRYANT, G.F., ADIMULA, I., RIVA, C. and BRUSSAARD, G. [1999] Rain Attenuation Statistics from Rain Cell Diameters and Heights, International Journal of Satellite Communications.

CAPSONI, C., METRICCIANI, E. and PARABONI, A. [1980] First attempts of modelling the Earth-to-space radio propagation using SIRIO measurements in the 11 and 18 GHz bands, Proc. URSI (Commission F) International Symposium on Effects of the lower atmosphere on radio propagation at frequencies above 1 GHz, Lennoxville, Canada.

CAPSONI, C., FEDI, F., MAGISTRONI, C., PARABONI, A and PAWLINA, A. [1987] Data and theory for a new model of the horizontal structure of rain cells for propagation applications, Radio Science, Vol. 22, 395-404.

CHADA, R. and LANE, J.A. [1977] Effect of scattering in measurements of rain attenuation by passive radiometry, Electron. Lett., Vol. 13, 7, 177-178.

CHU, T.S. and HOGG, D.C. [1968] Effects of precipitation on propagation at 0.63, 3.5 and 10.6 microns. BSTJ, Vol. 47, 5, 723-759.

COST 205 [1985a] Influence of the atmosphere on Earth-satellite radio propagation at frequencies above 10 GHz: Precipitation studies. COST-Project 205 - Report EUR 9923 EN. Also in Alta Frequenza, Vol. LIV, 3, 116-132.

COST 205 [1985b] Influence of the atmosphere on Earth-satellite radio propagation at frequencies above 10 GHz: Frequency and polarization scaling of rain attenuation, COST-Project 205 - Report EUR 9923 EN. Also in Alta Frequenza, Vol. LIV, 3, 157-181.

COST 205 [1985c] Influence of the atmosphere on Earth-satellite radio propagation at frequencies above 10 GHz: Statistical properties of attenuation due to rain. COST-Project 205 - Report EUR 9923 EN, Also in Alta Frequenza, Vol. LIV, 3, 133-139.

CRANE, R.K. [1977] Prediction of the effects of rain on satellite communication systems, Proc. IEEE, Vol. 65, 3, 456-474.

CRANE, R.K. [1980] Prediction of attenuation by rain. IEEE Trans. Comm., Vol. COM-28, 9 (ISSN 0090-6778), 1717-1733.

DEBRUNNER, W.E. [1980] The prediction of rain attenuation statistics, Ann. des Télécomm., Vol. 35, 11-12.

DER-PHONE, L. and HSING-YI, C. [2002] An empirical formula for the prediction of rain attenuation in frequency range 0.6 - 100 GHz. IEEE Transactions on Antennas and Propagation, Volume: 50, Issue: 4, 545 – 551.

DINTELMANN, F. and ORTGIES, G. [1989] Semi-empirical model for cloud attenuation prediction, Elec. Letts., Vol. 25, 1487-1488.

DISSANAYAKE, A., ALLNUTT, J. and HAIDARA, F. [1997] A prediction model that combines rain attenuation and other propagation impairments along Earth satellite paths, IEEE Transactions on Antennas and Propagation, Vol. 45, No. 10, 1546-1558.

DISSANAYAKE, A., ALLNUTT, J. and HAIDARA, F. [2001] Cloud attenuation for SHF and EHF applications, Int. J. Satell. Commun., vol. 19, 335-345.

DISSANAYAKE, A., ALLNUTT, J. and HAIDARA, F. [2002] A Prediction Model that Combines Rain Attenuation and Other Propagation Impairments Along Earth-Satellite Paths', Online Journal of Space Communications, 2, 36.

DRUFUCA, G. [1974] Rain attenuation statistics for frequencies above 10 GHz from rain-gauge observations, J. de Recherches Atm., 399-411.

DUTTON, E.J., DOUGHERT, H.T. and MARTIN, R.F. [1974] Prediction of European rainfall and link performance coefficients at 8 to 30 GHz, NTIS, US Department of commerce, Report AD/A-000804.

FEDI, F., MERLO, U. and MIGLIORINI, P. [1977] Effect of rain structure profile along a path on rain induced attenuation, Ann. des Télécomm., Vol. 32, 11-12.

FEDI, F. [1980] Rain attenuation on Earth-satellite links: a prediction method based on point rainfall intensity. Proc. URSI (Commission F) International Symposium on Effects of the lower atmosphere on radio propagation at frequencies above 1 GHz, Lennoxville, Canada.

FEDI, F. [1981] Prediction of attenuation due to rainfall on terrestrial links, Radio Sci., Vol. 16, 5, 731-743.

FEDI, F. and PARABONI, A. [1986] A new prediction method for attenuation beyond 10 GHz based on a model of raincells characterized by exponential shape, Proc. URSI (Commission F) Symposium, Durham, USA.

FIMBEL, J. and JUY, M. [1977] Affaiblissements différentiels à 13 GHz sur 53 km - comparaison à des mesures simultanées à 20,5 GHz, Ann. des Télécomm., Vol. 32, 11-12, 454-458.

FLAVIN, R.K [1996] Satellite link rain attenuation in Brisbane and a proposed new model for Australia, Telstra Research Laboratories, Report N. 8375.

FURUHAMA, Y., IHARA, T., FUJITA, M., SHINOZUKA, T., NAKAMURA, K. and AWAKA, J. [1980] Propagation characteristics of millimetre and centimetre waves of ETS-II classified by rainfall types, Ann. des Télécomm., Vol. 36, 24-32.

FURUHAMA, Y. and IHARA, T. [1981] Remote sensing of path-averaged raindrop-size distributions from microwave scattering measurements, IEEE Trans. Ant. Prop., Vol. AP-29, 275-281.

GARCIA-LOPEZ, J.A., HERNANDO, J.M. and SELGA, J.M. [1988] Simple rain attenuation prediction method for satellite radio links, IEEE Trans. Ant. Prop., Vol.36, 3, 444-448.

GIBBINS, C.J., WALDEN, C.J. [2003] A study into the derivation of improved rain attenuation regression coefficients, Radicommunications Agency Report No. AY4359, available from http://www.radio.gov.uk/topics/research/research-index.htm

GODDARD, J.W.F. and CHERRY, S.M. [1984a] Site diversity advantage as a function of spacing and satellite elevation angle derived from dual-polarization radar data, Radio Sci., Vol.19, 231-237.

GODDARD, J.W.F. and CHERRY, S.M. [1984b] Quantitative precipitation measurements with dual linear polarization radar, 22nd Conference on Radar Meteorology, Zürich, Switzerland.

GOLDHIRSH, J. [1980] Estimation of slant path rain attenuation using radar - A comparative analysis of radar derived and beacon measured fade over a multi-season period. Proc. URSI Commission F International Symposium on Effects of the lower atmosphere on radio propagation at frequencies above 1 GHz, Lennoxville, Canada.

GUNN, R. and KINZER, G.D. [1949] The terminal velocity of fall for water droplets in stagnant air. J. Meteorol., Vol. 6, 4, 243-248.

HALL, M.P.M., CHERRY, S.M., GODDARD, T.W. and KENNEDY, E.R.K. [1980] Raindrop size, and rainfall rate measured by dual polarization radar, Nature, Vol. 285, 5762, 195-198.

HARDEN, B.N., NORBURY, J.R. and WHITE, W.J.R. [1978a] Estimation of attenuation by rain on terrestrial radio links in the UK at frequencies from 10 to 100 GHz. IEE J. Microwaves, Optics and Acous., Vol. 2, 4, 97-104.

HARDEN, B.N., NORBURY, J.R., TRACEY, M.A. and WHITE, W.J.R. [1978b] Attenuation ratios and paths diversity gains observed in rain on a network of short terrestrial links at frequencies near 11, 20 and 36 GHz. IEE Conf. Proc. No. 169.

HARRIS, J.M. and HYDE, G. [1977] Preliminary results of COMSTAR 19/29 GHz beacon measurements at Clarksburg, Maryland, COMSAT Tech. Rev., Vol. 7, 599-629.

HAWORTH, D.P. [1980] Plane wave spectrum treatment of microwave scattering by hydrometeors on an earth-satellite link, AGARD Conf. Proc. No. 284.

HODGE, D.B. and AUSTIN, G.L. [1977] The comparison between radar- and radiometer-derived rain attenuation for Earth-space links, Radio Sci., Vol. 12, 5, 733-740.

HOGG, D.C. [1973] Intensity and extent of rain on Earth-space paths, Nature, Vol. 43, 337-338.

HOUZE, R.A. [1977] Stratiform rain in regions of convective: a meteorological paradox? Bulletin of the American Meteorological Society, 3, 230-255.

IHARA, T. and FURUHAMA, Y. [1981] Experimental study of frequency scaling of centimetre and millimetre wave rain attenuation, Trans. Inst. Electron. Comm. Engrs., Japan, Vol. E64, 497-498.

IHARA, T., FURUHAMA, Y. and MANABE, T. [1984] Inference of raindrop-size distribution from rain attenuation statistics at 12, 35 and 82 GHz. Trans. IECE Japan, Vol.E67, 4, 211-217.

JOSS, J., THAMS, J.C. and WALDVOGEL, A. [1968] The variation of raindrop-size distribution at Locarno, Proc. of International Conference on Cloud Physics, Toronto, Canada.

JOSS, J., CAVALLI, R. and CRANE, R.K. [1974] Good agreement between theory and experiment for attenuation data. J. de Recherches Atm., Vol. 8, 299-318.

KHARADLY, H.M.Z. and CHOI, A.S.V. [1988] A simplified approach to the evaluation of EMW propagation characteristics in rain and melting snow, IEEE Trans. Ant. Prop., AP-36, 282-296.

KHEIRALLAH, H.N. and OLSEN, R.L. [1981] Comparison of a one- and a two-frequency technique for frequency scaling of rain attenuation statistics, Electron. Lett., Vol. 18, 2, 51-53.

KNEIZYS, F.X., SHETTLE, E.P., GALLERY, W.O., CHETWYND Jr., J.H., ABREU, L.W., SELBY, J.E.A. and FENN, R.W. [1983] Atmospheric transmittance/radiance: computer code LOWTRAN 6. AFGL-TR-80-00187, Air Force Geophysical Laboratory, Lexington MA, USA 01731.

LAI-IUN LO, FANNIN, B.M. and STRAITON, A.W. [1975] Attenuation of 8.6 and 3.2 mm radio waves by clouds, IEEE Trans. Ant. Prop., Vol. AP-23, 782-786.

LAWS, J.O. and PARSONS, D.A. [1943] The relation of raindrop size to intensity, Trans. Amer. Geophys. Union, Vol. 24, 452-460.

LEITAO, M.J. and WATSON, P.A. [1986] Method for prediction of attenuation on Earth-space links based on radar measurements of the physical structure of rainfall, IEE Proc., 133, 4, 429-440.

LI, H.J., ZHANG, C.Q., LIAO, L. and ZHANG, G.F. [1987] An improved model for the prediction of rain attenuation statistics. IEE Conf. Publ. No.274, Proc. Fifth Int. Conf. on Antennas and Propagation (ICAP 87), York, UK, 226-229.

LI, L.W., KOOI, P.S., LEONG, M.S. and YEO, T.S. [2000] Integral equation approximation to microwave specific attenuation by distorted raindrops: the Pruppacher-and-Pitter model, Electrotechnology 2000: Communications and Networks. [in conjunction with the] International Conference on Information Engineering, 3-7, 600 – 604.

LIN, S. H. [1977] Nationwide long-term rainrate statistics and empirical calculation of 11 GHz microwave rain attenuation, Bell Syst. Tech. J., 56, 1581 – 1604.

LIN, S.H., BERGAMANN, H.J. and PARSLEY, M.V. [1980] Rain attenuation on Earth-satellite paths - Summary of 10-year experiments and studies, BSTJ, Vol.59, 183-228.

LIST, R., DONALDSON, N.R. and STEWARD, R.E. [1987] Temporal evolution of drop spectra to collisional equilibrium in steady and pulsating rain, J. Atmosph. Sci., 44, 362-372.

MAGGIORI, D. [1981] Computed transmission through rain in the 1-400 GHz frequency range for spherical and elliptical drops and any polarization, Alta Frequenza, Vol. L, 5, 262-273.

MAITRA, A. and GIBBINS, C. J. [1999] Modeling of raindrop size distributions from multiwavelength rain attenuation measurements, Radio Sci., 34, 657 – 666.

MANABE, T., IHARA, T. and FURUHAMA, Y. [1984] Inference of drop size distribution from attenuation and rain rate measurements, IEEE Trans. Ant. Prop., AP-32, 474 – 478.

MARSHALL, J.S. and PALMER, W.McK. [1948] The distribution of raindrops with size. J. Meteorol., Vol. 5, 165-166.

MASSAMBANI, O. and RODRIGUES, C.A.M. [1987] Tropical rain attenuation of microwaves as predicted from dropsize distribution measurements, Proc. Int. Microwave Symp., Rio de Janeiro, 2, 1025-1031.

MATRICCIANI, E. [1980] Earth-space rain cell modelling through SIRIO propagation data, Electron. Lett., Vol. 16, 81-82.

MATRICCIANI, E., [1991] Rain attenuation predicted with two-layer rain model, European Transactions on Telecommunication, Vol. 2, 6, 715-727.

MATRICCIANI, E. [1996] Physical-mathematical model of the dynamics of rain attenuation based on rain rate time series and a two-layer vertical structure of precipitation, Radio Science, Vol. 31, 281-295.

McCORMICK, G.C. and HENDRY, A. [1975] Principles for the radar determination of the polarization properties of precipitation, Radio Sci., Vol. 10, 4, 421-434.

McEWAN, N.J., ALVES, A.P., POON, H.W. and DISSANAYAKE, A.W. [1980] OTS propagation measurements with auxiliary instrumentation. Proc. URSI (Commission F) International Symposium on Effects of the lower atmosphere on radio propagation at frequencies above 1 GHz, Lennoxville, Canada.

McEWAN, N.J., BASHIR, S.O., CONNOLLY, C. and EXCELL, D. [1985] The effect of sand and dust particles on 6/4 and 14/11 GHz signals on satellite-to-Earth paths, University of Bradford, Report 379.

MISHCHENKO, M. I., HOVENIER, J. W. and TRAVIS, L. D. [2000] Light Scattering by Non-Spherical Particles. Theory, Measurements and Applications, Academic Press, San Diego, Ca., USA.

MISME, P. [1966] Etude expérimentale de la propagation des ondes millimétriques dans les bandes de 5 et 3 mm ,Ann. des Télécomm., Vol. 21, 1-2, 226-234.

MISME, P. and FIMBEL, J. [1975] Détermination théorique et expérimentale de l'affaiblissement par la pluie sur un trajet radioélectrique, Ann. des Télécomm., Vol. 30.

MISME, P. and WALDTEUFEL, P. [1980] A model for attenuation by precipitation on a microwave earth-space link, Ra. Sci., Vol.15, 655-667.

MOORADIAN, G.C., GELLER, M., STOTTS, L.B., STEPHENS D.H. and KRAUTWALD, R.A. [1979] Blue-green pulsed propagation through fog. Appl. Opt., Vol. 18, 429-441.

MORITA, K. and HIGUTI, I. [1976] Prediction methods for rain attenuation distributions of micro and millimetre waves, Rev. Elec. Comm. Labs., Vol. 24, 5-6.

MOUPFOUMA, F. [1984] Improvement of a rain attenuation prediction method for terrestrial microwave links, IEEE Trans. Ant. Prop., AP-32, 1368 – 1372.

MOUPFOUMA, F. and MARTIN, L. [1995] Modelling of the rainfall rate cumulative distribution for the design of satellite and terrestrial communication systems, Int. J. Satellite Comm., Vol.13, 105-115.

MULLER, E.E. [1977] Long-term rain attenuation observations at 13, 19 and 28 GHz. ESA SP 138, European Space Agency, Paris, France.

NADENENKO, L.V. and SVIATOGOR, V.V. [1974] Issledovanie vliania osadkov na ustoychivost signala v diapasone 12 GHz. (Study of the effect of precipitation on signal stability in the 12 GHz band). Elektrosviaz, 12.

NUSPL, P.P., DAVIES, N.G. and OLSEN, R.L. [1975] Ranging and synchronization accuracies in a regional TDMA experiment. Proc. Third International Conference on Digital Satellite Communications, Kyoto, Japan.

OGUCHI, T. [1977] Scattering properties of Pruppacher-and-Pitter form raindrops and cross-polarization due to rain. Calculations at 11, 13, 19.3 and 34.8 GHz. Radio Sci., Vol. 12, 1, 41-51.

OLSEN, R.L., ROGERS, D.V. and HODGE, D.B. [1978] The aR^b relation in the calculation of rain attenuation, IEEE Trans. Ant. Prop., Vol. AP-26, 2, 318-329.

POIARES BAPTISTA, J.P.V. and SALONEN, E.T. [1998] Review of rainfall rate modelling and mapping Proceedings of URSI Open Symposium, CLIMPARA'98.

PRUPPACHER, H.R and PITTER, R.L. [1971] A semi-empirical determination of the shape of cloud and rain drops. J. Atmosph. Sci., 28, 86-94.

RADIO SCIENCE [1984] Special issue on multiparameter radar measurements of precipitation, Vol 19.

RAY, P.S. [1972] Broadband complex refractive indices of ice and water, Appl. Opt., Vol. II, 1836-1844.

RICE, P.L., HOLMBERG, N.R. [1973] Cumulative Time Statistics of Surface-Point Rainfall Rates. IEEE Trans. Commun., COM-21, 10, 1131-1136.

ROGERS, D.V. and OLSEN, R.L. [1976] Calculation of radio wave attenuation due to rain at frequencies up to 1000 GHz. CRC Report No. 1299, Communications Research Centre, Dept. of Communications, Ottawa, Canada.

ROGERS, D.V. and OLSEN, R.L. [1983] Multiple scattering in coherent wave propagation through rain, COMSAT Tech. Rev., Vol. 13, 2, 385-401.

ROGERS, R.R. [1976] Statistical rainstorm models: their theoretical and physical foundations, IEEE Trans. Ant. Prop., Vol. AP-31, 547-566.

ROGERS, R.R., RADHAKANT, S. and MASSAMBANI, O. [1981] New radar studies of slant-path attenuation due to rain, Ann. des Télécomm., 36, 40-47.

RUE, O. [1981] Theory for attenuation in rain. The influence of the probability function of the equivalent rain cell diameter, Central Administration of Swedish Telecommunications, Report RL 16/80.

RUE, O. [1985] Influence of the atmosphere on Earth-to-satellite links at frequencies above 10 GHz. TELE, 2 (English Edition, Sweden).

RUE, O. [1988] The statistical dependence of rain height on rain rate, and its use in rain attenuation prediction, Swedish Telecom Report R1 01/88.

SEGAL, B. [1982] Rain attenuation statistics for terrestrial microwave links in Canada. CRC Report No. 1351, Communications Research Centre, Dept. of Communications, Ottawa, Canada.

SILVA MELLO, L.A.R, PONTES, M.S., SOUZA, R.M. and PÉREZ-GARCIA, N.A. [2007] Prediction of rain attenuation in terrestrial links using the full rainfall rate distribution, Electronics Letters, v. 43, p. 1442-1443.

SILVA MELLO, L.A.R and PONTES, M.S. [2008] A unified method for the prediction of rain attenuation in slant path and terrestrial links using the full rainfall rate distribution, Proc. ISART/ClimDiff2008, Cleveland, USA.

STRICKLAND, J.I. [1974] The measurement of slant path attenuation using radar, radiometers, and a satellite beacon, J. de Recherches Atm., Vol. 8, 347-358.

STUTZMAN, W.L. and DISHMAN, W.K. [1984] A simple model for the estimation of rain-induced attenuation along earth-space paths at millimeter wavelengths, Radio Science, Vol. 19, 946-951.

TAKADA, M. and NAKAMURA, S. [1966] Attenuation of 11 Gc waves by wet snowfall, Rev. Elec. Comm. Labs., Vol.14, 1-2, 347-358.

TATTELMAN, P., and SCHARR, K.G. [1983] A model for estimating one-minute rainfall rates, American Meteorological Society, Vol. 22.

TERVONEN, J. and SALONEN, E. [2000] Test of recent cloud attenuation models, Millenium Conference on Antennas and Propagation, AP2000.

UIJLENHOET, R. [2001] Raindrop size distributions and radar reflectivity – rain rate relationships for radar hydrology, Hydro. Earth Syst. Sci., Vol. 54, 4, 615 – 627.

ULBRICH, C. W. [1983] Natural variations in the analytical form of the raindrop size distribution. J. Clim. Appl. Meteorol., 22, pp 1764 – 1775.

UPTON, S.A.J., HOLT, A.R. and EVANS, B.G. [1987] Long term frequency scaling of attenuation. IEE Conf. Publ. No.274, Proc. Fifth Int. Conf. on Antennas and Propagation (ICAP 87), York, UK, 15-18.

VAN DE HULST, H.C. [1957] Light Scattering by Small Particles, Wiley, New York, NY, USA.

VEYRUNES, O. [2000] Influence des hydrométéores sur la propagation des ondes électromagnétiques dans la bande 30 – 100 GHz: Etudes théoretiques et statistiques. Ph.D Thesis, University of Toulon and Var.

YAMADA, M., OGAWA, A., FURUTA, O. and YOKOI, H. [1978] Measurement of rain attenuation by dual-frequency radar, International Symposium on Antennas and Propagation, Sendai, Japan.

YAMADA, M., KARASAWA, Y., YASUNAGA, M. and ARBESSER RASTBURG, B. [1987] An improved prediction method for rain attenuation in satellite communications operating at 10-20 GHz, Radio Sci., Vol.22, 6.

YANG-SU KIM, YONG-SEOK CHOI, HYUNG-SOO LEE and JEONG-KI PACK [2001] The effect of drop shape and size distribution on the specific rain attenuation. Proc. URSI Comm. Meeting on Climatic Parameters in Radio wave Propagation Prediction, CLIMPARA'2001, Budapest, Hungary, 39 – 42.

ZAVODY, A.M. [1974] Effect of scattering by rain on radiometer measurements at millimetre wavelengths. Proc., IEE, Vol. 21, 257-263.

ZHAO, Z.W., ZHANG, M.G. and WU, Z.S. [2000] An analytic model of specific attenuation due to rain, 25th International Conference on Infrared and Millimeter Waves, Conference Digest, 12-15, 471 – 472.

ZHAO, Z.W., LIN, L.K. and LIU, Y. [2004] Prediction models for rain effects on Earth-space links, 2004 Asia-Pacific Conference, Proceedings, 22 – 25.

ZHAO, Z.W., LIN, L.K. and LU, C.S. [2007] A prediction model of rain attenuation based on the distribution of rain cell, Chinese Journal od Radio Science, Vol. 22, 184-186.

CCIR Documents

[1974-78]: 5/161 (United Kingdom).

[1978-82]: 5/23 (Japan).

CHAPTER 8

Radio emissivity of atmosphere and ground

8.1 Introduction

All matter emits energy in the form of electromagnetic waves. Both the intensity and frequency characteristics of the emitted radiation depend on the physical temperature of the source and on its physical properties.

The field of physics related to the measurement of the incoherent radiant electromagnetic energy emitted by all material media is called radiometry. Radiometry is also a method of passive remote sensing since the observed scenario is self-excited by virtue of its natural emission. This emission has the features of a wideband incoherent signal similar to the noise generated by the measuring system itself. Hence a radiometer receiver needs to be a wideband device with very high sensitivity, to measure the noise-like radiation.

Passive remote sensing is used to provide information in Earth observation, radioastronomy and in communication services. In the latter two cases natural radio emission, other than a limiting factor, as the noise entering the receiving antenna, is also seen as a measure of the absorptive properties of the medium and used to derive path attenuation on Earth-satellite radio links. Once the emission features of the atmosphere are related to the absorption of its constituents, the corresponding propagation parameters can be determined. Therefore microwave radiometers are used for remote-monitoring of atmospheric variables on a continuous operational basis, with accuracies rivalling those of balloon-borne observations.

The radiometric approach to radiowave propagation is twofold: on the one hand path attenuation and excess path length are directly derived from the brightness temperature measured at the radiometer operational frequency, on the other hand the derived attenuation is used to retrieve the atmospheric constituents, by means of which the attenuation can be estimated at other frequencies. This procedure, typically applied in the absence of rain, allows a determination of the reference level for calibrating the beacon attenuation and an estimation of the atmospheric water contents, both vapour and liquid, by means of which the atmospheric path attenuation can be calculated at other frequencies. Proper simplifying assumptions are needed to perform these goals, which substantially limit the validity to low attenuations related to non-rainy conditions [Barbaliscia, 1994].

To assess the likely intensities of radio emission received by a particular system, it is necessary to consider the space-time distribution of the emitting sources and the directional properties of the receiving antenna.

As mentioned, the intensity of radio emission depends on frequency. From about 30 MHz to about 1 GHz it will be dominated by galactic noise, but this will generally be exceeded by man-made noise in populated areas. In the 1-10 GHz range the dominant factor can be either galactic noise, emissions from the sun and rain, as well as emission from the surface of the Earth. Recommendation ITU-R P.372 provides detailed information on noise emission by various sources. Above 10 GHz the dominant emission is contributed by the surface of the Earth and by the absorptive constituents of the atmosphere, gases and hydrometeors, the latter becoming very severe. At the absorption bands of oxygen and water vapour, the noise temperature will closely approach the physical temperature of the absorbing medium (usually less than about 290 K for the Earth's

atmosphere). Information about spectroscopic lines of the gaseous constituents and pollutants may be found in [Pointer and Pickett, 1984].

Fundamentals of radiative transfer are briefly presented in § 8.2, generating the basic algorithms for the calculation of the brightness temperature resulting at the observing antenna. Sections 8.3 and 8.4 concern the radiative features of atmosphere and ground, respectively. Section 8.5 deals with the radiometric estimation of path attenuation and excess path length. The inversion procedure used to retrieve the atmospheric water total content from radiometrically measured brightness temperatures is described in § 8.6.

8.2 Radiative transfer

8.2.1 Fundamentals

The electromagnetic emission radiated by matter depends on the physical temperature and on other characteristics.

In a gas, any emission line corresponds to a specific transition from one energy level to another one. The intensity of this emission depends on the number of collisions among the particles, which in turn depends on the gas density and on the kinetic energy, the latter resulting in the thermodynamic or physical absolute temperature. Since the energy levels are quantized, the radiation spectrum in gases is then essentially formed by distinct frequency lines.

Passing from gases to liquid and solids, the density, and consequently the frequency of the collisions, increases so that the radiation spectrum becomes effectively continuous and almost all frequencies are radiated.

The probabilities of excitation and decay of molecular and atomic energy levels, which are responsible for absorption and emission respectively, are governed by both the collision effects and the radiation intensity. Since the same mechanisms govern emission and absorption, the corresponding spectra are identical for any substance.

The radiation incident upon the surface of a substance is normally partly reflected and partly absorbed. An ideal material which absorbs all the incident radiation at all the frequencies, reflecting none, is called a black body; the latter, in turn, is a perfect absorber and then a perfect emitter, as well.

The intensity of the radiation can be expressed in terms of the spectral brightness which represents the specific radiated power, per unit area, solid angle and bandwidth.

Planck's radiation law, essentially based on the quantization of the energy levels, relates the spectral brightness uniformly radiated by a black body in all directions to its physical temperature and to frequency:

$$B_f = \frac{2hf^3}{c^2\left(e^{hf/kT} - 1\right)} \qquad \mathrm{Wm^{-2}\ sr^{-1}\ Hz^{-1}} \tag{8.1}$$

where:

B_f : black body spectral brightness ($\mathrm{Wm^{-2}\ sr^{-1}\ Hz^{-1}}$)

h : Planck's constant = 6.63×10^{-34} Joule s

f : frequency (Hz)

k : Boltzmann constant = 1.38×10^{-23} Joule $\mathrm{K^{-1}}$

T : absolute temperature (K)

c : velocity of light = 3×10^{8} $\mathrm{ms^{-1}}$.

In the long wavelength limit (hf/kT<<1) the exponential in equation (8.1) can be approximated obtaining:

$$B_f = \frac{2 f^2 \mathrm{k} T}{\mathrm{c}^2} \tag{8.2}$$

which is the Rayleigh-Jeans approximation, valid in the microwave region up to some 300 GHz for bodies at ambient temperatures (300 K: Earth and heavy rain). For much lower temperatures, such as for the clear atmosphere, the fractional deviation of equation (8.2) with respect to equation (8.1) becomes significant above 50 GHz.

In the case of real materials, usually referred to as grey bodies, part of the incident energy is reflected and the emission may be direction-dependent. Real materials are therefore neither perfect absorbers nor emitters.

In the real case, in the Rayleigh-Jeans approximation, the spectral brightness in a given direction is:

$$B_f = \frac{2 f^2 \mathrm{k} T_b}{\mathrm{c}^2} \tag{8.3}$$

where the emitted power is linearly proportional to T_b, called brightness temperature of the material or black body-equivalent radiometric temperature, which is the physical temperature of a black body emitting the same power. This temperature is therefore the fundamental observable in radiometry. Since the power emitted by a black body is the maximum possible at a given physical temperature T, the brightness temperature of a real material is always lower with respect to its physical temperature. The direction-dependent emissivity ε of a real body, defined as the ratio between its brightness temperature T_b and thermodynamic temperature T, is then always less than 1 and equal to 1 only for the ideal black body case.

It should be noted that in equation (8.3) the material is assumed to be homogeneous and of uniform temperature.

8.2.2 Radiative transfer equation

The energy radiated by a medium and its corresponding brightness temperature results from the interaction between radiation and matter, which basically consists of the combination of extinction and emission processes occurring in the medium.

The extinction effect which results in the reduction of the intensity of the radiation traversing the medium is the sum of the absorption (transformation into heat) and the scatter by virtue of which part of the incident energy is in turn radiated in all directions. The radiation is the result of thermal emission and of scattering.

The thermal emission must be equal to the absorption when thermodynamic equilibrium occurs (Kirchhoff's law).This condition is only fulfilled for an isothermal, absorbing medium (black body). In most practical situations this does not apply. However, the less rigorous hypothesis of "local" thermodynamic equilibrium may be assumed, if any volume element of the medium at a certain local temperature has the same absorption and emission characteristics that it would have in the state of thermodynamic equilibrium at that temperature. This is, in practice, the case when the collision process prevails on the radiation process, as it happens for materials of sufficiently high density. For this condition to apply, neither an isothermal medium nor an isotropic radiation intensity is required.

The output of a radiometer receiver can be related to the brightness temperature T_b, along the direction of the antenna main beam, as resulting from the contribution of a layer of the medium at level *r*, by [Ulaby *et al.*, 1982]:

$$T_b(r) = T_0 \mathrm{e}^{-\tau(0,r)} + \int_0^r k_e(r')\left[(1-a)T(r') + aT_{SC}(r')\right] e^{-\tau(r',r)} dr' \quad \text{K} \tag{8.4}$$

where:

$T_b(r)$: brightness temperature at the receiving antenna (K)

$T(r')$: physical temperature at level r' (K)

T_0: brightness temperature at the boundary (K)

T_{SC}: average scattered radiation temperature (assuming isotropic scattering) (K)

k_e: extinction coefficient (nepers/m)

k_s: scattering coefficient (nepers/m)

a: scattering albedo k_s/k_e

τ: optical thickness, defined as: $\tau(r,r') = \int_{r'}^{r} k_e(r')dr'$ (nepers).

This equation, known as radiative transfer equation, governs the interaction of radiation through a medium and states that the brightness temperature of a given scenario is related to the physical temperature and characteristics, composition and density, of the medium. The direct expression of the brightness temperature in terms of physical temperature follows up to the microwave region from the Rayleigh-Jeans approximation.

The radiative transfer equation applies in the most general case, describing radiative processes in any scenario. In the case of atmospheric radiometry, the general solution of equation (8.4) involves absorption and scattering in all directions and leads to highly complicated formulations.

The occurrence of liquid water in the atmosphere, typically in the form of clouds and rain, invokes scattering processes. The effect of scattering on radiative transfer depends on two factors: the magnitude of the scattering albedo relative to the absorption coefficient (or the single scattering albedo) and the scattering phase function. The former determines the total scattering intensity, whilst the latter represents the directional distribution of the scattering field. Complicated calculations and several assumptions must be made to examine separately the various practical situations. To ignore the scattering phenomena is a significant simplification, which can be assumed rigorously only in the case of total absence of liquid. The cases when large drops are present are in principle doubtful and typically result in underestimating the total path attenuation.

The complexity of equation (8.4) is drastically reduced when scattering may be neglected, that is under clear sky conditions, in the absence of liquid. When clouds and/or rain are present, scattering by water droplets may be negligible, depending upon the density and drop-size distribution of the water droplets relative to the wavelength. Scattering effects may be ignored for any atmosphere below 10 GHz. As a first approximation, the non-scattering assumption is also valid for non-precipitating clouds and light rain-rate conditions, up to 50 GHz.

Local thermodynamic equilibrium conditions might be assumed, moreover, for the lower and denser layers of the atmosphere, which are responsible for most of the absorption and where the collision process is dominant in establishing the medium temperature. This condition is satisfied up to about 20 km.

For a non-scattering atmosphere in local thermodynamic equilibrium the description of radiative transfer is simplified and the brightness temperature T_b is related to absorptive and emissive properties of the medium by:

$$T_b = T_0 \mathrm{e}^{-\tau(0,\infty)} + \int_0^{\infty} k_a(r) T(r) e^{-\tau(0,r)} dr \quad \mathrm{K} \tag{8.5}$$

where:

T_b: brightness temperature at the radiometer antenna (K)

T_0: cosmic background temperature (K)

$T(r)$: physical temperature of the atmosphere at the level r (K)

$k_a(r)$: absorption coefficient (nepers/m)

$\tau(0,r) = \int_0^r k_a(r©) dr©$: absorption from ground level to level r (optical depth) (nepers)

$\tau(0,\infty) = \int_0^{\infty} k_a(r') dr'$: opacity or total atmospheric absorption (nepers).

Equation (8.5) states that the sky brightness is given by the sum of the cosmic background brightness and of the emission by the infinite single atmospheric layers along the considered path, both reduced by the absorption of the atmosphere underneath. Consequently the lower layers give the larger contribution to T_b, in comparable conditions of the physical temperature T. In general, T_b depends on the vertical profile of the temperature and absorption coefficients, the latter, in turn, corresponding to the vertical distribution and characteristics of the relevant components.

The simplified equation (8.5) can be used, independently of radiometric observations, according to the direct approach, when the brightness temperature of the atmosphere is calculated from the known vertical distributions of the physical parameters and of the absorption coefficients. This procedure is commonly adopted in theoretical models making use of radiosonde data [Liebe, 1989; Liebe *et al.*, 1993].

8.2.3 Brightness temperature

The emission in the microwave region is usually measured by a microwave radiometer which is a passive device, consisting of an antenna, a receiver and an instrument showing the amount of the received power. The received power is proportional to the brightness temperature observed by the antenna in main lobe direction from the surrounding media. The brightness temperature, in turn, may be derived in the Rayleigh-Jeans approximation of Planck's law, which is valid up to microwave frequencies.

Two typical configurations can be identified: i) up-looking antenna, which is the case of atmospheric radiometry, relevant to satellite radiocommunications and radioastronomy, ii) down-looking antenna which, other than the downlink in satellite communication, also concerns remote sensing of the Earth's surface.

i) The brightness temperature Tbup measured at the surface by an upward-looking antenna, in a non-scattering, non-reflecting atmosphere, is simply given by equation (8.5).

ii) The expression of the brightness temperature Tbdwn as seen by a satellite-borne downward-looking antenna having angle of incidence θ, should take into account the contributions along two paths (see Figure 8.1):

– Path A: that of the atmospheric radiation T_{bup}, that is reflected by the surface toward the satellite antenna;

– Path B: that seen by the down-looking antenna with angle of incidence θ.

$$T_{bdwn} = T_{atm2} + \left(eT_{surf} + \rho T_{bup}\right)e^{-\tau(0,r_2)} \tag{8.6}$$

where:

T_{atm2} is the brightness temperature of the atmosphere along path B, given by Equation (8.5) with the cosmic background contribution being subtracted.

eT_{surf} is the brightness temperature of the Earth's surface.

ρT_{bup} is the brightness temperature along path A, given by equation (8.5), reflected by the Earth's surface.

$\left(eT_{surf} + \rho T_{bup}\right)e^{-\tau(0,r_2)}$ is the total resultant brightness temperature of the Earth's surface, attenuated by the atmosphere along path B.

T_{surf}: physical temperature (K) of the Earth's surface,

e: emissivity of the surface ($0 \le e \le 1$),

ρ: reflectivity of the surface ($0 \le \rho \le 1$), (square of reflection coefficient; $e + \rho = 1$)

θ: angle of incidence.

A smooth surface is assumed for simplicity, so that the specular reflection approximation is valid.

FIGURE 8.1

Contributions to the brightness temperature T_{bdwn} received by a satellite-borne satellite

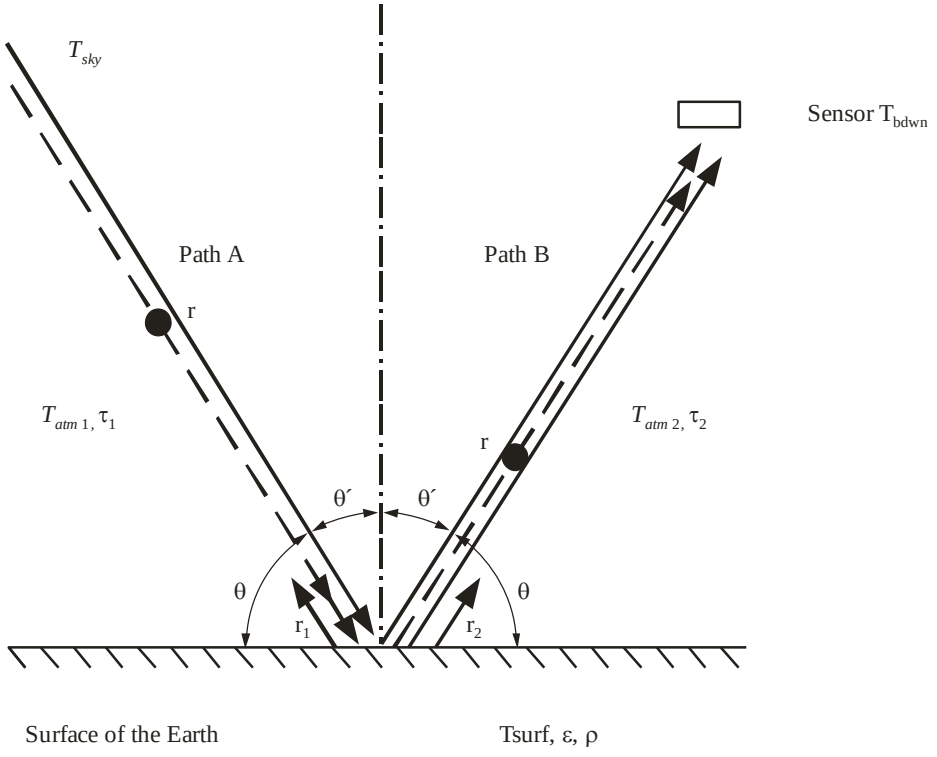

Under some assumptions significant simplifications may be made.

For a down-looking antenna in the window above 3 GHz and below about 10 GHz both the extraterrestrial noise and the emission from atmospheric constituents may be ignored, in a first approximation.

Equation (8.6) then simplifies to:

$$T_{bdwn} = eT_{surf} + \rho T_0 \tag{8.7}$$

In the case of up-looking radiometry, if the physical temperature $T(r)$ is replaced by a mean radiating temperature T_{mr}, that up to 40 GHz may be assumed equal to the ambient temperature, equation (8.5) simplifies to:

$$T_{bup} = T_{mr}\left(1-10^{-A/10}\right) + T_0 e^{-A/4.34} \tag{8.8}$$

where: A is the one-way attenuation through the atmosphere (dB) and T_0 is the cosmic background temperature.

The values of atmospheric brightness temperature at any elevation angle θ may be obtained by simply multiplying the one at the zenith direction by cosec θ, if a horizontally stratified atmosphere can be assumed.

For elevation angles higher than 70 degrees, the correspondent error is less than 1% [Waters, 1976].

In the estimation of antenna temperature, the antenna pattern and particularly radiation from the surface of the Earth into antenna side lobes must be considered.

8.3 Atmospheric emissivity

The atmosphere is a thermodynamic system which surrounds the Earth up to some 100 km. In most microwave propagation applications, however, only the lower layer, say up to 20 km, containing the bulk of the atmospheric mass, is of relevance.

From a thermodynamic point of view the atmosphere can be thought of as a heat engine where the sun provides the energy input and infrared radiation cooling to space serves as the exhaust. Latent heat exchanges, which do not involve temperature variations, result in phase transitions, evaporation and condensation, that provide additional cooling and warming to the air, respectively. Other sources and exhausts occur, in terms of matter, via the evaporation of water in the soil and the precipitation of atmospheric water.

As far as radiative transfer is concerned, the atmosphere may be regarded as a medium which consists of gaseous, liquid and solid constituents. Among the liquid and solid constituents, the hydrometeors (rain, snow, clouds) are the dominant factor in the microwave region, while other particles, such as dust, smoke and sand, are of minor importance in general.

The main gaseous constituents of the atmosphere are nitrogen, oxygen, argon, carbon dioxide (totalling 99.999 volume % of dry air), and water vapour, which is a variable constituent. Among these gases, only oxygen and water vapour cause severe absorption in the microwave region, while gases which have no electric or magnetic dipole moment do not absorb microwaves [Gibbins, 1988]. In the submillimetre and infrared region, the dominant gases, which cause absorption, are water vapour and carbon dioxide.

Since the atmosphere may be considered to exhibit local thermodynamic equilibrium in the lowest 20 km, its emissivity follows from the absorption and scattering properties (see Chapters 2 and 6).

Figure 8.2 shows the brightness temperature of the atmosphere for a ground-based receiver, excluding the cosmic noise contribution of 2.7 K or other extraterrestrial sources, for frequencies between 1 and 340 GHz [Smith, 1982]. The curves are calculated for the atmospheric gases, oxygen and water vapour, for seven different elevation angles from $\theta = 90°$ (zenith) to $\theta = 0°$ (horizon). Figure 8.2 is chosen to represent an average atmosphere (i.e., water vapour concentration of 7.5 g/m^3). The temperature profile is from the 1976 US Standard Atmosphere [NOAA *et al.*, 1976] (15°C surface temperature). Figure 8.3 offers an expanded version of Figure 8.2 for frequencies below 60 GHz.

For all the calculations the model assumed is the reference atmosphere as from Recommendation ITU-R P.369. The total pressure is that for the standard atmosphere (1 013 hPa) at sea level with the water vapour pressure added to it. This will give values of 1 023 hPa for 7.5 g/m^3 of water vapour.

An exponential decrease of water vapour with height is assumed, with a scale height of 2 km up to the level of the tropopause, above which the water vapour profile given by Harries [1976] is used. The decrease in pressure of the dry atmosphere is also governed by an exponential law, whereas the decrease in temperature (6.5°C/km) is linear up to a height of about 12 km. With these assumptions it is possible to evaluate the zenith noise temperature from humidity, temperature and pressure data of the surface. These data are in reasonable agreement with the limited amount of experimental data available [Clark *et al.*, 1984; Gibbins *et al.*, 1975].

In some cases the assumptions above are not valid, especially in regions where very high relative humidities occur, such as for equatorial regions. In particular, the evaluation of zenith brightness temperature is not accurate if atmospheric inversions of temperature and humidity occur.

A radiative transfer study including cloud effects has been carried out in the United States [Slobin, 1982]. Zenith brightness temperatures have been computed from meteorological data for a typical year selected from a database of 15 years for each of 15 locations. Results from two US locations, Yuma, Arizona (5.5 cm annual rainfall) and New York City (98.5 cm annual rainfall) are given in Figures 8.4a and 8.4b for five different frequencies. It can be seen from the curves that the noise temperature at zenith for 90 GHz may be lower than for 44 GHz. This is the case for very low zenith brightness temperatures, which means that the water vapour content is very low (lower than about 3 g/m^3).

FIGURE 8.2

Brightness temperature (clear air) for 7.5 g/m^3 water vapour concentration (surface temperature and pressure equal to 15°C and 1 023 mb); θ is the elevation angle [Smith, 1982]

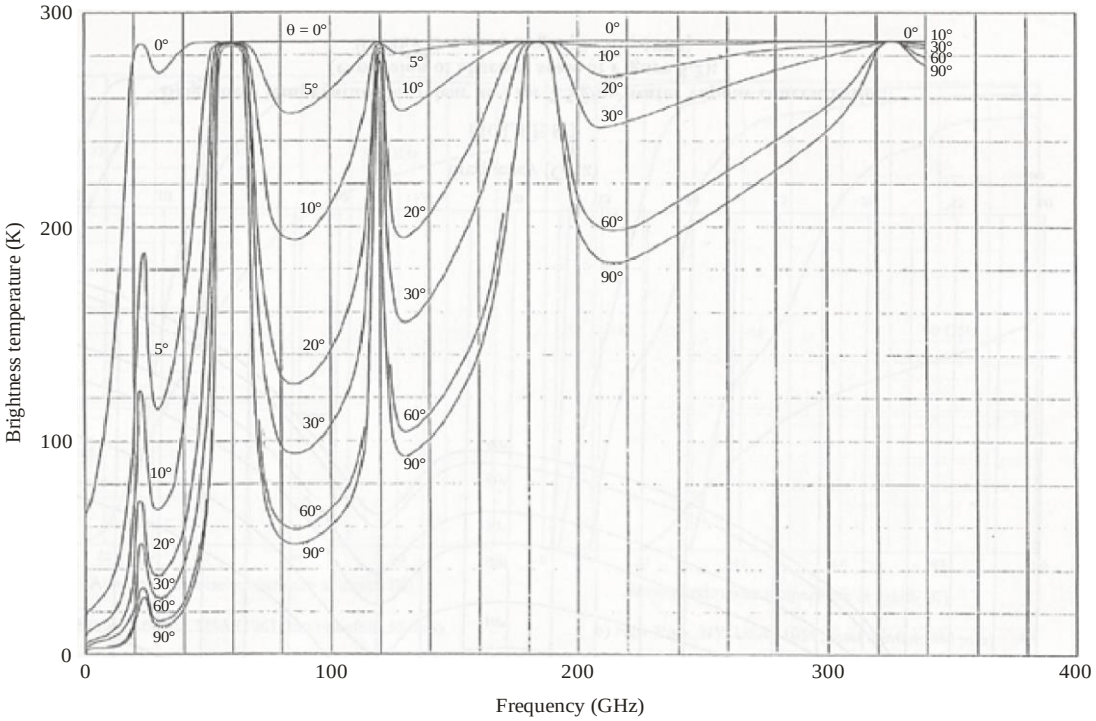

Radio-Meteo. 08-02

FIGURE 8.3

Brightness temperature for (clear air) for 7.5 g/m^3 water vapour concentration (expansion of abscissa scale of Figure 8.2); θ is the elevation angle [Smith, 1982]

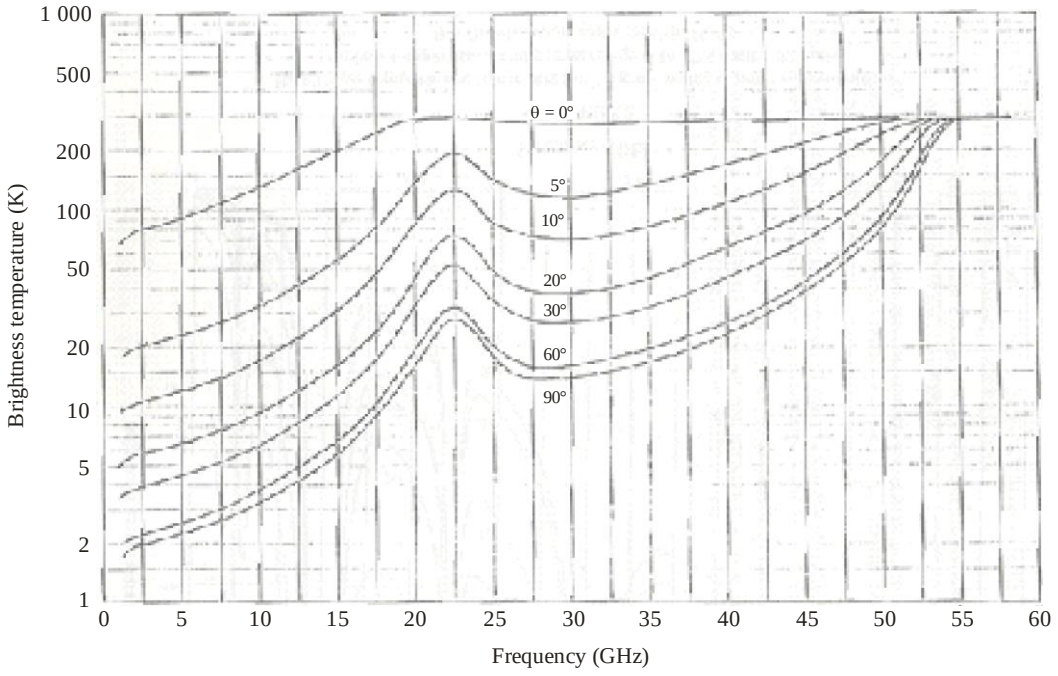

Radio-Meteo. 08-03

FIGURE 8.4

Fraction of the time the zenith sky noise (brightness) temperature is equal to or less than the abscissa value for a typical year [Slobin, 1982]

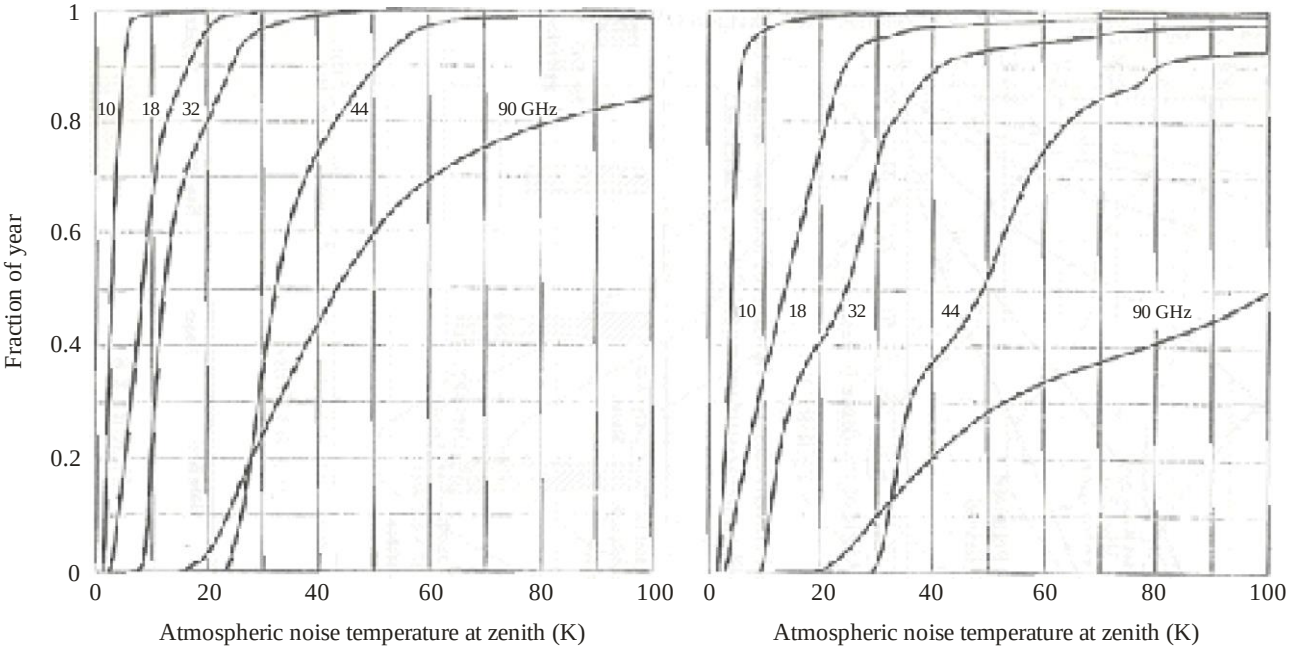

8.4 Ground emissivity

Basic properties of a smooth Earth surface are given in Figure 8.5. Emissivity (left scale) and power reflection coefficient (right scale) of sea water, moist and dry soil are given for the case of plane surfaces at 10 GHz, for vertical and horizontal polarization [Ulaby *et al.*, 1981].

Sea water emissivity is relatively low (< 0.4) at normal incidence, due to the relatively high real and imaginary parts of the dielectric constant. When the angle of incidence θ increases, the emissivity increases in vertical polarization, while it decreases in horizontal polarization; the maximum difference between the two polarizations is observed when the Brewster angle is approached.

Both real and imaginary parts of soil dielectric constant are lower than those of sea water, with a consequent increase of zenith emissivity and reduction of the difference between the two polarizations when $\theta > 0$. Of course, these effects are more evident when the soil is dry.

The curves of Figure 8.5 have been obtained under the plane-surface assumption. In reality, the roughness and the presence of discrete small elements (scatterers), like vegetation leaves and stems or snow grains, tend to modify the surface behaviour producing, in general, an increase in zenith emissivity and a reduction in the difference between the two polarizations.

FIGURE 8.5

Calculated reflectivities and emissivities as a function of incidence angle at 10 GHz
Calculation based on plane-surface model (Ulaby *et al.*, 1981)

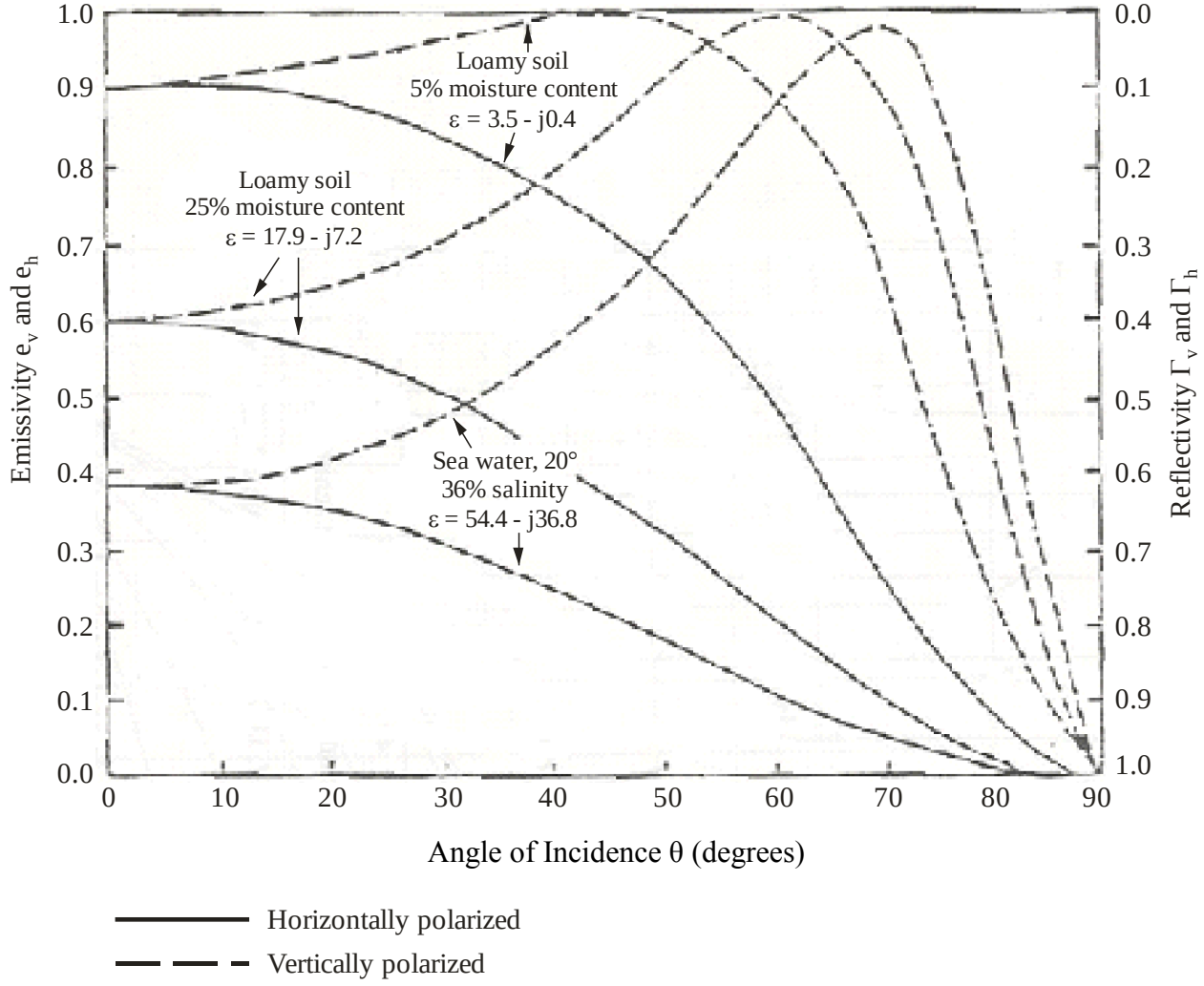

Radio-Meteo. 08-05

Figure 8.6 shows experimental values of zenith emissivity, measured over some natural surfaces in the range 1-35 GHz [Ulaby *et al.*, 1982]. In general, the lower emissivities are associated with smooth surfaces and with the presence of water, while the higher emissivities are associated with low moisture, high roughness and the presence of discrete scatterers (as in snow and in vegetation).

FIGURE 8.6

Range of values that the microwave nadir emissivity may cover for various classes of targets (Ulaby *et al.*, 1982)

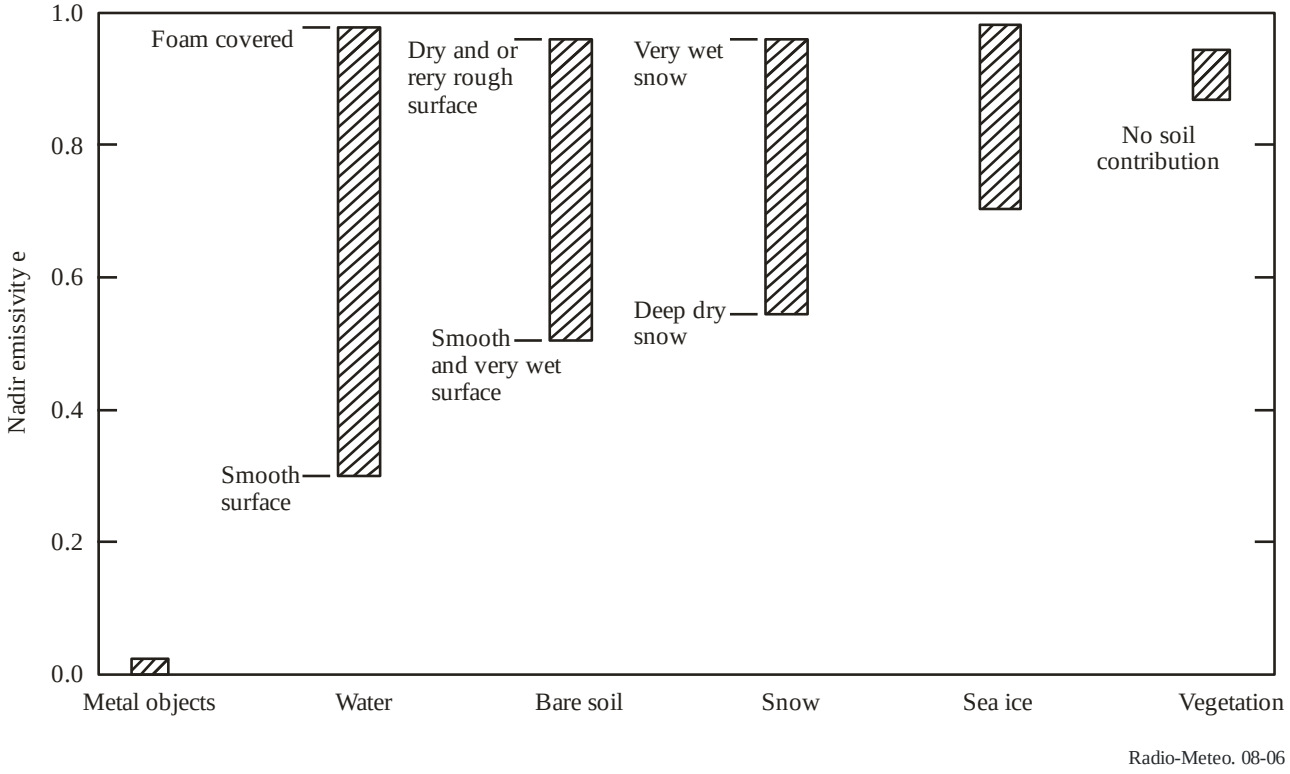

For sea water both the real and imaginary parts of sea water dielectric constant are relatively high in the range 1-40 GHz, due to polarisability, dielectric losses and salinity conduction. As a consequence of this, for plane surfaces, the emissivity, and hence the brightness temperature, are low. However, at the high frequencies the presence of wind and foam may generate appreciable emissivity increases [Nordberg *et al.*, 1971].

Bare soil emissivity is essentially controlled by two parameters: roughness and moisture content. For $\theta < \approx 40°$ and for frequencies higher than 10 GHz the emissivity of rough, dry soils is relatively high (typically 0.9-0.95). The emissivity decreases when the soil is smooth and/or moist or when the frequency is low. Low emissivity values (0.5-0.6) can be reached for moist smooth soils at low frequencies (1-5 GHz) [Ulaby *et al.*, 1986].

As far as vegetation is of concern, at frequencies higher than some 10 GHz, radiation emitted by vegetation dominates the contribution of the underlying soil, even in the case of short vegetation. In the case of forests or agricultural crops with relatively large leaves and stems (like corn and sunflower) the vegetation contribution is important also down to 1.4 GHz. The microwave emissivity of vegetated surfaces is generally higher than 0.85 and shows small differences between vertical and horizontal polarization [Ferrazzoli *et al.*, 1992].

Snow effects on emission are generally important at high frequencies (typically above some 10 GHz). The emissivity is controlled by the total amount of snow (expressed in centimetres of equivalent water) and by the wetness. The presence of deep layers of dry snow can make the emissivity decrease to values of 0.8 at 10 GHz and 0.6 at 37 GHz. On the other hand, high emissivity values are obtained in the case of wet snow [Ulaby *et al.*, 1982].

For a satellite in the geostationary orbit, the antenna temperature may be obtained by calculating the brightness temperature in each direction by Equation (8.6) for known atmospheric and surface conditions, and then integrating the resulting values over the antenna pattern (main lobe). This has been done for a satellite with a Gaussian Earth coverage beam assuming average ground and atmospheric conditions for frequencies of 1 to 50 GHz [Njoku and Smith, 1985]. The results are given in Figure 8.7.

FIGURE 8.7

Weighted brightness temperature of the Earth as a function of longitude viewed from geostationary orbit at frequencies between 1 and 51 GHz

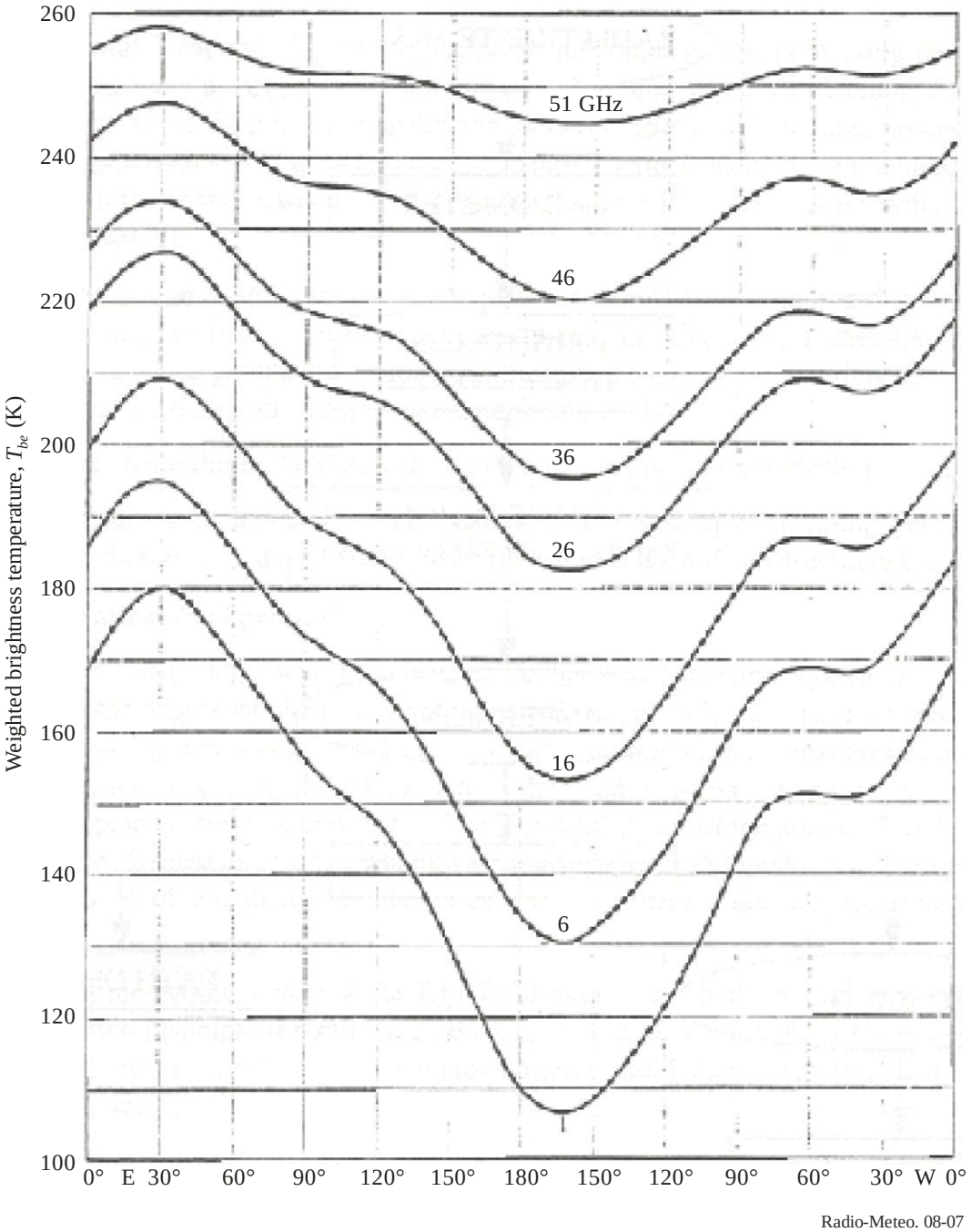

Radio-Meteo. 08-07

8.5 Radiometric estimation of attenuation and path length

8.5.1 General

The radio path behaviour through the atmosphere is characterized by two principal quantities: the path attenuation and the path delay, which can both be expressed in terms of the complex refractivity (see Recommendation ITU-R P.453):

$$N = N0 + N'(f) + j\,N''(f) \tag{8.9}$$

The attenuation depends on the imaginary part $N''(f)$, whilst the delay is related to the two real terms.

The three terms of the complex refractivity are functions of the physical state of the air, that is, its temperature, pressure and water vapour density. Once these parameters are known, the refractivity and, in turn, attenuation and path delay, can be obtained in terms of these physical parameters.

The radiative transfer equation relates the radiometrically measured brightness temperature T_b to the vertical profiles of atmospheric temperature and absorption, the latter, in turn depending upon the distribution of the absorbing components. Hence equation (8.5), the simplified expression of the radiative transfer equation, can be used to derive estimates of both path attenuation and excess length by means of inversion algorithms.

It should be kept in mind, however, that, since equations (8.4) and (8.5) are integral equations, the inversion procedure does not usually have a straightforward solution.

8.5.2 Radiometric estimation of attenuation

The typical application of radiometric measurements of brightness temperature is the derivation of the path attenuation at the radiometer frequency. Introducing the effective or mean radiating temperature T_{mr} defined as:

$$T_{mr} = \frac{\int k_a(r)T(r)e^{-\tau(0,r)}dr}{\int k_a(r)\,e^{-\tau(0,r)}dr} \quad \text{K} \tag{8.10}$$

Equation (8.5) may be simplified into:

$$T_b = T_0\,(1\text{-}t) + T_{mr}\,t \quad \text{K} \tag{8.11}$$

where t is the transmissivity of the medium ($t = e^{-\tau}$)

This equation, when solved with respect to t, gives for the attenuation in decibels the expression:

$$A = 10\log_{10}\left(\frac{T_{mr} - T_0}{T_b - T_0}\right) \quad \text{dB} \tag{8.12}$$

which is the equation commonly used to convert the radiometrically measured brightness temperature T_b into the path attenuation A. The use of equation (8.12) should be, however, limited to low values of the path attenuation. As the latter increases, in fact, the radiometer measures values of brightness temperature T_b closer and closer to the atmospheric effective radiating temperature T_{mr}, thus leading to a severe reduction in the accuracy of the calculated attenuation.

T_{mr}, which comprises information on the vertical dependence of the atmospheric physical properties, depends on frequency and on the local physical and climatological parameters. The use of this single constant to replace a meteorological varying profile does not appreciably affect the accuracy of the inversion algorithm up to 50 GHz and for sky brightness temperatures lower than some 100 K (i.e. in the absence of rain). An error in T_{mr} of 10 K results, in fact, in about a 5% error in A, at 30 GHz, negligible in a first-step approximation.

T_{mr} (typically around 270 K) is usually estimated from the surface temperature or from atmospheric soundings over monthly climatological averages. A linear relationship can be assumed for a first estimate of T_{mr} from the surface temperature T_s multiplying the latter by 0.95 in the 20 GHz band and by 0.94 for the 30 GHz window.

The direct derivation of the path attenuation at the same operational frequency of the radiometer via equation (8.12) is the simplest inversion of the radiative transfer equation (8.5), for the case of low atmospheric absorption and in the absence of scattering. The temperature profile is replaced by one constant value and the absorption characteristics along the path are integrated in terms of the total resulting absorption.

This procedure has been commonly used in the past, as the main radiometric application in radio propagation for obtaining attenuation statistics in the absence of a satellite beacon. Since the frequencies were relatively low (11/14 GHz), the condition of low attenuation was generally satisfied, even during rainy events.

8.5.3 Estimation of propagation path delay

The electrical path length for a radio signal propagating through the atmosphere is longer than the physical path by a distance termed "excess electrical path length" R, which is proportional to the integral of the profile of refractivity N along the path. The excess path length is often expressed in terms of the corresponding "path delay" time. The exact value of R is critical for several applications, such as radioastronomy (VLBI), missile tracking, spacecraft navigation and satellite-based positioning systems (GPS) [Solheim, 1993].

Both the ionosphere and the troposphere are responsible for the path delay. Only the tropospheric effects will be considered here. Path delay due to the ionosphere is considered in Recommendation ITU-R P.531.

Since the contribution to the path delay due to hydrometeors is two orders of magnitude lower with respect to gases, it may be neglected and the non-dispersive refractivity can be written empirically as the sum of the component due to dry air plus that due to water vapour, as given in Recommendation ITU-R P.453.

The total resultant excess path length can be correspondingly expressed as the sum of dry and wet components:

$$R_{tot} = R_{dry} + R_{wet} = 0{,}00228\,P + \frac{1\,790\,V}{T_s} \quad \text{cm} \tag{8.13}$$

where P is the total pressure (hPa), T_S the surface temperature (K) and V (kg/m^2) is the total content of water vapour along the path.

The value of R_{tot} ranges from 220 to 270 cm, at sea level in the zenith direction. By far the largest contribution is due to the dry atmosphere, which is also accurately modelled and directly proportional to atmospheric pressure. Therefore, R_{dry}, which is about 240 cm, is not the main source of inaccuracy provided that barometric pressure is accurately measured.

The wet component, R_{wet}, due to the polar nature of water molecules, ranges from 5 to 60 cm. Since this is a highly variable component of tropospheric delay, it is the main source of error for precise geodesy and positioning systems and must be therefore measured very accurately.

Common techniques are based on radiosonde measurements of temperature and water vapour profiles, but are not representative of the time variability and tend to fail when the measured V is applied to low-elevation paths, where the assumption of horizontal stratification cannot be applied.

Radiometric measurements can greatly help provide estimates of the vapour content and hence of R_{wet} along the actual path of interest. Although the vapour radiometric emission is proportional to local temperature, whereas the refractivity due to water vapour has an inverse relationship to temperature, radiometric retrievals of water vapour have proven to be very accurate. This is presumably due to the concentration of water vapour in the lowest levels of the atmosphere at rather consistent temperatures.

The accuracy achieved by radiometric estimation of the excess path length amounts to a few millimetres at zenith and some 2 cm for very low elevation angles.

8.6 Passive remote sensing of atmospheric composition

8.6.1 General

In several cases path attenuation is required at frequencies different from those at which radiometers are operated, often in bands where the effects of the atmospheric minor constituents are relevant to propagation applications, typically for the definition of the "clear sky" level and for the removal of the periodical fluctuations due to the system itself.

In these cases a form of frequency scaling is needed. A series of measurements at different frequencies is then required to carry out a more detailed inversion of equation (8.5) to retrieve the density of atmospheric constituents as a function of altitude. From this knowledge attenuation may then be derived at other frequencies.

The dependence of brightness temperature on atmospheric parameters is not linear. The vertical distribution of the response in terms of brightness temperature, can be described by means of the weighting functions, which express the relative contribution to the brightness increment at any level due to the individual components. Although profiles of the weighting functions are calculated for temperature, water vapour and liquid water at several frequencies, the retrieval of the full vertical distributions of atmospheric water via radiometric measurements is not simple and not strictly required for radio propagation applications.

A satisfactory simplification is offered when considering that the integrated contents of vapour and liquid along the path are proportional to the radiometrically derived attenuation. The proper choice of the radiometric frequencies which satisfy that requirement best, then allows the retrieval of the total atmospheric water contents and, hence, the estimation of the resulting attenuation at any frequency, by means of absorption models and estimates of the excess path length, as well.

8.6.2 Atmospheric water content

In a non-rainy, non-scattering, atmosphere the total absorption coefficient k_a can be in general expressed as the sum of the absorption contributions of oxygen, water vapour and liquid water:

$$k_a = k_{o2} + k_v + k_L \quad \text{dB/km} \tag{8.14}$$

In moderate humidity conditions, the absorption coefficients are approximately proportional to the density of oxygen, water vapour and liquid water, respectively.

The total attenuation can then be written as:

$$A = A_o + A_v + A_L = A_o + a_v V + a_L L \quad \text{dB} \tag{8.15}$$

where V and L, expressed in kg/m^2 or mm, are the integrated or total vapour and water contents, respectively, along the path and a_v, a_L (dB/mm) are the corresponding mass absorption coefficients.

Equation (8.15) can be used to calculate the atmospheric attenuation in the absence of rain at a given frequency once that the integrated heights V and L are given. The values of A_o and of a_v and a_L are obtained on the basis of radiosonde soundings by applying theoretical models for calculating the absorptions due to oxygen, vapour and water [Liebe, 1989; Liebe *et al.*, 1993].

Other than directly measuring the total water contents from upper-air soundings, the radiometric retrieval of V and L is possible, making use of equation (8.15) at two appropriate frequencies, which allows the real-time estimation of the attenuation at the required frequency, directly along the observed path [Solimini, 1988].

It should be noted that the integrated contents are approximate descriptors of the vertical distributions of water. In fact different profiles can correspond to the same values of V and L. Nevertheless, they can satisfactorily perform estimates of the atmospheric characteristics, as far as the total path absorption is concerned.

8.6.3 Radiometric retrieval of atmospheric water content

For a dual-channel radiometer operating at two frequencies f_1 and f_2 Equation (8.15) can be written as:

$$A_1 = A_{o1} + a_{v1} V + a_{L1} L \quad \text{dB} \tag{8.16a}$$

$$A_2 = A_{o2} + a_{v2} V + a_{L2} L \quad \text{dB} \tag{8.16b}$$

where A_1 and A_2 are the attenuations derived from the radiometric brightness temperatures via Equation (8.12).

The inversion of equations (8.16a) and (8.16b) allows estimates of the two quantities V and L from radiometric measurements of the path attenuation at two frequencies, chosen in such a way that the emitted radiation is particularly sensitive to water vapour at one of the frequencies and to cloud liquid water at the other.

The retrieval of total water vapour content V is dependent on the height profile of water vapour density. When this profile is approximately exponential, a frequency on one of the two wings of the absorption peak at 22.235 GHz may be chosen in such a way that the pressure broadening effect compensates for the profile effect. In that case the retrieval of V is independent of the scale height of the profile. For this reason the frequency of 20.6 GHz or 23.8 GHz is often chosen as the lower frequency, with high sensitivity to water vapour. The higher frequency, which is more sensitive to liquid water, is often chosen as 31.5 GHz, since this frequency is in a protected (radioastronomy) band [Westwater *et al.*, 1990]. In general, the larger the difference in terms of absorption of the two components at the two frequencies, the better the accuracy of the retrieval.

Equations (8.16a) and (8.16b) can be inverted deriving the individual expressions for V and L, as follows:

$$V = c_{0v} + c_{1v} A_1 + c_{2v} A_2 \tag{8.17a}$$

$$L = c_{0L} + c_{1L} A_1 + c_{2L} A_2 \qquad (8.17b)$$

where the c_{ij} are the inversion coefficients that summarize the microwave physical properties of the atmosphere through the mass absorption coefficients a_{ij} of equations (8.16a) and (8.16b) The inversion coefficients c_{ij} are calibrated from radiosonde data on a statistical basis by the use of theoretical models.

The procedure for the radiometric retrieval of atmospheric water contents and of the correspondent path parameters is schematically illustrated in Figure 8.8.

FIGURE 8.8

Procedure for radiometric retrieval of path attenuation

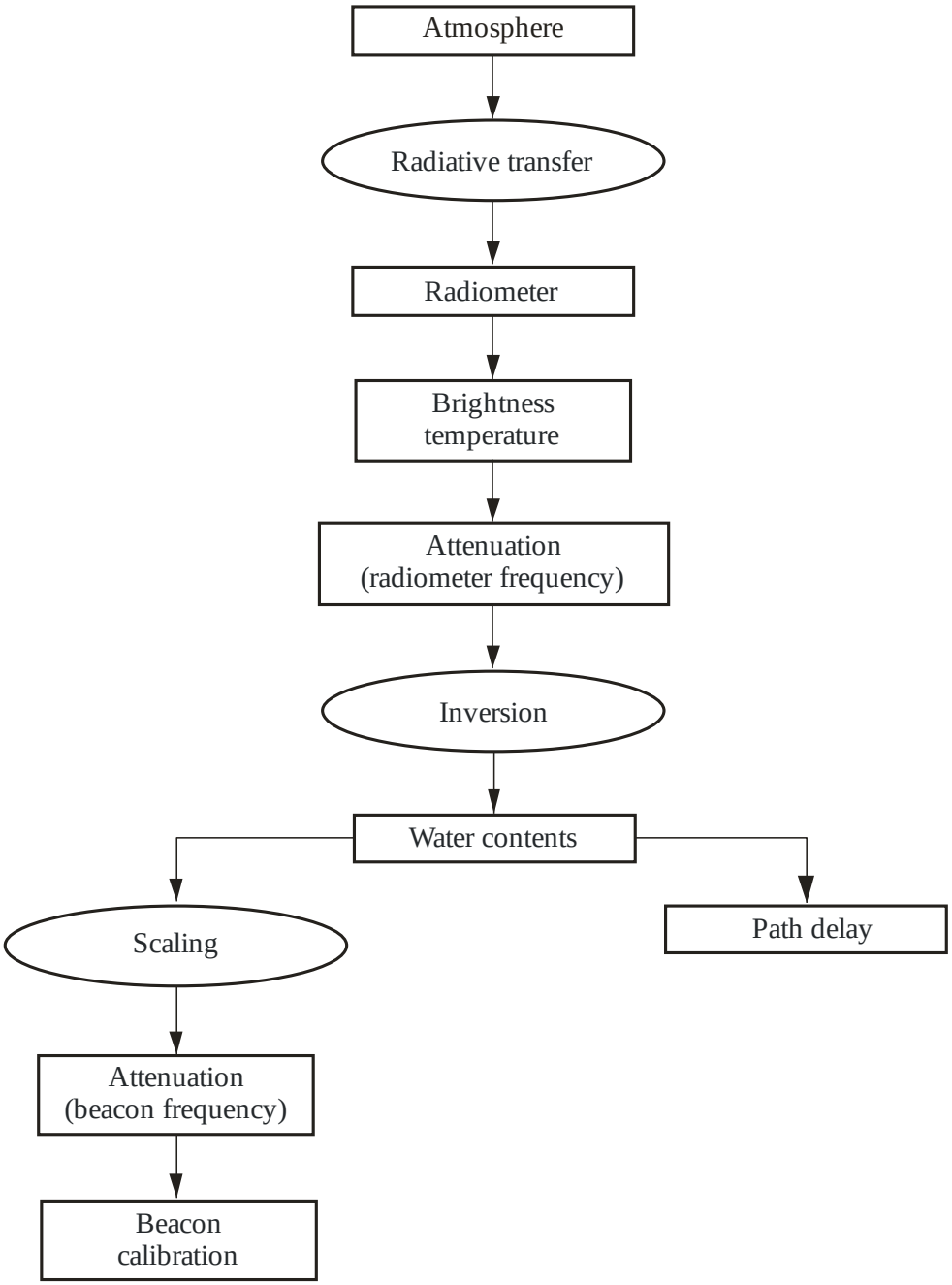

8.6.4 Retrieval and scaling coefficients

The retrieval and scaling coefficients c_{ij} and a_{ij} are the basic parameters for deriving the atmospheric water contents from radiometric measurements and for evaluating the attenuation at other frequencies, respectively.

They both depend on frequency and temperature and, to a minor extent, on V and L, through a cross-related dependence that links a_v to L and a_L to V.

In the complete procedure both the c_{ij} and the a_{ij} are required, the former at the radiometric frequencies, the latter at the scaled frequency. Since those coefficients are related to each other, only the a_{ij} are used in most of the cases also because of their physical consistency. The mass absorption coefficients a_{ij}, and hence the retrieval coefficients c_{ij}, can be calculated via both a physical method and regressive algorithms.

The physical method is solely based on radiosonde data, from which the total attenuation in equation (8.15) is computed by means of theoretical models. The total water vapour content V is obtained from the profile of the water vapour density directly measured by the radiosonde.

More difficulties arise when the total liquid L is to be estimated, since the radiosonde does not sense directly liquid water. Hence the presence and density of liquid must be established by means of other quantities, typically the local vapour density $\rho_v(z)$. Although sophisticated models have been developed to that purpose, the occurrence and the total amount of liquid are still the source of significant inaccuracies.

This uncertainty, however, is present in the statistical linear regression analysis, as well, which is commonly applied for the retrieval of the c_{ij} coefficients, directly from radiometric measurements, via equations (8.17a) and (8.17b). According to this approach, in fact, the radiometrically measured attenuations are compared to the values of V and L obtained from radiosonde soundings, over a statistically significant database.

It should be noted that the values of A_o for oxygen, being simply a total zenith attenuation, should be corrected accordingly for the actual elevation. The correction for oxygen may be done through the cosecant law.

The vapour mass absorption coefficient a_v shows a very limited space-time variability, which allows the use of only one value for wide regions. The variability is more pronounced in the case of a_L, which shows fluctuations among the sites and between summer and winter leading to differences of a few tenths of dB, in terms of the total liquid water attenuation. This behaviour can be attributed to both the temperature dependence and to the limitations of the criteria assumed to determine presence and quantity of liquid.

The sensitivity of the scaled attenuation to errors in the coefficients a_{ij} is not very high. Variations of 0.01 dB/mm in the a_v value, lead to less than 0.1 dB of error in A in clear air and to 0.4 dB in humid conditions (V = 40 mm). For the liquid coefficient a_L, an error of 0.1 dB/mm causes variations of 0.1 dB in wet sky (L = 1 mm).

Several factors contribute to the error in the radiometric determination of the atmospheric attenuation. The retrieval of V and L requires, in particular, both the physical measurement of radiation and the estimation of a number of parameters, each contributing to the total uncertainty [Westwater, 1978].

First, as far as equation (8.12) is concerned, the mean radiating temperature, T_{mr}, cannot be exactly determined unless the complete vertical distribution of the temperature is known. Using climatological data, however, the standard deviation of T_{mr} is limited to within a few Kelvin below 40 GHz.

The oxygen attenuation A_o is given as constant, in equation (8.15) and in the subsequent retrieval procedure, while for a given location and season it varies by about 5%, due to changes in temperature and pressure.

Furthermore, the values of total water vapour V are related to the radiometric measurements of the brightness temperature and hence to all the factors determining the absolute calibration of the instrument.

Errors are also present in water vapour attenuation coefficients, arising from uncertainties in molecular constants and due to variations in the vertical absorption profiles, which cannot be predicted climatologically.

Cloud liquid is more critical because of the pronounced dependence of the water absorption coefficient on the temperature (see Chapter 7). Without independent information on cloud base temperature, base height or thickness, the uncertainty in average cloud temperature can easily be around 5°C.

In conclusion, when the quantity of water is high, say more than 5 mm of total height, the error rises seriously and is likely to affect the vapour retrieval as well.

REFERENCES

BARBALISCIA, F. [1994] Reference Book on Radiometry and Meteorological Measurements, 2nd. OPEX Workshop, ESA WPP-03 Vol.3, Noordwijk, 8-10 Nov. 1994.

CLARK, W.W., MILLER, J.E. and RICHARDSON, P.H. [1984] Sky brightness temperature measurements at 135 and 215 GHz. IEEE Trans. Ant. Prop., Vol. AP 32, 929-933.

FERRAZZOLI, P., PALOSCIA, S., PAMPALONI, P., SCHIAVON, G. and SOLIMINI, D. [1992] Sensitivity of Microwave Measurements to Vegetation Biomass and Soil Moisture Content: A Case Study. IEEE Trans. on Geoscience and Remote Sensing, Vol. GE-30, No. 4, pp. 750-756.

GIBBINS, C.J., WRENCH, C.L. and CROOM, D.L. [1975] Clear sky atmospheric emission measurements at frequencies of 22, 95, 110, 123 and 150 GHz. Int. J. of Infrared and Mm-Waves, Vol. 5, 1443-1472.

GIBBINS, C.J. [1988] The effects of the atmosphere on radio wave propagation in the 50 - 70 GHz frequency band. Journal of the Institution of Electronic and Radio Engineers, Vol. 58, No. 6 (Suppl.), pp. S229-S240.

HARRIES, J.E. [1976] The distribution of water vapour in the stratosphere. Rev. Geophys. Space Phys., Vol. 17, 565-575.

LIEBE, H.J. [1989] *MPM* An atmospheric millimetre-wave propagation model. Int. Journal of Infrared and Millimetre waves, No. 10, pp. 631-650.

LIEBE, H.J., HUFFORD, G.A., COTTON, M.G. [1993] Propagation modelling of moist air and suspended water/ice particles at frequencies below 1 000 GHz. AGARD 52nd Specialists' meeting of The EM Wave Propagation Panel, Palma de Majorca, Spain, 17-21 May 1993.

NJOKU, E.G. and SMITH, E.K. [1985] Microwave antenna temperature of the Earth from geostationary orbit. Radio Sci., Vol. 20, 3, 591-599.

NOAA, NASA and USAF [1976] US Standard Atmosphere, 1976. US Supt. of Documents, Washington, DC, 20402, Stock No. 003-017-00323-0.

NORDBERG, W., CONAWAY, J., ROSS, D.B. and WILHEIT, T. [1971] Measurements of microwave emission from a foam-covered sea, J. Atmos. Sci., 38, 429-435.

POINTER, R.L. and PICKETT, H.M. [1984] Submillimetre, millimetre and microwave spectral line catalogue. JPL Publication 80-23, Rev. 2, Caltch, JPL, Pasadena, CA, 91103, USA.

SLOBIN, S.D. [1982] Microwave noise temperature and attenuation of clouds: Statistics of these effects at various sites in the United States, Alaska and Hawaii. Radio Sci., Vol. 17, 6, 1443-1454.

SMITH, E.K. [1982] Centimetre and millimetre wave attenuation and brightness temperature due to atmospheric oxygen and water vapour. Radio Sci., Vol. 17, 6, 1455-1464.

SOLHEIM, F.S. [1993] Use of pointed water vapour radiometer observations to improve vertical GPS surveying accuracy. Thesis submitted to the Faculty of the Graduate School of the University of Colorado for the degree of Doctor of Philosophy, Dept. of Physics.

SOLIMINI, D. [1988] Measurement of atmospheric water content by ground-based microwave radiometry. FUB Internal Report 1B4588.

ULABY, F.T., MOORE, R.K. and FUNG, A.K. [1981] Microwave Remote Sensing. Active and Passive, Vol. 1. Addison Wesley, Reading (USA).

ULABY, F.T., MOORE, R.K. and FUNG, A.K. [1982] Microwave Remote Sensing. Active and Passive, Vol. 2. Addison Wesley, Reading (USA).

ULABY, F.T., MOORE, R.K. and FUNG, A.K. [1986] Microwave Remote Sensing. Active and Passive", Vol. 3. Artech House, Deadham (USA).

WATERS, J.V. [1976] Absorption and emission by atmospheric gases. Methods of Experimental Physics, Vol. 12B, Radio Telescopes, Ed. M.L. Meeks, 142-176, Academic Press, New York, NY, USA.

WESTWATER, Ed R. [1978] The accuracy of water vapour and cloud liquid determination by dual-frequency ground-based microwave radiometry. Radio Science, Vol. 13, No. 4, pp. 677-685.

WESTWATER, Ed. R., SNIDER, Jack B., FALLS, Michael J. [1990] Ground-based radiometric observations of atmospheric emission and attenuation at 20.6, 31.65, and 90.0 GHz: A comparison of measurements and theory. IEEE Transactions on Antennas and Propagation, Vol. 38, No. 10, pp. 1569-1580.

WATERS, J.V. [1976] Absorption and emission by atmospheric gases. Methods of Experimental Physics, Vol. 12B, Radio Telescopes, Ed. M.L. Meeks, 142-176, Academic Press, New York, NY, USA.

WESTWATER, Ed R. [1978] The accuracy of water vapour and cloud liquid determination by dual-frequency ground-based microwave radiometry. Radio Science, Vol. 13, No. 4, pp. 677-685.

WESTWATER, Ed. R., SNIDER, Jack B., FALLS, Michael J. [1990] Ground-based radiometric observations of atmospheric emission and attenuation at 20.6, 31.65, and 90.0 GHz: A comparison of measurements and theory. IEEE Transactions on Antennas and Propagation, Vol. 38, No. 10, pp. 1569-1580.

CHAPTER 9

Cross-polarization and anisotropy

By using orthogonal polarizations, two independent information channels using the same carrier frequency can be transmitted over a single link. While the orthogonally polarized channels are completely isolated in theory, some degree of interference between them is unavoidable owing to the non-perfect polarization characteristics of the antennas and depolarizing effects on the propagation path. The main sources of this cross-polarization at centimetre and millimetre wavelengths are hydrometeor absorption and scattering.

Cross-polarization occurs due to the lack of spherical symmetry of the hydrometeors and to their tendency to have a preferred orientation.

Several administrations have carried out experiments aimed at collecting data and developing methods to predict depolarization; of these some foresaw to assess the complete transfer matrix of the medium while other focused on direct measurements of depolarization. The first approach, more complete, allowed a deeper insight on the physical mechanisms producing depolarization and lead directly to the concept of transfer medium “anisotropy” and average orientation of the hydrometeors, “canting angle”, a pair of basic parameters (called “quasi physical”) governing the whole phenomenon of depolarization. The second approach, more essential, allowed investigating directly the relationship between depolarization and attenuation, the ultimate objective for the design of telecommunication systems.

The two approaches have been demonstrated to be of mutual benefit for the determination of some primary model parameters and for the possibility of cross-validation.

This chapter lays the foundation of the whole topic presenting, first, the mathematical background for the quasi physical parameters and successively their relationship with the quantities of interest in the engineering practice: depolarization (XPD) and co-polar attenuation (CPA).

9.1 Mathematical background

The hydrometeors can be very well modelled as bodies with rotational symmetry whose orientation is determined by the angles of the rotational axis with respect to a reference system. Assuming as a reference a Cartesian system composed by the *x*-*y* axes laying on the transverse plane and the *z* axis along the propagation direction, the projection of the rotational axis on the *x*-*y* plane defines, along with the *z* axis, a plane often referred to as "first principal plane (or simmetry plane) of the particle". A "second principal plane" can then be defined as the one containing the propagation direction and perpendicular to the first one. The traces of the principal planes on the transverse plane are referred to as "principal directions".

No cross-polarization would occur if the EM field vector incident on each particle were oriented along one of the two principal directions. In the opposite case, due to the differential amplitude and phase of the two components of the forward-scattered field along the two principal directions, cross-polarization occurs.

9.1.1 Polarization state of a wave

The generic expression of the electric strength vector in a TEM wave propagating along the z axis is:

$$\boldsymbol{E}(t) = \mathrm{Re}(\boldsymbol{E}e^{j(\omega t - kz)}) = \mathrm{Re}[(\boldsymbol{u}_x E_x + \boldsymbol{u}_y E_y)e^{j(\omega t - kz)}] =$$

$$\boldsymbol{u}_x |E_x| \cos(\omega t - kz + \varphi_x) + \boldsymbol{u}_y |E_y| \cos(\omega t - kz + \varphi_y) \tag{9.1}$$

where:

$\boldsymbol{E}$ is a complex vector whose components $E_x = |E_x| e^{j\varphi_x}$ and $E_y = |E_y| e^{j\varphi_y}$ are two phasors (complex amplitudes), $\boldsymbol{u}_x$ and $\boldsymbol{u}_y$ are unit vectors in the x- and y-directions, ω is the angular frequency, t the time and k the wavenumber.

In general the tip of the electric vector (9.1) describes an ellipse which can be characterized by means of different equivalent parameters: considering that the absolute powers are of no interest for polarization-related problems, the parameters describing the size of the ellipse are neglected being instead of interest only the ones describing the aspect of the ellipse such as the axial ratio and the inclination of the axes. The representations that can be found in the scientific literature are based on two real- or one complex- parameter. Some of the most significant are:

A *Linear polarization ratio:* $P_l = \dfrac{E_y}{E_x}$ (9.2)

B *Circular polarization ratio:* $P_C = \dfrac{E_{rhcp}}{E_{lhcp}} = \dfrac{1 + jP_l}{1 - jP_l}$ (9.3)

where:

$$E_{rhcp} = \frac{1}{\sqrt{2}}(E_x + jE_y) \text{ and } E_{lhcp} = \frac{1}{\sqrt{2}}(E_x - jE_y) \tag{9.4}$$

are the amplitudes of the right- and left-hand circularly polarized components respectively.

C *Complex polarization angle*: $\Phi = \varphi + j\varphi'$ (9.5)

defined by the equations: $e^{j2\Phi} = P_c$ or $\tan(\Phi) = P_l$ (9.6)

This parameter allows expressing a generic polarization vector in the ***canonical form***:

$$\boldsymbol{E} = \boldsymbol{u}_x \cos\Phi + \boldsymbol{u}_y \sin\Phi \quad \text{or} \quad \boldsymbol{E} = \begin{pmatrix} \cos\Phi \\ \sin\Phi \end{pmatrix} \tag{9.7}$$

where $\Re\mathrm{e}(\Phi) = \varphi = \dfrac{1}{2}\angle P_c =$ and $\Im\mathrm{m}(\Phi) = \varphi' = -\dfrac{1}{2}\ln|P_c|$ or $\Phi = \tan^{-1}(P_l)$ (9.8)

(φ in Radians and φ' in Neper; note that in the case of is right-hand circular polarization $\varphi' = -\infty$ while for left-hand circular polarization $\varphi' = +\infty$)

D "*axial ratio*" and "*polarization angle*" the first one being the ratio between the major and the minor axis of the ellipse:

$$r = \frac{1+|P_c|}{1-|P_c|} = \frac{1+e^{-2\varphi'}}{1-e^{-2\varphi'}} = \cot\text{anh}\left(\varphi'\right) \tag{9.9}$$

and the second one, equal to φ, the angle between the major axis and the *x* axis, see Figure 9.1.

Notice that equation (9.9) is unambiguous as the two resulting values differ by π and therefore identify a single direction. Also note that if the ellipse is described in the right-hand sense, the axial ratio is negative and vice-versa. For linear polarization, the axial ratio approaches infinity.

FIGURE 9.2.1.A

Polarization ellipse

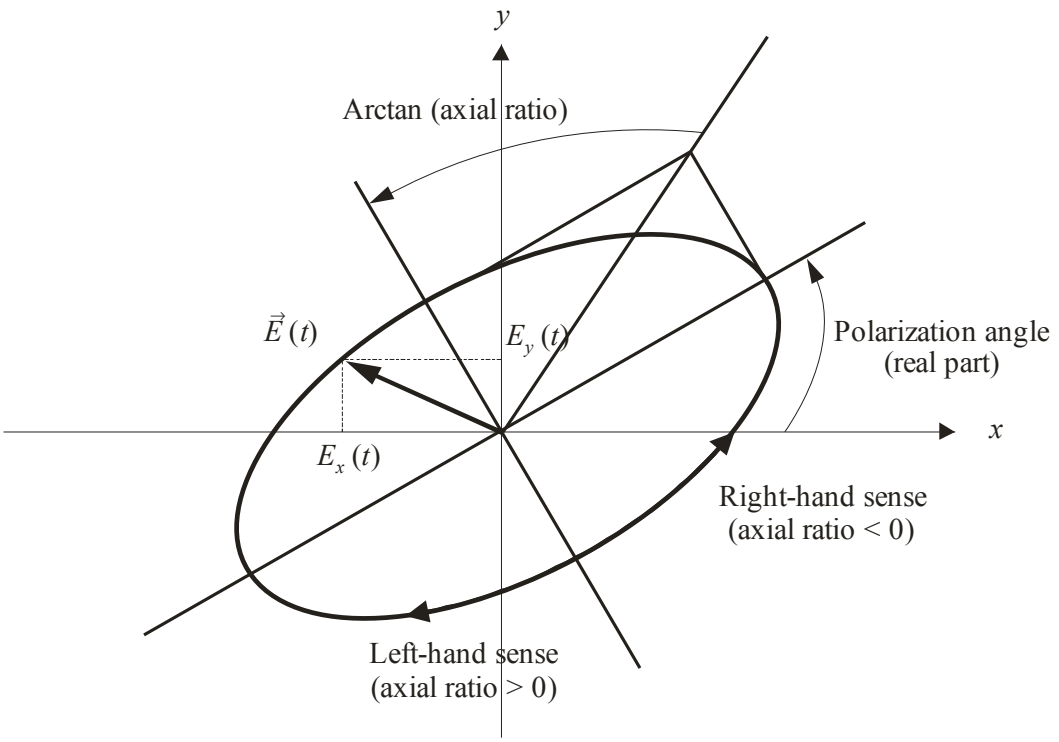

Radio-Meteo. 09-01

E "*Reduced components" electric field*: $\boldsymbol{E} = \boldsymbol{u_x}\cos\alpha + \boldsymbol{u_y}\sin\alpha\ e^{j\psi}$ (9.10)

With this normalization the total power is constrained to assume a fixed value and the x-component is assumed as phase reference. The first parameter, α, whose range is 0 to $\frac{\pi}{2}$, gives the power partitioning between the x- and y-components while the second parameter $\psi = \varphi_y - \varphi_x$ is the relative phase between these components and can assume any value in the turn-angle. The main advantage of this representation is that it never becomes singular, whichever polarization is considered.

The algebraic passages to transform these parameters into the ones describing the other representations are straightforward in both senses and omitted for sake of conciseness.

9.1.2 Orthogonal polarizations

Two generic polarizations $\boldsymbol{E}_d$ (called conventionally direct-polarization) and $\boldsymbol{E}_x$ (called cross-polarization) are orthogonal when the total power transported by the sum $\boldsymbol{E}_d + \boldsymbol{E}_x$ equals the sum of the powers transported singularly by each polarization; this happens when their scalar product is zero:

$$\boldsymbol{E}_d \cdot \boldsymbol{E}_x^* = 0 \tag{9.11}$$

(orthogonality condition). Making reference to the representation (9.10) and calling α_d, ψ_d the parameters characterizing $\boldsymbol{E}_d$ (direct-polarization) and α_x, ψ_x the ones characterizing $\boldsymbol{E}_x$ (cross-polarization), the orthogonality condition becomes:

$$\alpha_x = \frac{\pi}{2} - \alpha_d \qquad \text{and } \psi_x = \psi_d + \pi \tag{9.12}$$

or, equivalently:

$$P_{l,d} P_{l,x}^* = P_{c,d} P_{c,x}^* = -1 \tag{9.13}$$

The ellipses of two orthogonal polarizations have the same axial ratio, axes orientation exchanged and have opposite sense.

Any generic vector $\boldsymbol{A}$ can be decomposed along these polarizations to give the components A_d and A_x such that:

$$\boldsymbol{A} = A_d \ \boldsymbol{E}_d + A_x \ \boldsymbol{E}_x \tag{9.14}$$

These are given by the scalar products:

$$A_d = \boldsymbol{A} \cdot \boldsymbol{E}_d^* \quad \text{and} \quad A_x = \boldsymbol{A} \cdot \boldsymbol{E}_x^* \tag{9.15}$$

9.1.3 Dual-polarization transfer channel

The general way to describe a dual-polarization radio channel makes use of a matrix which relates the input electric strength components to the output strength components:

$\begin{pmatrix} E_{xt} \\ E_{yt} \end{pmatrix}, \begin{pmatrix} E_{xr} \\ E_{yr} \end{pmatrix}$ Transmitted and Received electric strength vector (9.16)

$\begin{pmatrix} T_{xx} & T_{xy} \\ T_{yx} & T_{yy} \end{pmatrix}$ Transfer matrix whose generic element T_{ij} gives the received electric strength component along the i axis when a unit vector alone is transmitted along the j axis. (9.17)

$$\begin{pmatrix} E_{xr} \\ E_{yr} \end{pmatrix} = \begin{pmatrix} T_{xx} & T_{xy} \\ T_{yx} & T_{yy} \end{pmatrix} \cdot \begin{pmatrix} E_{xt} \\ E_{yt} \end{pmatrix} \text{ Basic transfer channel equation} \tag{9.18}$$

(Notice that the determinant of this matrix is invariant to any rotation of the reference system)

$\delta_{xy} = T_{xy} / T_{yy}$ Complex cross-polarization ratio (received on x when transmitted on y)

$\delta_{yx} = T_{yx} / T_{xx}$ Complex cross-polarization ratio (received on y when transmitted on *x*) (9.19)

$XPD_y = -20\log_{10}\left|\delta_{xy}\right|$ "cross-polarization" or "cross-polar discrimination" (transmitted from *y*) (9.20)

$XPD_x = -20\log_{10}\left|\delta_{yx}\right|$ "cross-polarization" or "cross-polar discrimination" (transmitted from *x*)

$XPI_x = -20\log_{10}\left|\frac{T_{xy}}{T_{xx}}\right|$ "cross-polar isolation" (signals received on *x* when transmitted from *x* and *y*) (9.21)

$XPI_y = -20\log_{10}\left|\frac{T_{yx}}{T_{yy}}\right|$ "cross-polar isolation" (signals received on *y* when transmitted from *y* and *x*)

$$\Delta A_{xy} = T_{xx} / T_{yy} \qquad \text{complex co-polar ratio} \tag{9.22}$$

$\begin{pmatrix} C_{rr} & C_{rl} \\ C_{lr} & C_{ll} \end{pmatrix}$ transfer matrix in circular polarization, where (9.23)

$$\left.\begin{aligned} C_{rr} &= \frac{1}{2}\left[\left(T_{xx}+T_{yy}\right)+j\left(T_{yx}-T_{xy}\right)\right] \\ C_{ll} &= \frac{1}{2}\left[\left(T_{xx}+T_{yy}\right)-j\left(T_{yx}-T_{xy}\right)\right] \\ C_{rl} &= \frac{1}{2}\left[\left(T_{xx}-T_{yy}\right)+j\left(T_{yx}+T_{xy}\right)\right] \\ C_{lr} &= \frac{1}{2}\left[\left(T_{xx}-T_{yy}\right)-j\left(T_{yx}+T_{xy}\right)\right] \end{aligned}\right\} \tag{9.24}$$

$\delta_{rl} = C_{rl} / C_{ll}$ cross-polarization ratio in circular polarization
(received right-hand when transmitted) (9.25)

$\delta_{lr} = C_{lr} / C_{rr}$ cross-polarization ratio in circular polarization
(received left-hand when transmitted) (9.26)

$$\boldsymbol{E}_{\mathrm{I,II}} = \begin{pmatrix} T_{yy} - T_{xx} \mp \sqrt{(T_{yy}-T_{xx})^2 + 4T_{xy}T_{yx}} \\ -2T_{yx} \end{pmatrix} =$$

$$= \begin{pmatrix} C_{rl} + C_{lr} \mp \sqrt{(C_{rr}-C_{ll})^2 + 4C_{rl}C_{lr}} \\ j(C_{rr}-C_{ll}) + j(C_{rl}-C_{lr}) \end{pmatrix} = \text{eigenvectors} \tag{9.27}$$

(vectors passing through the medium without being depolarized; linear polarization components even if expressed with the “C” parameters).

$$G_{\mathrm{I,II}} = \exp(-\Gamma_{\mathrm{I,II}}) = \tfrac{1}{2}\left[(T_{yy} + T_{xx}) \pm \sqrt{(T_{yy} - T_{xx})^2 + 4T_{xy}T_{yx}} \right] =$$

$$= \tfrac{1}{2}\left[C_{rr} + C_{ll} \pm \sqrt{(C_{rr} - C_{ll})^2 + 4C_{rl}C_{lr}} \right] \quad \text{eigenvalues} \tag{9.28}$$

(complex ratio between the output- and the input-components of the eigenvectors when passing through the medium).

The eigenvalues are invariant with respect to any rotation of reference system; their product, also invariant, gives the determinant of the transfer matrix.

The eigenvectors can be represented in the canonical form (9.7):

$$\boldsymbol{E}_I = \begin{pmatrix} \cos\varphi_I \\ \sin\varphi_I \end{pmatrix}, \boldsymbol{E}_{II} = \begin{pmatrix} \cos\varphi_{II} \\ \sin\varphi_{II} \end{pmatrix} \tag{9.29}$$

which puts in evidence the pair of parameters φ_I and φ_{II} which fully define the axes orientations and the axial ratios of the characteristic polarization ellipses (see equations (9.6) and (9.7)); these angles are called characteristic canting angles of the medium.

The parameters Γ_I and Γ_{II} in equation (9.28) express the eigenvalues in exponential form and give the attenuation (in Nepers) and the extra phase shift (in Radians) suffered by the eigenpolarizations when crossing the medium.

In the polarization-related problems the absolute magnitudes of the input and output vectors are of no interest and therefore the transfer matrix terms can be arbitrarily normalized. This reduces the number of parameters of actual interest from four to three (complex). Accordingly, the ratio between the eigenvalues can be considered, without losing generality, instead of the two eigenvalues separately. Making reference to the exponents $\Gamma_{I,II}$ the eigenvalues ratio is expressed by the difference:

$$\Delta = \Gamma_{II} - \Gamma_I \tag{9.30}$$

called “anisotropy”. (First eigenpolarization is defined as the less attenuated one so that the real part of the anisotropy turns out positive by definition)

In conclusion the three complex parameters φ_I, φ_{II} and Δ fully define the behaviour of the most generic channel as far as the polarization properties are of concern; of these $\varphi'_I, \varphi'_{II}$ and Δ are invariant with respect to any reference axes rotation while φ_I, φ_{II} vary in opposite sense with respect to a rotation of the reference axes, so defining the absolute orientation of the eigenpolarization ellipses.

A further parameter, not independent from these, called "longitudinal homogeneity index" and defined as

$$L = \frac{T_{xy} - T_{yx}}{T_{xx} + T_{yy}}, \tag{9.31}$$

can also be considered for completeness; its value is zero in the case of longitudinally homogeneous medium. It is also invariant with respect to any reference axes rotation.

9.1.4 Simplified medium models

The general description considered above rarely needs to be applied in its full complexity. Two simplified models can be used in practice, without appreciable loss of accuracy. They are, in decreasing order of complexity, the "homogeneous medium model" which can be characterized by two complex parameters (four real), and the "principal planes model" which can be characterized by three real parameters [Dintelmann, 1994], [COST 205, 2002]. By cascading two media of this latter type another model “Two populations model” allowing the separation of rain- from ice-effects can be envisaged. This model can be described by four real parameters provided that some simplifying hypotheses about the rain and ice populations are made (see later) [Martellucci *et al.*, 1993] .

9.1.4.1 Longitudinally homogeneous medium model

With this assumption, valid in a wide range of practical circumstances, the conditions:

$$T_{xy} = T_{yx} \quad \text{(or equivalently } C_{rr} = C_{ll} \text{ or } L = 0) \tag{9.32}$$

$$E_I \cdot E_{II} = 0\,, \tag{9.33}$$

and:

$$p_{l,I}\, p_{l,II} = -1 \tag{9.34}$$

apply; these conditions allow writing the two eigenpolarizations in canonical form as:

$$\boldsymbol{E}_{\mathrm{II}} = \begin{pmatrix} \cos\Phi \\ \sin\Phi \end{pmatrix}\,, \quad \boldsymbol{E}_{\mathrm{I}} = \begin{pmatrix} -\sin\Phi \\ \cos\Phi \end{pmatrix} \tag{9.35}$$

It follows that the eigenvectors give rise to two ellipses with the same axial ratio and interchanged axes orientations. A single complex polarization angle is then sufficient to characterize both the eigenpolarizations; of the two possible angles, the one formed by the second eigenpolarization (the most attenuated) with respect to the *x* axis is considered as representative of the medium; this angle is referred to, in the literature, as "complex canting angle". The two eigenpolarizations are geometrically but not energetically orthogonal (i.e. they are not fully decoupled) as the relative ellipses are not described in opposite sense of rotation (notice indeed that equation (9.34) is not the orthogonality condition (9.13)).

Using the anisotropy and the complex canting angle the transfer matrix can be written as [Capsoni *et al.*, 1981] :

$$\boldsymbol{T} = \exp\left(-\frac{\Gamma_I + \Gamma_{II}}{2}\right) \begin{pmatrix} \cosh(\Delta/2) - \sinh(\Delta/2)\cos 2\Phi & -\sinh(\Delta/2)\sin 2\Phi \\ -\sinh(\Delta/2)\sin 2\Phi & \cosh(\Delta/2) + \sinh(\Delta/2)\cos 2\Phi \end{pmatrix} \tag{9.36}$$

in which, when Δ approaches 0, i.e. the medium becomes isotropic, the matrix approaches unity and the exponential-form coefficient gives the ordinary propagation term. Notice that this coefficient, invariant with varying the reference axes orientation, equals the determinant of the whole transfer matrix (9.17); moreover the determinant of the matrix in brackets is unit.

Using the circular-polarization field-components we have, correspondingly:

$$\boldsymbol{E}_{\mathrm{II}circ}=\begin{pmatrix} e^{j\Phi} \\ e^{-j\Phi} \end{pmatrix},\boldsymbol{E}_{\mathrm{I}circ}=\begin{pmatrix} je^{j\Phi} \\ -je^{-j\Phi} \end{pmatrix},\boldsymbol{T}=\exp(-\frac{\Gamma_I+\Gamma_{II}}{2})\begin{pmatrix} \cosh(\Delta/2) & -\sinh(\Delta/2)e^{j2\Phi} \\ -\sinh(\Delta/2)e^{-j2\Phi} & \cosh(\Delta/2) \end{pmatrix} \quad (9.37)$$

The cross-polarization ratios in the two cases are

$$\delta_{xy,yx}=\frac{-\tanh(\Delta/2)\sin 2\Phi}{1\pm\tanh(\Delta/2)\cos 2\Phi},\ \delta_{rl,lr}=-\tanh(\Delta/2)e^{\pm 2j\Phi} \quad (9.38)$$

Straightforward expressions for the evaluation of the anisotropy and canting angle, starting from the cross-polarization ratios, are:

$$\Delta=\ 2\ \mathrm{arctanh}\sqrt{\delta_{rl}\delta_{lr}}\ ;\ \Re e(\Phi)=\frac{1}{2}\left[\angle\delta_{rl}-\angle\sqrt{\delta_{rl}\delta_{lr}}\pm\pi\right],\ \Im m(\Phi)=\frac{1}{4}\ln\left|\delta_{lr}/\delta_{rl}\right| \quad (9.39)$$

(sign of the square-root of Δ non-negative, $\Re e(\Phi)$ reduced into the range $-\pi/2$ *to* $\pi/2$).

9.1.4.2 Principal planes model

This model is characterized by the same conditions as the previous one plus the following one:

$$\frac{1}{\delta_{xy}}-\frac{1}{\delta_{yx}}=\text{real}\ \ (\text{or equivalently}\ \left|\delta_{rl}\right|=\left|\delta_{lr}\right|\ \text{or}\ \Phi=\text{real}) \quad (9.40)$$

In this case the two eigenpolarizations turn out to be linear and orthogonal to each other. This case, the first historically conceived in the literature, is particularly intuitive as it describes the case of equi-aligned hydrometeors axes or all the hydrometeors principal planes parallel to each other. In this case the common orientation of the canting angles determines the so called "principal planes of the whole medium", referred as P.P., or "principal directions" along which two linearly polarized waves propagate without being depolarized. Actually the parallelism of all the single-hydrometeors symmetry directions is a too severe restriction as, in principle, the model applies also to the case of symmetrical distribution of the axes orientations (in which case the P.P. are given by the average direction) or in the case of small hydrometeors, when the Rayleigh scatter applies.

When the P.P.s exist, by choosing a reference system parallel to the principal directions, the transfer matrix becomes diagonal and the real and imaginary parts of the anisotropy, $\Re e(\Delta)$ and $\Im m(\Delta)$, become the differential attenuation and phase shift along the P.P.s. Even though the natural units for these quantities are Np and Rad, for practical reasons these parameters are usually given in dB and degrees.

For their relation with the physical reality of the medium, the parameters "anisotropy", "canting angle" and "longitudinal homogeneity index" are termed "quasi-physical parameters".

9.1.4.3 Two-hydrometeor population model

In the case of weakly polarizing media (anisotropies less than say, 1-2 dB and 10-20 degrees, a condition almost always verified in practice) a simplified model reflecting the behaviour of two interacting families of hydrometeors (typically rain and ice) can be assessed [Martellucci *et al.*, 1993]. For this purpose we can put in cascade the two media by multiplying the respective matrices and successively force the global medium to obey to the condition of homogeneous medium by putting, in place of the two terms of the principal diagonal of equation (9.37), their averages.

From this expression, for small anisotropies, we have, in normalized form:

$$\begin{bmatrix} C_{rr} & C_{rl} \\ C_{lr} & C_{ll} \end{bmatrix} = \begin{bmatrix} 1 & -\frac{\Delta_1}{2} e^{j2\Phi_1} \\ -\frac{\Delta_1}{2} e^{-j2\Phi_1} & 1 \end{bmatrix} \cdot \begin{bmatrix} 1 & -\frac{\Delta_2}{2} e^{j2\Phi_2} \\ -\frac{\Delta_2}{2} e^{-j2\Phi_2} & 1 \end{bmatrix} \cong$$
$$\cong \begin{bmatrix} 1 & -\frac{\Delta_1}{2} e^{j2\Phi_1} - \frac{\Delta_2}{2} e^{j2\Phi_2} \\ -\frac{\Delta_1}{2} e^{-j2\Phi_1} - \frac{\Delta_2}{2} e^{-j2\Phi_2} & 1 \end{bmatrix} \tag{9.41}$$

where the parameters $\Delta_1, \Delta_2, \Phi_1$ and Φ_2 are the unknown and the circular polarization ratios are supposed known (either measured or calculated).

From these expressions the parameters of the two families can be separately assessed provided that some further physical assumptions about the two families can be made. This is the case of medium constituted by rain and ice where the following assumptions can be made: Φ_1 = real because the large drops (the most anisotropic) tend to be equi-aligned, Φ_2 = real because for the ice needles the Rayleigh scatter applies well. Moreover, by writing the rain anisotropy in polar form: $\Delta_1 = d_1 e^{j\alpha_1}$, it has been found that the argument α_1 is reasonably constant and well predicted by assuming a certain raindrop size distribution; similarly, as for the ice family, the anisotropy is an almost purely imaginary quantity as dry ice, to a first approximation, does not produce attenuation; we can then write $\Delta_2 = jd_2$ with d_2 real. The four quantities d_1, d_2, ϕ_1 and ϕ_2 are then determined by inversion of equation (9.41). Their value is given by:

$$d_1 = \frac{\left|\delta_{rl} + \delta_{lr}^{*}\right|}{\cos\alpha_1}, \; d_2 = \frac{\left|\delta_{lr}^{*} e^{j\alpha_1} - \delta_{rl} e^{-j\alpha_1}\right|}{\cos\alpha_1} \tag{9.42}$$

$$\Phi_1 = \frac{1}{2}\left[\angle(\delta_{rl} + \delta_{lr}^{*}) \pm \pi\right], \; \Phi_2 = \frac{1}{2}\left[\angle(\delta_{rl} e^{-j\alpha_1} - \delta_{lr}^{*} e^{j\alpha_1}) + \frac{\pi}{2}\right]$$

The hypothesis of two in-cascade homogeneous layers of hydrometeors, one made up of rain and the second of ice crystals, has been adopted by several researchers [Amaya, 2000; Van de Kamp, 2004] when proposing methods to separate the contributions of rain and ice to depolarization during mixed events.

9.2 Microphysics of the depolarizing medium

In this section, largely based on material developed in [COST 255, 2002; Van de Kamp, 1994, Martellucci & Paraboni, 1998], we consider the longitudinally homogeneous medium model described by equation (9.36); let us put

$$\Gamma_I + \Gamma_{II} = (\gamma_x + \gamma_y)l \tag{9.43}$$

where:

l = length of the uniform dispersion of particles, the specific propagation constants $\gamma_{x,y}$ are defined as:

$$\gamma_x = jk + \frac{2\pi}{k^2}\sum S_{xx}(f,a,\vartheta,\varphi)$$
$$\gamma_y = jk + \frac{2\pi}{k^2}\sum S_{yy}(f,a,\vartheta,\varphi) \tag{9.44}$$

and the anisotropy and complex canting angle are given by:

$$\Delta = \frac{2\pi}{k^2}\sqrt{\sum(S_2 - S_1)exp(+2j\varphi)\cdot\sum(S_2 - S_1)exp(-2j\varphi)} \tag{9.45}$$

$$\Phi = \frac{j}{4}\ln\left[\frac{\sum(S_2 - S_1)exp(-2j\varphi)}{\sum(S_2 - S_1)exp(+2j\varphi)}\right] \tag{9.46}$$

In all these expressions the sum is performed over all the particles in one cubic meter contained in the dispersion and:

f = frequency

a = equivolumetric radius of the particle

θ, φ = angles that describe the spatial orientation of the rotational axis of each particle with respect to the propagation direction z, ($0 < \vartheta \le \pi$) and in the transverse plane ($-\frac{\pi}{2} < \varphi \le +\frac{\pi}{2}$)

k = $\frac{2\pi}{\lambda}$ wave-number

$S_1(\theta)$, $S_2(\theta)$ = co-polar forward-scattering amplitudes of the single-particle scattering matrix, when the incident electric field is linearly polarised along the symmetry planes (longitudinal plane "1" defined by propagation direction and rotational axis, longitudinal plane "2" containing the propagation direction and perpendicular to plane "1") [Poiares Baptista, 1994] .

$S_{xx,yy}$ = terms of the single-particle scattering matrix with generic orientation:

$$\left.\begin{aligned} S_{xx} &= \frac{S_1+S_2}{2} + \cos(2\varphi)\frac{S_2-S_1}{2} \\ S_{xx} &= \frac{S_1+S_2}{2} - \cos(2\varphi)\frac{S_2-S_1}{2} \\ S_{xy} &= S_{yx} = \frac{S_2-S_1}{2}\sin(2\varphi) \end{aligned}\right\} =$$

co-polar forward-scattering amplitudes of the single particle scattering matrix, when the longitudinal plane "2" is canted of an angle φ with respect to the reference plane xz.

9.2.1 Existence of the Principal Planes

The medium is characterized by the existence of the principal planes (Φ real), when at least one of the following conditions holds:

1) the scattering matrix of the particles can be calculated using the Rayleigh approximation for spheroidal particles (in which case all the differences $(S_2 - S_1)_i$ in equation. (9.46) have all the same argument φ_i and the argument of the logarithm turns out to be $e^{-4j\Phi}$ with Φ real, or
2) the statistical distribution of the orientation of the rotational axes is a symmetric function (in which case each φ_i can be written as $\varphi_0 + \Delta\varphi_i$ ($\varphi_0 = average$) and each term $e^{2j\varphi_i}$ gives rise to a single real term $\cos(2\Delta\varphi_i)$ owing to the simultaneous presence of a particle with "$+\Delta\varphi_i$" and one with "$-\Delta\varphi_i$" with equal weight. It follows $\Phi = \varphi_0$ real).

This is verified for all the following physical models of the medium.

9.2.2 Equi-aligned raindrop-axes model

In this case there is a unique value of θ_o and φ_o. The anisotropy and the canting angle of the medium are given by:

$$\Delta = \frac{2\pi}{k^2} l \int n(a)\left[S_2(f,a,\theta_0) - S_1(f,a,\theta_0)\right] da \tag{9.47}$$

$$\Re\mathrm{e}(\Phi) = \varphi_0 \ , \ \Im\mathrm{m}(\Phi) = 0 \tag{9.48}$$

where $n(a)$ is the raindrop size distribution.

This case is suitable to represent the intense rain characterized by large oblate ellipsoidal raindrops, especially in the case of terrestrial radio links where the limited turbulence or wind shear has a little effect on the drops axes spreading.

In Figures 9.2.A and 9.2.B [COST 255, 2002] an example of rain-induced depolarization, evaluated using the present model, is shown. In the calculations this parameter has been evaluated for a given rain intensity, assumed uniform over the whole rainy path-length; the same assumption has been made to evaluate the co-polar attenuation CPA and finally the XPD has been directly plotted as a function of CPA; the following further assumptions have been made:

- Frequencies (Italsat): 18.7, 39.6 and 49.5 GHz
- Water temperature = 0 °C
- Water refractive index calculated after [Ray, 1972]
- Shape of drops = oblate spheroids
- Link elevation = 41 degrees
- Drop axes alignment: θ_0 = 59 degrees (complement of the elevation), φ_0 = 5, 10, 30 and 45 degrees (these latter angles can be considered as the polarization angles of the linear polarization as seen by the Earth-station in clear air)
- Raindrop size distribution = Marshall-Palmer
- Scattering matrix of drops calculated using the point-matching technique [Oguchi, 1983]
- Rainy path-length = 1 km

FIGURE 9.2.A

Rain-induced XPD in circular polarization as a function of attenuation for 18.7, 39.6 and 49.5 GHz

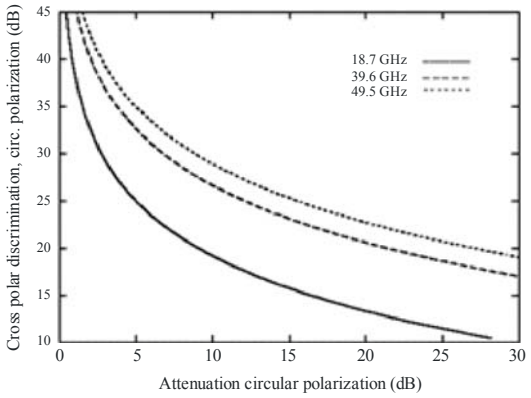

FIGURE 9.2.B

Rain-induced XPD in linear polarization as a function of attenuation for 49.5 GHz and 5, 10, 30 and 45 degrees polarizationangles with respect to horizontal

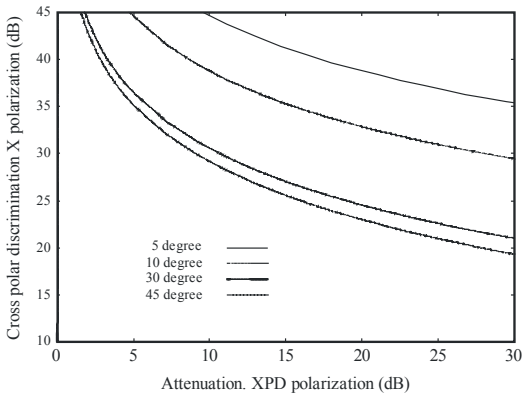

Radio-Meteo. 09-02

9.2.3 Raindrops with Gaussian distribution of orientations

This model assumes that the longitudinal canting angle θ and the transverse canting angle φ of the hydrometeor axes are random variables characterized by two Gaussian mutually uncorrelated distributions. In this case the total anisotropy and canting angle of the medium are given by:

$$\Delta = r\frac{2\pi}{k^2} l \int n(a)\left[S_2(f,a,\theta_0) - S_1(f,a,\theta_0)\right] da \tag{9.49}$$

$$\Re\mathrm{e}(\Phi) = \varphi_0 \ , \quad \Im\mathrm{m}(\Phi) = 0 \tag{9.50}$$

These expressions are similar to the (9.47) and (9.48) of the previous section but here θ_0 and φ_0 are the averages angles of the projections of the axes on the longitudinal and transverse planes respectively and r is a *reduction coefficient of the anisotropy*, given by:

$$r = \frac{1}{2}\left[1 + exp\left(-2\sigma_\theta^2\right)\right] exp\left(-2\sigma_\varphi^2\right) \tag{9.51}$$

where the σ's are the standard deviations of θ and φ. An estimate of the reduction coefficient in a terrestrial link has been performed in [Aresu *et al.*, 1993]: a value near 0.6 has been found; in satellite paths a lower value is expected.

This model is appropriate to represent relatively light rain, especially in satellite paths crossing intense turbulence layers. It is worth noting that the anisotropy tends to decrease with increasing elevation angle for two reasons: 1- the rainy path length tends to decrease so reducing both the attenuations and phase shifts, and 2- the angle θ_0 (close to the complement of the elevation angle) decreases as well so reducing the asymmetry of the drops as seen along the propagation axis.

More recently, a 2-D video disdrometer has been used to derive information on drop size distributions, and shape, orientation and oscillation of individual drops [Thurai *et al.*, 2007]. This information has then been used to calculate XPD along an earth-space link. The results are expected to better reflect real measurements compared to calculations that use models for the drops DSD, shape and orientation angle distributions.

9.2.4 Ice-needles in clouds

Even though the ice-particles in clouds can be of various shapes (spheres, pellets, hexagonal crystals, plates, needles etc.) the assumption that the majority of them is constituted by needles is usually made and a model in which only these are present is usually assumed [COST 255, 2002].

Due to aerodynamic, gravitational and electrostatic forces the ice-needles are often assumed to lay in the horizontal plane; two extreme situations can then be considered: the case where the axes of the needles are equi-aligned and the opposite case in which all the orientations in the horizontal plane are simultaneously present with the same weight (uniform distribution).

The characteristic canting angle appears real for two reasons: because the forward E.M. scattering obey to the Rayleigh approximation and because of the symmetric distribution of the axes orientations.

In the case of equi-aligned ice-needles the canting angle is given by:

$$\Re\mathrm{e}(\Phi) = \arctan\left[-\cot(\gamma)\sin(\beta)\right] \qquad \Im\mathrm{m}(\Phi) = 0 \tag{9.52}$$

where:

γ : angle formed by the (horizontal) ice-needles axes with respect to the vertical plane containing the propagation axis, and

β : elevation angle

In the opposite case of uniform distribution of the axes orientations, the first principal plane of the medium is always vertical.

As for the anisotropy, its value is given by:

$$\Delta = \Delta_{max}(l)\sqrt{B^2 + C^2} \tag{9.53}$$

where Δ_{max} is the maximum anisotropy corresponding to the theoretical case of ice-needles equi-aligned in the transverse plane, its value being given by:

$$\Delta_{max} = j\frac{(\varepsilon - 1)\pi}{\lambda} I \cdot (c_2 - c_1) \tag{9.54}$$

The meaning of the parameters in these expressions is the following:

$\varepsilon = \varepsilon_r - j\varepsilon_r = n^2 =$ complex permittivity of ice

λ = wavelength [mm]

I = total ice content along the slant path [mm]

$$c_{1,2} = \frac{1}{1 - (\varepsilon - 1)a_{1,2}}$$

$$a_1 = \frac{m}{2\cdot\left(m^2-1\right)}\left[m - \frac{1}{2\cdot\sqrt{m^2-1}}\ln\left(\frac{m+\sqrt{m^2-1}}{m-\sqrt{m^2-1}}\right)\right], \quad a_2 = 1-2a_1$$

$m = a/b > 1$

a,b = major and minor axes of the particle

$$B = \sin(\beta) < \sin[2\cdot(90-\gamma)] >$$

$$C = < \cos[2\cdot(90-\gamma)] > -0.5\cdot\cos^2(\beta)\cdot < \cos[2\cdot(90-\gamma)]-1 >$$

$< > =$ ensemble average of the parameter

In Figure 9.3.A [Paraboni, 1997; COST 255, 2002] an example of clouds-induced depolarization XPD_{clouds} in circular polarization is shown; this quantity has been evaluated by using the present model and assuming that the (horizontal) ice-needles orientation is transverse to the propagation path. To a difference of the previous case however, here the attenuation is negligible and is then unfit to act as independent parameter to evaluate the depolarization; the total columnar ice content encountered along the path has then be assumed as conditioning variable; this choice appears to be very convenient considering that the ice-content is a quantity which can be retrieved in standard meteorological data-banks. In Figure 9.3.B we show the XPD_{clouds} assuming various ice-needles orientation γ in the horizontal plane. In this case the canting angle $\Re e(\Phi)$ consequent to the variation of γ has been assumed as independent parameter.

FIGURE 9.3.A

Cloud-induced XPD_{cloud} in circular polarization as a function of the columnar ice-content for the frequencies 18.7, 39.6 and 49.5 GHz

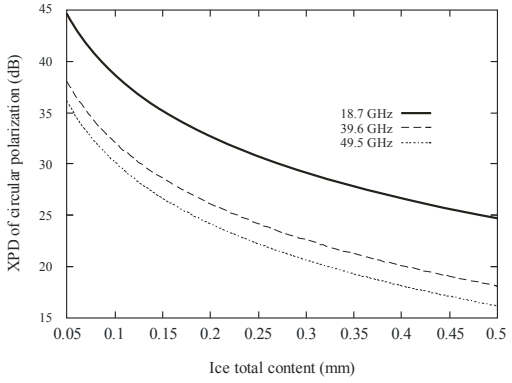

FIGURE 9.3.B

Cloud-induced XPD_{cloud} in linear and circular polarizations as a function of the apparent canting angle for the frequency 49.5 GHz

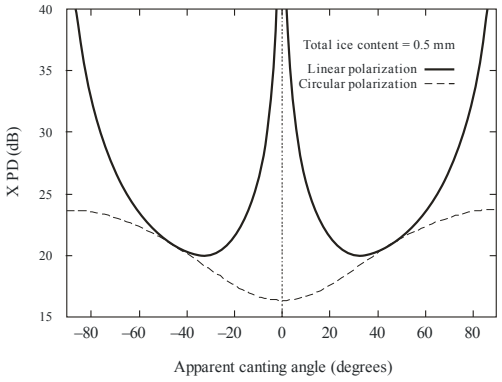

Radio-Meteo. 09-03

Observations using radar signals correlated with Ka-band beacon measurements in Japan suggest that plate-type crystals, such as sector plates and dendrites with general flat and wide shapes may play an important role on depolarization along earth-space paths [Maekawa *et al.*, 1993].

9.2.5 Ice depolarization during rainfall

This case is the most problematic as the simultaneous occurrence of rain and ice (relatively frequent) leaves room to a very wide range of combinations, both in magnitude and phase. One attempted approach to this problem is the one of relating, in statistical sense, the total columnar ice-content I [mm] to the rain intensity so that an unique parameter, the co-polar attenuation CPA, can act as driving parameter both for the XPD induced by rain and by ice [Paraboni *et al.*, 1997]. The proposed relation is:

$$I_i = a_i \cdot R + b_i \tag{9.55}$$

where:

i = 20%, 50%, 80% indicates the percentiles of the statistics of ice-content conditioned to the rain intensity R and the parameters

$a_i = 0.0067, 0.0032, 0.0016$
$b_i = 0.07, 0.04, 0.02$
apply for the above values of "i" and $R < 30$ mm/h

while:

$a_i = 0$
$b_i = 0.7, 0.4, 0.2$
apply for the above values of "i" and $R > 40$ mm/h

Identified as a fundamental parameter in the calculation of *XPD* due to ice, methods have been proposed for the extraction of I [mm] from time series of ice-induced differential phase shift obtained from *XPD* measurements after separating the contributions of rain and ice to depolarization [Amaya and Vanhoenacker-Janvier, 2000]. The use of I [mm] so derived, to calculate *XPD* at other frequencies over the same path should enable the estimation of more accurate distributions than methods based entirely on predictions.

9.3 Model parameters assessment

The assessment of the total degradation of radio-channel utilizing dual polarization would require, in principle, to know the joint statistics of the co-polar attenuation (CPA) and depolarization (XPD). In practice this data is rarely available in the literature and the more limited information contained in the average *XPD* conditioned to CPA is utilized. A further simplification of the problem is the one of considering the relationship between pairs of "equiprobable" values of these variables; fortunately the equiprobable XPD value is not too different from the conditional average [Van de Kamp, 2001]. This makes it possible to compare the values obtainable by averaging the theoretical above-described *XPD* values with the "equiprobable" measured values usually found in the literature. To this goal, considering that most of the short-term variations around the average *XPD* are due to the fast fluctuations of the canting angle around the vertical, it appears justified to assume, in the above formulae:

$$< \Phi > = \Phi_0 = -\tau \tag{9.56}$$

$$< \theta > = \theta_0 = 90^o - \beta \tag{9.57}$$

where τ is the link polarization angle with respect to the horizontal and β the link elevation.

From the equations (9.38) and (9.20) the rain-induced *XPD*, XPD_{rain}, can be derived; to this purpose the following further approximations are made:

$$\tanh\left(\frac{\Delta}{2}\right) \cong \frac{\Delta}{2} \quad \text{(small argument approximation)} \tag{9.58}$$

$$|\Delta| \approx K \cdot CPA^{\xi} \quad (K \text{ and } \xi \text{ dependent on physical parameters like frequency, elevation, spread of the canting angles ecc.)} \tag{9.59}$$

$$\ln\left[1+\frac{\Delta}{2}\cos(2\tau)\right] \approx CPA \cdot \cos(2\tau) \quad \text{(nearly-unit argument approx.)} \tag{9.60}$$

so that:

$$XPD_{rain} = -20\log\left|K \cdot CPA^{\xi} \cdot sen(2\tau)\right| + \tilde{K} \cdot CPA \cdot \cos(2\tau) \tag{9.61}$$

where K and $\tilde{K}$ do not depend on CPA and τ. From this equation the standard expression of the *XPD* always encountered in the Recommendation ITU-R P.618 can be derived:

$$XPD_{rain} = -V\log_{10} CPA + U(f) - C_{\tau} - C_{\beta} + C_{\sigma} + Z \cdot CPA \tag{9.62}$$

where:

V: (exact value depending on frequency – see below)

U: takes into account the main dependency on frequency

C_{τ}: takes into account the polarization angle τ

C_{β}: takes into account the link elevation angle β

C_{σ}: takes into account the spreading of the orientation axes

$Z = 0$ in circular polarization while in linear polarization takes into account polarization and elevation angles.

Based on the experimental data available in the literature these parameters have been identified by various authors and by the ITU-R; the most recent of them are reported in Table 9.1.

TABLE 9.1

Parameters for Eq. 9.62 for the XPD_{rain} as a function of rain-CPA

Authors	**V**	**U**	C_τ	C_β	C_σ	**Z**
ITU-R (1)	$30.8f^{-0.21}$ 6 ≤ *f* < 9 GHz $12.8f^{0.19}$ 9 ≤ f < 20 GHz 22.6 20 ≤ f < 40 GHz $13.0\,f^{0.15}$ 40 ≤ f < 55 GHz	60 log f-28.3 for 6 ≤ f <9 GHz 26 log f+4.1 for 9 ≤ f <36 GHz 35.9 log f – 11.3 36 ≤ f ≤ 55 GHz	10log[1-0484(1+cos(4τ))] (4), (5)	20log ($\cos^2\beta$)	$0.0053\sigma^2$(p) (6)	0
Cost 255 f ≥ 40 (2)	20	26 log f	10log[1-0484(1+cos(4τ))] (4), (5)	20log ($\cos^2\beta$)	0.0052σ(p) (6)	0
Van de Kamp (3)	16.9	20 log f for f < 30 -7+25 log f for 30 ≤ f ≤ 50	20log(sin2τ) (5)	41log (cosβ)	8	0.075 · $\cos^2\beta$ · cos(2τ) (5)

(1) [ITU-R, 2009; Nowland *et al*., 1977]

(2) [Cost 255, 2002], the only method assessed up to 49.5 GHz

(3) [Van de Kamp, 2001], parameters optimized over the whole set of XPD-CPA data available in the open literature up to year 2000 [Dissanayake *et al.* 1980; Chu, 1982; Stutzman et Runyon, 1984; Nowland *et al.*, 1977].

(4) Differently from the "natural" term 20log(sin2τ) this expression does not foresee any polarizations giving rigorously null depolarization, a typical effect of an average canting angle Φ_o admitting an imaginary part i.e. of non- existence of the principal planes.

(5) For circular polarization use τ = 45°

(6) The only probability-dependent term which takes into account the microphysical nature of precipitation: σ(1%)=0° , σ(0.1%)=5° , σ(0.01%)=10°

In order to consider the additional depolarization due to the presence of ice particles, the ITU-R method suggests the evaluation of XPD_{ice} as:

$$XPD_{ice} = XPD_{rain} \cdot 0.5 \cdot [0.3 + 0.1 \log P] \tag{9.63}$$

where P is the probability (in %) and then to combine the two polarizations as:

$$XPD_{tot} = XPD_{rain} - XPD_{ice} \tag{9.64}$$

REFERENCES

AMAYA, C., [2000] Separation of rain and ice contributions to depolarization on slant path links, Proc. 5th International Symposium on Antennas, propagation and EM Theory – ISAPE2000, Beijing, China, pp 29-32, August 2000

AMAYA, C and VANHOENACKER-D., [2000] Estimation of the effective ice content on earth-satellite paths from dual-polarisation measurements at Ka-band, IEE Proceedings on Microwaves, Antennas and Propagation, Vol.147, No.4, pp 315-319, August 2000

ARESU A., MARTELLUCI A. and PARABONI A., [1993] Experimental assessment of rain anisotropy and canting angle in horizontal path at 30 GHz, IEEE Trans. on Antennas and Propagation, Vol. 41, No. 9, pp 1331-1335, Sept. 1993

COST ACTION 255, [2002] Radiowave propagation modelling for SatCom services at Ku-band and above, Final Report, March 2002

CAPSONI C., PARABONI A., FEDI F., MAGGIORI D., [1981] A model-oriented approach to measure rain induced crosspolarization, Annal. de Telecommunicat., Vol. 36, No. 1-2, Jan-Feb. 1981

CHU T.S., [1982] A semi-empirical formula for microwave depolarization versus rain attenuation on Earth-space paths, IEEE Trans. Commun., COM-30(12), pp 2550-2554, 1982

DINTELMANN F., [1994] Reference book on depolarisation, OPEX-ESA WPP-083, 1994

DISSANAYAKE A.W, HAWORTH D.P. and WATSON P.A., [1980] Analytical models for cross-polarisation on Earth space radio paths for frequency range 9-30 GHz, Annal. de Telecommunicat., Vol. 35, No. 11-12, pp 398-404, 1980

ITU-R, P 618-10, [2009] Propagation data and prediction methods required for the design of Earth-space telecommunication systems, 2009

MAEKAWA Y., SOCK CHANG N. and MIYAZAKIi A., [1993] Ice depolarizations on Ka band (20 GHz) satellite-to-ground path and correlation with radar observations, Radio Science, Vol. 28, No. 3, pp 249-259, May-June 1993

MARTELLUCCI A., MAURI M. and PARABONI A., [1993] The physical basis of depolarization, Proceedings of Olympus Utilization Conference, (Sevilla, Spain), pp. 573-581, April 1993

MARTELLUCCI A., and PARABONI A., [1998] Test and development of models of atmospheric crosspolar discrimination for satellite communication systems at Ka- and V-band, Proceed. of the First International Workshop on Radiowave Propagation Models for SatCom Services at Ku-band and Above, Estec, Noordwijk, The Netherlands, 28-29 Oct. 1998

NOWLAND W.L., OLSEN R.L. and SHKAROFSKY I.P., [1977] Theoretical relationship between rain depolarisation and attenuation, Electronics Letters, Vol. 13, No. 22, pp.676-678, Oct. 1977

OGUCHI T., [1983] Electromagnetic wave propagation and scattering in rain and other hydrometeors, Proc. IEEE, Vol. 71, No. 9, pp. 1029-1078, Sept. 1983

PARABONI A., MARTELLUCCI A. and POLONIO R., [1977] A probabilistic model of rain and ice depolarization based on experimental estimation of the atmospheric ice content, Proc. SBMO/IEEE International Microwave and Optoelectronics Conference, Natal, Brazil, pp. 707-712, Aug. 1997

POIARES BAPTISTA J.P.V. (Editor), [1994] Reference book on radar, OPEX-ESA WPP-083, Nov. 1994

RAY P. S., [1972] Broad Band Complex refractive index of ice and water, Applied Optics, Vol. 11, No. 8, 1972.

STUZMAN W.L. and RUNYON D.L. [1984] The relationship of rain-induced cross polarization discrimination to attenuation for 10 to 30 GHz Earth-space radio links, IEEE Trans. on Antennas and Propagation, AP-32(7), pp. 705-710, 1984

THURAI M., HUANG G., BRINGI V. and SCHONHUBER M., [2007] Calculations of XPD spread for 20 GHz fixed satellite systems using 2-D video disdrometer data, Proc. 2nd European Conference on Antennas and Propagation, on CD, Edinburgh, U.K., 11-16 Nov. 2007

VAN DE KAMP, M.M.J.L., SMITS E.J.M., HERBEN M.H.A.J. and BRUSSAARD G., [1994] Experimental verification of existing rain depolarization models, Archiv fuer elektronic und uebertragungstechnik, No.48(3), pp. 173-176, 1994

VAN DE KAMP, M.M.J.L, [2001] Depolarisation due to rain: the XPD-CPA relation, International Journal on Satellite Communication, Vol. 19, Issue 3, pp. 285-301, 2001

VAN DE KAMP, M.M.J.L, [2004] Separation of simultaneous rain and ice depolarisation, IEEE Trans. on Antennas and Propagation, Vol. 52, No. 2, pp. 513-523, 2004

CHAPTER 10

Statistical aspects of modelling

10.1 Variability of atmospheric processes

This chapter deals with the variability of any time-varying radiometeorological quantity, and is of special relevance to the telecommunication system designer who has to meet the "any month" (statistical) performance criteria or who wants to assess the risk on system availability regarding the inter-annual (i.e. year-to-year) variability of propagation phenomena (especially rain attenuation).

Radiometeorological quantities are random processes that exhibit a complex time dependence with time-scales varying from milliseconds to many years. The obvious seasonal dependence of many of such quantities implies that the random process is cyclo-stationary, and this means that during a relatively short observation time (e.g. one month, one year) the observed performance of a radio link may deviate considerably from the performance averaged over many years. For this reason many ITU-R performance criteria are expressed in terms of the "worst-month" reference period (Recommendation ITU-R P.581). Many propagation prediction methods basically predict, directly or indirectly, the statistics for the "worst-month" period.

For designers and users alike, there is, in addition, a need for methods that allow the evaluation of the performance of radio links when considered over shorter periods of observation. These methods should be of a general nature, since the questions posed may vary from one application to another.

Section 10.1.2 presents a general method to evaluate the natural variability of a radiometeorological parameter relative to its long-term average for observation times that are multiples of one month (e.g. "worst-month", second "worst-month", yearly).

Section 10.1.1 presents definitions of many parameters used in Chapter 10.

10.1.1 Definitions

Statistics

The simplest statistical characterization of a radiometeorological stochastic quantity, symbolized by $\underline{s}$, is by its probability distribution $p(s)$:

$$p(s) = \text{probability } (\underline{s} > s)$$

where: s denotes a threshold value

p is sometimes called the long-term distribution or the distribution for an average year.

Likewise the "average annual worst-month" probability distribution p_w:

$$p_w(s) = \text{probability } (\underline{s} > s \mid \text{in the worst-month period})$$

Here, only a sub-population of propagation events that occur in the worst-month period as defined in Recommendation ITU-R P.581 is considered.

The time fraction of excess (t.f.e.)

A more general distribution than the probability distribution is the time fraction of excess (t.f.e.) that the stochastic quantity $\underline{s}$ exceeds certain threshold values s within well-defined observation periods. This period may be limited, e.g. the month May 1972, or infinite; e.g. all May months. In the last case, the t.f.e. can be interpreted as a probability distribution.

The individual monthly t.f.e. $\underline{X}$

Taking the observation periods as each of the calendar months of each year leads to an infinite set of t.f.e. values:

$X_{jm}(s)$ = the t.f.e. in month m of year j, for the chosen threshold value s

(m = 1, 2, ..., 12, j = ..., 1988, 1989, ...).

In practice the values of X_{jm} may vary considerably from month-to-month and year-to-year. In fact $X_{jm}(s)$ may be considered to be the realization, in month m of year j, of the stochastic quantity $\underline{X}(s)$ with well-defined statistical properties.

The annual worst-month t.f.e. $\underline{W}$

The annual worst-month t.f.e. of the radiometeorological stochastic quantity $\underline{s}$, in year j, is defined for a given threshold value s as:

$W_j(s)$ = the maximum of $X_{jm}(s)$ from the 12 months (m = 1, 2, ...,12) in year j.

W_j can be considered to be the realization, in year j, of the stochastic quantity $\underline{W}$.

NOTE – The above definition [Crane and Debrunner 1978] [Brussaard and Watson, 1979] also defines the worst-month period in each year j; this period may be different for different threshold values s.

The average annual worst-month t.f.e., p_w

This is simply defined as the ensemble average of the annual worst-month t.f.e. values:

$$p_W(s) = <\underline{W}(s)>$$

For practical purposes, p_w can be equated to the probability that $\underline{s} > s$ within the infinite period of all annual worst-months.

The average annual t.f.e., p

Defining the time periods to be individual years leads to the infinite ensemble of realizations of annual t.f.e. $\underline{Y}(s)$. The ensemble average of this stochastic quantity leads to the average annual t.f.e. $<\underline{Y}(s)>$. In practice this distribution is equal to the basic probability distribution $p(s)$ introduced in § 10.1.2:

$$p(s) = <\underline{Y}(s)>$$

10.1.2 Concepts and models

The general approach

In the general approach, the outages, performances, etc. of a radio link during extreme time periods are predicted not from the usually scarce amount of data pertaining to rare events but extrapolated

from the bulk of propagation data pertaining to less extreme periods through use of general statistical models. For example, when five years of data are available the worst-month characteristics are determined through analysis of the whole of the 5 x 12 monthly data instead of only using the five annual worst-month data.

The starting point for the general approach is the Complementary Cumulative Distribution Function (CCDF), *F*, composed of the ensemble of realizations of the monthly time fraction of excess $\underline{X}$:

$$F(X) = \text{Probability}\ (\underline{X} > X)$$

From this so-called CCDF (see Annex 10.A.1) the statistical distributions of time fraction of excess for other reference periods (which are integer multiples of a month) can be derived (e.g., the distribution of the yearly time fraction of excess $\underline{Y}$ or the distribution of the annual worst-month time fraction of excess $\underline{W}$) using combinatorial statistical methods.

The CCDF

For a large class of radiometeorological quantities, the CCDF, *F(X)*, has been found to be a conditional exponential:

$$F(X) = C_0 \exp(-X/C_1) \tag{10.1}$$

$$\{0 < C_0 < 1, X > 0\}$$

where the parameters C_0, C_1 are usually dependent on the threshold level being considered. This distribution was first proposed by [Crane and Debrunner, 1978] and has been extensively confirmed by [Mawira, 1980] [COST 205, 1985a] [COST 205, 1985b] [Dellagiacoma and Tarducci, 1987] for threshold levels pertaining to long-term probabilities less than 1%. For threshold levels pertaining to long-term probability values greater than 1%, the fit to the data often produces values of C_0 greater than 1 [Poiares Baptista *et al.*, 1989] [Fukuchi *et al.*, 1985].

For such cases the above model can be extended as follows [Mawira, 1989]:

$$F(X) = \exp(-(X - C_1 \ln(1/C_0))/C_1) \tag{10.2}$$

$$\{X > C_1 \ln(1/C_0), C_0 > 1\}$$

where X is modelled as the sum of a constant, $C_1 \ln (1/C_0)$, and an exponentially distributed stochastic component with mean C_1.

Annex 10.A.2 describes a procedure for estimating the parameters C_0 and C_1 from a set of observed monthly time fractions of excess.

Since the average monthly t.f.e. $\langle X \rangle$ is approximately p for the average year, the parameter C_1 in the above model may be replaced by p/C_0 so the relationship $C_0(p)$, in combination with prediction methods for p, provides a full characterization of the CCDF F.

The elimination of the threshold parameter is more than a purely mathematical convenience, since it has been observed that the relationship $C_0(p)$ is mainly determined by the underlying meteorological processes while the specific radio link parameters are only of secondary importance [Mawira, 1980; Yon *et al.*, 1984; COST 205 1985a; COST 205 1985b; Fukuchi *et al.*, 1985]. Therefore, once this relationship has been established for a given process it can be used in the variability estimations for radio links with differing parameters (e.g. frequency, path-length, elevation-angle, etc.).

Other CCDFs proposed include the conditional lognormal distribution [Crane, 1991] and the shifted Gamma distribution [Fukuchi and Watson, 1989]. For an extensive discussion of the subject, see [Mawira, 1999].

The population of the monthly time fraction of excess

When C_0 is smaller than 1 the average number of months per year that have values of $\underline{X}$ greater than 0 is:

$$M_0 = 12\, C_0 \tag{10.3}$$

with $M_0 < 12$ months; for the extended model, where $C_0 > 1$ and $M_0 = 12$.

Theoretically, therefore, the population of $\underline{X}$ may be considered to be composed of two distinct sets, the first of which consists of 12-M months in each year with $\underline{X} = 0$, and a second subset which may produce $\underline{X} > 0$, consisting of M active months per year with $M_0 < M \leq 12$.

Within the active population subset the distribution of $\underline{X}$ is given by:

$$F_M(X) = C_{0M} \exp(-X/C_1) \tag{10.4}$$

with

$$C_{0M} = C_0\, 12/M$$

$$\{0 < C_0 < 1;\ 0 < C_{0M} < 1\}$$

In general, the exact value of M cannot be determined from the aggregate distribution $F(X)$, however for practical applications, it is often sufficient to take M values between 12 and $12C_0$ [Mawira, 1985].

10.2 Worst-month statistics

10.2.1 The ITU-R definition

In the design of radio links (e.g. satellite-to-Earth, terrestrial-microwave) the detrimental influence of radiometeorological effects must be considered. These effects generally are stochastic in nature and exhibit seasonal variations, and the occurrence of rare but severe events.

A specification of the required grade of service done solely on the basis of the simple probability distribution (the distribution associated with an infinitely long reference period) will not reflect the complex time behaviour. One way to deal with this problem is to use conditional statistics defined for special reference periods with peak propagation activities. An alternative approach is to define, together with the system requirements, an acceptable risk that the impairments due to radiometeorological effects may exceed the requirement.

In the past, the ITU, following the practice of ITU-T, in its classical formulation of noise requirements defined as the reference period "any month" and "any year". This implies a risk equal to zero and is incompatible with either of the two approaches mentioned or, for that matter, with any sensible statistical analysis.

The solution to this enigma, first suggested by [Brussaard and Watson, 1979] and adopted by ITU-R (Recommendation ITU-R P.581), has been to define the "average annual worst-month" as the statistical equivalent of the undefined term "any month". The term "any year" is usually equated with "average year".

10.2.2 Calculation method using *Q*

In general, most models predict the long-term distribution p using radiometeorological data. The worst-month distribution p_w is then calculated through the conversion factor Q which is defined as the ratio of the average annual worst-month t.f.e. to the average annual t.f.e., both taken at the same threshold level:

$$Q = p_w / p \tag{10.5}$$

Examination of the relationship between Q and p for a large variety of propagation effects have shown that the power law form:

$$Q = Q_1 \text{ x } p^{-\beta} \tag{10.6}$$

$$\{1 < Q < 12\}$$

is applicable for the probability range (0.001% < p < 3%), [Segal, 1980]. For the higher probability values (p > 3%), a constant $Q = Q_1 3^{-\beta}$ appears to be applicable up to about p = 30%, while for p > 30% a power law form is valid with Q = 1 at the 100% level [Poiares Baptista *et al*., 1989].

For some uses it is preferable to express Q as a function of p_w:

$$Q = Q_1' \times p_w^{-\beta'} \tag{10.7}$$

with

$$Q_1' = Q_1^{\ 1/(1-\beta)} \text{ and } \beta' = \beta/(1-\beta).$$

Formulas relating Q as function of p with Q_1 and β as parameters are given in Recommendation ITU-R P.841. Table I in this Recommendation summarizes the values of Q_1, β found in various locations for several propagation effects. This table shows clearly the different climatic regions and the dependence with the propagation process, e.g. for north-west Europe the values of Q at the p = 0.01% level for terrestrial rain effects, slant-path rain effects and for ducting effects are respectively 5.5, 6.5 and 7.9.

For global planning purposes in satellite broadcast applications a single average relationship may be preferable:

$$Q_1 = 2.85, \beta = 0.13$$

or alternatively:

$$Q_1' = 3.3, \beta' = 0.15$$

These global values may be considered to represent a climate zone with reasonably benign seasonal variations.

When considering measured values of Q it is important to note that many years of data are required for reliable predictions. The deviation of error for Q from four years of data is approximately 10% to 20%, while for one year of observation, the deviation of error is about 30% [Mawira, 1985]. An analysis by [Casiraghi and Paraboni, 1989] performed on 176 site years of slant path attenuation data from some 40 stations in Western Europe [COST 205, 1985b] shows a best fit value Q_1 = 3.7,

$\beta = 0.13$ with an r.m.s. error of about 22%. This r.m.s. error is due to both the limited observation period of approximately four years per site and the climatic differences between stations.

10.2.3 Calculation method using C_0

The exact relationship between Q and C_0 can be derived using the conditional exponential model. A good approximation to this relationship is given by:

$$Q = 12/(1 + 3\ C_0) \qquad (10.8)$$

$$\{0 < C_0 < 1\}$$

for $M = 12$; while the upper envelope (for $M = 12\ C_0$) can be found by increasing the above value of Q by $(1 + 0.002/C_0)$, with an upper limit of 12 for the new value of Q. From this equation, C_0 can be estimated from measured values of Q, although C_0 should preferably be determined from the full population of X through a regression analysis as described in Annex 10.A.2.

The conditional exponential model has also been used for an analysis of the reliability of a direct estimate of Q from a limited number of years of observations [Segal, 1980]. The results show errors of approximately 30% for one year of observation, reducing to 10 to 20% for four years of observations. In [Dellagiacoma and Tarducci, 1987] the variability of Q obtained from limited observation periods as predicted from this model has been confirmed in tests carried out using a large rainfall intensity database (55 sites, each with 10 years of observations).

The relationship $C_0(p)$ can be considered to be a fundamental climatic "variability descriptor". Alternatively the relationship $Q(p)$ can be taken, since there is nearly a one-to-one correspondence between Q and C_0 (the relationship $Q(p)$ is at the moment more readily available than that of $C_0(p)$).

10.2.4 Variability aspects

In many cases it may be desirable to consider more extreme situations than that represented by the average of the annual worst-month t.f.e. $\underline{W}$. One possible scenario is to consider the average worst-month in N years with $N > 1$. Alternatively the variability of $\underline{W}$ can be considered; this method is preferable since it does not require a different worst-month definition.

The conditional exponential model, given in § 10.1.2, can be used to determine the probability distribution of $\underline{W}/p_w$ as a function of C_0 or respectively Q [Mawira, 1989, 1999]. The results are given in Figure 1 of Recommendation ITU-R P.678 where the values of the annual worst-month t.f.e. $\underline{W}$, normalized to p_w, are shown for various percentiles and as a function of Q. As an example of the use of this figure: for the threshold level x with $Q = 6$, 10% of the annual worst-month t.f.e. values W will have an t.f.e. which is 1.7 times greater than that of p_w. Therefore, once Q is known for a given threshold level the more extreme annual worst-month t.f.e. can be predicted using Figure 1 of Recommendation ITU-R P.678.

10.3 Annual statistics

10.3.1 Crane model

10.3.1.1 Variability aspects

The annual t.f.e. $\underline{Y}$, (see § 10.1.1) is a stochastic variable that exhibits a year-to-year variability that can be quantified by its coefficient of variation:

$$\Omega_y = \sigma_y / p \tag{10.9}$$

where σ_y is the standard deviation of $\underline{Y}$. The conditional exponential model predicts the following relationship [Mawira, 1980]:

$$\Omega_y = \sqrt{\frac{1}{6C_0}\frac{1}{M}} \tag{10.10}$$

$$\{0 < C_0 < 1\}$$

The upper and lower bounds of Ω_y correspond to M = 12 and M = 12 C_0. The validity of this equation has been confirmed using extensive slant path attenuation data [COST 205, 1985b]. The analysis leading to equation (10.10) also gives the formula for the probability distribution of $\underline{Y}$. This formula, which is derived theoretically from the conditional exponential model, expresses the probability distribution of $\underline{Y}$ as the sum of a number of Gamma distributions. The Gamma distribution itself has also been tested satisfactorily as a model for the distribution of $\underline{Y}$ by [Fukuchi and Watson, 1989]. Numerical calculations show that the distribution of $\underline{Y}/p$ is very similar to the distribution of $\underline{W}/p_w$ [Howell *et al*., 1983]. As a result, Figure 1 of Recommendation ITU-R P.678 can also be used to characterize the variability of the annual time fraction of excess $\underline{Y}$, using the following modification:

$$Y/p = W/p_w \tag{10.11}$$

$$\text{for } Q > 6$$

and

$$Y/p = 1 + (1 - 0.12\,(6 - Q))\,(W/p_w - 1) \tag{10.12}$$

$$\text{for } Q < 6$$

10.3.1.2 Accuracy and model testing

When addressing the variability of radiometeological probability distributions, another aspect to be considered is the accuracy of the estimation of the average distribution (or any other parameter) taken from a limited set of (independent) observations. In [Mawira, 1999] the accuracy of the estimation of Q from a limited number of years of observation is investigated using the conditional exponential model.

Powerful tests are available for the analysis of the variability of independent samples from a stationary random process with a known probability distribution. If the probability distribution is known or assumed to be normal, the application of the statistical tests can be readily accomplished using standard tables. In other cases, a transformation of the observables may be required to obtain a normal distribution function.

In the absence of a suitable model, the long-term median cumulative distribution function (CDF) calculated from a series of long-term measurements may be used as a reference to test the validity of a new limited series of measurements. However, in most practical cases concerning propagation measurements, this long series will be absent. This problem may be circumvented by using a prediction model for the estimation of the long-term median CDF for each path and site. The use of a model for the estimation of the reference CDF will inevitably increase the estimation uncertainty due to modelling errors.

Observations of the annual variability of rain attenuation CDFs at specified probability values at 11 locations spanning seven rain-climate zones in Europe and the USA suggested that the variable

$$x = \ln(\text{measured value/predicted value})$$

is normally distributed. When applied to the attenuation exceeded for 0.01% of the year, a value of 0.29 was obtained for the standard deviation [Crane, 1990]. This value was estimated to consist of two components: a value of 0.17 for the location-to-location variations and a value of 0.23 for the year-to-year variations.

Once the reference distribution for the samples is established, individual series can be tested against the log-normal hypothesis. A test for large deviations or outliers then relies on the failure of the hypothesis that the observed deviation between the reference distribution and the distribution of ordered samples is consistent with the modelled deviation.

Conversely, the logarithmic variable x may be used to test the performance of prediction models against observed CDFs of attenuation. This is the basis for the definition of the testing variable in Recommendation ITU-R P.311. The rain attenuation prediction method in Recommendation ITU-R P.618 was selected because it produces the minimum least-square (logarithmic) deviation between the prediction method and measured data in the ITU-R Study Group 3 databank.

10.3.2 Inter-annual variability of rainfall rate and rain attenuation statistics

Annex 2 of Recommendation ITU-R P.678 predicts the inter-annual variability of rain attenuation and rainfall rate statistics [Jeannin *et al.*, 2013] [Boulanger *et al.*, 2013]. This approach computes the variability of the probability that the rain attenuation (or rainfall rate) exceeds a given value.

This model assumes the inter-annual fluctuations of rain attenuation (or rainfall rate) statistics are asymptotically normally distributed around the long-term probability of exceedance, p, with a yearly variance that is composed of the estimation variance and the inter-annual climatic variance.

The estimation variance is based on the correlation function of the underlying Bernoulli process and is a function of the exceedance probability.

The inter-annual climatic variance is the annual variation of the probability of rain attenuation or rainfall rate around the long-term probability of rain attenuation or rainfall. In this case, the annual probability is considered to be a random variable with a long-term average and inter-annual variance.

The inter-annual climatic variability is assumed to be due to the variation in the yearly occurrence of rain rate or rain attenuation p_o^y. This assumption suggests that the conditional CCDF $P(A > A^* | A > 0)$ of rain attenuation or $P(R > R^* | R > 0)$ of rainfall rate are invariant from one year to another [Rosenfeld *et al.*,.1990] [Kedem *et al.*, 1990] [Elthir and Bras, 1993] [Sauvageot, 1994] [Xie and Arkin, 1996] [Nzeukou and Sauvageot, 2002]. Particularly, for rainfall rate, it follows that the yearly rain amount M_T *[mm]* is given by:

$$\mathrm{M_T} = P_o^y \times \overline{R} \times T\,, \tag{10.17}$$

$$M_T = P_o^y \times \overline{R} \times T \,, \tag{10.17}$$

where $\overline{R} = E[R > R^* | R > 0]$ *[mm.h^{-1}]* is the conditional average rainfall rate (i.e. when it is raining) and T *[h]* is the integration duration (i.e. one year). Finally, the inter-annual climatic variance is given by:

$$\sigma_C^2 = \left(\frac{\sqrt{\text{var}(M_T)}}{E[M_T]} \cdot p \right)^2 \tag{10.18}$$

where the term $\sqrt{\frac{var(M_t)}{E[M_T]}}$ is known as the climatic ratio, r_c, and is location dependent. Annex 2 of Recommendation ITU-R P.678 provides digital maps of r_c.

10.4 Risk and reliability concepts

Currently the ITU specifies performance/availability objectives for radio networks using average cumulative distributions (e.g. average year, average worst month). While this method has in the past served the radio network planners well, changes in the telecommunication market environment have created the need for a broader range of grade of service concepts. Ideally the system designer must be able to make the trade-off between, on the one hand, the cost of the envisaged new network and, on the other hand, the satisfaction of the users of such a network. The current ITU performance/availability objectives do not help the designer in making such analysis. In general it can be stated that when there is dynamic economic interaction between users and service providers, a more sophisticated approach to performance/availability objectives will be needed. In looking for such new approaches it is logical to pay attention to concepts more commonly used in reliability engineering, such as risk, return period and mean time to failure. However, account must always be made for the specific properties of radio propagation environments (e.g. cyclo-stationarity of weather-related propagation). Furthermore, since new propagation experiments are very expensive, it is desirable that the information for the new concepts can be extracted from available data in a reliable manner.

10.4.1 Risk analysis

10.4.1.1 First approach

In this approach the relevant parameter is the "risk" that a certain system meeting long-term objectives will function unsatisfactorily for a subset of users during a certain (shorter) time span.

The "risk" can be expressed as fraction of the users experiencing a lower grade of service than what nominally may be expected. Another way is to express the "risk" as the probability that an individual user within a shorter time span will experience a lower grade of service than what the system would provide on average. This implies a variability analysis where data on the expected unavailability has to be supplemented with data on variability of the unavailability. The models for the monthly periods may easily be used to define, for a monthly reference period, risk percentiles or return periods for fixed threshold levels.

Figure 1 of Recommendation ITU-R P.678 provides the necessary information to evaluate risk associated with worst-month t.f.e. values. Applying equations (10.11) and (10.12) above allows this evaluation for annual t.f.e. values.

For other reference periods new analyses are needed, requiring the generation of CCDFs of the occurrence of fades or interferences for that reference period.

Annex 10.A.3 provides two examples to clarify the procedure for the calculation of the outage and fade margin associated with given risk or confidence intervals.

The same procedure may be used to evaluate the risk/confidence associated with an extra fade margin or with a relaxed (higher) outage specification.

10.4.1.2 Estimation of the risk associated with propagation margin

Given a rain attenuation, A, exceeded for a probability, p, Annex 3 of Recommendation ITU-R P.678 provides a method to estimate the risk that the yearly probability will exceed $p_{\mathcal{R}}$.

This estimation approach could be extremely useful for system designers and satellite operators, especially if financial penalties are demanded when a target yearly availability is not achieved.

Two examples of the risk for two radio links at 20 GHz between two Earth stations located in Ottawa (Canada) and Quito (Ecuador) are shown in Figure 10.1. The CCDFs were predicted by Recommendation ITU-R P.618 and the error in the predicted CCDF (σ_M^2 in Step 5 of Annex 2 of Recommendation ITU-R P.678) is assumed to be 0.

FIGURE 10.1

Risk $\Re$ on the yearly availability for Ottawa (Canada) (a) and Quito (Ecuador) (b) radio links at 20 GHz

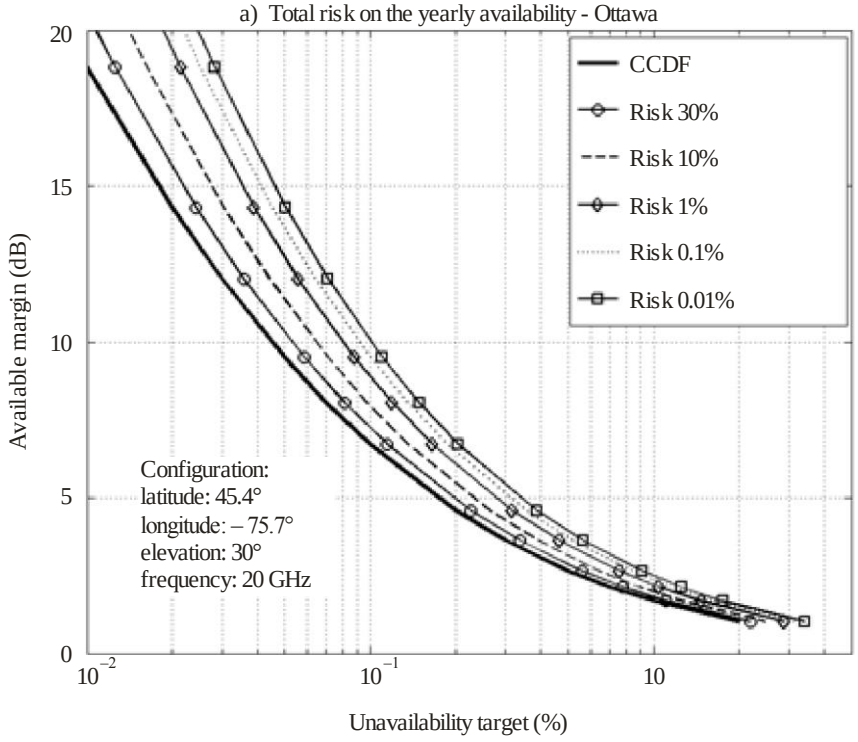

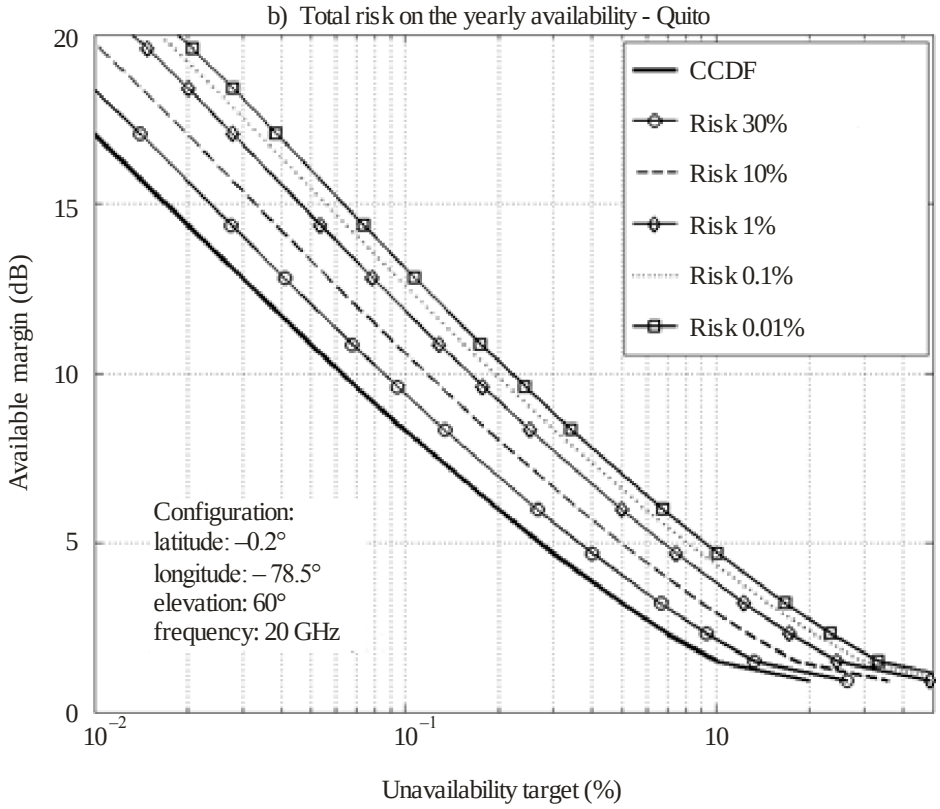

Radio-Meteo. 10-01

For Ottawa configuration,

– starting from an available margin of 6.7 dB,
  - the availability of 99.9% is guaranteed with a risk $\Re$ =50% (initial prediction),
  - the availability of 99.83% is guaranteed with a risk $\Re$ =1%,
  - the availability of 99.80% is guaranteed with a risk $\Re$ =0.01%.
– Reciprocally, to guarantee a targeted yearly availability of 99.9%,
  - with a risk $\Re$ =50%, a margin of 6.7 dB is needed (initial design),
  - with a risk $\Re$ =1%, a margin of 8.9 dB is needed,
  - with a risk $\Re$ =0.01%, a margin of 10.1 dB is needed.

For Quito configuration,

– starting from an available margin of 8.3 dB,
  - the availability of 99.9% is guaranteed with a risk $\Re$ =50% (initial prediction),
  - the availability of 99.75% is guaranteed with a risk $\Re$ =1%,
  - the availability of 99.66% is guaranteed with a risk $\Re$ =0.01%.

– Reciprocally, to guarantee a targeted yearly availability of 99.9%,
  - with a risk $\Re$ =50%, a margin of 8.3 dB is needed (initial design),
  - with a risk $\Re$ =1%, a margin of 11.9 dB is needed,
  - with a risk $\Re$ =0.01%, a margin of 13.1 dB is needed.

10.4.2 Return period

The return period is defined as the average time period between the occurrence of two consecutive outages or failures of the system. Mathematically it is the inverse of the probability of outage multiplied by the sampling time unit.

A return period of *N* years implies that there is an average annual "risk" (probability of occurrence) of 1/*N* that the value in question is exceeded.

The risk that a value with a return period of *N* years (average annual probability of occurrence 1/*N*) is exceeded at least 1 time in a particular period of *M* years is given by

$$P_{N,M} = 1 - (1 - 1/N)^M \tag{10.22}$$

This is essentially the determination of the distribution function of the worst year, analogous to the "worst-month" evaluation [Brussaard and Watson, 1979].

The concept of return period does not give additional information in addition to the probability distribution. Nevertheless, by the usage of this concept the performance/outage objectives may be brought closer to the experience of the users.

10.4.3 Mean time to failure

Here the performance is measured by the time between occurrences of two subsequent failures of a given service. Obviously a lot of consideration must be given to what constitutes a failure. Several failure modes can be defined (ranging from mild failure to catastrophe), in which the duration of outages is also considered. In order to apply this concept one must have detailed knowledge of the time structure of propagation phenomena. Fade duration statistics must therefore be enhanced with a statistical process model (e.g. Markov model for duration of fades or inter-fade periods). Related concepts: hazard rate, force of mortality.

10.4.4 Other considerations

In mobile radio and broadcasting systems the performance objectives are usually expressed in coverage and availability percentages which must be met at the edge of the cell or coverage area. There is an ambiguity in this definition with regard to cell edge and the size of area element to use. With the advent of microcells it may be questioned whether this still is a good concept. For such small areas the risk associated with not providing proper coverage is difficult to assess from the point of view of statistical modelling. Another aspect which has not been addressed yet is that related to objective temporal effects (to be distinguished from the pseudo-temporal effects due to motion of the users). Ducting effects may change the propagation properties around a large area, producing interference and loss of capacity. While the time percentage of severe ducting may be less than 1%, it may result in deterioration of communication quality for many users.

10.4.5 Relation to services

1) For fixed radio (terrestrial and satellite) services integrated in ISDN, the statistical description of propagation effects in terms of average distributions such as “average annual” and “average annual worst month” distributions seems at the moment to be adequate.

2) For more specialised services (e.g. Television Relay, Broadcast, Video-conferencing and VSAT services) the need is to deliver with a high likelihood of success, within a particular time interval, a required grade of service. For example, unavailability may be specified to be less than a certain, contractually agreed, value. In this case the contractor (the service provider) must assess the risk of not providing the required service against cost. This implies a variability analysis where data on the expected unavailability have to be supplemented with data on variability of the unavailability.

3) Average statistics and variability data with other reference time period than the month or the year may also be needed. Very detailed statistics, such as fade duration and inter-fade duration statistics are of interest for estimating recovery times after loss of synchronisation and the expected waiting time of a video-conference user momentarily cut off by severe fading. Such an estimate is needed, for example, if the option of rescheduling the service at a later time is to be offered to the user. In the latter case an analysis of the associated risk is needed for determining the appropriate tariffs of this service.

10.4.6 Risk of occurrence of outages

The probability of occurrence of outages of a given duration is a parameter that may be used for the evaluation of the risk of outage associated with a particular quality specification. In the context described above, the occurrence of outages of long duration is particularly interesting.

The occurrence of extreme values in many cases has an exponential distribution. At Eindhoven University of Technology, an analysis was made of the extreme values of the duration of fades experienced in the reception of the 20 GHz Olympus beacon at the satellite earth station of Eindhoven University of Technology (EUT). For this analysis a dataset of fade events for various threshold levels and including start time and end time of each event, was used.

This analysis [Brussaard, 1995] resulted in a conditional exponential model for the occurrence of long fades. According to this model, fade durations longer than 60 seconds that are due to convective rain (5 dB and higher for the 20-GHz link at EUT) are exponentially distributed. This leads to an extremely simple model for risk assessment for conditions of deep fading. If the total exceedance at the threshold level of interest is X_0 and a fraction F_0 of this exceedance is due to fades of longer duration than 60 seconds, then the total number of fade events follows from

$$N_0 = F_0 X_0 / C_1$$

where C_1 is the average duration for the conditional exponential distribution

$$P(X_0 \geq x) = \exp(-(x\text{-}60)/C_1) \quad \text{for all } x > 60$$

Values of $F_0 = 0.90$ and $C_1 = 425$ seconds were found for fades > 5 dB at 20 GHz.

If the cumulative distribution function (CDF) of attenuation is known, the CE model allows a very simple evaluation of risk parameters such as:

– the number of fade events where a specified threshold level is exceeded for a specified time duration;

– the risk of experiencing a system outage of a specified duration.

10.5 Conclusions

Usage of the CCDF F of the monthly time fraction of excess offers great flexibility for predicting and analysing the variability of time fraction of excess in various extreme conditions. F can adequately be modelled as conditional exponential, so that the relationship $C_0(p)$ can be considered to be the basic "climatological" data required for predicting the relative variability of various extreme statistics around the mean statistics.

At the moment, the “risk” concept seems to be the most suitable for extending the current ITU performance/availability criteria. This “risk” concept does not require any changes to the structure of the performance objectives; rather, it gives the network designer another tool to design the radio network. As an example, the usefulness of estimating the inter-annual variability of rain attenuation statistics has been illustrated through guidelines for the design of future high frequency satellite communication systems. Furthermore, as long as the chosen observation period is not shorter than a month, not very large amounts of new propagation data need to be acquired, since sound models for the variability of the monthly distributions are already available. For shorter time period re-analysis of existing data is required.

The conditional exponential model also provides basic information for the evaluation of risk parameters in outage specifications.

ANNEX 10.A.1

Rank-order statistics

The term "rank-order statistics" refers to the method by which the cumulative probability distribution of a random variable can be estimated from observed data. The algorithm for this method is given in Steps 1 and 2 in Annex 10.A.2. In this method each data sample is assigned a probability value. There is no need to use "bin-classes" to determine the cumulative distribution function.

According to [Gumbel, 1958] the m-th largest value, $\underline{X}_m$, of N independent observations of a random variable $\underline{X}$ should be assigned the (cumulative) probability value:

$$p_m = <F(\underline{X}_m)>$$

where <...> denotes the ensemble averaging and $F()$ denotes the probability distribution of $\underline{X}$. This at first sight seems to be a tautology since $F()$ is not known; the intention of the measurements is precisely to determine $F()$. However, the theoretical analysis of [Gumbel, 1958] shows that:

$$<F(\underline{X}_m)> = m/(N + 1)$$

and p_m is therefore independent of $F()$.

[Gumbel, 1958] also shows that $F(\underline{X}_m)$, the "reduced variable", has a Beta distribution.

ANNEX 10.A.2

Determination of C_0 and C_1 from measured data

Step 1: Order the N observed monthly time fractions of excess such that:

$$X_1 > X_2 > \ldots\ldots\ldots\ldots > X_N$$

Step 2: Assign to each X_i the probability value p_i:

$$p_i = i/(N+1) \tag{10.23}$$

$$\{i = 1, 2, \ldots., N\}$$

Step 3: Determine L from:

$$\sum_{i=L}^{i=N} X_i = 0.05 \sum_{i=1}^{i=N} X_i \tag{10.24}$$

Step 4: Determine C_0 and C_1 by regression on the data (X_i, $\ln(p_i)$), i = 1, ..., L, assuming the linear form:

$$n(p) = \ln(C_0) - X/C_1 \tag{10.25}$$

ANNEX 10.A.3

Risk assessment

Examples of outage and fade margin calculation associated with risk or confidence

a) Outage calculation

– The ratio Q associated with an annual t.f.e. of 0.01% for satellite-Earth paths in N.W. Europe is given by Recommendation ITU-R P.841 as Q = 6.5.

– Recommendation ITU-R P.678 shows that for Q = 6.5 a worst-month t.f.e. of 1.8 times the average has an average risk of 10% of being exceeded (return period ten years).

– Therefore, at a risk level of 10%, the worst-month outage is 1.8 x 6.5 x 0.01 = 0.117% for a threshold (link margin) that is, on average, exceeded for 0.01% of the time.

b) Fade margin calculation

Suppose the following requirement is given: at a confidence level of 95%, a worst-month t.f.e. (outage) of 0.1% may not be exceeded on a satellite link in Japan. We must now use an iterative procedure:

1) Make an initial estimate for the normalized parameter, e.g. 2.
2) For an average worst-month t.f.e. of 0.1/2 = 0.05% in Japan (Q = 4; β = 0.13) the factor Q is 7.7 (Recommendation ITU-R P.841).
3) For Q = 7.7, the normalized parameter associated with a confidence level of 95% (return period 20 years) is 2.6 (Recommendation ITU-R P.678).
4) Repeat steps 2 and 3 to confirm that the result converges to a value of 2.6.
5) The average annual t.f.e. (outage) to be considered is therefore .1/2.6/7.7 = 0.005%.
6) The margin required now follows from the general fading prediction (Recommendation ITU-R P.618).

REFERENCES

BOULANGER, X., JEANNIN, N., FERAL, L., CASTANET, L. LACOSTE and CARVALHO, F [2013] Inter-Annual Variability, Risk and Confidence Intervals Associated with Propagation Statistics. Part II: Parameterization and Applications, submitted to International Journal of Satellite Communications and Networking, under review.

BRUSSAARD, G. and WATSON, P.A. [1979] Annual and annual-worst-month statistics of fading on Earth-satellite paths at 11.5 GHz. Electronic Letters, Volume 14, 9, pp. 278-280.

BRUSSAARD, G. [1995] Extreme-value analysis of outage durations due to rain in satellite communication systems, URSI Comm. F Open Symposium, Ahmedabad, India.

CASIRAGHI, E. and PARABONI, A. [1989] Assessment of CCIR worst-month prediction method for rain attenuation. Electronic Letters, Volume 25, 1.

CRANE, R.K. and DEBRUNNER, W.E. [1978] Worst-month statistics. Electronic Letters, Volume 14, 2, pp. 38-40.

CRANE, R.K. [1990] Rain attenuation measurements: variability and data quality, Radio Science, Vol. 25, No. 4, pp. 455-473.

CRANE, R.K. [1991] Worst-month: A new approach, Radio Science, 26, 4, pp. 801-820.

COST 205, [1985a] Influence of the atmosphere on Earth-satellite radio propagation at frequencies above 10 GHz; precipitation studies - Report EUR 9923 EN, also in Alta Frequenza, Volume 54, 3, pp. 116-132.

COST 205, [1985b] Influence of the atmosphere on Earth-satellite radio propagation at frequencies above 10 GHz; rain attenuation statistics - Report EUR 9923 EN, also in Alta Frequenza, Volume 54, 3, pp. 182-193.

DELLAGIACOMA, G. and TARDUCCI, D. [1987] A different approach to worst-month rain statistics: Theory and experimental results, Radio Science, Volume 22, 2, pp. 266-274.

ELTHIR, E. A. B. and BRAS, R. L. [1993], Estimation of the fractional coverage of rainfall in climate models, Journal of Climate, vol. 6, no. 4, pp. 639–656.

FUKUCHI, H., KOZU, T., and TSUCHIYA, S. [1985] Worst-month statistics of attenuation and XPD on Earth-space path, IEEE Trans. Ant. Prop., Volume AP-33, pp. 390-396.

FUKUCHI, H. and WATSON, P.A. [1989] Statistical stability of cumulative distributions of rainfall rate in the UK, Proc. IEE, Volume 136, Pt. H., No. 2, pp. 105-109.

GUMBEL, E.J. [1958] Statistics of extremes, Columbia Univ. Press.

HOWELL, R.G., THIRLWELL, J. and EMERSON, D.J. [1983] 11/14 GHz depolarization measurements along the OTS slant-path at Martlesham Heath, England, IEE Conf. Publ., 219, part 2, pp. 121-126, IEE Third International Conference on Antenna and Propagation (ICAP 83) University of East Anglia, Norwich, United Kingdom.

JEANNIN, N., BOULANGER, X., FERAL, L., CASTANET and L. LACOSTE [2013] Inter-Annual Variability, Risk and Confidence Intervals Associated with Propagation Statistics. Part I: Theory of Estimation, submitted to International Journal of Satellite Communications and Networking, under review.

KEDEM, B., CHIU, L. S. and NORTH, G. R. [1990], Estimation of mean rain rate: Application to satellite observations, J. Geophys. Res., 95(D2), 1965–1972, doi:10.1029/JD095iD02p01965.

MAWIRA, A. [1980] Statistics of rain rates, some worst-month considerations, Ann. des Telecomm., Volume 35, 11-12, pp. 423-428.

MAWIRA, A. [1985] Variability of worst-month quotient Q, Electronic Letters, Volume 21, pp. 1073-1074.

MAWIRA, A. [1989] Prediction of the yearly and worst-month time fraction of excess using the conditional exponential model, Report 789/RNL/89, PTT research - Neher Labs.

MAWIRA, A [1999] Variability of Monthly Time Fraction of Excess of Atmospheric Propagation Parameters, PhD thesis, Eindhoven University of Technology, ISBN 90-72125-65-7

NZEUKOU, A. and SAUVAGEOT, H. [2002], "Distribution of rainfall parameters near the coasts of France and Senegal", Journal of Applied Meteorology, vol. 41, no. 1, pp. 69–82.

POIARES BAPTISTA, J.P.V., KUBISTA, E., WITTERNIGG, N. and RANDEU, W.L. [1989] Worst-month statistics for high outage probabilities, IEE Conf. Publ. No. 301, part 2, pp. 10-13, ICAP 89, Univ. of Warwick, Coventry, United Kingdom.

ROSENFELD, D., ATLAS, D., and SHORT, D. A. [1990] The estimation of convective rainfall by area integrals: 2. The Height-Area Rainfall Threshold (HART) method, J. Geophys. Res., 95(D3), 2161–2176, doi:10.1029/JD095iD03p02161.

SAUVAGEOT, H. [1994], The probability density function of rain rate and the estimation of rainfall by area integrals, Journal of Applied Meteorology, vol. 33, no. 11, pp. 1255–1262.

SEGAL, B. [1980] The estimation of worst-month precipitation attenuation probabilities in microwave system design, Ann. des Telecomm., Volume 35, 11-12, pp. 429-433.

XIE, P. and ARKIN, P. A. [1996], Analyses of Global Monthly Precipitation Using Gauge Observations, Satellite Estimates, and Numerical Model Predictions, J. Climate, 9, 840–858, doi: http://dx.doi.org/10.1175/1520-0442(1996)009<0840:AOGMPU>2.0.CO;2

YON, K.M., STUTZMAN, W.L. and BOSTIAN, C.W. [1984] Worst-month rain attenuation and XPD statistics for satellite paths at 12 GHz, Electronic Letters, Volume 20, pp. 646-647.

International Telecommunication Union
Sales and Marketing Division
Place des Nations
CH-1211 Geneva 20
Switzerland
Fax: +41 22 730 5194
Tel.: +41 22 730 6141
E-mail: sales@itu.int
Web: www.itu.int/publications

ISBN 978-92-61-14451-7 SAP id 38634

Printed in Switzerland
Geneva, 2014
Photo credit: Shutterstock®